

University of Strathclyde

Department of Electronic and Electrical Engineering,

Glasgow, United Kingdom.

**PERFORMANCE AND RELIABILITY  
STUDIES OF ATMOSPHERIC PLASMA  
SPRAYING RANEY NICKEL ELECTRODES  
FOR ALKALINE ELECTROLYSERS**

By

Daniel Szymon Chade

A thesis presented in fulfilment of the requirements for the degree of

*Doctor of Philosophy*

2014

## **Copyright Statement**

*This thesis is the result of the author's original research. It has been composed by the author and has not been previously submitted for examination which led to the award of a degree.*

*The copyright of this thesis belongs to the author under the terms of the United Kingdom Copyright Acts as qualified by University of Strathclyde Regulation 3.50. Due acknowledgment must always be made of the use of any material contained in, or derived from, this thesis.*

**Signed**

**Date**

## Acknowledgments

I would like to acknowledge the contribution of many people to this research project without whom, this work would not be possible.

First of all I would to express my deep gratitude to my current supervisors: Dr Leonard Berlouis, Prof. David Infield and my former supervisor Prof. Andrew Cruden for their guidance and support during all the doctoral programme duration, but also European Research Development Fund for providing research grant.

I would like to acknowledge Prof. David Dvorak and Tomek Miklis for their contribution that was very helpful in writing one of the thesis chapters and Force Technology, Denmark, especially Mr Peter Tommy Nielsen and Dr Troels Mathiesen for delivering samples, that allowed me to conduct major part of the experimental work.

I would like to thank Neil Hodgson for electrochemical cell production and help in its design, but also the crew of mechanical and electrical workshops in Electronic and Electrical Engineering Department (Kevin, David, George) for doing all the rest of the things that I was not able to do only by myself.

I would like to thank all the friends that shared the office space with me during this period of time especially: Evelyn, Chin Teng, Mahdi, Sikai, Maria Carla, Andy and Douglas for a very pleasant time.

Finally, special thanks to my parents to whom I would like to dedicate this work and who always mentally helped me in all type of life situations. *Dziękuję za wsparcie, byliście osobami na które zawsze mogłem liczyć.*

## **Abstract**

This PhD main aim was the examination of the Atmospheric Plasma Spraying Raney nickel electrodes samples with strong emphasis on electrochemical characterisation and investigation of the degradation/deactivation mechanisms which occur within the electrodes structure.

Nowadays research in alkaline electrolysis mainly aims to improve efficiency, extend durability and decrease the price of electrolyser units. One of the methods to achieve all of these goals is the development of novel electrode types. Raney nickel electrodes manufactured by Force Technology (Denmark) using a novel atmospheric plasma spraying method (APS), have been shown to exhibit good performance with low overpotential towards the hydrogen evolution reaction (HER). In comparison to the other electrode production methods APS is considered also to be relatively cheap. To our knowledge, this is the first time APS has been applied for the production of Raney nickel electrodes for water electrolysis. APS is cheaper and simpler than actually used vacuum plasma spraying, making it more suitable for mass production of the electrodes.

For a purpose of experimental work the laboratory environment was set-up which consisted of the electrochemical cells and the data acquisition devices. The methods of Tafel extrapolation, cyclic voltammetry, electrochemical impedance spectroscopy, scanning electron microscopy were applied, that allowed to estimate electrochemical parameters of the samples. Characterisation work concluded, that overall performance of the tested samples have been attributed to the very high electrochemical active area as well as enhanced kinetics obtained for these samples following the chemical and electrochemical activation procedures

Investigation of degradation mechanisms work part identified hydrides impact as a main source of deactivation for cathodes. To prevent, this effect techniques of hydrides oxidation and activation of the electrolyte were tested however, neither of them was able to eliminate hydrides impact completely. The overall work is



concluded that suppressing hydrides impact should be possible by improving electrodes manufacturing process for example by application of molybdenum coatings.

The performed study is supplemented by two additional outcomes. First of them is electrochemical measurement device, which concept was created and initial prototype was built using cheap electronic components. Second one is feasibility study of application of hydrogen storage technologies to increase hybrid wind energy-diesel electricity generation system efficiencies.

## Contents

1. Introduction to the thesis.....	1
1.1. Thesis motivation and objectives .....	1
1.2. Methodology .....	2
1.3. Thesis structure overview.....	3
2. Introduction.....	6
2.1. Energy issues .....	6
2.2. Hydrogen economy – Hydrogen as an energy vector in comparison with other methods .....	8
2.3. Hydrogen storage methods.....	15
2.4. Hydrogen production methods .....	18
2.5. Water electrolyzers .....	22
3. Electrolysis background.....	31
3.1. Basic electrochemistry of electrolyser cells .....	31
3.2. Fundamentals of alkaline electrolyzers cell design .....	38
4. Experimental.....	47
4.1. Experimental system set-up.....	47
4.1.1. Electrolyser cell design .....	47
4.1.2. Electrochemical measurements system implementation.....	52
4.2. Experimental techniques .....	53
4.2.1. Tafel extrapolation .....	53
4.2.2. Cyclic voltammetry (CV).....	54
4.2.3. Electrochemical impedance spectroscopy (EIS).....	56
4.2.4. Scanning electron microscope (SEM).....	59
4.3. System components description .....	60
4.3.1. Chemical reagents .....	60
4.3.2. Electrochemical measuring equipment .....	62
4.3.3. Soldering equipment .....	62
4.3.4. Reference electrodes .....	62
4.3.5. Insulation.....	63

4.3.6.	Membrane/Diaphragm .....	63
5.	Alkaline electrolyser system troubleshooting.....	67
6.	Evaluation of Raney nickel electrodes prepared by atmospheric plasma spraying for alkaline water electrolyzers .....	77
6.1.	Introduction .....	77
6.2.	Experimental setup .....	79
6.2.1.	General system configuration .....	79
6.2.2.	Working electrode sample preparation .....	80
6.2.3.	Experimental procedures employed .....	83
6.3.	Results and discussion.....	84
6.3.1.	Cyclic voltammetry .....	86
6.3.2.	Potentiodynamic analysis and Tafel extrapolation .....	90
6.3.3.	Electrochemical impedance spectroscopy.....	94
6.4.	Conclusions .....	103
7.	Operational tests under variable load conditions of atmospheric plasma spraying Raney nickel electrodes.....	110
7.1.	Introduction .....	110
7.2.	System setup and experimental .....	116
7.3.	Results and discussion.....	117
7.3.1.	Stable load operation and impact of hydride formation.....	118
7.3.2.	Oxidation of hydrides on the electrodes .....	120
7.3.3.	In situ activation of the electrolyte.....	129
7.3.4.	Variable load operation .....	135
7.3.5.	Single cell electrolyser tests .....	138
7.4.	Conclusions and summary.....	144
8.	Design of the prototype of electrochemical measurement device .....	149
8.1.	Hardware design.....	149
8.2.	Electrochemical experimental testing.....	153
8.3.	Bubbles impact investigation .....	158
8.4.	Conclusions .....	164
9.	Feasibility study of wind to hydrogen system for Arctic remote locations – Grimsey island case study .....	166

9.1.	Introduction .....	166
9.1.1.	Wind to hydrogen projects review.....	167
9.1.2.	Grimsey island description .....	168
9.2.	Research methodology .....	169
9.2.1.	Project assumptions and basic model data.....	169
9.2.2.	System components and architecture.....	171
9.2.3.	Component costs and parameters.....	172
9.2.4.	Economical parameters .....	175
9.3.	Results and discussion.....	175
9.3.1.	Wind-diesel system.....	176
9.3.2.	Wind-diesel-hydrogen system.....	178
9.3.3.	Wind-hydrogen system .....	183
9.4.	Conclusions .....	185
10.	Summary .....	190
10.1.	Future work .....	191
APPENDIX: List of Publications .....		193

## List of figures

### Chapter 2

Figure 2-1. Growth in the use of primary energy in different world regions (left); Growth in the use of different fuels in the world (right).....	7
Figure 2-2. Historical variation in the amount of new oil discovered per year and in the consumption of oil per year. Source: Aleklett (2006).....	8
Figure 2-3. Power density vs. energy density of various energy storage systems.....	10
Figure 2-4. Honda FCX Clarity - hydrogen/fuel cell vehicle .....	12
Figure 2-5. Hydrogen powered plane concept .....	13
Figure 2-6. Hydrogen storage methods with temperature and weight dependence ...	16
Figure 2-7. Gaseous hydrogen storage cylinders types.....	17
Figure 2-8. Estimated world hydrogen production and use (2008) .....	19
Figure 2-9. Future potential costs of electrolytic hydrogen .....	22
Figure 2-10. Alkaline electrolysis cell concept.....	23
Figure 2-11. PEM electrolysis cell concept .....	25

### Chapter 3

Figure 3-1. Cell potential for hydrogen production by water electrolysis as a function of temperature .....	32
Figure 3-2. Dependence of exchange current density for hydrogen evolution reaction on the strength of the metal-hydrogen bond formed in the electrode reaction .....	35
Figure 3-3. A qualitative comparison of the energy losses caused by reaction resistances, ohmic resistances, ionic resistance and bubble resistance .....	36
Figure 3-4. 3D plot of the conductivity of aqueous solutions of KOH as a function of temperature and concentration .....	39
Figure 3-5. Schematics of configurations a – monopolar, b - bipolar electrolysers ..	41
Figure 3-6. Basic cell structure of bipolar electrolyser .....	42

## Chapter 4

Figure 4-1. 1 <sup>st</sup> prototype of alkaline water electrolyser .....	48
Figure 4-2. Domains of corrosion, immunity and passivation of copper at 25°C.....	50
Figure 4-3. Electrolyser design made of glass .....	51
Figure 4-4. Three electrode set-up .....	52
Figure 4-5. Experimental determination of exchange current density using the Tafel's equations .....	54
Figure 4-6. Cyclic voltammetry waveform.....	55
Figure 4-7. Cyclic voltammogram of plain nickel sample immersed in 30% KOH solution.....	56
Figure 4-8. (a) Equivalent circuit for a simple electron transfer couple O/R at an inert electrode held at the equilibrium potential for a solution containing oxidants and reactants (reductants) (b) the corresponding Argand diagram.....	58
Figure 4-9. Schematic drawing of electron and x-ray optics of SEM.....	60

## Chapter 5

Figure 5-1. Rotating Disc Electrode system overview.....	68
Figure 5-2. Potential (Current density) curves on 10 Hz and 30 Hz rotating speed of Raney nickel.....	69
Figure 5-3. Electrode used for vertical electrode configuration .....	70
Figure 5-4. Potential (Current density) curves for electrodes before optimisation in rotating disc electrode configuration.....	74
Figure 5-5. Potential (Current density) curves for electrodes after optimisation with vertical electrodes orientation .....	75

## Chapter 6

Figure 6-1. SEM micrographs of the 30 $\mu\text{m}$ and 100 $\mu\text{m}$ Raney nickel samples before and after chemical activation .....	82
Figure 6-2. SEM micrographs of the 300 $\mu\text{m}$ Raney nickel samples cross section before and after chemical activation .....	83

Figure 6-3. Cyclic voltammograms of Raney nickel samples at the temperature of 70°C. Scan rate = 50 mV/s.....	88
Figure 6-4. Cyclic voltammograms of the Raney nickel 100 µm sample as a function of temperature. Scan rate = 50 mV/s.....	90
Figure 6-5. Potentiodynamic scans of Raney nickel 30 µm sample as a function of temperature.....	93
Figure 6-6. Potentiodynamic scans of Raney nickel 100 µm sample as a function of temperature.....	94
Figure 6-7. Randles equivalent circuit model for Raney nickel.....	95
Figure 6-8. EIS data at different temperatures (a) 30°C; (b) 50°C; (c) 70°C for Raney nickel 30 µm sample as a function of potential .....	98
Figure 6-9. EIS data at different temperatures (a) 30°C; (b) 50°C; (c) 70°C for Raney nickel 100 µm sample as a function of potential .....	100
Figure 6-10. Electrolyte resistance as a function of potential and temperature for 100 µm sample.....	103

## Chapter 7

Figure 7-1. Electrolyser response to rapid cycling.....	111
Figure 7-2. Degradation of Hydrogenics alkaline water electrolyser in a function of intermittent load cycles .....	112
Figure 7-3. Cathode polarisation potentials during longer term experiments. T = 70°C, charging current 100 mA/cm <sup>2</sup> , 100 s averaged currents from three replicate experiments for (▲) bare Ni and (■) Ni with Fe coating .....	113
Figure 7-4. Overvoltage of Raney cathode as a function of the residual Al content, T=100°C, 10M KOH.....	114
Figure 7-5. Reference voltage of VPS electrodes measured at 80°C and 300 mA/cm <sup>2</sup> as a function of time.....	115
Figure 7-6. Biologic (left) and Solartron (right) electrochemical interfaces working two separate experiments in the fume cupboard.....	117
Figure 7-7. Deactivation of Raney nickel 100 µm sample under constant load operation under constant current density of 300 mA/cm <sup>2</sup> .....	119

Figure 7-8. A - Operation of 100 $\mu\text{m}$ electrode sample under current density of $-0.3 \text{ A/cm}^2$ , within subsequent cycles separated with oxidation process, B - Oxidation currents for every cycle under $-0.85 \text{ V}$ potential.....	121
Figure 7-9. A - Operation of 100 $\mu\text{m}$ electrode sample under current density of $-0.3 \text{ A/cm}^2$ , within subsequent cycles separated with oxidation process, B - Oxidation currents for every cycle at $-0.2 \text{ V}$ potential.....	123
Figure 7-10. A - Operation of 100 $\mu\text{m}$ electrode sample under current density of $-0.2 \text{ A/cm}^2$ , within subsequent cycles separated CV measurements, B – cyclic voltammograms for each cycle - $50 \text{ mV/s}$ scan rate .....	125
Figure 7-11. $j(\text{V})$ curve of operated sample initially, after 24 and 48 hours.....	127
Figure 7-12. Comparison of the time effect of vanadium influence for Raney nickel cathode performance .....	130
Figure 7-13. Comparison of the time effect of molybdenum influence for Raney nickel cathode performance .....	131
Figure 7-14. A - Deactivation of Raney nickel electrode in stable load with oxidation cycles, B - Reactivation of Raney nickel electrode in stable load with oxidation cycles after adding vanadium to the electrolyte.....	133
Figure 7-15. Comparison of the performance of Raney nickel electrodes deactivated by hydrides in pure KOH electrolyte and with addition of vanadium and/or molybdenum compounds .....	134
Figure 7-16. A- Intermittent operation time impact, B – Electrodes $j(\text{v})$ curves before and after operation.....	136
Figure 7-17. Comparison of one of the initial (A) and further (B) cycles during intermittent load operation .....	137
Figure 7-18. Anode and cathode $j(\text{V})$ curves measured in 3 electrodes system configuration .....	139
Figure 7-19. $j(\text{V})$ curves of single cell - measured and calculated data – initial conditions.....	140
Figure 7- 20. A - Registered performance change during 1 <sup>st</sup> and 2 <sup>nd</sup> cycle operation under $200 \text{ mA/cm}^2$ current density, B - Comparison of $j(\text{V})$ curves of single cell at initial conditions, after 1 <sup>st</sup> cycle and after 2 <sup>nd</sup> cycle.....	141
Figure 7-21. Comparison of cathode initial and final performances .....	142



Figure 7-22. Comparison of anode initial and final performances .....	143
Figure 7-23. $j$ (V) curves of single cell - measured and calculated data – final conditions .....	143

## Chapter 8

Figure 8-1. Electronic amplifiers box .....	151
Figure 8-2. Current and temperature sensors box .....	151
Figure 8-3. Labview user interface .....	152
Figure 8-4. Full system overview.....	153
Figure 8-5. Current fluctuations overview under constant load of 3.65 V .....	154
Figure 8-6. Voltage time effect overview for theoretically set value of 3.65 V .....	155
Figure 8-7. Temperature time effect overview under constant load of 3.65 V .....	156
Figure 8-8. Variable load operation comparison.....	157
Figure 8-9. Open cell photo .....	159
Figure 8-10. Applied voltage for bubble effect analysis.....	160
Figure 8-11. Current with fluctuations caused by bubbles .....	160
Figure 8-12. Current fluctuation zoom.....	161
Figure 8-13. Electrode surface just before bubbles release 115.45 s .....	162
Figure 8-14. Electrode surface just after bubbles release 115.73 s.....	162

## Chapter 9

Figure 9-1. Comparison between the average hourly load of 2010 and 2011 .....	170
Figure 9-2. Comparison of annual wind and load profile for Grimsey.....	171
Figure 9-3. System layout in HOMER software.....	172
Figure 9-4. Percentage of excess electricity generated and net presents costs of the investment over lifetime in a function of wind turbines amount .....	178
Figure 9-5. Lifetime cash flow summary of WHD system.....	181
Figure 9-6. Comparison of stored hydrogen, excess electrical production and diesel generation monthly – WHD system.....	182

Figure 9-7. Comparison of stored hydrogen, excess electrical production - WH system..... 185

## List of tables

### Chapter 2

Table 2-1. Mass and volume of alternative hydrogen storage system for a mid-sized hydrogen fuel cell automobile, with 3.0 kg of stored hydrogen (sufficient for 610 km driving range) ..... 11

Table 2-2. Comparison of technologies for H<sub>2</sub> production from natural gas ..... 20

### Chapter 3

Table 3-1. Water electrolyser developers and cell operating conditions ..... 44

### Chapter 4

Table 4-1. List of chemical reagents used and their suppliers ..... 61

Table 4-2. Membrane - Celgard 3501 specifications ..... 64

### Chapter 5

Table 5-1. Factors influencing alkaline electrolyser system performance ..... 73

### Chapter 6

Table 6-1. Force Technology APS electrodes performance compared to current results ..... 86

Table 6-2. Electroactive area estimation from CV measurements ..... 89

Table 6-3. Tafel analysis on the catalyst samples as a function of temperature ..... 91

Table 6-4. Fitted parameters obtained for EIS data for the 30  $\mu\text{m}$  sample as a function of temperature and applied potential ..... 97

Table 6-5. Fitted parameters obtained for EIS data for the 100 $\mu\text{m}$ sample as a function of temperature and applied potential .....	99
Table 6-6. Fitted parameters obtained for EIS data for the 300 $\mu\text{m}$ sample as a function of temperature and applied potential .....	101

## **Chapter 7**

Table 7-1. EIS parameters for 100 $\mu\text{m}$ sample just after activation and after 24 hours and 48 hours operation .....	128
--	-----

## **Chapter 8**

Table 8-1. Estimated basic parameters of built DAQ device .....	158
---	-----

## **Chapter 9**

Table 9-1. Summary of basic system parameters .....	174
Table 9-2. Simulation results for wind-diesel systems .....	177
Table 9-3. Optimal size of components for wind-hydrogen-diesel electricity generation system with sensitivity of each parameter considered .....	179
Table 9-4. Economical comparison of wind-hydrogen-diesel electricity generation system with diesel .....	180
Table 9-5. Optimal size of components for wind-hydrogen electricity generation system with sensitivity of each parameter considered .....	183
Table 9-6. Economical comparison of wind-hydrogen electricity generation system with diesel .....	184

## **Abbreviations list**

AC	Alternating Current
APS	Atmospheric Plasma Spraying
CAES	Compressed Air Energy Storage
COE	Cost of Energy
CPE	Constant Phase Element
CV	Cyclic Voltammetry
DAQ	Data Acquisition device/system
DOE	Department of Energy
EIS	Electrochemical Impedance Spectroscopy
HFCHV	Hydrogen Fuel Cell Hybrid Vehicle
IPCC	Intergovernmental Panel on Climate Changes
IRR	Internal Rate of Return
NPC	Net Present Costs
NREL	National Renewable Energy Laboratory
O&M	Operation and Maintenance
PCB	Printed Circuit Board
PEM	Proton Exchange Membrane
PURE	Promoting Unst Renewable Energy
RDE	Rotating Disc Electrode
SEM	Scanning Electron Microscope
SOEC	Solid Oxide Electrolyser Cell
SPP	Simple Payback Period
UPS	Uninterruptible Power Supply
VPS	Vacuum Plasma Spraying
WD	Wind-Diesel
WH	Wind-Hydrogen
WHD	Wind-Hydrogen-Diesel

## Physical symbols and constants

A	Surface/cross-sectional area (cm <sup>2</sup> )
C <sub>dl</sub>	Double layer capacitance (F)
CPE-T	Constant phase element magnitude
CPE-P	Constant phase element phase
E	Electrochemical potential (V)
E <sub>cell</sub>	Cell potential/voltage (V)
E <sub>rev</sub>	Reversible potential/voltage (V)
E <sub>tn</sub>	Thermoneutral potential/voltage (V)
F	Faraday constant (96485 J)
H <sub>rate</sub>	Hydrogen production rate (mol/s)
HHV	Higher Heating Value (286 kJ/mol)
I	Current (A)
j	Current density (A/cm <sup>2</sup> )
j <sub>0</sub>	Exchange current density (A/cm <sup>2</sup> )
k	Specific conductivity (S/m)
LHV	Lower Heating Value (244 kJ/mol)
OCP	Open Circuit Potential (V)
p	Pressure (bar)
p <sub>0</sub>	Standard pressure (1 bar)
R	Ideal gas constant (8.314 J/K* <sup>o</sup> mol)
R	Resistance (Ω)
R <sub>ct</sub>	Charge transfer resistance (Ω)
R <sub>s</sub>	Electrolyte resistance (Ω)
R <sub>u</sub>	Uncompensated resistance (Ω)
t	Time (s)
T	Temperature (°C, K)
T <sub>0</sub>	Standard temperature (25° <sup>o</sup> C)
U	Voltage (V)
α	Electron transfer coefficient
β	Tafel slope (mV/dec)

$\beta_c$	Cathodic Tafel slope (mV/dec)
$\Delta G$	Gibbs free energy (J/mol)
$\Delta H$	Enthalpy change (J)
$\Delta S$	Entropy change (J/K)
$\epsilon_{HHV}$	Efficiency based on higher heating value (%)
$\epsilon_{LHV}$	Efficiency based on lower heating value (%)
$\eta_{\text{activation}}$	Activation overpotential/losses (V)
$\eta_{\text{Faradaic}}$	Faradaic efficiency (%)
$\eta_{\text{ohmic}}$	Ohmic overpotential/losses (V)
$\nu$	scan rate (mV/s)

# **1. Introduction to the thesis**

## **1.1. Thesis motivation and objectives**

There has been increased interest in alkaline water electrolysis in the first decade of 21<sup>st</sup> century. The technology is the most mature and commercialised of all the known types of electrolyzers used for hydrogen production. One reason for the growth of this technology is the demand for hydrogen as a future ecological and renewable energy carrier to be applied in transport, stationary applications or in mobile devices. H<sub>2</sub> may also act as excellent energy storage mechanism for variable load electrical energy generators such as wind turbines or photovoltaic panels.

Nowadays research in alkaline electrolysis mainly aims to improve efficiency, extend durability and decrease the price of electrolyser units. One of the methods to achieve all of these goals is the development of new electrode types. By way of example, Raney nickel electrodes manufactured by Force Technology (Denmark) using atmospheric plasma spraying method (APS) have been shown to exhibit good performance with low overpotential towards the hydrogen evolution reaction (HER). In comparison to other electrode production methods APS is considered also to be relatively cheap. To our knowledge, this is the first time when APS has been applied for the production of Raney nickel electrodes for alkaline water electrolyzers, so all the executed experiments contribute to the actual state of knowledge and attest to the novelty of the performed research work.

The main aim of the research presented in this thesis was to investigate the parameters responsible for giving good performance for the various different APS electrode types and to investigate these electrochemically. The investigation of degradation effects that occur during long term operation and under intermittent load regimes was a specific objective of the study. The planned research was designed to check and verify the robustness of these electrodes for application in commercial alkaline water electrolyzers prior to potential further APS technology



commercialisation. The research would also deliver knowledge about the conditions necessary to obtain high energy efficiencies for the hydrogen reaction as well as yielding information on the degradation mechanisms that normally occur inside alkaline electrolyser units.

As part of the research work undertaken an electrochemical measurement device to test the electrodes was constructed. The motivation for this part of work was that much lower costs were involved in the manufacture of this prototype device in comparison with commercially available electrochemical measurement systems.

The final part of the thesis presents a feasibility study of hydrogen storage technology used with wind turbines, and implemented on the island of Grimsey (Iceland). The demonstration was to assess the potential of hydrogen storage technology for present and future commercialisation.

## **1.2. Methodology**

For the experiments, several different configurations of electrochemical cells were tested. The final design used consisted of a single cell electrolyser made of glass, with a water jacket around it for temperature control. Thus, the functionality of this laboratory device included, as well as temperature regulation and gas separation, the ability to directly observe bubble generation at the electrodes. Some of the experiments performed also involved tests in a single vessel compartment, using the three-electrode configuration (along with a reference electrode) instead of the conventional two-electrode setup.

For the data acquisition, an electrical system was constructed using low-price electronic components. This low-cost prototype device worked well and showed similar basic functionality during real experiments compared to the commercial systems. However, the precision in the measurements was not sufficient to enable work on small electrodes samples of 1 cm square where correspondingly low currents would be involved. Thus, commercial measurement systems were employed

during the major part of the work where electrodes examined were of *ca.* 1 cm<sup>2</sup> area. Nevertheless, the home-built device did enable bubble observation experiments to be performed, which are described later on in this thesis.

The commercial instruments used in the testing of the APS electrodes were the Solartron SI 1286 and the Biologic SP-150 electrochemical interfaces. Both of these devices were able to operate simultaneously which in fact doubled the speed of collecting data from all the prepared electrodes. The electrochemical techniques which were applied during the investigation of the APS electrodes samples were: cyclic voltammetry, electrochemical impedance spectroscopy and Tafel extrapolation. Additional surface analyses were done using a scanning electron microscope.

The final part of the research work describes a feasibility study where the modelling of the wind-hydrogen system for remote communities was examined with the aim of supporting/replacing an existing diesel generator. This part of the thesis work involved application of HOMER energy software for micro-grid simulation.

### **1.3. Thesis structure overview**

The overall thesis structure, chapter by chapter, can be summarised as follows:

- Chapter 2. This chapter presents a general review of hydrogen technology status. It describes the motivation for hydrogen implementation such as the energy issues which world is currently experiencing, stating its main advantages, drawbacks and future challenges. Also presented are the different applications, production and storage methods for hydrogen.
- Chapter 3. This chapter describes the fundamental electrochemistry of the electrolysis process. It also presents the basics of the alkaline electrolyser, the cell design including the commonly used materials, cell configuration, and operational conditions.

- Chapter 4. This chapter contains information about the experimental configurations employed during work. All the instrumentation and analysis methods that were used during overall research work are described.
- Chapter 5. This chapter presents the problems that were experienced during electrolyser system design, configuration and presents general solutions that were found to overcome them.
- Chapter 6. The results from the APS Raney nickel electrode electrochemical characterisation are presented in this chapter. Data from the techniques of Tafel extrapolation, cyclic voltammetry, electrochemical impedance spectroscopy and scanning electron microscopy are given along with their analyses and interpretation.
- Chapter 7. The main topic of this chapter was the investigation of the degradation mechanisms that occurred during variable load operation on the APS electrodes. It identifies and describes the main physical phenomena that are responsible for the electrode degradation processes, but also proposes solutions for the problems identified.
- Chapter 8. The design of the home built electrochemical interface prototype measurement device is described. The chapter describes the instrument and a performance comparison with commercially available measurement devices. Results of general tests showing the impact of bubbles obtained using the specially constructed test cell are also presented.
- Chapter 9. This chapter is focused on a feasibility study describing the possible use of hydrogen storage system integrated with wind turbines and a diesel generator on Grimsey island. For the purpose of this work, the HOMER microgrid modelling software was used.

- Chapter 10. Summary, conclusions and future work are presented here.

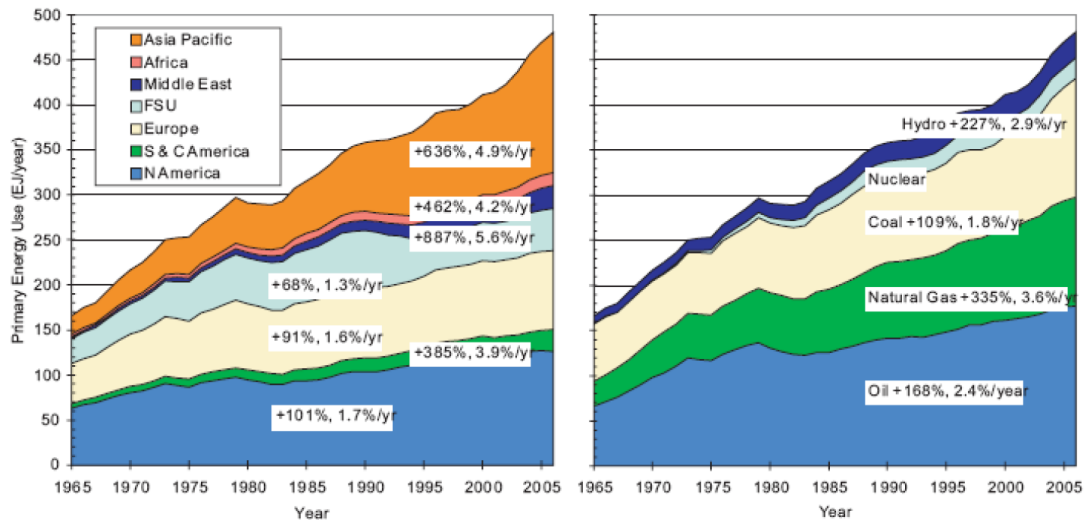
## **2. Introduction**

### **2.1. Energy issues**

The world is now starting to face a number of very serious problems in connection with the energy economy and these issues are expected to worsen during the next few decades. The problems can be divided into two main categories: ecological and sustainable issues. The first is connected with the impact of pollution arising from the burning of fossil fuels and the second one is a threat of natural resources depletion.

On the ecological side, gases such as carbon dioxide (CO<sub>2</sub>), sulphur dioxide (SO<sub>2</sub>) and nitrogen oxides (NO<sub>x</sub>) emitted from fossil fuels are known to be harmful to health by causing many diseases on humans and other living organisms. The illnesses caused by air pollution are respiratory and cardiovascular affecting the throat and leading to inflammation, chest pain, and congestion [1]. The World Health Organization estimates, that every year air pollution leads to about premature 100,000 deaths and 725,000 years of life lost in Europe [1]. Another negative ecological consequence which is very probably caused by fossil fuels usage is the global warming effect, from greenhouse gases emitted from fuels, mainly carbon dioxide (CO<sub>2</sub>) and methane (CH<sub>4</sub>) [2]. According to the report by the Intergovernmental Panel on Climate Changes (IPCC); the global surface temperature increased  $0.74 \pm 0.18$  °C between the start and the end of the 20th century [3]. The IPCC concludes that most of the temperature increase was observed since the middle of the 20<sup>th</sup> century and it was caused by increasing concentrations of greenhouse gases as a result of human activity, such as fossil fuel burning and deforestation. One main outcome of global warming is an increase of sea levels due to glacier melting, leading to flooding of near sea areas. Other predicted effects of global warming are: an increased number of hurricanes, droughts, spread of diseases and extinction of some species of animals [3]. Environmental pollution comes from the majority of

technologies being used for energy production. In the *Figure 2-1* it can be seen that about 90% of total energy produced in the world comes from the fossil fuels viz. oil, natural gas and coal. This figure also shows how fast energy consumption worldwide has grown. Even if energy sources are not be substituted by any other ecological fuels, the environmental pollution and global warming effects will still increase.



*Figure 2-1. Growth in the use of primary energy in different world regions (left); Growth in the use of different fuels in the world (right). Biomass, wind and solar energy are excluded, while hydro and nuclear electrical energy production were converted to primary energy equivalents assuming a conversion efficiency of 38%, FSU=Former Soviet Union. Source of data: BP Statistical Review 2007,*

*www.bp.com [2]*

The second aspect of future energy issues is sustainability of the resources. *Figure 2-2* shows oil discoveries and oil consumption over the period 1965-2005. These oil discoveries peaked in the 1960s and since then are decreasing, while consumption is still increasing (*Figure 2-2*) [2]. Traditional energy sources are predicted to deplete over the next several decades and the reserves are becoming seriously reduced. This will result in rising of prices for traditional fuels. In 2014, total world reserves were estimated to be 1,687.9 billion barrels, which should be enough to last 53.3 years at the current production rates [4].

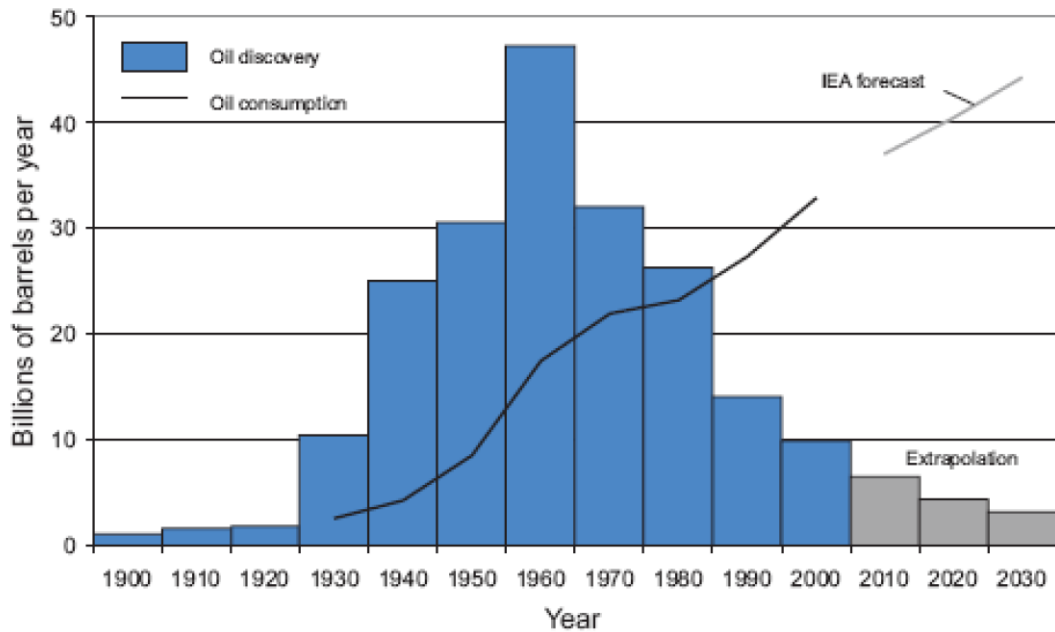


Figure 2-2. Historical variation in the amount of new oil discovered per year and in the consumption of oil per year. Source: Aleklett (2006) [2]

In summary then, although the oil depletion problem is predicted not to occur in the very near future there is however a serious threat for the middle of 21<sup>st</sup> century. On the other hand environmental matters need instant action now as some of the effects of climate change are considered to be irreversible. Additionally, air pollution has a major impact on human health, particularly in the growing Asian economies. The solution for both issues might be a transition to renewable energy, with its key features of ecology and sustainability.

## 2.2. Hydrogen economy – Hydrogen as an energy vector in comparison with other methods

It is often stated, that the future global energy balance will consist of various different energy sources including a significant renewable energy contribution. Local renewable energy generation usually is determined by regional potential. For example in Scotland, the future of energy is considered to be dominated by wind [5]

as the country has outstanding wind potential. In Iceland actually, almost 100% of its electrical energy comes from renewable energy sources (73% geothermal, 27% hydropower), [6], due to the high volcanic activity in the region responsible for geothermal generation and good river potential also. In Africa, photovoltaic panels are believed to be the future of energy due to the very good solar radiation conditions there [7].

Hydrogen and fuel cell technology should have a position among energy sources such as wind, solar, geothermal and hydro energy, as different forms of renewable electricity can be used to produce hydrogen through the electrolysis process. What is distinctive about hydrogen in the context of other storage methods is that it can be easily used as an energy carrier for applications that have no direct grid connection for example cars, laptops or remote locations such as island sites. In practice hydrogen's role is to act as an energy accumulator, to store energy delivered by different suppliers, thus helping to match time varying supply and demand. What is very promising about the hydrogen economy is that H<sub>2</sub> can be obtained using water electrolysis which can be renewable and ecologically sound process, if electrical energy for hydrogen production is delivered from renewable energy source.

In today's world the role of energy accumulators mainly include fossil fuels (such as oil, gas) and traditional batteries. There are also relatively new methods of storing energy under development for example: super-capacitors, flywheels and flow batteries. Storage technologies are often characterised in terms of specific energy and power density, which are related to weight and volume. Basically every potential storage technology needs to be compact with small weight and volume. As is indicated in *Figure 2-3*, hydrogen in fuel cell technology is characterised by very high specific energy compared to other methods. That makes hydrogen ideal to be used for applications requiring constant power over long period of time.



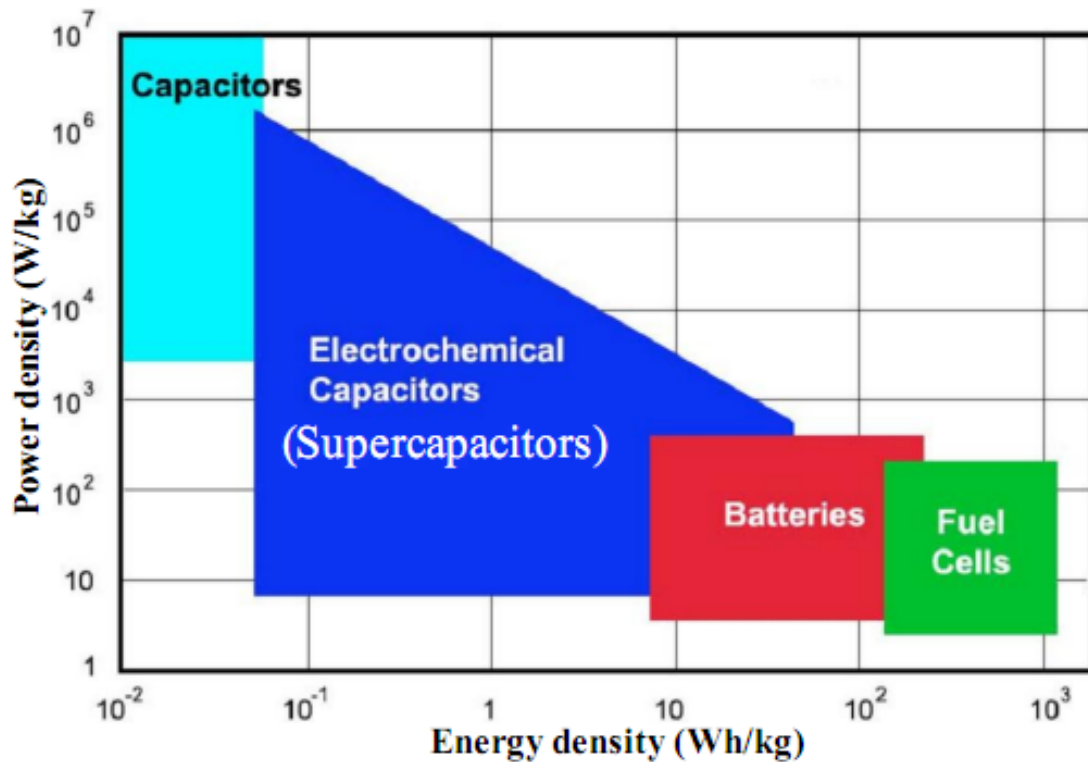


Figure 2-3. Power density vs. energy density of various energy storage systems [8]

For transport applications pure hydrogen is c.a. 3 times lighter than gasoline or aircraft fuel for a given energy. The problem comes however with the weight and size of the storage system [9]. Table 2-1 compares three different methods of hydrogen storage to gasoline for medium size car to give a driving range of 610 km in terms of volume, mass and energy density (assuming an energy consumption of 7.67 litres of gasoline per 100 km and a tank volume of 46.8 litres) [9]. Compressed hydrogen at 700 atmospheres has less than one tenth of the energy density of a full gasoline tank, but it is projected that 4.2 times less energy will be required for fuel cell vehicle (mainly due to high efficiency of electrical motors). It means that the volume of the storage system will need to be 2.6 times larger, thus requiring 0.077 m<sup>3</sup> of supplementary space which should be manageable. If we consider the other storage methods, liquid hydrogen requires maintaining temperature below 20 K which is difficult for a passenger car. The alternative solid storage arrangement in metal hydrides appears to be too heavy currently as overall system would weight 230 kg, which is over 5 times heavier than for today gasoline car.

	Fuel + storage system (kg)	Mass % fuel	Volume (l) System Fuel	System energy density (MJ/litre)	Ratio of system masses	Ratio of system volumes
<b>Compressed H<sub>2</sub> gas @ 345 atm</b>	64.5	4.8	175 107	2.07	1.41	3.55
<b>Compressed H<sub>2</sub> gas @ 700 atm</b>	85.4	3.8	126 55	2.87	1.86	2.56
<b>Liquid H<sub>2</sub></b>	25.5	13.1	99 47.1	3.64	0.56	2.02
<b>Metal hydride (TiFeH<sub>2</sub>)</b>	230	1.92	40.9	11.36	5.02	0.83
<b>Gasoline</b>	45.9	75	49.1 46.7	30.69	1.00	1.00

*Table 2-1. Mass and volume of alternative hydrogen storage system for a mid-sized hydrogen fuel cell automobile, with 3.0 kg of stored hydrogen (sufficient for 610 km driving range) [9]*

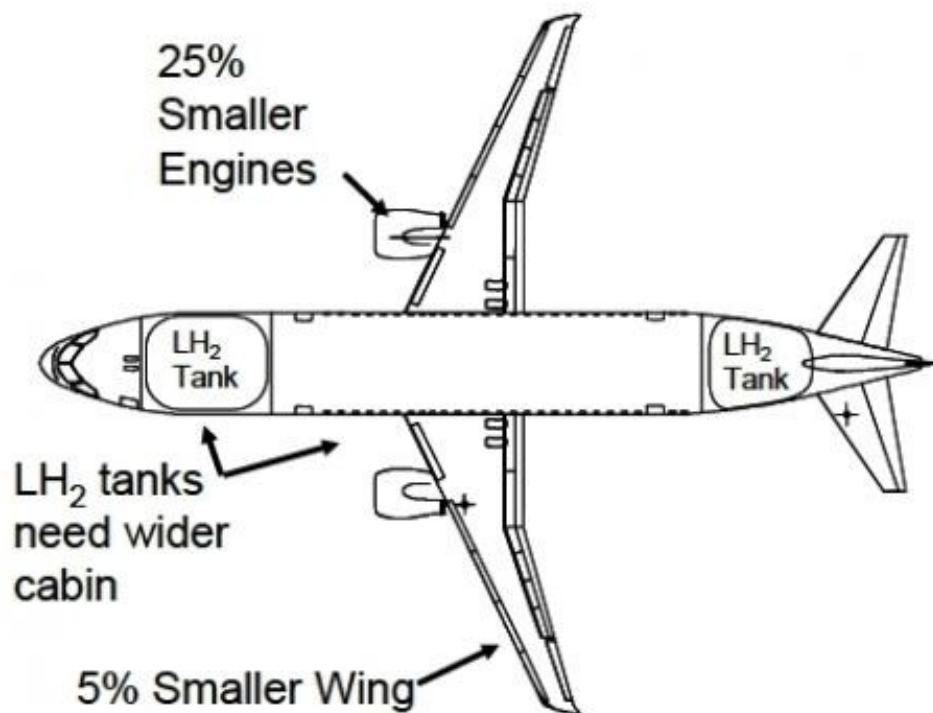
An example of a fuel cell car prototype is the Honda FCX Clarity, which is shown in *Figure 2-4*. It represents sedan vehicles class and from the beginning it was designed as fuel cell vehicle, which means it is taking full advantage of the package/layout freedom that has been enabled by the application of fuel cell technology [10]. The performance of the FCX clarity is comparable to gasoline cars of similar class. It uses an electric motor powered by a 100 kW fuel cell stack. Its maximum speed is 100 miles/h and the maximum range without refuelling is 270 miles [11]. The hydrogen storage used on-board of the vehicle is gaseous cylinder type with maximum pressure of c.a. 340 atm [12].



*Figure 2-4. Honda FCX Clarity - hydrogen/fuel cell vehicle [10]*

An alternative for hydrogen/fuel cell vehicles are battery powered electric vehicles. As can be seen from *Figure 2-3*, batteries have lower specific energy values comparing to fuel cells, which is one of the main drawbacks of this technology. The actual driving range of electric cars is smaller compared to the fuel cell ones and this is mostly because of the weight of the battery pack. In the case of today's battery electric cars, their range does not normally exceed 100 miles [13]. However, it has been suggested that for the Tesla Roadster prototype it might be even as high as 378 km [14]. Charging time is another drawback of battery technology, which usually takes several hours. For instance for the Tesla Roadster, the minimum charging time is 3.5 hours [14], comparing to 4 minutes refuelling time of a hydrogen car [15]. Smaller range and longer charging time is not an obstacle however, for electric car commercialisation, as a 100 km daily range is suitable for 90% of U.S. customers daily [16], but the current state of art is not able to compete with hydrogen for long range transport. Nowadays electric cars technology is predicted to be commercially produced at a faster rate due to its lower price, but hydrogen/fuel cell technology in long term perspective might become cost competitive [17, 18]. Also hydrogen/fuel cell technology is considered to be used in range extenders for electric cars in nearer future [9]. The concept of range extenders would assume usage of hydrogen/fuel cell-battery electric vehicle hybrid. The application of hydrogen in such a case would occur when battery capacity would be not sufficient for driving certain range daily.

In terms of future air transport, hydrogen for planes can bring more benefits, as it has some advantages over the jet fuel. The great asset of hydrogen in this application is its mass, which is lighter than any of the alternatives, leading to possibility of smaller engines usage. Additionally low temperature liquid type hydrogen storage, broadly considered for aircraft purposes, can be used to cooling down some parts of the aeroplane. The challenge though is still the fact that hydrogen planes will need to have a new design with fuel storage not situated inside the wings, which is typical nowadays. Such an arrangement would cause too much heat loss and so, cylindrical tanks to be placed in front and back of passenger compartment are being considered. These though, might lead to penalty in the lift to drag ratio [9]. The hydrogen plane concept is shown in *Figure 2-5*.



*Figure 2-5. Hydrogen powered plane concept [19]*

Liquid hydrogen can also be used for marine transportation utilising aero-derivative gas turbines or internal combustion engines as ships power ratings (50 - 100 MW) are too large to be powered from fuel cells. Because of the low mass of hydrogen greater loads could be accepted and also usage of hydrogen could decrease

drastically emissions, which is big issue in case of ships. Although marine transport uses only 3% of global oil, it is responsible for 14% of SO<sub>x</sub> and 16% of NO<sub>x</sub> world emissions [9].

Apart from hydrogen usage as energy vector for transport applications it can also have a certain role in the stationary market. One of the scenarios considered can be the situation when renewable electricity exceeds demand, for example in Scotland where wind energy potential is one of the best in the world. In 2020 it is targeted to generate 100% of gross annual electricity consumption from wind [20]. Such a large amount of unpredictable, variable energy generation requires substantial energy storage to become truly viable. One of the possible solutions is the use of water electrolyzers for hydrogen generation using the excess electricity. Hydrogen produced in such a way can be stored and used for electricity regeneration to the grid via a fuel cell system or transported and utilised later in different applications. Another potential scenario is in remote locations where there is no direct grid connection. In such a case hydrogen can be transported by vehicle or pipeline to generate electricity on-site. This scenario type is an ecological alternative to today's diesel generators that are common for electricity generation in these remote locations.

Other potential stationary applications of hydrogen are special niche solutions in small scale systems. Example of such an application might be fuel cell system used in Redwood National Park in north western California, where it provides power supply for telecommunication devices. During normal operation, when there is enough sun radiation, the power is supplied by the hybrid system connecting PV arrays and batteries. During the winter period, such a solution is not sufficient for all the energy needs and power needs to be delivered from an external source. For this purpose, a proton exchange membrane (PEM) fuel cell was installed. Hydrogen is delivered to the PEM device directly from industrial cylinders and provides power during rainy and cloudy days. Such a configuration means maintenance costs are lower than providing bigger solar arrays with batteries. Moreover usage of non ecological technology is prohibited in the national park due to potential noise and air pollution generation [21]. Some of the advantages of hydrogen technology can also

be in uninterruptible power supplies (UPS). This type of UPS systems can be used in the buildings where heavy loads on the floor are restricted, as in case of tower blocks. For instance fuel cell UPS actually is operated in a 21-storey building in downtown Toronto, where it provides 20 kW of power for air conditioning and server load [22]. In this particular application, batteries were too bulky and diesel generators were too expensive to be used.

It is also worth to noticing, that portable electronic devices might yet be another application for hydrogen in near future. Fast-developing technologies such as cell phones, computers, camcorders, and cordless tools, have led to an increase in the demand for high-performance power (energy) sources. Currently, rechargeable batteries are the major players in the market for powering portable devices. Nonetheless, as energy demands increase with the popularisation of broadband-mobile computing and an ever-increasing number of functions and applications, existing battery technology has come up against new competition, such as mobile fuel cells. Hydrogen should be able to provide compact solutions with high specific energy. Currently metal-hydrides, chemical hydrides and fuel reformers are considered as candidates for providing hydrogen [24]. It is also considered that the commercialisation of portable fuel cells is the application most likely to occur first [25, 26].

### **2.3. Hydrogen storage methods**

As was mentioned above, hydrogen can be stored using various methods. The choice of storage method is usually dependent on the application, as certain storage types can only be applied in certain conditions. *Figure 2-6* presents the different storage methods with their operating temperature and corresponding weight. As can be seen, hydrogen can be stored in all 3 major physical states: gaseous, liquid and solid.


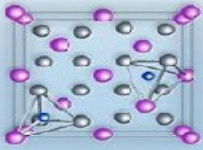

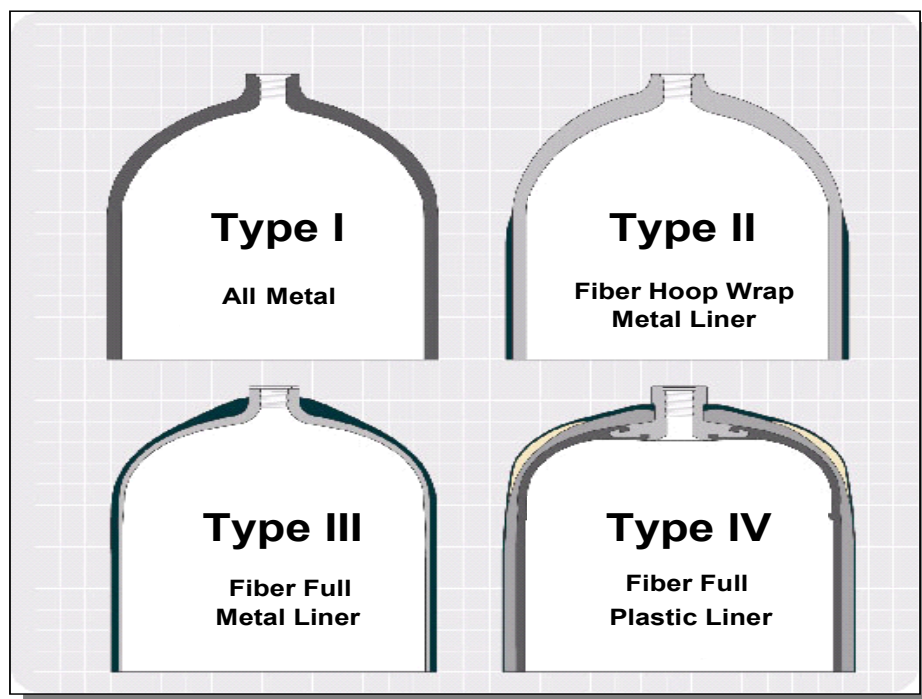
		
Liquid hydrogen	Interstitial metal hydride	Compressed hydrogen
LH <sub>2</sub>	Laves Phase Comp. / FeTiH <sub>x</sub> / LaNi <sub>5</sub> H <sub>x</sub>	CGH <sub>2</sub>
100 mat.wt.%	2 mat.wt.%	100 mat.wt.%
<b>Operating temperature</b>		
-253°C	0 - 30°C	25°C
<b>Corresponding energy to release hydrogen in MJ per kg H<sub>2</sub></b>		
0.45	15	n/a

Figure 2-6. Hydrogen storage methods with temperature and weight dependence

[27]

The most common method of hydrogen storage is as a gas. This method is the most mature, but it is still under development as hydrogen storage in pressures exceeding 700 atm is very challenging task. The major challenge here is proper design which is able to resist high pressures without leakage. Compressed storage is normally utilised under room temperature conditions and its major application is on-board storage for hydrogen vehicles. It could also be used for stationary and portable applications. Gaseous storage tank types are divided into 4 categories. Each of them differs with construction, maximum pressure and application (*Figure 2-7*). Type 1 tanks are made of steel or aluminum and their maximum storage pressure is 200 bars. Type 2 tanks are made of metal wrapped with filament windings (usually glass fibre) around the cylindrical part and their maximum pressure is 299 bars. Type 3 tanks are made of composite materials (fibreglass and carbon fibre) with a metal liner (aluminum or steel) with the pressure of 438 bars and type 4 tanks are pure composite tanks (mainly carbon fibre) with polymer liner (mostly thermoplastic polymers, of the polyethylene or polyamide type) resisting pressure up to 661 bars [28]. A major advantage in the use of composite storage tanks is their lower weight and smaller

volume compared to metal type. On the other hand they are also more expensive. Polymer tanks are used in applications where physical dimensions of storage system play a crucial role, such as transport. In case of stationary applications, where light weight and small volume of the system is not a limitation, tanks of 1<sup>st</sup> and 2<sup>nd</sup> category are more popular. It is worth noting that compression of hydrogen is an energy consuming process. Compression from atmospheric pressure to 350 atm takes about 10% of energy content and to 700 atm 14% of energy (based on hydrogen lower heating value) [9]. The pressurisation energy needed can be reduced for example by usage of high pressure electrolyzers units that are becoming popular nowadays.



*Figure 2-7. Gaseous hydrogen storage cylinders types [29]*

Liquid hydrogen storage is not as commercialised as gaseous storage. However, it has some advantages comparing to other methods. First of all, its major asset is high volumetric density of about  $70.8 \text{ kg/m}^3$ , which corresponds to the same gaseous  $\text{H}_2$  at 788 atm pressure [9]. On the other hand liquid storage requires temperature below  $-253^\circ\text{C}$  and that is very difficult for a lot of applications to maintain and is also energy consuming. Additionally, the liquefaction process needs a large portion of energy to



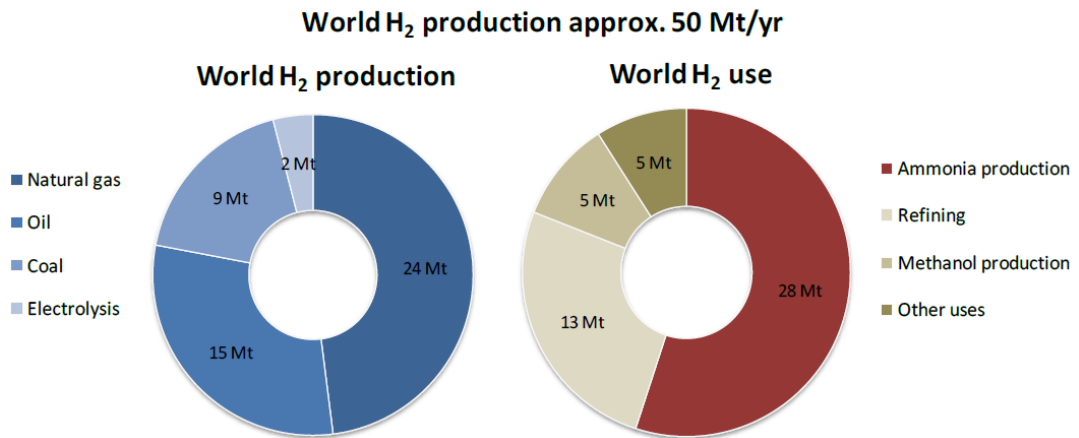
be delivered, which minimally is 3.9 kWh/kg (11.8% of H<sub>2</sub> lower heating value) according to theoretical estimations and real liquefiers consume 8-13 kWh/kg depending on a scale [30]. These issues practically limit today liquid hydrogen usage to applications where high purity is required or as a transport vector to remote locations (using pipeline for example). Liquid hydrogen is also commonly considered as storage method for future hydrogen airplanes [9]. Although some prototypes of cars with liquid storage have been produced [29], the actual market situation trend shows that gaseous storage will be probably become more widely used for vehicle fuelling applications in the future.

Third type of hydrogen storage, which might have some applications in the future, is solid type storage. This technology is actually in the research and development phase and for its purpose metal hydrides such as: MgH<sub>2</sub>, NaAlH<sub>4</sub>, LiAlH<sub>4</sub>, LiNH<sub>2</sub>, LiH are considered to be used [31]. Usually hydride storage is based on a phenomenon that certain materials have potential to form stable hydrides when they are exposed on hydrogen gas under certain pressure, temperature conditions. Hydrogen stored in such a way can be decomposed by changing pressure/temperature conditions. Different storage materials are characterised by distinct conditions of hydrogen adsorption/desorption. Solid storage's main asset is its low volumetric density. On the other hand gravimetric density is much higher comparing to gaseous or liquid storage (*Table 2-1*). Actually major research effort for solid storage development are focused on decreasing its weight, solving a problem of fast refuelling and providing stability of the materials for numerous refilling cycles operation [31].

## **2.4. Hydrogen production methods**

Hydrogen production is actually a large and growing industry, with production amount estimated to be 45-50 million tons each year [32], worth approximately 135 billion USD in 2005 [33]. There exist two primary applications of hydrogen nowadays. About over half is used to produce ammonia (NH<sub>3</sub>), which is subsequently utilised in fertiliser production processes and about 25% is utilised in hydrocracking process during petroleum refining. The other remaining part is consumed for methanol production and different applications [32] (*Figure 2-8*). Nowadays hydrogen is produced using several methods. Most of the manufacturing

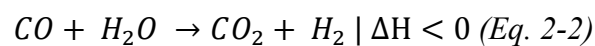
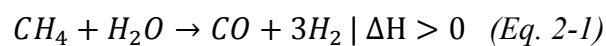
processes involve usage of fossil fuels such as: natural gas (48% of global hydrogen production), oil (30%), coal (18%) and only 4% percent is obtained using water electrolysis [32] (*Figure 2-8*).



*Figure 2-8. Estimated world hydrogen production and use (2008) [32]*

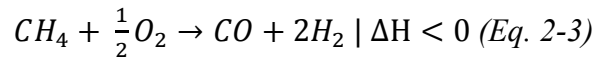
Production from natural gas is performed by 3 main chemical processes which are: steam reforming, partial oxidation and auto-thermal reforming. Although, there exist more concepts for hydrogen from natural gas production, none of them is close to commercialisation [34].

Steam reforming involves endothermic conversion of methane and water vapour into hydrogen and carbon monoxide (*Eq. 2-1*). The heat is usually supplied from the combusted methane feed-gas. The process operating temperature ranges from 700 to 850°C, and pressure from 3 to 25 bars. The reaction emits around 12% of CO, which can be subsequently converted into CO<sub>2</sub> and H<sub>2</sub> by water shift reaction (*Eq. 2-2*) [34].



Partial oxidation of natural gas occurs when hydrogen is obtained by the partial combustion of methane with oxygen to produce carbon monoxide and hydrogen (*Eq. 2-3*). An advantage of this process is that heat is produced through exothermic

reaction, so more compact design is possible. CO obtained in the process can react with H<sub>2</sub>O to produce H<sub>2</sub> as is described by the equation (Eq. 2-2) [35].



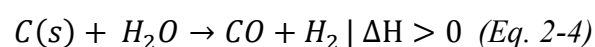
Auto-thermal reforming is a connection of both steam reforming (Eq. 2-1) and partial oxidation (Eq. 2-3). The total process is exothermic, so the heat is released from the reaction. The operation temperature in this case varies in range between 950 and 1100°C, with possible maximum pressure up to 100 bars. CO produced in this method can subsequently be utilised in water shift reaction (Eq. 2-2). Auto-thermal reforming often requires purification of produced gases, which increases the costs significantly and reduces the overall efficiency [34].

Comparison of technologies for hydrogen production from natural gas is summarised inside a table (Table 2-2).

Technology	Steam methane reforming	Auto-thermal reforming and partial oxidation
<b>Benefits</b>	High efficiency	Smaller size
	Low Emissions	Simple system
	Low costs for large units	Low costs for small units
<b>Challenges</b>	Complex system	Lower efficiency
	Sensitive to natural gas qualities	Hydrogen purification
		High emissions

Table 2-2. Comparison of technologies for H<sub>2</sub> production from natural gas [34]

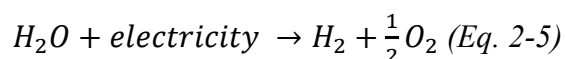
In case of hydrogen production from coal it can be obtained by gasification processes such as: fixed bed, fluidised bed or entrained flow. Practically the most popular process is entrained flow which is the most efficient technology. A typical reaction process is seen in an equation (Eq. 2-4), where carbon and water are transformed into carbon monoxide and hydrogen [34].



Entrained flow is an endothermic reaction, and as such requires additional heat, similarly as with methane reforming. Although hydrogen production from coal is commercially mature, it is much more complex and expensive process compared to hydrogen production from natural gas, as well as less efficient. However, since coal is an abundant resource in a lot of parts of the world, it continues to be broadly used [34].

During the refining process, the direct production of hydrogen from crude oil practically does not occur [36]. Hydrogen in refineries is obtained as a by-product of the processes of hydrofining, petrol reforming, methanol production and ethylene production. Currently, the focus of the available methods for hydrogen production from crude oil is on gas cleaning [36].

Only a small fraction of the commercial world hydrogen production is from water electrolysis (*Figure 2-8*). Water electrolysis is the processes where water molecule is split into hydrogen and oxygen using electrical energy (*Eq. 2-5*).



Hydrogen produced through water electrolysis is not responsible for any harmful emissions to the atmosphere and can be sustainable, if the electricity used comes from renewable energy sources. Electrocatalytic production of hydrogen is specifically considered for off peak electricity, which should drastically decrease costs that are the biggest barrier for large scale electrolysis commercialisation. The predicted costs of future hydrogen from electrolysis divided into capital, electricity, operation and maintenance are presented in *Figure 2-9*.

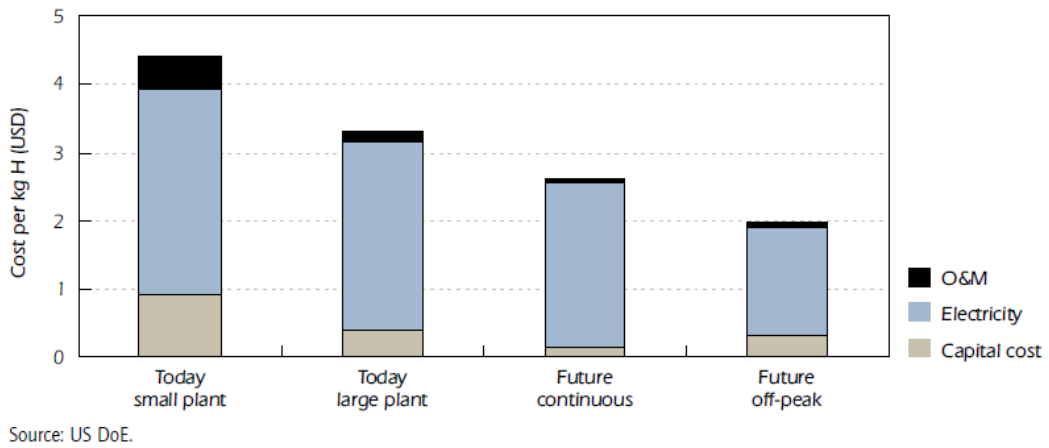


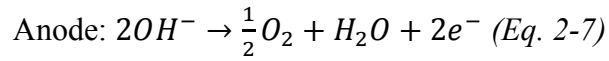
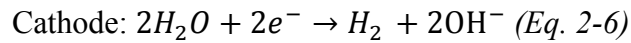
Figure 2-9. Future potential costs of electrolytic hydrogen [34]

## 2.5. Water electrolyzers

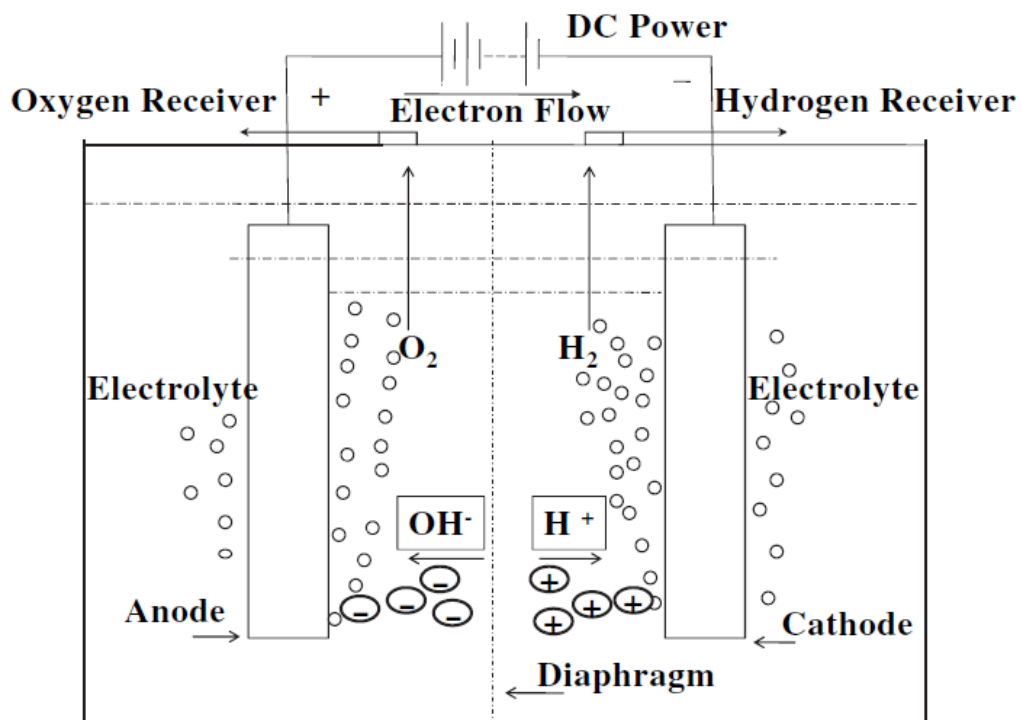
Today only a small quantity of hydrogen is produced by water electrolysis, which constitutes around 4% of global production [32]. Water electrolysis process can be illustrated by simple equation of splitting water into hydrogen and oxygen molecules (Eq. 2-5). The electrolyser, where the reactions take place, in the simplest concept consists of two electrodes: anode (where the oxygen is produced) and cathode (where the hydrogen is produced). Two electrodes are connected to direct electrical power supply, which allows the decomposition of water reaction to occur. Electrodes are separated by an electrolyte which provides ionic conductivity between them. Depending on the electrolyser type, the electrolyte can be in liquid or solid form and can be selectively conductive for cations, anions or both. Today among different water electrolyzers 3 main types can be distinguished which are: alkaline, proton exchange membrane (PEM) and solid oxide. Each of these groups has its own specific design and differs with operating conditions, state of commercialisation and potential applications.

Alkaline water electrolysis is the most mature and commercialised method of hydrogen production among all electrolysis types. As an electrolyte it commonly uses an aqueous solution of potassium hydroxide, which provides the ionic

conductivity between electrodes. Inside the electrolysis cell the following reactions take place:



Both cathodes and anodes for alkaline electrolyzers are typically based on nickel with additions of other catalysts. The electrodes inside the electrolyser are separated by the diaphragm to prevent mixing of gases inside electrolyser. The alkaline electrolysis cell concept is illustrated in a *Figure 2-10*.

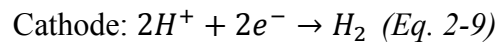
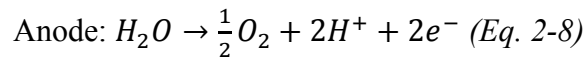


*Figure 2-10. Alkaline electrolysis cell concept [37]*

The operation temperature of the alkaline electrolyser usually ranges between room temperature and 100°C. Theoretically the lowest temperature is limited by the water freezing and the highest limit is due to water evaporation. It is worth noting however, that alkaline electrolyser designs exist which can operate at higher temperatures [38].

The working pressures of such alkaline electrolyzers through can be up to 25 bars [34].

Proton exchange membrane (PEM) electrolyzers are actually at the early stages of commercialisation. The costs of this technology is still greater than alkaline electrolyzers although it is predicted that in future, the cost should become more competitive with new development in materials and stack design [34]. The main advantages of PEM against alkaline are: more compact design, higher operating pressure and increased safety due to lack liquid, caustic electrolytes [34]. PEM electrolyzers today are practically limited to small scale applications below 20 kW. The principles of PEM electrolyzers operation are represented by the equations:



Nafion, a solid polymer electrolyte, is typically the membrane used for PEM electrolyzers. The cathodes for this electrolyser type usually consist of platinum or palladium alloys and the anodes are made of iridium and ruthenium [39]. The operating temperatures are similar to the alkaline types with maximum value not exceeding the boiling point of water. The PEM electrolysis concept is presented in a *Figure 2-11*.

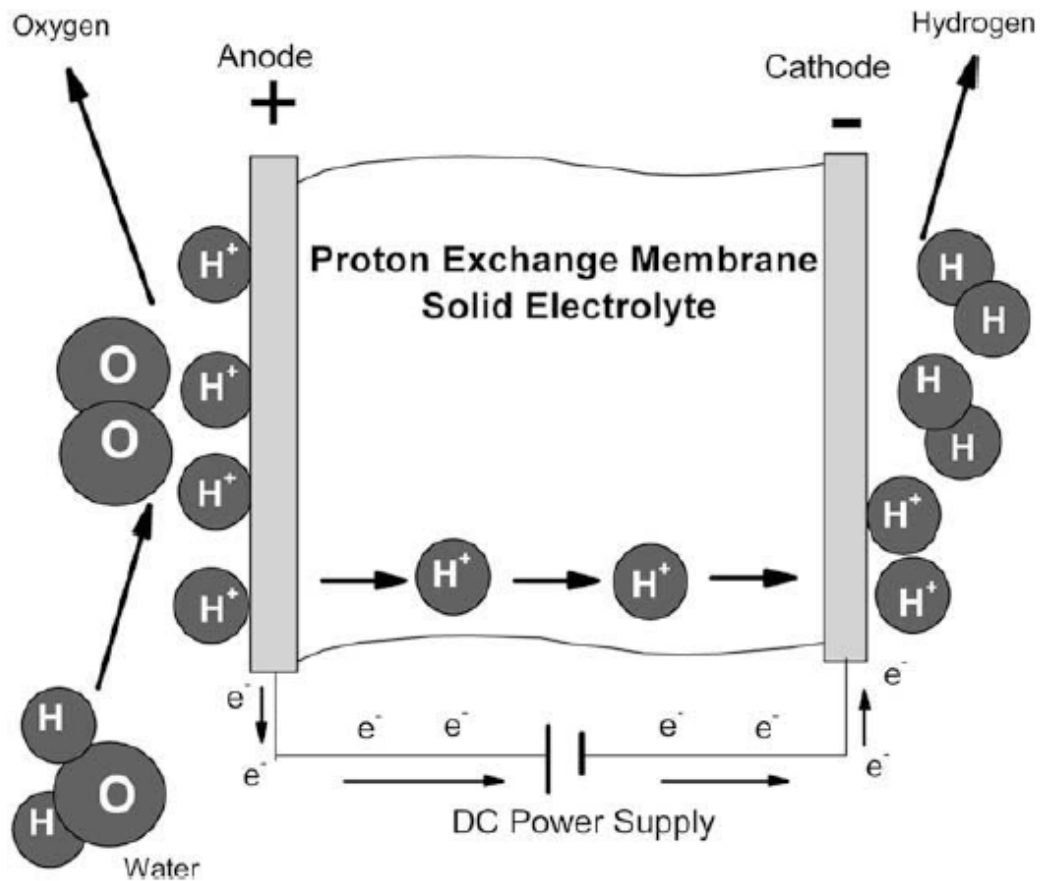


Figure 2-11. PEM electrolysis cell concept [35]

The solid oxide is relatively new electrolyser type, and is still currently in research and development phase. Comparing to the two discussed above, it has a significantly higher operating temperature which varies between 700 and 1000°C [34]. Elevated temperatures allow operation with lower electrical energy requirement. Due to this, solid oxide electrolyser cells (SOEC) can be readily integrated with nuclear and geothermal energy technologies to make hydrogen production more efficient [40]. The design of the SOEC is based on a ceramic membrane such as yttria-stabilised zirconia (YSZ), which conducts oxygen anions ( $O^{2-}$ ). Electrodes for SOEC cells are made of metals such as nickel and/or cobalt for the cathode and electronically conducting mixed oxides, such as lanthanum strontium manganite, for the anode [40]. The research and development challenges for the SOEC are mainly focussed on the investigation of new materials suitable to resist high working temperatures.



## References:

1. World Health Organisation. *Health aspects of air pollution*. Results from THE WHO project “Systematic review of health aspects of air pollution in Europe”..  
[http://www.euro.who.int/\\_\\_data/assets/pdf\\_file/0003/74730/E83080.pdf](http://www.euro.who.int/__data/assets/pdf_file/0003/74730/E83080.pdf) ,  
accessed 14th September 2014
2. L. D. Harvey. *Energy and the new reality 1. Energy efficiency and the demand for energy services*. First published 2010 by Earthscan. ISBN: 978-1-84971-072-5
3. S. Solomon, D. Qin, M. Manning, Z. Chen, M. Marquis, K.B. Averyt, M. Tignor, H.L. Miller. *Climate change 2007. The physical science basis*. The Intergovernmental Panel on Climate Change. Cambridge University Press, Cambridge, United Kingdom and New York, NY, US, ISBN: 978-0521-88009-1
4. BP company. *BP Statistical Review of World Energy*. June 2014,  
<http://www.bp.com/content/dam/bp/pdf/Energy-economics/statistical-review-2014/BP-statistical-review-of-world-energy-2014-full-report.pdf>, accessed 14<sup>th</sup> September 2014
5. <http://www.scotland.gov.uk/Topics/Built-Environment/planning/National-Planning-Policy/themes/renewables>, accessed 14<sup>th</sup> September 2014
6. International Renewable Energy Agency. *Africa’s renewable future. The path to sustainable growth*.  
[http://www.irena.org/DocumentDownloads/Publications/Africa\\_renewable\\_future.pdf](http://www.irena.org/DocumentDownloads/Publications/Africa_renewable_future.pdf), accessed 14<sup>th</sup> September 2014

7. *Electric cars: the truth about the cost – and range.*  
<http://www.telegraph.co.uk/motoring/columnists/mike-rutherford/9525189/Electric-cars-the-truth-about-the-cost-and-range.html>,  
accessed 14<sup>th</sup> September 2014
8. <http://www.seas.ucla.edu/~pilon/EDLCs.htm>, accessed 14<sup>th</sup> September 2014
9. L. D. Harvey. *Energy and the new reality 2. Carbon-free energy supply*. First published 2010 by Earthscan. ISBN: 978-1-84971-073-2
10. M. Hasegawa, Y. Takagi. *Realizing an “FCV sedan form” for a new Honda fuel cell vehicle*. SAE International, 2009
11. <http://www.popularmechanics.com/cars/reviews/drives/4232381>, accessed 14<sup>th</sup> September 2014
12. <http://automobiles.honda.com/fcx-clarity/specifications.aspx>, accessed 14<sup>th</sup> September 2014
13. R. von Helmolt, U. Eberle. *Fuel cell vehicles: Status 2007*. Journal of Power Sources, Vol. 165, Issue 2, 20 March 2007, pp. 833–843
14. <http://www.teslamotors.com/roadster/specs>, accessed 14<sup>th</sup> September 2014
15. K. Kendall, B.G. Pollet, A. Dhir, I. Staffell, B. Millington, J. Jostins.  
*Hydrogen fuel cell hybrid vehicles (HFCHV) for Birmingham campus*.  
Journal of Power Sources, Vol. 196, 2011, pp. 325–330
16. <http://www.dvdtalk.com/dvdsavant/s2798who.html>, accessed 14<sup>th</sup> September 2014

17. G. J. Offer, D. Howey, M. Contestabile, R. Clague, N. P. Brandon.  
*Comparative analysis of battery electric, hydrogen fuel cell and hybrid vehicles in a future sustainable road transport system.* Energy Policy, Vol. 38, 2010, pp. 24–29
18. International Energy Agency. IEA Energy Technology Essentials: Fuel Cells. April 2007.  
<http://www.iea.org/publications/freepublications/publication/essentials6.pdf>, accessed 14<sup>th</sup> September 2014
19. [http://www1.eere.energy.gov/hydrogenandfuelcells/storage/metal\\_hydrides.html](http://www1.eere.energy.gov/hydrogenandfuelcells/storage/metal_hydrides.html), accessed 11<sup>th</sup> August 2013
20. <http://www.scotland.gov.uk/Topics/Built-Environment/planning/National-Planning-Policy/themes/renewables>, accessed 14<sup>th</sup> September 2014
21. P. A. Lehman, C. E. Chamberlin, J. I. Zoellick, R. A. Engel. *A photovoltaic/fuel cell power system for a remote telecommunications station.* Photovoltaic Specialists Conference, 2000. Conference Record of the Twenty-Eighth IEEE
22. <http://news.thomasnet.com/companystory/Hydrogenics-and-APC-Deliver-Fuel-Cell-Backup-Power-System-to-Toronto-Internet-Service-Provider-515023>, accessed 14<sup>th</sup> September 2014
23. <http://www.linnet-tec.co.uk/installation-of-aurigagen-hydrogen-fuel-cell-back-up-system-in-glasgow-call-centre/>, accessed 14<sup>th</sup> September 2014
24. I. Sona, W. Shin, Y. Lee, S. Lee, J. Ahn, S. Han, H. Kweon, J. Kim, M. Kim, J. Park. *35-We polymer electrolyte membrane fuel cell system for notebook computer using a compact fuel processor.* Journal of Power Sources, Vol. 185, 2008, pp. 171–178

25. <http://www.navigantresearch.com/research/fuel-cells-for-portable-power-applications>, accessed 3<sup>rd</sup> July 2013
26. <http://www.seas.ucla.edu/~pilon/EDLCs.htm>, accessed 14<sup>th</sup> September 2014
27. R. von Helmolt, U. Eberle. *Fuel cell vehicles: Status 2007*. Journal of Power Sources, Vol. 165, Issue 2, 20 March 2007, pp. 833–843
28. *The hydrogen pathway. Onboard storage of hydrogen*. CLEFS CEA – No. 50/51, Winter 2004/2005
29. C. Gearhart. *Lecture materials for FC 605 – Fuel cells in transportation module*. The school for renewable energy science – Master of science, postgraduate studies. Akureyri, University of Iceland, 2009
30. R. Wurster. *Lecture materials for FC 604 – Hydrogen Storage module*. The school for renewable energy science – Master of science, postgraduate studies. Akureyri, University of Iceland, 2009
31. [http://reporter.leeds.ac.uk/press\\_releases/current/biodiesel.htm](http://reporter.leeds.ac.uk/press_releases/current/biodiesel.htm), accessed 14<sup>th</sup> September 2014
32. *Hydrogen production and storage. R&D priorities and gaps*. International Energy Agency, Hydrogen Co-ordination Group, 2006
33. P. Zakkour, G. Cook. *CCS Roadmap for Industry: High-purity CO<sub>2</sub> sources*. Carbon Counts Company (UK) Ltd., 2010
34. Hydrogen Production from Fossil Sources, Document Tracking ID: 4948, <http://www.roads2hy.com>, accessed 14<sup>th</sup> September 2014

35. D. Stolten, D. Krieg, M. Weber. *An overview on water electrolysis*. Institute for fuel cells, Juelich Research Center, Germany. 5<sup>th</sup> International Workshop on Hydrogen and Fuel Cells WICaC, 2010
36. F. Allebrod, C. Chatzichristodoulou, M. B. Mogensen. *Alkaline electrolysis cell at high temperature and pressure of 250 °C and 42 bar*. Journal of Power Sources, Vol. 229, 2013, pp. 22-31
37. K. Zeng, D. Zhang. *Recent progress in alkaline water electrolysis for hydrogen production and applications*. Progress in Energy and Combustion Science, Vol. 36, 2010, pp. 307–326
38. L. Ma, S. Sui, Y. Zhai. *Investigations on high performance proton exchange membrane water electrolyzer*. International Journal of Hydrogen Energy, Vol. 34, 2009, pp. 678–684
39. M. Ni, M. Leung, D. Leung. *Technological development of hydrogen production by solid oxide electrolyzer cell (SOEC)*. International Journal of Hydrogen Energy, Vol. 33, 2008, pp. 2337- 2354
40. International Energy Agency, *Iceland: Electricity and Heat for 2011*. <http://www.iea.org/statistics/statisticssearch/report/?&country=ICELAND&year=2011&product=ElectricityandHeat>, accessed 14<sup>th</sup> September 2014

### 3. Electrolysis background

As was stated in the previous chapter, the electrolysis process can be summarised by one, simple overall chemical equation (Eq. 2-5). On the other hand, the individual electrochemical processes occurring during electrolysis as well as the design of the electrolyser itself are much more sophisticated. This chapter describes in detail the basics of the electrolyser operation, the fundamentals of the electrochemical reactions taking place and examining the design of typical devices, including some advanced commercial units.

#### 3.1. Basic electrochemistry of electrolyser cells

A number of processes are involved in the delivery of power to an electrolyser and can be considered as barriers requiring energy to overcome. These barriers can be divided into 3 main categories which are: equilibrium (reversible) potentials for the breakdown of water, activation or overpotential and ohmic losses. Each of these barriers is linked to different electrochemical phenomenon.

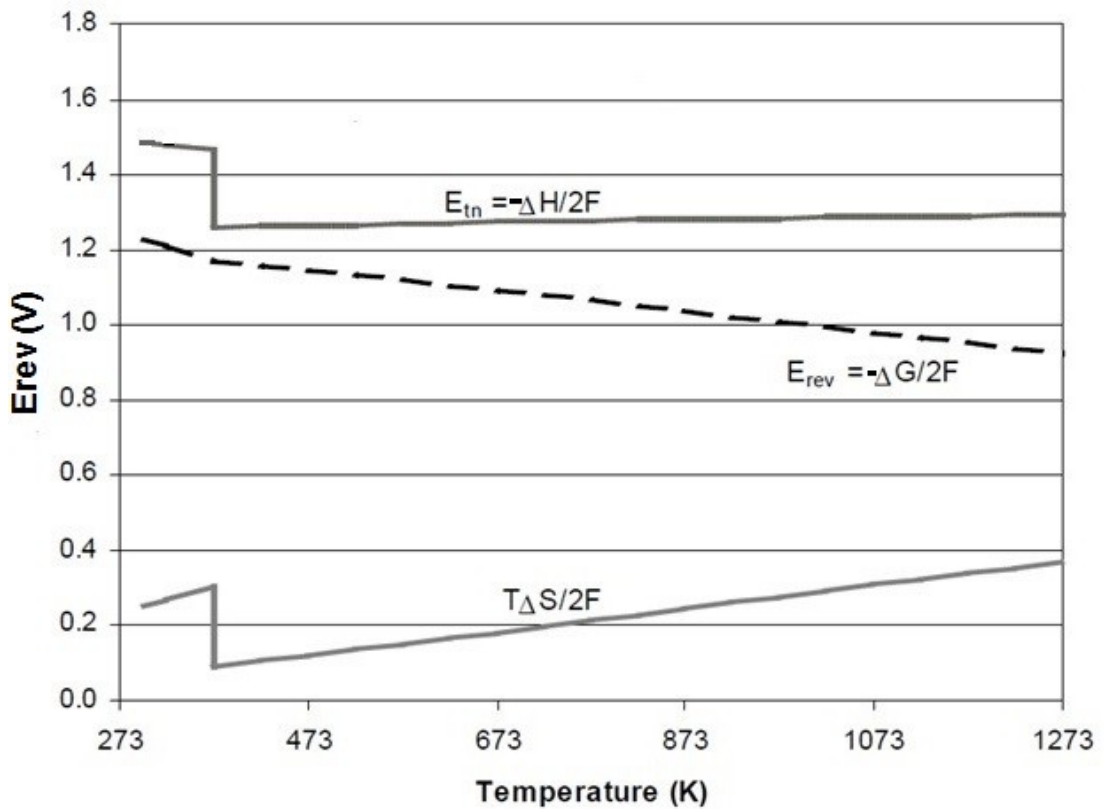
The equilibrium potentials are directly connected with the water structure, which is one of the most stable substances in the nature [1]. To produce hydrogen and oxygen from water, the minimum potential applied to the electrolyser must exceed the difference in the equilibrium potential between the hydrogen evolution and oxygen evolution reactions at the cathode and anode, respectively. The reversible potential ( $E_{rev}$ ) is a function of Gibbs free energy ( $\Delta G$ ) (Eq. 3-1),

$$E_{rev} = \frac{-\Delta G}{n \times F} \text{ (Eq. 3-1),}$$

where  $n$  is the number of moles of transferred electrons in the reaction and  $F$  is the Faraday constant. The Gibbs free energy value is directly related to the electrolysis reaction enthalpy change ( $\Delta H$ ), entropy change ( $\Delta S$ ) and temperature ( $T$ ) of reaction (Eq. 3-2).

$$\Delta G = \Delta H - T \times \Delta S \text{ (Eq. 3-2)}$$

Enthalpy by definition is described as the system internal energy or thermodynamic potential [2], which in the case of electrolysis is the minimum amount of energy that needs to be supplied for reaction to occur. This energy can normally be provided by thermal and/or electrical form. Thermal energy delivered is proportional to the entropy value and increases with temperature rise, which results in a decrease in the reversible potential. *Figure 3-1* shows how  $E_{rev}$  decreases with temperature rise.



*Figure 3-1. Cell potential for hydrogen production by water electrolysis as a function of temperature [3]*

In the same figure (*Figure 3-1*) two types of voltage are revealed as a function of temperature, *viz.*, the reversible and the thermoneutral potential. The reversible relates only to electrical energy whereas the thermoneutral potential is the total energy that needs to be delivered for water electrolysis to occur, which is composed of both electrical and heat energies. The characteristic decrease in the entropy and of the thermoneutral potential at the temperature of 373 K is due to change in the physical state of water from liquid to gaseous.

Based on the energy changes occurring, the Faradaic efficiency ( $\eta_{\text{Faradaic}}$ ) and the thermal efficiency ( $\eta_{\text{Thermal}}$ ) can be calculated. These use the Gibbs free energy change and the enthalpy of water decomposition respectively, as energy input as shown in the equations *Eq. 3-3*, *Eq. 3-4*:

$$\eta_{\text{Faradaic}} = \frac{\Delta G}{\Delta G + \text{Losses}} = \frac{E_{\text{tn}}}{E_{\text{cell}}} \quad (\text{Eq. 3-3})$$

$$\eta_{\text{Thermal}} = \frac{\Delta H}{\Delta G + \text{Losses}} = \frac{E_{\text{rev}}}{E_{\text{cell}}} \quad (\text{Eq. 3-4})$$

Both equations can be simplified as follows, when operation at standard temperature (25°C) and pressure conditions (1 atm) is considered (*Eq. 3-5*, *Eq. 3-6*):

$$\varepsilon_{\text{Faradaic}} = \frac{1.23 \text{ (V)}}{E_{\text{cell}}} \quad (\text{Eq. 3-5})$$

$$\varepsilon_{\text{Thermal}} = \frac{1.48 \text{ (V)}}{E_{\text{cell}}} \quad (\text{Eq. 3-6})$$

The values of Faradaic efficiencies are always less than 1, while thermal efficiency can be greater than 1, if electrolysis operates below thermoneutral voltage. It is also worth noting is that the reversible voltage is also a function of temperature and it can be easily calculated for various temperatures and pressure conditions using Nernst equation (*Eq. 3-7*):

$$E(T, p) = E_0(T_0, p_0) + \frac{\Delta S}{nF}(T - T_0) - \frac{RT}{nF} \ln(p_{\text{H}_2}) \quad (\text{Eq. 3-7})$$

Additional to the water decomposition potential discussed above, the overpotential for the hydrogen and oxygen formation reactions need to be provided. This is directly connected with cathode and anode properties such as the nature

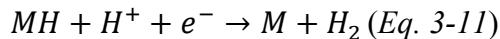
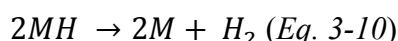
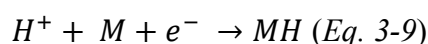


(composition, morphology) of the materials employed. The activation overpotential of each electrode ( $\eta_{\text{electrode}}$ ) can be described by Tafel's equation:

$$\eta_{\text{electrode}} = 2.3 * \frac{RT}{\alpha F} * \log\left(\frac{j}{j_0}\right) \text{ (Eq. 3-8)}$$

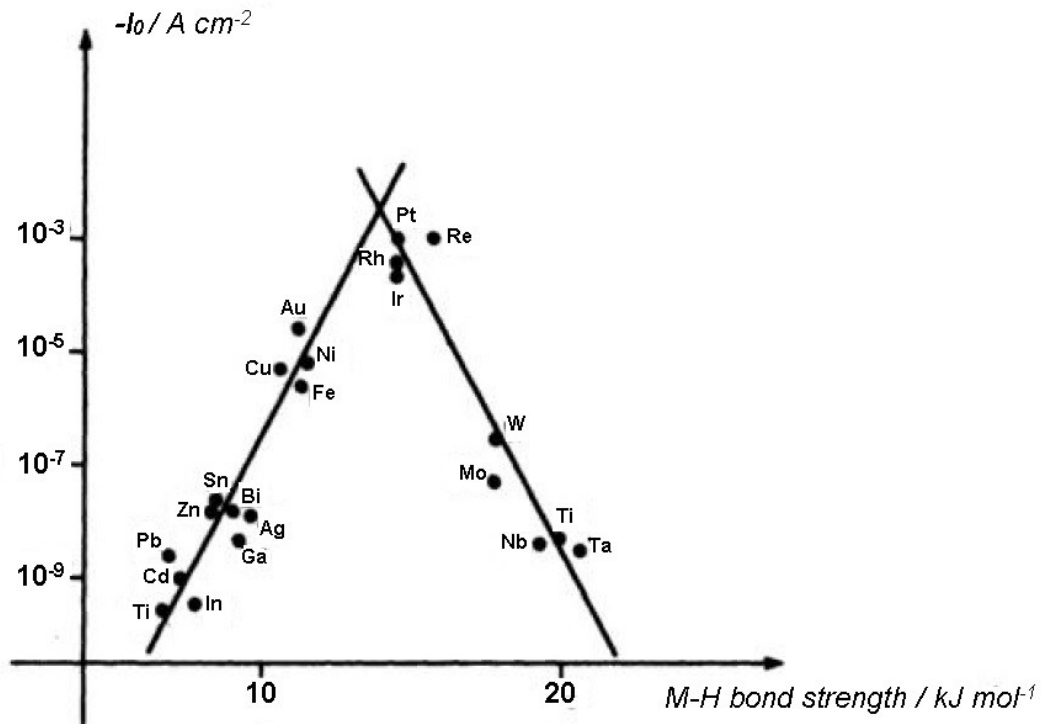
As can be seen, the electrode overpotential is logarithmically proportional to current density ( $j$ ) and inversely logarithmically proportional to exchange current density ( $j_0$ ). This suggests that the lower current density applied, the lower the overpotential needed, which means that in practice, an increase in the active area of the electrode would decrease activation losses. The key parameter though in determining the overpotential is the exchange current density. This parameter is very much dependent on the electrode material employed and in particular on their electrocatalytic properties towards electrochemical reaction under investigation.

The hydrogen evolution reaction mechanism can be shown by the equations:



The first part of the reaction (Eq. 3-9) involves adsorption process where bonding between hydrogen proton ( $H^+$ ) and electrode material (M) is created through a reduction process. An adsorbed hydrogen atom (MH), hydrogen particle is created. According to the literature, two alternative mechanisms are then considered to follow this initial step and these are given by the equations: Eq. 3-10, and Eq. 3-11. Which mechanism occurs and which of its elementary reactions within it is the rate determining step is strongly dependent on the electrode material. In fact, the best catalytic materials are those M–H bonds the intermediate strength. For example if hydrogen atom creates too strong a bonding to the surface, a lot of energy will be required to release it for the 2<sup>nd</sup> step. Conversely, if it is too weak, then the surface concentration of the adsorbed hydrogen atom remains very low which inhibits the second step in the process. The exchange current density which expresses the kinetics of the hydrogen evolution reaction is thus a function of the bonding strength

and for the HER, it is shown in the *Figure 3-2* As can be seen, the materials which are broadly used as catalysts for hydrogen evolution reaction such as platinum, nickel have the bonding strength close to the optimum value and these material types provide the best electrode for HER. The situation looks similar in the case of the oxygen evolution reaction on anodic part of the electrolyser.



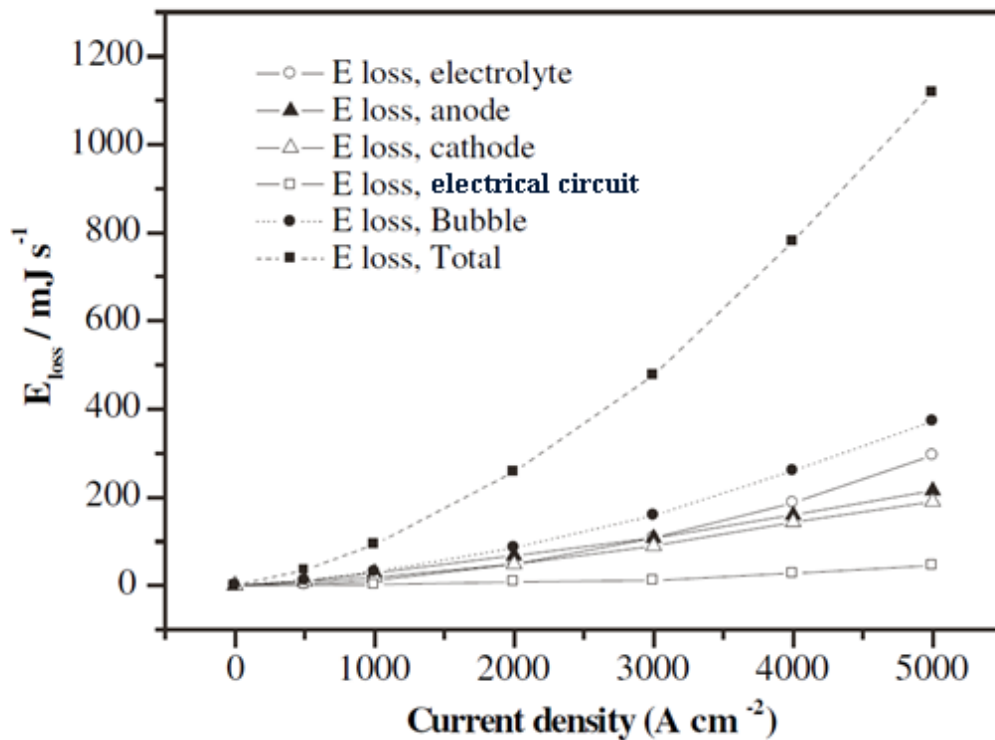
*Figure 3-2. Dependence of exchange current density for hydrogen evolution reaction on the strength of the metal-hydrogen bond formed in the electrode reaction [4]*

The third kind of losses that needs to be considered inside the electrolyser is that of ohmic losses and this can be described by Ohm's law:

$$\eta_{ohmic} = IR = I \left( \frac{l}{k \times A} \right) \text{ (Eq. 3-12)}$$

Ohmic losses are proportional to current (I) and resistance of the conductor (R). Resistance is proportional to length of the conductor and inversely proportional to its cross-sectional area (A) and specific conductivity (k). In case of the electrolyser, neglecting any losses in the solid (electrode and contacts) conductors, the main source of ohmic loss comes from the electrolyte, which provides the ionic pathway

for the current between electrodes. Thus, it is very important to use highly conductive materials for electrodes and connectors and keep the inter-electrode gap as low as possible. An additional factor which can be taken into account in the case of alkaline electrolyzers is the electrical resistance arising from the presence of gas bubbles that are formed during the electrolysis. Gas bubbles have lower electrical conductivity than the electrolyte and their amount produced inevitably increases with the current. A further ohmic loss in case of alkaline electrolyzers will also arise from the presence of the diaphragm or separator, which is present to keep the gases produced inside electrolyte separated [1]. It must be noted that circuit to supply electrical power to electrolyser unit also increases ohmic losses value however its impact is normally very low. A qualitative comparison of energy losses caused by reaction resistances, ohmic resistances and bubble resistance for alkaline electrolyser is presented in *Figure 3-3*.



*Figure 3-3. A qualitative comparison of the energy losses caused by reaction resistances, ohmic resistances, ionic resistance and bubble resistance [1]*

In conclusion therefore, to estimate the overall cell voltage ( $E_{cell}$ ), all losses in the circuit need to be summed up. Such a calculation is presented by *Eq. 3-13*:

$$E_{cell} = E_{rev} + \eta_{activation} + \eta_{ohmic} \text{ (Eq. 3-13)}$$

The overall cell efficiency, based on the amount of hydrogen produced and so, on the energy carried by hydrogen is another parameter that is very often referred to in the literature. The overall efficiency can be evaluated by either measuring the amount of evolved hydrogen or by assuming that the overall current is related only to the production of hydrogen at the cathode. Since the current efficiency inside practical electrolyser systems can be higher than 99.9% [1], such an assumption thus introduces only a very small error. The hydrogen rate ( $H_{rate}$ ) produced is described by the equation:

$$H_{rate} = \frac{I}{n \times F} \left[ \frac{\text{mol}}{\text{s}} \right] \text{ (Eq. 3-14)}$$

where  $I$  is current,  $n$  is amount of electrons for each mole of  $H_2$  formed and  $F$  is the Faraday constant.

Typically two definitions of overall efficiency are used; one is based on the higher heating value (HHV) and the other on the lower heating value (LHV) for hydrogen, 286 kJ/mol and 244 kJ/mol, respectively. The difference between these two values comes from the fact that HHV takes into account latent the heat of vaporisation of water as the water product is condensed. In case of LHV, the latent heat of water vaporisation is not recovered as the water product remains in gaseous form. Efficiencies based on HHV ( $\epsilon_{HHV}$ ) and LHV ( $\epsilon_{LHV}$ ) in case of electrolysers are normally based on an assumption that certain amount of input electrical power ( $P_{in}$ ) delivered, generates corresponding amount of output power ( $P_{out}$ ) in a form of hydrogen. In such case efficiency is equal to the ratio of the output power to the input power. The input power is a multiplication of the current ( $I$ ) and voltage ( $U$ ), that are delivered to the electrolyser unit. The output power is proportional to the rate of hydrogen generation ( $H_{rate}$ ), which can be calculated from *Eq. 3-14*, which is multiplied by the value of HHV (*Eq. 3-15*) or LHV (*Eq 3-16*).

$$\varepsilon_{HHV} = \frac{P_{out}}{P_{in}} = \frac{H_{rate} \times HHV}{U \times I} = \frac{HHV}{U \times n \times F} \quad (Eq. 3-15)$$

$$\varepsilon_{LHV} = \frac{P_{out}}{P_{in}} = \frac{H_{rate} \times LHV}{U \times I} = \frac{LHV}{U \times n \times F} \quad (Eq. 3-16)$$

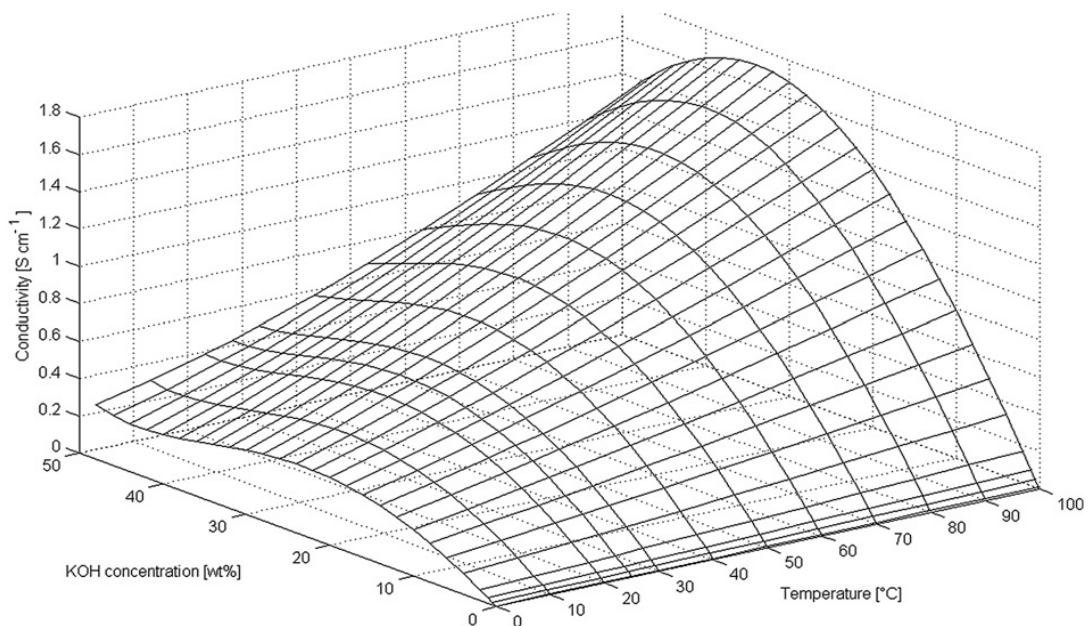
### 3.2. Fundamentals of alkaline electrolyser cell design

The electrolyser unit typically consists of the anode and cathode separated by a membrane (diaphragm) and these are immersed in the electrolyte. The materials and design of each of these components are important in maintaining high performance of the electrolyser and in this paragraph, these components are described for typically used electrolyser configurations.

Clearly, the most critical and important part of the electrolyser are the electrodes since this is where the electrochemical reactions occur. The materials employed for electrode production should provide as high an electrocatalytic surface as possible, be corrosion resistant in the strong caustic environment at the elevated temperatures and under intermittent operation) and be of low cost. Arguably, one of the best materials which satisfy these criteria are the noble metals platinum and palladium but they are also very expensive. In practice, the materials most frequently employed in commercial units are nickel and/or steel alloys. The advantage of nickel over steel is that it has far better electrocatalytic activity for both hydrogen and oxygen evolution reactions and it is also more corrosion resistant [5]. However, nickel is more expensive than steel. To lower the price, combinations of nickel and steel within a single electrode (for example: nickel plated steel [1]) have proved popular. To improve the electrocatalytic activity, additions of other materials have been performed with the nature of the addition used depending on the desired electrochemical reaction. For the cathode reaction, the most popular catalysts include compounds of molybdenum, cobalt, vanadium, zinc and aluminium [1] whereas for the anode reaction, the use of compounds of cobalt, ruthenium and perovskite-type oxides are widespread [1, 6]. Electrodes are also produced using various techniques with the aim of obtaining porous, stable structures at the lowest possible costs. Porous electrode structures present very high electrochemical surface area for

reaction to occur and this decreases activation losses. Techniques commonly used for porous electrode manufacture are: electrodeposition, plasma spraying, thermal decomposition, sintering or arc melting [1, 6].

The produced electrodes are immersed in the electrolyte which provides ionic conductivity between them as well as the electroactive species, which in this case is the solvent itself. Usually for alkaline electrolyzers, aqueous potassium (KOH) and sodium hydroxides (NaOH) solutions at various concentrations are used. Both KOH and NaOH compounds are good conductors. Due to the fact that KOH is more conductive and cheaper, it is normally preferred over NaOH [7]. A 25-30 wt% potassium hydroxide concentration is widely adopted in commercial electrolyzers [4]. The reason for usage of such a concentration is that it shows the highest conductivity on that level [8], which minimises ohmic losses. Electrolyte conductivity also increases with temperature [8, 9], which is one of the reasons why alkaline electrolyzers are often operated at elevated temperature. *Figure 3-4* shows the conductivity of KOH solution as a function of concentration and temperature.



*Figure 3-4. 3D plot of the conductivity of aqueous solutions of KOH as a function of temperature and concentration [9]*

To separate the electrode reactions and so prevent the mixing of hydrogen and oxygen inside the cell, a diaphragm or membrane separator is used. Another key property of the separator is that it has to be permeable for ions and since the presence of the diaphragm increases ohmic losses, its resistance should be as small as possible. In this respect the thicknesses of the separators used tend to be very low. The first commercialised membrane for use in alkaline electrolyzers was asbestos. However it was found not being enough corrosion resistant in the alkaline environment at elevated temperatures [1]. Furthermore, many health issues have been related to the use of asbestos and it has since been replaced by other materials [10]. Since the 1970s, the separation materials gradually shifted towards the polymers direction, for example, perfluorosulphonic acid, arylene ether and polytetrafluoroethylene [10], [11], which are common today. As well as the traditional diaphragms, new designs of advanced alkaline electrolyzers can use so called zero gap configuration, which utilises hydroxide conductive, porous membranes [5, 12]. In such a design, the membrane is tightly sandwiched between the electrodes. Zero gap configuration decreases ohmic losses compared to traditional design but on the other hand, it induces problems with gas transportation and bubbles being trapped inside the electrode pores [5]. The known zero gap membrane structures are: ceramic ( $\text{BaTiO}_3$ ), metal oxide (NiO) or polymer based [5, 12].

The cell configuration is another important parameter which influences the electrolyser performance. Two different arrangements, monopolar and bipolar can be distinguished. In the monopolar configuration alternate electrodes in the stack are directly connected to the positive or negative terminals, resulting in the total voltage required to be approximately the same as that for a single cell pair (*Figure 3-5.a*). In case of bipolar arrangement, only first and last electrodes in the stack are connected to the power supply and this induces a positive potential on the electrode surface facing the negative electrode whereas its opposite surface, facing the positive electrode, becomes negative. This is repeated at all electrodes in the stack resulting in bipolar electrodes separated by the electrolytes solution (*Figure 3-5.b, Figure 3-6*). The total voltage applied in this case is then the sum of individual cell voltages [1]. Bipolar arrangement brings a reduction of ohmic losses on the electrical system connectors, but its manufacture requires much greater precision to prevent leakage of

gas and electrolyte between the compartments [13]. It is worth noting that one of the design trends in electrolyser cells is to minimise the distance between the electrodes in order to reduce ohmic losses. However, if this gap is too small, it may induce short circuit currents and electric sparks, posing an explosion hazard. In practice then, an optimal gap distance has to be identified [1].

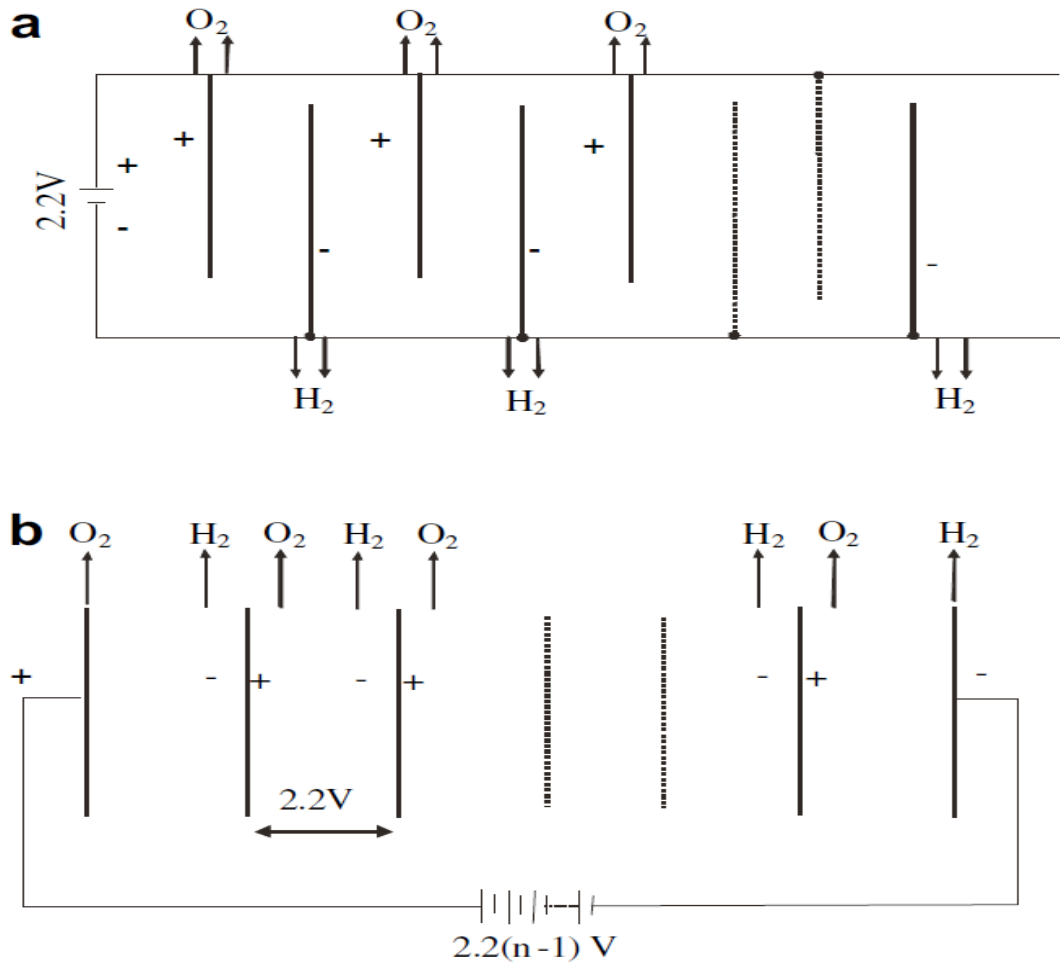


Figure 3-5. Schematics of configurations a – monopolar, b - bipolar electrolyzers [1]



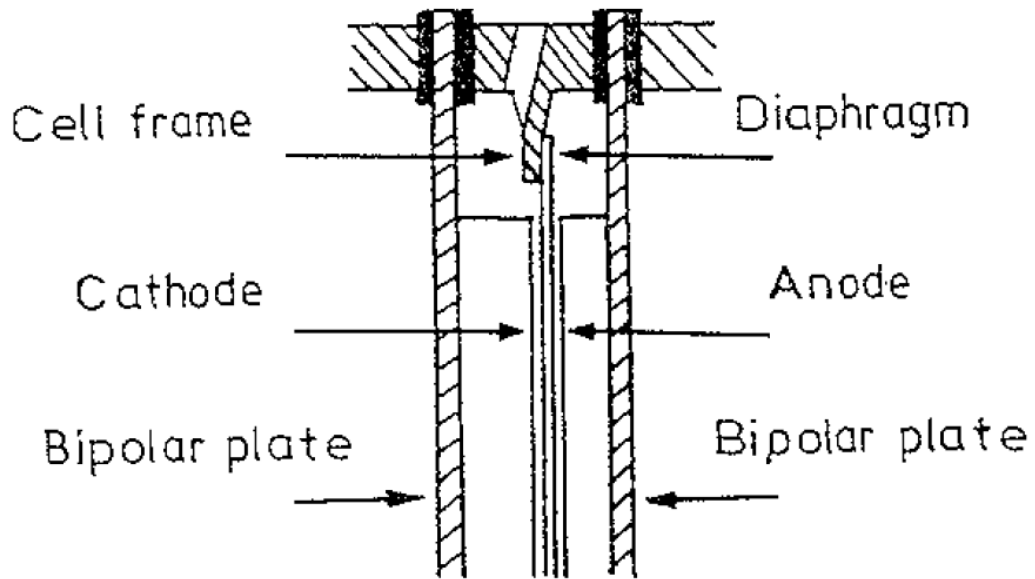


Figure 3-6. Basic cell structure of bipolar electrolyser [5]

Temperature and pressure of operation as well as the flow speed of the electrolyte all have a major impact on the electrolyser performance. The temperature of operation for conventional electrolysers usually is in the range of 70-90°C [1]. One reason for this is that the kinetics of the reaction is greatly improved at elevated temperatures, thus reducing activation as well ohmic losses in the cell. Additionally, small decrease in equilibrium voltage is also observed with the temperature rise. However, the higher the operating temperature, the more water is lost due to the evaporation and the more demanding the requirement of corrosion resistant materials employed in the cell [6, 12]. A significant number of commercial electrolysers also operate under high pressure conditions. The main motivation for the latter is the minimisation of the energy requirements needed for further compression of hydrogen for gaseous storage [14]. The high pressure also leads to a decrease in ohmic losses associated with gas bubbles on the electrode surface as it reduces bubbles volume and also slightly decreases the open circuit voltage [1, 4]. The drawbacks of operations at higher pressure are the need of better sealing materials and more durable membranes [1].

Operational details of some commercial alkaline electrolysers are presented in *Table 3-1* [6]. As can be seen the best overall efficiencies (the lowest operation voltage and the highest current density) are achieved for electrolysers which use nickel containing electrodes. The use of nickel-plated steel is widespread due to large cost reductions in comparison to application of pure nickel alone. Furthermore, the bipolar configuration are the most common and provide highly efficient systems, compared to the Electrolyzer Corp. Ltd monopolar unit. It is worth bearing in mind though, that highly efficient electrolysers are also the more expensive and so, before choosing an electrolyser for a specific application, a detailed cost analysis of the investment needs to be performed.

Parameter	De Nora S.A.P	Norsk Hydro	Electrolyzer Corp. Ltd.	Teledyne energy systems
<b>Cell Type</b>	B-FP	B-FP	M-T	B-FP
<b>Anode</b>	Expanded Ni-Plated Mild steel	Activated Ni-coated Steel	Ni- plated steel	Ni screen
<b>Cathode</b>	Activated Ni-plated Steel	Activated Ni-coated Steel	Steel	Ni screen
<b>Pressure (MPa)</b>	Ambient	Ambient	Ambient	0.2
<b>Temperature (°C)</b>	80	80	70	82
<b>Electrolyte</b>	29% KOH	25% KOH	28% KOH	35% KOH
<b>Current density(A m<sup>-2</sup>)</b>	1500	1750	1340	2000
<b>Cell voltage (V)</b>	1.85	1.75	1.9	1.9
<b>Current efficiency (%)</b>	98.5	98.5	>99.9	NR
<b>Oxygen purity</b>	99.6	99.3-99.7	99.7	>98.0
<b>Hydrogen purity</b>	99.9	98.9-99.9	99.9	99.99

*Table 3-1.* Water electrolyser developers and cell operating conditions (abbreviations B-FP – bipolar filter-press construction; M-T – monopolar tank, NR – no record) [1]

## References:

1. K. Zeng, D. Zhang. *Recent progress in alkaline water electrolysis for hydrogen production and applications*. Progress in Energy and Combustion Science, Vol. 36, 2010, pp. 307–326
2. Oxford dictionaries,  
<http://oxforddictionaries.com/definition/english/enthalpy>, accessed 14<sup>th</sup> September 2014
3. S. Prince-Richard. *A Techno-Economic Analysis of Decentralized Electrolytic Hydrogen Production for Fuel Cell Vehicles*. B. A. Sc., Université Laval, 1996, Dissertation work
4. D. Pletcher, F. C. Walsh. *Industrial electrochemistry*. 2nd ed. London: Blackie Academic & Professional, 1990
5. H. Wendt. *Electrochemical Hydrogen Technologies. Electrochemical Production and Combustion of Hydrogen*. Elsevier, 1990
6. K. Kinoshita. *Electrochemical oxygen technology*. 1st edition. New York: John Wiley & Sons, 1992
7. S. Morgan. *Difference Between Sodium & Potassium Hydroxide*.  
<http://www.livestrong.com/article/455076-difference-between-sodium-potassium-hydroxide/>, accessed 14<sup>th</sup> September 2014
8. R. J. Gilliam, J. W. Graydon, D. W. Kirk, S. J. Thorpe. *A review of specific conductivities of potassium hydroxide solutions for various concentrations and temperatures*. International Journal of Hydrogen Energy, Vol. 37, 2012 pp. 16505-16514

9. F. Allebrod, C. Chatzichristodoulou, P. L. Mollerup, M. B. Mogensen. *Electrical conductivity measurements of aqueous and immobilized potassium hydroxide*. International Journal of Hydrogen Energy, Vol. 32, 2007, pp. 359-364
10. V. M. Rosa, M. B. F. Santos, E. P. Dasilva. *New materials for water electrolysis diaphragms*. International Journal of Hydrogen Energy, Vol. 20, 1995, pp. 697–700
11. M. A. Hickner, H. Ghassemi, Y. S. Kim, B. R. Einsla, J. E. McGrath. *Alternative polymer systems for proton exchange membranes (PEMs)*. Chemical Reviews, Vol. 104, 2004, pp. 4587–612
12. D. Pletcher, X. Li. *Prospects for alkaline zero gap water electrolyzers for hydrogen production*. International Journal of Hydrogen Energy, Vol. 36, 2011, pp. 15089-15104
13. J. Bockris, B. Conway, E. Yeager, R. White. *Comprehensive treatise of electrochemistry*. New York. Plenum Press. 1981
14. DOE Fuel Cell Technologies Program Workshop: Manufacturing Progress and Barriers.  
[http://www1.eere.energy.gov/hydrogenandfuelcells/pdfs/mfg2011\\_ib\\_frnk.pdf](http://www1.eere.energy.gov/hydrogenandfuelcells/pdfs/mfg2011_ib_frnk.pdf), accessed 14<sup>th</sup> September 2014

## **4. Experimental**

The aim of this chapter is to describe general laboratory procedures and techniques that were used during experimental work. Detailed description of the used equipment, chemicals and investigation techniques employed are also presented.

### **4.1. Experimental system set-up**

Of the main configuration, two functional parts can be distinguished, and these are described in first two subsections of this section. The first subsection describes the electrochemical cell design and deals with issues such as: proper materials application, cell geometry and functionality. The second part describes the design of the data acquisition system (DAQ) used for delivering electrical power and controlling system parameters operation.

#### **4.1.1. Electrolyser cell design**

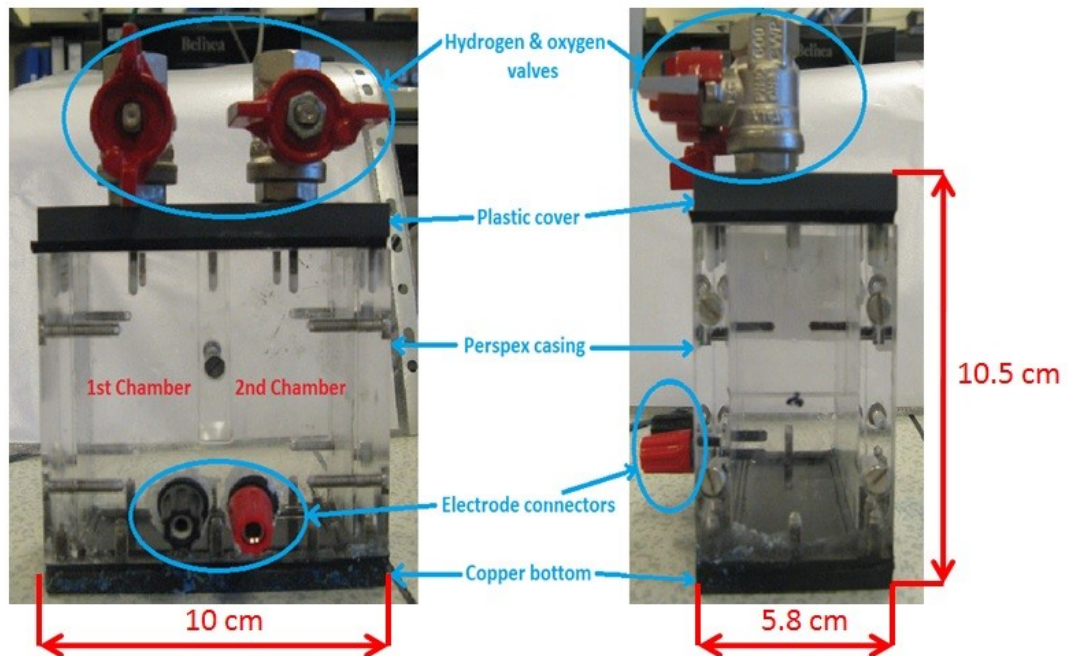
Alkaline electrolysers operate in highly caustic, liquid environment at elevated temperatures and within the device all three states of matter are involved. Such operation conditions require highly resistant materials and proper sealing, and these were indeed identified as the main challenges in obtaining proper cell design. This section presents two concepts, which might be used during any practical system implementation in future and provides description of mistakes made, which any constructor of laboratory alkaline electrolyser systems should be aware of. Practical implementation of final concept was able to fulfil all assumptions regarding the system stability and functionality.

The requirements for system functionality were:

- the ability to operate at elevated temperatures with temperature regulation
- evolved gas separation
- the ability to capture the evolved gases

- the ability to observe the electrodes surfaces within electrolyser so as to be able to investigate gas bubbles formation and release
- the possibility of using smaller electrodes sizes (such as 1 cm × 1 cm square samples)

The first electrolyser system configuration tested was a cubic shaped vessel made of perspex side walls, copper base sealed with gaskets from EPDM rubber and a plastic cover with two metal valves (*Figure 4-1*). The overall dimensions of the electrolyser were: 10.5 cm × 10 cm × 5.8 cm.



*Figure 4-1. 1<sup>st</sup> prototype of alkaline water electrolyser*

All the parts were connected using stainless steel screws. All the materials used had a thickness of 8 mm, except for the EPDM rubber which had a thickness of 3 mm. It was observed that after drilling each screw thread in the Perspex material, it needed to be cooled. Otherwise it showed tendencies to crack, which was probably caused by exposure to elevated temperatures caused by mechanical friction from drilling, leading to mechanical stress. Mechanical treatment of the other used materials did

not lead to these problems. Inside the vessel two chambers were present (one for each electrode) separated by Perspex wall with a diaphragm in the bottom part. Each chamber had dimensions of 3.8 cm × 3.8 cm × 8 cm. The vessel was designed to be placed on a heating plate so as to heat up the electrolyte and so maintain the elevated temperatures. The electrodes inside the electrolyser were soldered to steel screws, which were connected to the power supply using 4 mm connectors. Each screw that was designed to be removed frequently was mounted in a threaded metallic insert, as friction during driving a screw, as noted above could damage the structure of the Perspex thread. During the soldering process of the nickel and stainless steel electrodes, an aggressive solder flux was needed to remove oxides from the metal/alloy surface as otherwise, creating a joint between the electrical contact and the electrode was not possible. For the performed experiments a flux based on phosphoric acid was used. During electrolyser operation, it was indispensable to provide proper covering of the soldering material (for example with epoxy resin) to avoid contact with the electrolyte. Both tin and lead, which are the most common soldering materials, are not resistant to the highly alkaline environment [1]. An additional challenge was the choice of an appropriate proper material for the base part of the electrolyser. Such a material should be characterised by good thermal conductivity, corrosion resistance and be of reasonable price. In the case of copper as can be seen from the Pourbaix diagram (*Figure 4-2*) the corrosion process in alkaline solution starts occurring when the pH is greater than ca. 13. The 30% KOH solution had a pH of 13.27, which is very close to theoretical corrosion value. Literature has also described the corrosion resistance of copper for KOH solution as good or with minimal corrosion [2, 3]. To verify the corrosion resistance, an experiment was conducted, during which a piece of copper was immersed inside the KOH solution and its weight was measured before and after the experiment. Although the weight difference measured before and after exposing the metal to KOH solution was not noticeable, when applying the copper base of the electrolyser and filling with electrolyte for one day, it started leaking, indicating that corrosion resistance of the material was not sufficient for this application. Also as it can be seen from *Figure 4-2*, polarising the copper below a value of -0.6 V vs NHE would make this material



completely immune to corrosion in this alkaline environment. However, this was not tested in practice during the conducted experiments.

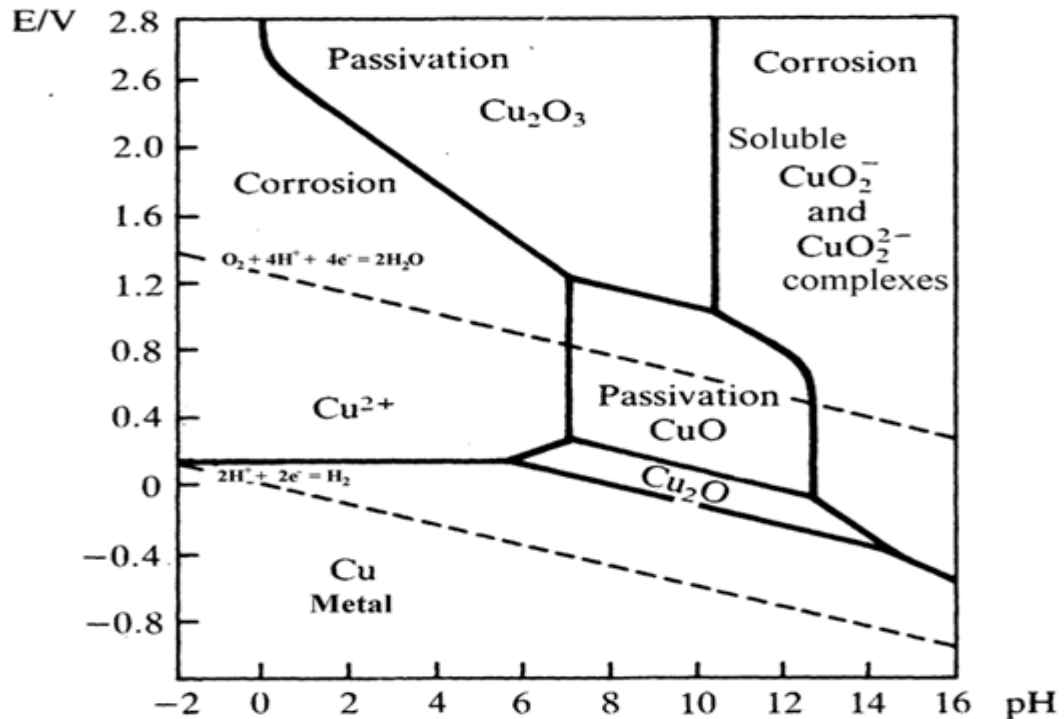
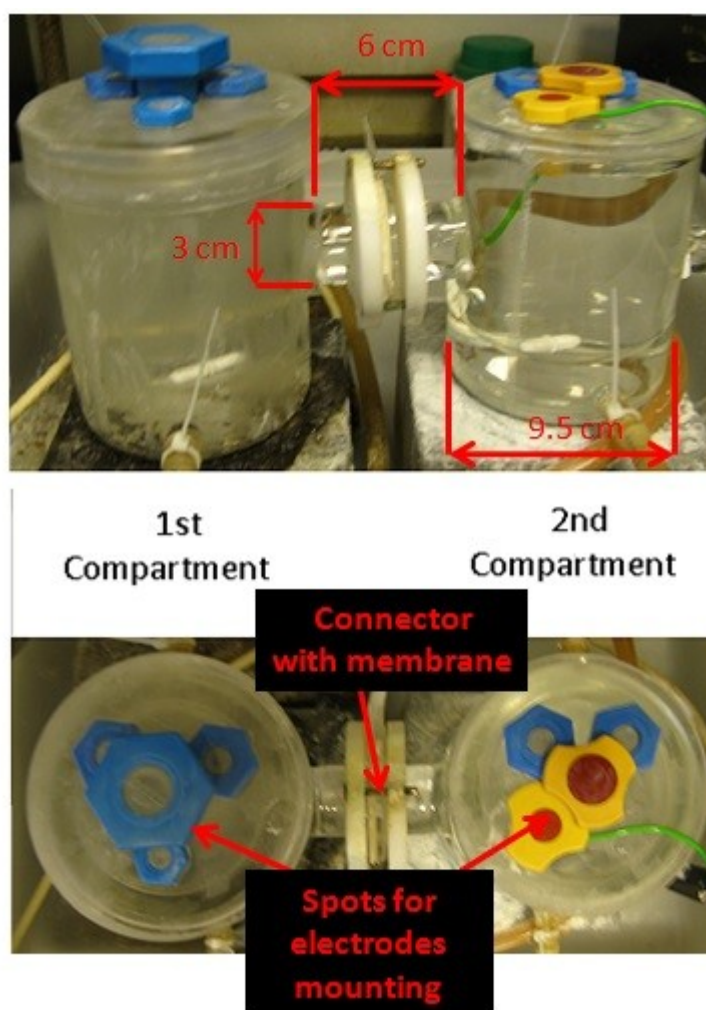


Figure 4-2. Domains of corrosion, immunity and passivation of copper at 25°C [1]

After taking into consideration the issues described above and difficulties with the first prototype of alkaline electrolyser, it was decided to implement another design, made from glass. The second electrolyser design consisted of two compartments connected together by a glass flange (Figure 4-3). Each of the compartments had a circular shape of 9.5 cm diameter with 11 cm depth. Each compartment was surrounded by outer jacket through which water was pumped from an external reservoir to heat up the electrolyte. The inner surface had dimensions of 7 cm diameter and 8 cm height. Temperature control was maintained in the electrochemical cell within  $\pm 1$  °C accuracy. To operate at elevated temperatures, the vessels were heated by water delivered from a Gallenkamp Thermo Stirrer 100 water bath. The connection, linking together the two chambers of electrolyser were tightened to each other flange by external screws and sealed with rubber. The internal diameter of the connections was 2.5 cm (3 cm external). Polymer diaphragm

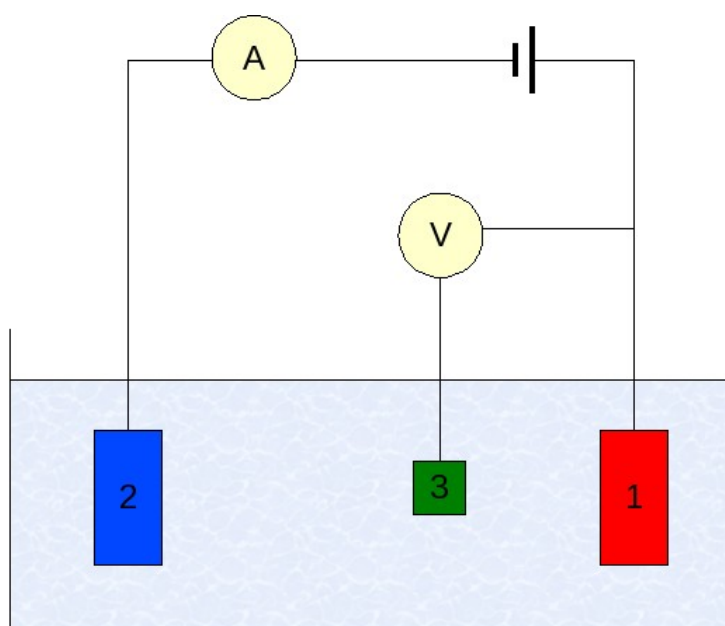
was made of Celgard 3501 and placed between the connections and its role was to prevent the mixing of the gases and at the same time provide ionic conductivity between two chambers. Each of two of the chambers was also placed on magnetic stirrer to avoid concentration gradients during the electrolysis. The vessels were covered with plastic lids with cavities, through which electrodes were mounted. This configuration showed excellent resistance against KOH electrolyte and was able to fulfil all the functionality requirements. Although during the experiments performed, the evolved gases were not captured, the system definitely allowed such a possibility in the future after further slight modifications.



*Figure 4-3. Electrolyser design made of glass*

### 4.1.2. Electrochemical measurements system implementation

For the electrochemical measurements, two main configurations were used. The first one was a single cell comprising the two electrodes and the second one was the three electrode system with counter and reference electrodes. During the normal operation of the electrolyser, the single cell configuration was used and constant current was applied between the anode and cathode electrodes. The three electrode system is more commonly used for control of the potential. Its concept is presented in a *Figure 4-4*.



*Figure 4-4. Three electrode set-up (1) working electrode; (2) counter electrode, (3) reference electrode [4]*

In the three electrode configuration, the potential is applied between working and reference electrodes. The counter electrode is always designed to provide much faster kinetics than that of the working electrode, so as not to limit reaction rate. It is thus usually made of a material which has very good electrocatalytic properties and/or its electrochemical area is very high. During the performed experiments, a platinum mesh counter electrodes was used. The characteristic feature of the reference electrode is that it must have a constant potential inside the electrolyte and

it is used as a reference point for working electrode. The choice of proper reference electrode is dependent on an application and the electrolyte used. Here, the mercury/mercuric oxide electrode was utilised, due to its good stability in alkaline solutions. The advantage of three electrode set-up was that it enables possibility of each electrode (cathode and anode) to be evaluated separately, which was also the main purpose of its application during performed experiments.

## 4.2. Experimental techniques

### 4.2.1. Tafel extrapolation

Tafel extrapolation is an electrochemical technique which yields data allowing the estimation of the parameters of exchange current density ( $j_0$ ), Tafel slope ( $\beta$ ), which describe the reactions kinetics. The exchange current density is a measure of the electron transfer activity at the equilibrium potential and the Tafel slope represents how much current is increased with potential rise [5]. This technique is performed using the three electrode configuration and it is based on Tafel's equation:

$$\log|j| = \log j_0 + \left| \frac{\eta}{\beta} \right| \quad (\text{Eq. 4-1})$$

where:

$$\beta = 2.3 \frac{RT}{\alpha nF} \quad (\text{Eq. 4-2})$$

To obtain the Tafel characteristics the potential (or current) is scanned from the value of equilibrium potential to the reaction region where relationship between  $\log |j|$  and overpotential  $\eta$  is linear. *Figure 4-5* presents typical characteristic which is obtained during such a scan and shows how values of  $j_0$  and  $\beta$  can be calculated.

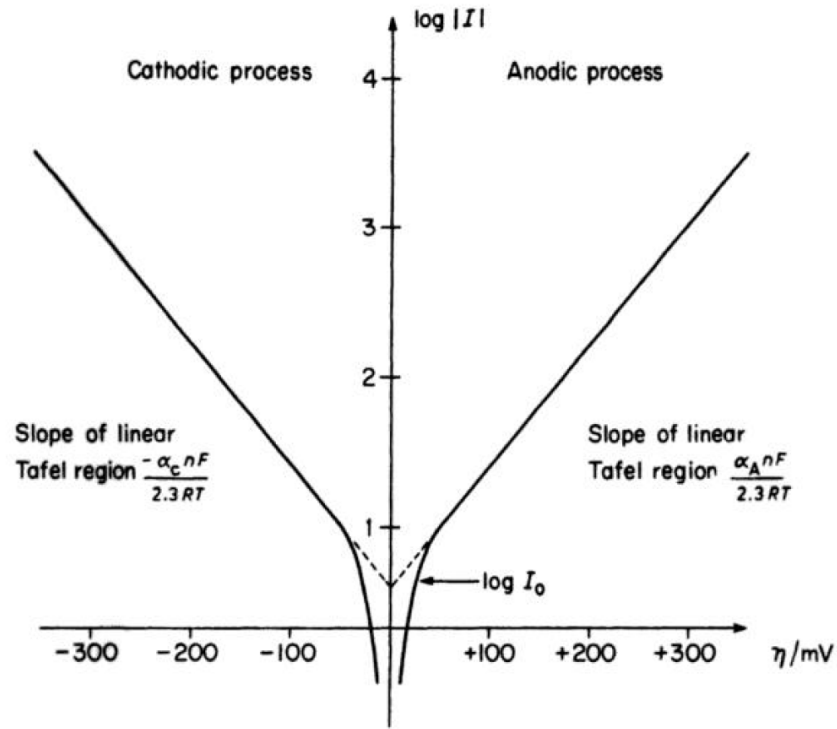


Figure 4-5. Experimental determination of exchange current density using the Tafel's equations [5]

#### 4.2.2. Cyclic voltammetry (CV)

Cyclic voltammetry is another electrochemical technique, which is especially popular for initial studies of the system. CV technique usually is applied on both qualitative and quantitative analysis to obtain kinetic parameters [5]. The basics of operation of cyclic voltammetry are given in the *Figure 4-6*. The potential is swept over a selected range at a constant scan rate. The experiment variables are: potential limits ( $E_1, E_2, E_3$ ), direction of the initial sweep and the potential scan rate ( $v$ ).

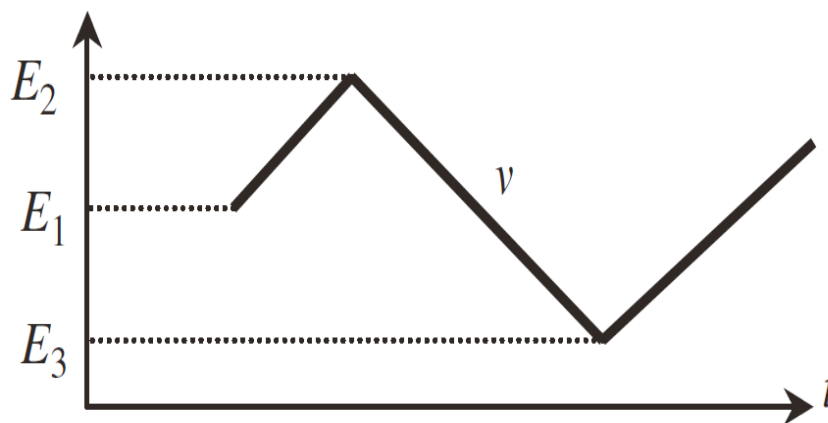


Figure 4-6. Cyclic voltammetry waveform [6]

Results of cyclic voltammetry normally are presented in current vs. potential curves as in Figure 4-7, which shows the results for a polished, nickel sample immersed in 30% KOH solution. In this case, the potential was scanned from a cathodic value of 0.3 V vs Hg/HgO down to -1.3 V, where the scan direction was reversed. Then it was scanned to 0.6 V and then back to 0.3 V. The characteristic features of such a graph are the current peaks which occur in certain potential ranges. Positive current peaks (anodic peaks) show the oxidation reactions and the ones with negative current (cathodic peaks) represent reduction processes. Each of the peaks can be associated with a different electrochemical process. In this example the peak at ca. -1.3V (1) corresponds to hydrogen evolution reaction, which starts occurring at the potential of around -1.1 V and its rate increases with cathodic polarisation. The reversal of potential at -1.3 V limited the HER process. The peak of label 2 is associated with the oxidation of  $\text{NiO}_x$  to  $\alpha\text{-Ni(OH)}_2$  [7]. This peak can be employed to calculate the electrochemical surface area of the nickel samples during experiments as described in the later sections. In the potential region of peak label 3,  $\alpha/\beta\text{-Ni(OH)}_2$  are oxidised to  $\beta\text{-NiOOH}$  [7]. Following this region at around 0.5 V the oxygen evolution reaction starts to occur, creating a rising current labelled peak number 4, which would continue to rise with anodic polarisation. The peak label 5 is the reduction Ni(III) oxyhydroxide back into  $\beta\text{-Ni(OH)}_2$  [7]. Similar shaped graphs are generally obtained for nickel based electrodes in alkaline solutions, although each type of the material has its own, specific cyclic voltammogram features. Cyclic voltammograms usually

differ with amount of peaks, their sizes and shapes depending on the system under study. Additionally the cyclic voltammetry method is also dependent on environmental conditions such as temperature and pressure, as well as the influence of electrochemical material pre-treatment. During the conducting experiments, it was very important to take all these factors into account in order to be able to achieve repeatable results.

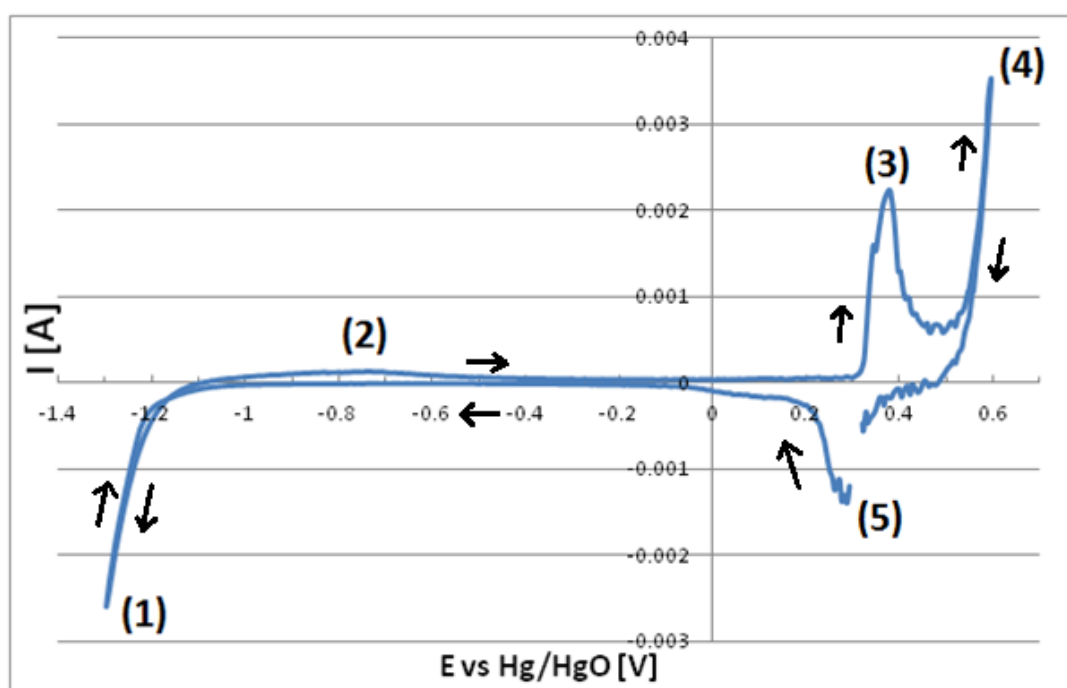


Figure 4-7. Cyclic voltammogram of plain nickel sample immersed in 30% KOH solution, 50 mV/s scan rate, Peaks interpretation: (1)- Hydrogen evolution reaction, (2) - oxidation of  $\text{NiO}_x$  to  $\alpha\text{-Ni(OH)}_2$ , (3) oxidation of  $\alpha/\beta\text{-Ni(OH)}_2$  to  $\beta\text{-NiOOH}$ , (4) – Oxygen evolution reaction, (5) – reduction of Ni(III) oxyhydroxide into  $\beta\text{-Ni(OH)}_2$

#### 4.2.3. Electrochemical impedance spectroscopy (EIS)

Electrochemical impedance spectroscopy is another electroanalytical technique. Its characteristic feature is that it uses small amplitude, sinusoidal, alternating current (AC), which is superimposed on an applied potential. Usually the applied sinusoidal perturbation is less than 10 mV [5]. In an impedance experiment, the output is analysed as a function of the perturbation frequency, over the range 20 kHz to 0.1 mHz [5]. The common presentation of the data is an Argand diagram (Figure 4-8)

*i.e.* a plot of the real vs imaginary components as a function of frequency. The interpretation of the diagram is always based on an equivalent circuit which is an electrical circuit that simulates the behaviour of the electrode reaction. The components of the equivalent circuit differ depending on the system under the study for example if it is a porous or a flat electrode surface. One of the most common equivalent circuits is illustrated in a *Figure 4-8*, with its corresponding Argand diagram. This shows that the charging/discharging of the electrochemical double layer capacitor occurs in parallel to the Faradaic reaction, here represented by the charge transfer resistance  $R_{ct}$  and the Warburg differential impedance  $W$ . Both arms of the circuit can have frequency dependent components.



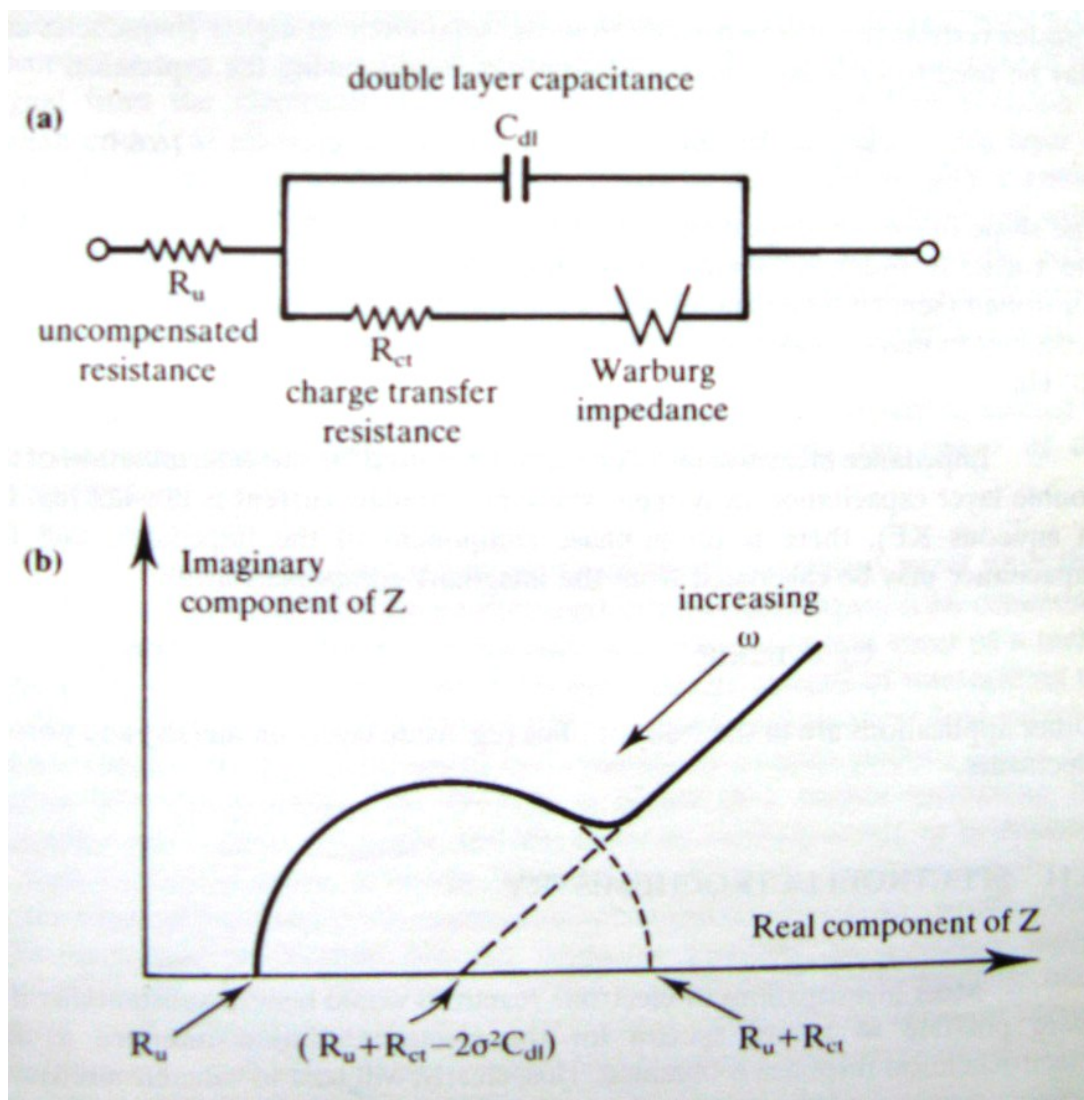


Figure 4-8. (a) Equivalent circuit for a simple electron transfer couple O/R at an inert electrode held at the equilibrium potential for a solution containing oxidants and reactants (reductants) (b) the corresponding Argand diagram [5]

The evaluation of the magnitude of each of the components might be used for the estimation of such parameters as: diffusion coefficient, electron transfer kinetics constant and double layer capacitance. The circuit also models the uncompensated resistance ( $R_u$ ) between the reference and working electrodes. The slope of linear portion at low frequency should be an angle of  $\pi/4$  ( $45^\circ$ ) to the x-axis.

#### 4.2.4. Scanning electron microscope (SEM)

SEM is a technique that provides high resolution images of the sample under examination. These measurements can reveal details about the samples such as their: morphology, chemical composition, crystalline structure and orientation of materials making up the sample [8]. In most cases the data are collected over selected areas of the sample that create two dimensional images. Magnification of typical SEM machine ranges from 20 to 30,000 with spatial resolution of 50 to 100 nm [8].

The fundamentals of the operation of the SEM are based on a phenomenon that accelerated electrons in SEM carry significant amounts of kinetic energy. This energy is dissipated when incident electrons are decelerated in the solid sample. These signals include: secondary electrons, backscattered electrons, diffracted backscattered electrons, photons, visible light and heat. Secondary electrons and backscattered electrons are typically used for imaging the sample viz. secondary electrons are most valuable for showing morphology and topography and backscattered electrons are used for illustrating contrasts in the composition of multiphase samples [8]. X-ray generation is obtained by collisions of the incident electrons with electrons in discrete orbitals of atoms in the sample. Characteristic x-rays are produced for each element in a compound that is excited by the electron beam. SEM analysis is generally non destructive method which means that its application do not lead to volume loss of the sample.

A typical SEM system consists of: electron source, electron lenses, sample stage, detectors for signals of interest and display/data output devices. Its schematics is shown in *Figure 4-9* [8]. SEM technique is critical for fields that require characterisation of solid materials. Most modern SEMs are relatively easy to operate, have user friendly interface and generate data in highly portable digital format. Their applications are usually limited by sample size which in case of vertical dimension rarely can exceed 40 mm [8]. Also samples which are likely to outgas at low pressures, for example wet samples are not suitable for conventional SEM.

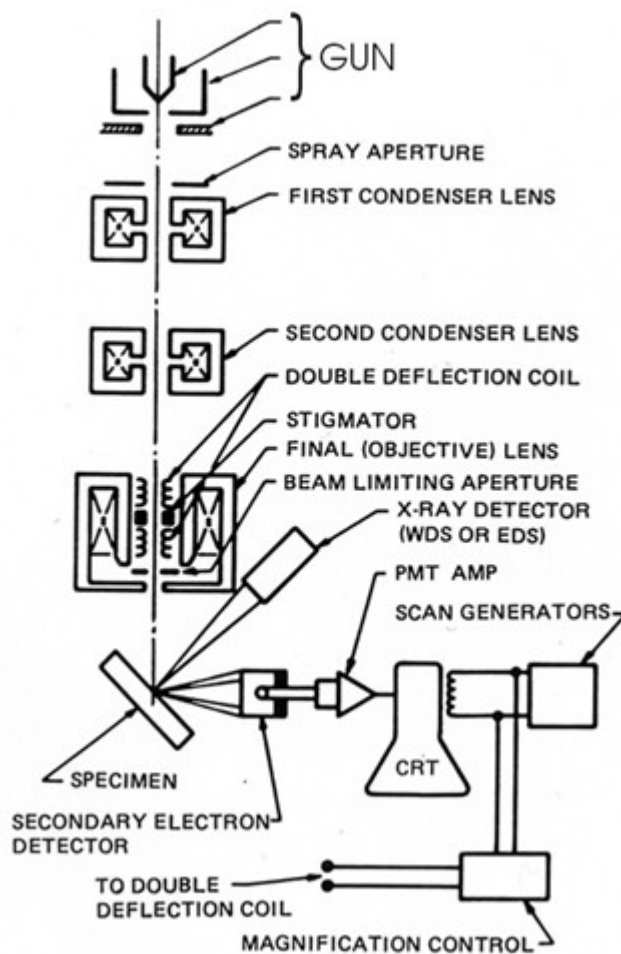


Figure 4-9. Schematic drawing of electron and x-ray optics of SEM [8]

### 4.3. System components description

This paragraph presents detailed technical specifications of chemicals and laboratory equipment used during experiments.

#### 4.3.1. Chemical reagents

All chemicals reagents shown in *Table 4-1* were used as received without further purification. All solutions were prepared using Milli-Q deionised water (resistivity: 18.2 MΩ cm at 25°C) [9].

Chemical Reagent	Comment	Supplier (s)
<b>Potassium Hydroxide</b> (KOH)	85% purity Molecular mass = 56.11 g/mol	Sigma Aldrich [10] Fisher Scientific UK [11] GPR
<b>Potassium sodium tartrate tetrahydrate</b> (C <sub>4</sub> H <sub>4</sub> KNaO <sub>6</sub> · 4H <sub>2</sub> O)	99% purity Molecular mass = 282.22 g/mol	Sigma Aldrich [10]
<b>Vanadium (V) Oxide</b> (O <sub>5</sub> V <sub>2</sub> )	99.6% purity Molecular mass = 181.88 g/mol	Sigma Aldrich [10]
<b>Sodium Molybdenum Oxide Dihydrate</b> (Na <sub>2</sub> MoO <sub>4</sub> · 2H <sub>2</sub> O)	99.5 – 103.0% purity Molecular mass = 241.95 g/mol	Alfa Aesar – A Johnson Matthey Company [11]
<b>Acetone (C<sub>3</sub>H<sub>6</sub>O)</b>	99% purity Molecular mass = 58.08 g/mol	Sigma Aldrich [10]
<b>Isopropyl Alcohol</b> ((CH <sub>3</sub> ) <sub>2</sub> CHOH)	99.7% purity Molecular mass = 60.10 g/mol	Sigma Aldrich [10]

Table 4-1. List of chemical reagents used and their suppliers

### **4.3.2. Electrochemical measuring equipment**

The electrochemical measuring devices, which were used during experiments were: Biologic SP-150 potentiostat/galvanostat, Biologic 10 A current booster, Solartron SI 1287 and Solartron frequency analyser 1255B. All the devices were powered from standard UK grid with sinusoidal voltage of 230 V RMS and 50 Hz.

### **4.3.3. Soldering equipment**

Soldering process played an important role in connecting electrodes to the data acquisition, which need to be done in a way to minimise contact resistance between wire and electrode sample. Nickel surface is generally difficult to solder due to existence of oxide coating and that is why it was required usage of phosphoric acid flux, which is recommended for nickel surface pre-treatment [12]. In this particular application Sylmasta phosphoric acid flux was used [13].

As soldering materials two types of soldering alloys were used. The first one was Multicore 5C (60 % tin 40 % lead) and the second one was Multicore 96SC (95.5 % tin, 3.5 % silver, 0.7 % copper). Both of soldering materials were suitable for the purposes of the experiments. However, due to the higher electrical conductivity and to minimise contact resistance, it was recommended to use Multicore 96SC type. The choice of the soldering iron in this case was not a very important factor and various ones were available inside laboratory. The only conditions which need to be fulfilled in the case of soldering iron, was that it needed to be able to maintain high enough temperature to be able to melt the soldering material as well as being small enough for work with electrodes samples of 1 cm × 1 cm size.

### **4.3.4. Reference electrodes**

As the reference electrode of choice, mercury/mercuric oxides (Hg/HgO) electrode was used. This type of the electrode is characterised by good stability, reproducibility and reversibility in alkaline environment [14] and it is described as the best choice for alkaline solutions [15]. Reference electrodes used during experiments were

obtained from Russell pH limited [16] and Sentek [17] and contained 30 % KOH solution within it.

#### **4.3.5. Insulation**

The insulation of the soldering material and uncoated connecting wire was provided by epoxy resin Araldite 2022, which is characterised by relatively short curing time, excellent bond to a wide range of composites, plastics, metal and good resistance for chemicals (including alkaline solutions) [18]. It was worth noting that not all epoxy resins on the market can fulfil these conditions, so before choosing one it is worth to check the detailed parameters of the resin used.

#### **4.3.6. Membrane/Diaphragm**

The role of membrane within the electrolyser was to separate the compartments where oxygen and hydrogen gases were produced. Several types of commercial membranes are available among at which the polymer type membranes are relatively popular. The key properties of the membrane are that it needed to be stable in the electrolyte environment and be permeable to ions. In the case of gas separation, pore size should not exceed 10  $\mu\text{m}$  for hydrogen separation at atmospheric pressure and porosity of at least 50% is desirable to keep electrical resistance low [19]. In case of Celgard 3501 which was applied during the electrolyser single cell experiments, all these conditions were fulfilled. Detailed parameters of Celgard 3501 membrane are presented in a *Table 4-2*.

<b>Basic Film Properties</b>	<b>Unit of Measure</b>	<b>Typical Value</b>
<b>Thickness</b>	$\mu\text{m}$	25
<b>Porosity</b>	%	55
<b>PP Pore Size (avg. diameter)</b>	$\mu\text{m}$	0.064
<b>TD Shrinkage @ 90°C /1 Hour</b>	%	0
<b>MD Shrinkage @ 90°C /1 Hour</b>	%	5
<b>Puncture Strength</b>	grams	335
<b>Tensile Strength, MD</b>	$\text{kg}/\text{cm}^2$	1055
<b>Tensile Strength, TD</b>	$\text{kg}/\text{cm}^2$	135

*Table 4-2. Membrane - Celgard 3501 specifications*

## References:

1. M. Pourbaix. *Atlas of electrochemical equilibria in aqueous solutions*. National Association of Corrosion Engineers, 1974
2. D. J. De Renzo. *Corrosion resistant materials handbook*. 1985 by Noyes Data Corporation. ISBN: 0-8155-1023-3
3. [http://www.roymech.co.uk/Useful\\_Tables/Corrosion/Corr\\_metals\\_1.html](http://www.roymech.co.uk/Useful_Tables/Corrosion/Corr_metals_1.html), accessed 1<sup>st</sup> October 2013
4. <http://en.wikipedia.org/wiki/Voltammetry>, accessed 14<sup>th</sup> September 2014
5. D. Pletcher. *A first course in electrode processes*. 1991 by The Electrochemical Consultancy. ISBN: 0951730703
6. C. G. Zoski. *Handbook of electrochemistry*. Elsevier, 2007. ISBN-10: 0-444-51958-0
7. D. S. Hall, C. Bock, B. R. MacDougall. *The electrochemistry of metallic nickel: oxides, hydroxides, hydrides and alkaline hydrogen evolution*. Journal of The Electrochemical Society, Vol. 160, Issue 3, 2013, pp. F235-F243
8. [http://serc.carleton.edu/research\\_education/geochemsheets/techniques/SEM.html](http://serc.carleton.edu/research_education/geochemsheets/techniques/SEM.html), accessed 14<sup>th</sup> September 2014
9. <http://www.millipore.com/>, accessed 14<sup>th</sup> September 2014
10. <http://www.sigmaaldrich.com/united-kingdom.html>, accessed 14<sup>th</sup> September 2014
11. <http://www.fisher.co.uk/>, accessed 14<sup>th</sup> September 2014



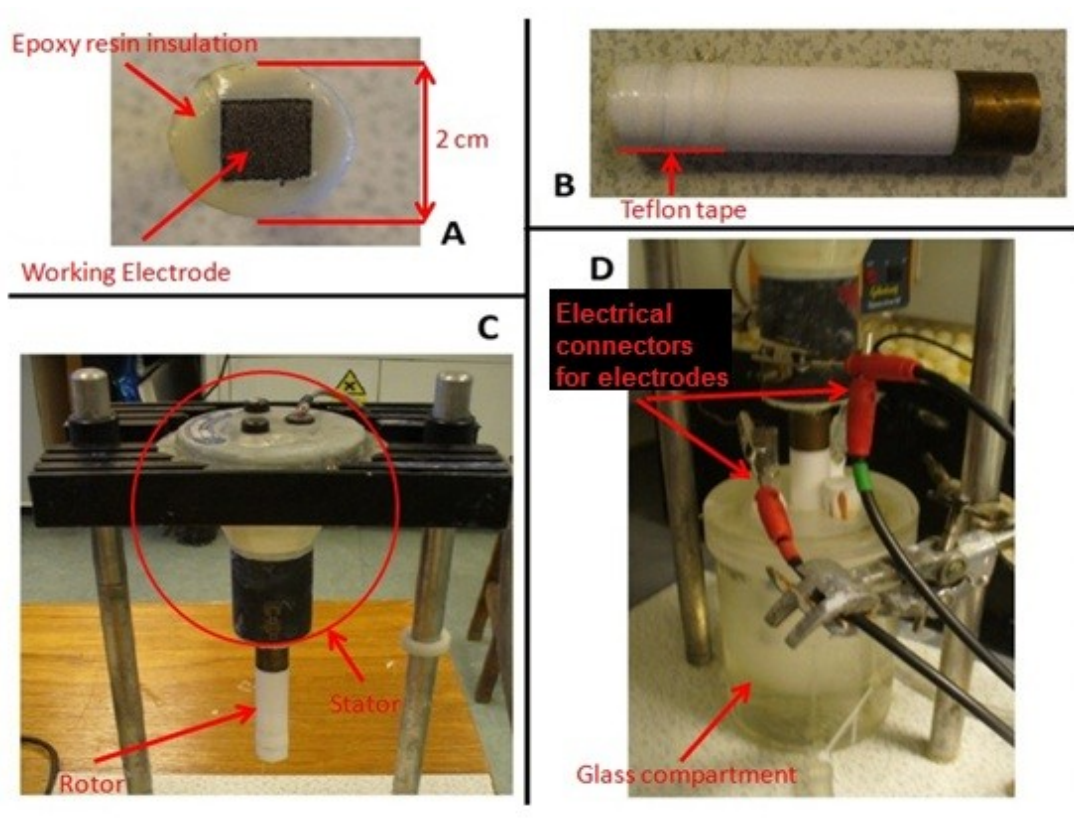
12. [http://www.somersetsolders.com/product.php/1028/0/phosphoric\\_acid\\_flux\\_f\\_or\\_stainless\\_steel\\_soldering](http://www.somersetsolders.com/product.php/1028/0/phosphoric_acid_flux_f_or_stainless_steel_soldering), accessed 14<sup>th</sup> September 2014
13. <http://www.sylmasta.com/acatalog/Phosphoric-Acid-Flux--50ml--224.html>, accessed 14<sup>th</sup> September 2014
14. T. T. Kam. *Some electrochemical studies of mercury/mercuric oxide electrode with an inner electrolyte of 33 wt-vol% sodium hydroxide*. *Electrochimica Acta*, Vol. 27, Issue 5, 1982, pp. 553-555
15. [https://www.koslow.com/reference\\_electrodes/5088/mercury\\_oxide\\_reference\\_electrode\\_5088?zenid=fa6f86d8a363a000f4efbc4dfd8fd42d](https://www.koslow.com/reference_electrodes/5088/mercury_oxide_reference_electrode_5088?zenid=fa6f86d8a363a000f4efbc4dfd8fd42d), accessed 14<sup>th</sup> September 2014
16. <http://www.thermoscientific.com>, accessed 14<sup>th</sup> September 2014
17. <http://www.sentek.co.uk>, accessed 14<sup>th</sup> September 2014
18. <http://docs-europe.electrocomponents.com/webdocs/0034/0900766b8003451b.pdf>, accessed 14<sup>th</sup> September 2014
19. H. Wendt. *Electrochemical Hydrogen Technologies. Electrochemical Production and Combustion of Hydrogen*. Elsevier, 1990

## 5. Alkaline electrolyser system troubleshooting

During the initial tests on the alkaline electrolyser, several issues arose that needed to be overcome before further experiments could continue. The purpose of this section is to describe these issues and explain how they were addressed.

For the tests, it was decided to use the 3 electrode system comprising working, reference and counter electrodes inside a single vessel. As a reference electrode, the mercury/mercuric oxide (Hg/HgO) electrode was used and a platinum foil acted as the counter electrode providing a high area surface. For electrochemical control and data acquisition, the Solartron SI 1286 Electrochemical Interface was used. The tests were performed in a 30% Potassium hydroxide (KOH) electrolyte inside the glass compartment at the temperature of 70°C. In these preliminary experiments, two main different system configurations were evaluated and these were the Rotating Disc Electrode (RDE) configuration with horizontal working electrode orientation with very well controlled mass transport and the vertical working electrode orientation with mechanical stirrer bar inside the electrolyte. Both of these configurations were tested with and without gas separation in the cell. Furthermore, different types of electrical contacts to the sample electrodes were checked in order to identify which gave the better performance under the operational conditions of the electrolyser.

The RDE system consisted of stator and rotor to which the activated Raney nickel electrode was attached using silver paint. The electrode holder was insulated from the electrolyte environment by epoxy resin at the bottom and Teflon tape at the sides (*Figure 5-1*). The RDE system also had the possibility of rotation speed control.



*Figure 5-1. Rotating Disc Electrode system overview: A – Raney nickel electrode attached on the bottom, B – rotating part of the system, C – Stator + rotor, D – System during experiments*

During the experiments with the rotating disc electrode system, relatively high voltage fluctuations were observed (*Figure 5-2*), especially at low rotation speeds. This could be attributed to gas bubbles that adhered to the electrode surface. As the electrode was in a horizontal orientation, the bubbles produced during electrolysis, could not easily escape the surface due to buoyancy force that acted towards electrode surface. These bubbles which adhered to the surface also decreased the efficiency of the electrode towards HER as they effectively reduced its active area. Increasing rotation velocity from 10 to 30 Hz decreased the voltage fluctuations and increased performance (*Figure 5-2*) as these bubbles were removed by centrifugal force.

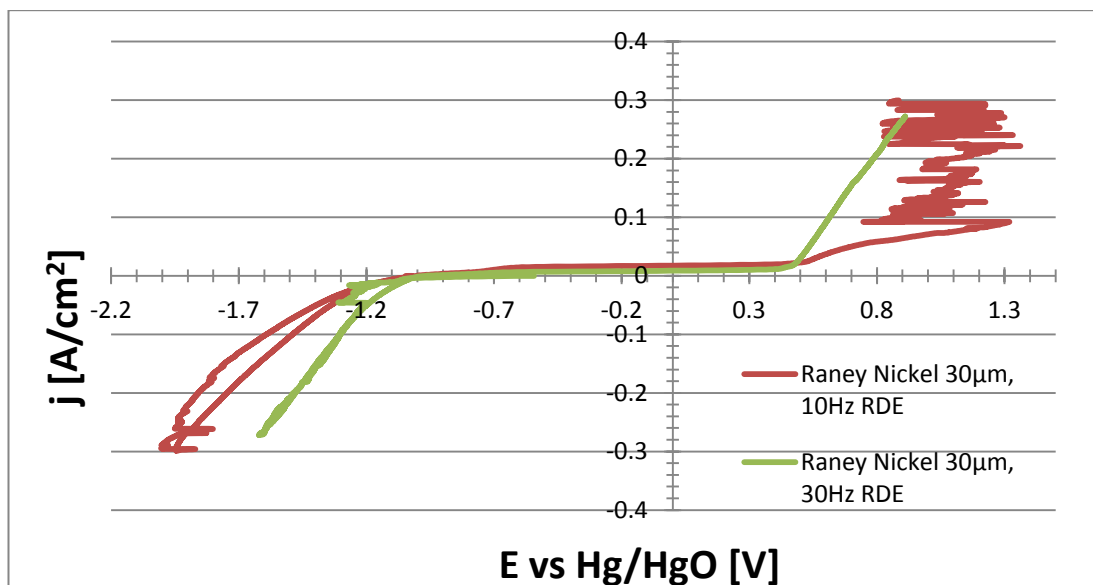
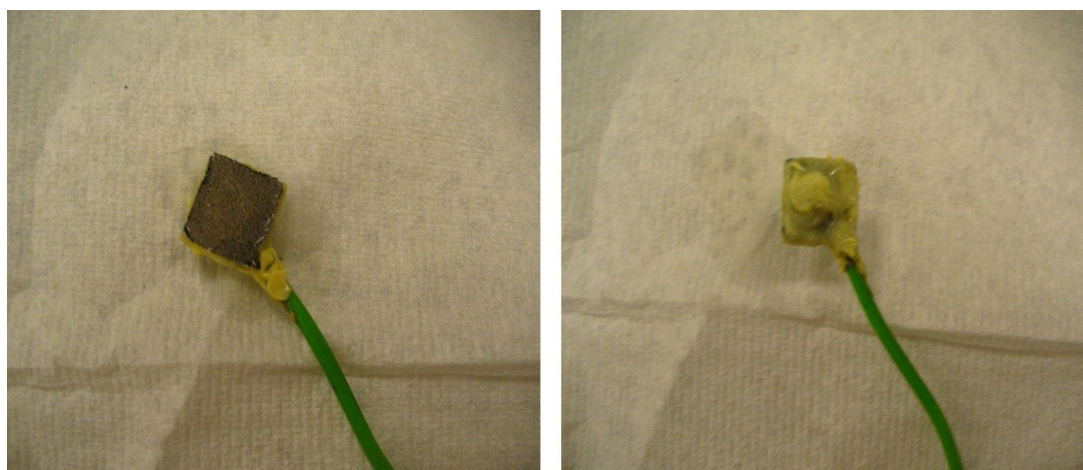


Figure 5-2. Current density (Potential) curves on 10 Hz and 30 Hz rotating speed of Raney nickel, Scan rate 0.1 mA/s

Despite this improvement though, the performance of the electrodes inside the RDE system was still not satisfactory and was indeed quite low compared to published, scientific data on similar electrodes types [1-4]. The reason for this was much too high contact resistance of the sample electrode to the holder when attached using silver conducting paint. Such a connection resulted in higher ohmic losses and because of this it was decided to abandon using RDE system and to create different system for testing the electrode samples.

The system with the vertical electrode configuration consisted of the sample electrode soldered to the contact wire, insulated and then put into the electrolyte in the vertical position. The reverse side of the electrode was insulated from the electrolyte by epoxy resin (Figure 5-3).



*Figure 5-3. Electrode used for vertical electrode configuration Left – front side of the electrode Right – reverse side of the electrode insulated by epoxy resin*

During the experiments a magnetic stirrer was used so as to keep the electrolyte chemically uniform. Bubbles removal from the electrodes surface with this system was satisfactory and no voltage fluctuations were observed. The scientific literature also revealed that bubbles release, could be additionally improved by adding chemical compounds which reduce the surface tension or by designed electrode surface structures made of hydrophilic materials with pore sizes lower than 10  $\mu\text{m}$  [5, 6].

One of the major challenges faced during this system evaluation was to minimise ohmic losses by providing good electrical contact to the sample electrode. To achieve this goal, the electrical contact wire was soldered to the non-activated surface of the electrode. It was very important to cover as large surface of non activated side of the electrode area by the soldering material as possible. Failure to do this usually led to bad electrical contact and so, large ohmic losses. It was also important to use soldering material with the best electrical conductivity (usually with high silver (Ag) content). Other sources of ohmic losses in the electrochemical systems are the connectors and cables, so due to that special attention should be paid to use the ones with as low resistance as possible.

All the soldering material on the surface was covered with epoxy resin (Araldite 2022) to make an insulation layer from the alkaline environment. After soldering and

insulating, the conductive side of the electrode was activated using a 30 % potassium hydroxide/10 % sodium tartrate solution. In this application the chosen epoxy resin (Araldite 2022) needed to be resistant to strong alkaline solutions and temperatures up to 100°C. Failure in choosing the proper epoxy resin resulted in insulation damage during the system operation which very likely cause the soldering material to come into contact with the electrolyte and corrode. The occurrence of such a situation often leads to cell failure and to the contamination of the electrolyte with soldering material.

The contamination of the electrolyte yields impurities, which engineers of electrochemical systems should be especially aware off. Dissolved particles inside the KOH electrolyte formed ions that could be deposited on the surface of the electrode and influence its performance (usually in the negative way). During the performed experiments, it did happen when the soldering material (composed mainly of tin (Sn) and lead (Pb)) was dissolved into the electrolyte and deposited on the cathode surface forming an outer layer. Due to this, the performance of the electrode significantly decreased as Pb and Sn have a much lower exchange current density than nickel for the HER. Once this electrolyte contamination occurred, it was very important to change or filter the electrolyte. Electrolyte contamination could also come from any material that comes into contact with the caustic electrolyte or from impurities in the chemicals used for preparation of the electrolyte solution [7]. Thus, special attention should always be paid in the use of corrosion resistant material, providing good electrical insulation and using high purity chemicals.

Another factor that could be influencing the electrolyser performance was the mixing of the gases (*viz.* H<sub>2</sub> and O<sub>2</sub>) produced during the operation. Experiments here were performed with and without gas separation, *i.e.* the anode and cathode compartments were either separated with a diaphragm or had a common compartment. Clearly, the function of the electrolyser is to produce H<sub>2</sub> free from any oxygen contamination at the cathode but the study here was to determine what impact (if any) oxygen in the electrolyte solution would have on the cathode performance. As it was, no significant deterioration in the cathode performance was observed during the operation of the cell over a period of a few hours.

In summary then, the main factors that influenced the proper functionality of the electrochemical system were quality of electrical contact; gas bubbles produced; electrolyte contamination and lack of adequate corrosion resistance of the contacts and soldering material. *Table 5-1* shows how each of these factors might influence the electrolyser system and suggests solutions to each of these issues. Although this list does not include all the factors that should be considered for system construction, it does however presents the difficulties that were noted and solved during the design of the current system.

Issue	Effect	Solution
<b>Bad electrical contact</b>	Performance drop, loss of voltage and energy efficiency	Maximise electrode surface area contact Use cables and connectors having low resistance.
<b>Bubbles effect</b>	Performance drop Voltage/Current fluctuations	Vertical electrode orientation Mechanical electrolyte circulation Chemical electrolyte additives to reduce surface tension Designed electrode structure/morphology Increasing rotation speed in RDE configuration
<b>Electrolyte contamination</b>	Performance impact	Use high purity chemicals for electrolyte preparation Use materials that do not corrode inside electrolyte environment
<b>Lack of gas separation</b>	Possible performance impact over long period of time	Application of diaphragm Putting electrodes inside separated compartments.
<b>Not sufficient corrosion resistance</b>	Electrolyte contamination Electrolyte leakage Performance change	Use materials that are corrosion resistant inside working environment

*Table 5-1. Factors influencing alkaline electrolyser system performance*

*Figure 5-4 and Figure 5-5 show comparisons of the  $j(E)$  curves that were achieved at the beginning of troubleshooting using the RDE system (Figure 5-4) and after optimising the cell, using the vertical electrode configuration (Figure 5-5) using*



plain nickel and Raney nickel electrodes. As can be observed, the reduction in the voltage fluctuations and an improvement in the general performance were significant (for each electrode type the same current densities were achieved for the lower voltage values). Making these improvements allowed results to be obtained which were comparable to the ones published in the literature for the same or similar electrode types [1-4].

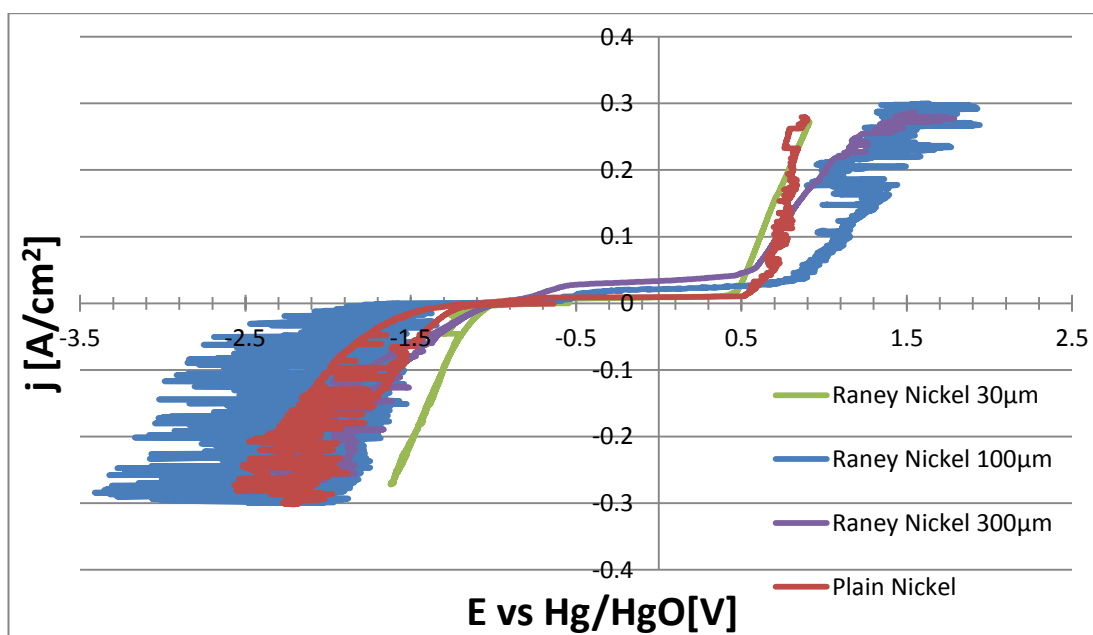


Figure 5-4. Current density (Potential) curves for electrodes before optimisation in rotating disc electrode configuration, Scan rate 0.1 mA/s

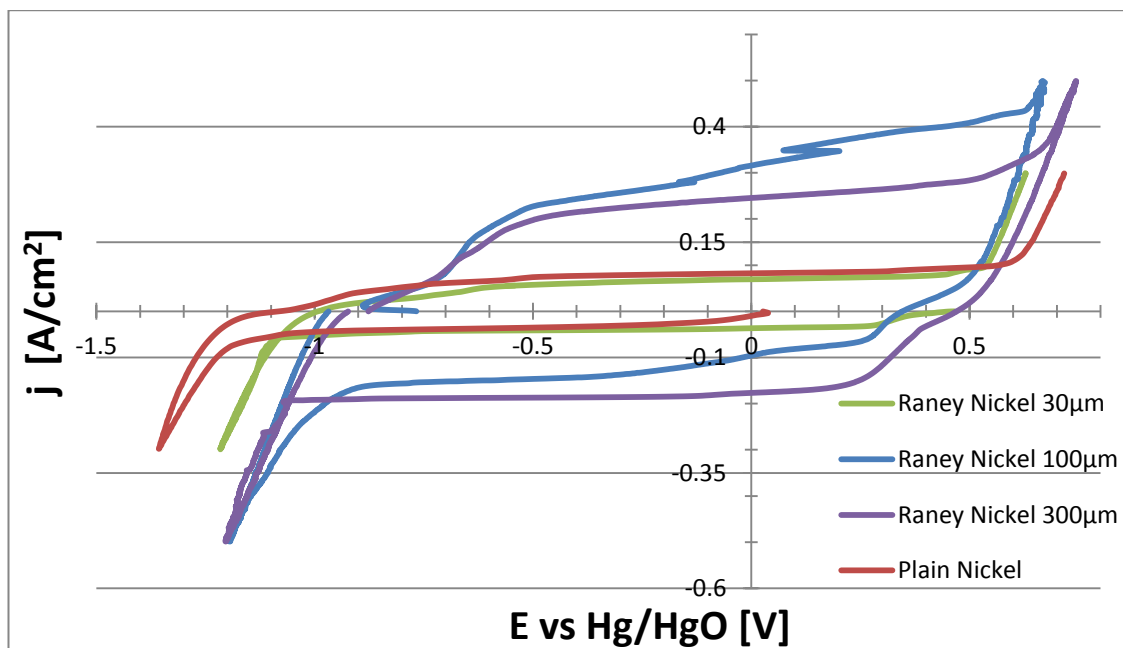


Figure 5-5. Current density (Potential) curves for electrodes after optimisation with vertical electrodes orientation, Scan rate 0.1 mA/s

## References:

1. P. T. Nielsen, T. Mathiesen, J. K. Kristensen, L. Hilbert, L. Yde. *Atmospheric plasma spraying of electrodes for conversion of electricity to hydrogen by high temperature alkaline electrolysis of water*. Proceedings of ITSC 2011, Sept. 27-29, Hamburg, Germany
2. D. Pletcher, X. Li, S. Wang. *A comparison of cathodes for zero gap alkaline water electrolyzers for hydrogen production*. International Journal of Hydrogen Energy, Vol. 37, 2012, pp. 7429-7435
3. M. P. Marceta Kaninski, S. M. Miulovic, G. S. Tasic, A. D. Maksic, V. M. Nikolic. *A study on the Co-W activated Ni electrodes for the hydrogen production from alkaline water electrolysis - Energy saving*. International Journal of Hydrogen Energy, Vol. 36, 2011, pp. 5227-5235
4. S. Marini, P. Salvi, P. Nelli, R. Pesenti, M. Villa, M. Berrettoni, G. Zangari, Y. Kiros. *Advanced alkaline water electrolysis*. Electrochimica Acta, Vol. 82, 2012, pp. 384–391
5. K. Zeng, D. Zhang. *Recent progress in alkaline water electrolysis for hydrogen production and applications*. Progress in Energy and Combustion Science, Vol. 36, 2010, pp. 307–326
6. H. Wendt. *Electrochemical Hydrogen Technologies. Electrochemical Production and Combustion of Hydrogen*. Elsevier 1990
7. L. Brossard, J.Y. Huot. *Influence of iron impurities on the time dependence of the hydrogen evolution reaction on platinum cathodes during electrolysis of 30% w/o KOH*. Journal of Applied Electrochemistry, Vol. 19, 1989, pp. 882-888

## **6. Evaluation of Raney nickel electrodes prepared by atmospheric plasma spraying for alkaline water electrolysers**

### **6.1. Introduction**

With limited amount of fossil fuels and increasing interest in sustainable energy, hydrogen produced from alkaline water electrolyser units, powered from renewable energy sources has grown in interest year on year. Hydrogen can be used in fuel cell devices to power automotive vehicles, electronic portable devices (such as laptops, mobile phones) and for stationary applications (uninterruptable power supplies as well as combined heat and power systems). Along with its zero carbon capability as an energy vector in substituting fossil fuels, hydrogen is also employed in industrial processes such as petroleum refining, ammonia production, manufacture of electronic components and high quality welding [1-6].

In Scotland, the government energy target for 2020 is to generate 100% of gross annual electricity consumption from renewable energy sources [7], mainly derived from wind turbines. Such a large amount of unpredictable, variable energy generation requires substantial energy storage capability to become truly viable. Alkaline water electrolysers provide an ideal solution to this problem as, with the current state of the art, they are able to respond in a timescale of less than 1 s to changing wind conditions [8].

Although alkaline water electrolysis technology appears to be mature enough to be implemented on a large scale within a renewable energy market, there is still a lot of R&D work needed to improve the efficiency and durability of these systems [2]. One way these goals could be achieved is through the development of new electrode types with novel catalysts. Electrodes and catalysts for the hydrogen evolution reaction HER have been extensively studied and reported in the literature [9-16]. For example, Pletcher *et al.* [9, 12] compared different cathode types and performed

stability tests on single cells in zero-gap configuration. These authors found that nickel–molybdenum and ruthenium oxide catalyst gave stable performances for HER over 10 days of electrolysis, whilst the overpotential for platinum increased with time. During these tests, a current density of  $1 \text{ A cm}^{-2}$  was achieved at a cell voltage of *c.a.* 2.1 V. Kaninski *et al.* [10] investigated the effects of cobalt and vanadium deposits on the nickel cathodes and concluded that these compounds could enhance significantly the HER performance through an increase of the real surface area and in the electrocatalytic activity. The work of Krstajic *et al.* [11] involved analysis of nickel–molybdenum cathode coatings using polarisation measurements, cyclic voltammetry and electrochemical impedance spectroscopy. It was concluded that the Ni–Mo coatings obtained by the electrodeposition technique provided high catalytic activity, but exhibited low stability. Nickel–iridium–carbon electrodes were developed and characterised by Solmaz [13]. It was observed that nickel–iridium deposits on nickel-modified carbon enhanced the HER activity. This effect was attributed to the creation of finer surface structures, leading to a high surface area and electrocatalytically active centres. The *in-situ* electrodeposition of nickel–molybdenum catalyst was investigated by Tasic *et al.* [14]. They also showed that the nickel–molybdenum compounds could significantly improve the electrolyser cathode performance by increasing active area and electrocatalytic activity. They too observed good stability during long term electrolysis. High surface area nickel-based skeletal catalysts were prepared and characterised by Martinez *et al.* [15]. These again showed high surface area and good performance for HER. The work of Ganesh and Lakshminarayanan [16] focused on the electrodeposition of nickel and obtained one of the highest roughness factors reported in the literature using nickel obtained from sulphamate bath.

Of the different catalyst types however, one of the best for the HER is Raney nickel. This catalyst type is produced by leaching aluminium or zinc from a precursor (Ni–Al or Ni–Zn) alloy by caustic solution, leaving a very porous material. Such a process causes the available surface area to increase and also leads to lower overpotentials for HER. A number of different techniques have been employed for Raney nickel preparation including: electrodeposition [17], plasma spraying [18-20],

rolling of Al and Ni foils followed by heat treatment [21, 22], pressing and heating of Ni + Al powders [18, 23], pressing Raney-Ni with fractal Ni powder [23], and sintering Ni [18, 24]. Raney nickel electrodes produced by the technique of vacuum plasma spraying (VPS) has exhibited one of the best efficiencies reported in the literature for HER [19, 20]. However, in this technique, complex devices and design are required to maintain the low pressure in the chamber during the plasma spray process [25].

In this chapter, the novel atmospheric plasma spraying (APS) production method was used to prepare the Raney nickel electrode materials. Compared to VPS, the atmospheric plasma spraying method is much cheaper and simpler. According to the APS manufacturer's documentation [26], the energy efficiency of these APS electrodes towards HER could be as high as 96% based on the Higher Heating Value (HHV) when operated at a current density of  $300 \text{ mA cm}^{-2}$ , and so making them promising candidates for use in future alkaline electrolyzers. The aim of this investigation was thus to evaluate the performance of the APS Raney nickel samples under different working conditions (temperature and current density) and identify the factors responsible for maintaining good and stable electrode performance. The understanding of these factors, at different temperatures and current densities is fundamental for future electrode improvements as well as providing knowledge on the key parameters of influence.

## **6.2. Experimental setup**

### **6.2.1. General system configuration**

The set-up used for the electrochemical studies consisted of a typical three-electrode configuration. The working electrode consisted of the Force Technology APS Raney nickel samples which were cut to dimensions of  $1 \text{ cm} \times 1 \text{ cm}$ . These were soldered to a piece of insulated Ni–chrome wire and sealed using epoxy resin to also isolate the

inactive side of the surface from the electrolyte. A platinum mesh of geometrical surface area much greater than that of the working electrode was used as the counter electrode. A mercury/mercuric oxide (Hg/HgO) electrode inserted into the working solution was used as the reference electrode. This has a standard potential  $E^\circ = 0.098 \text{ V}$  vs the standard hydrogen electrode. The measurement environment consisted of a single, jacketed vessel filled with 30% KOH solution. All solutions were prepared using Milli-Q de-ionised water (resistivity 18.2 M $\Omega$  cm). The vessel was heated by water delivered from a Gallenkamp Thermo Stirrer 100 water bath. Temperature control was maintained in the electrochemical cell to within  $\pm 1$  °C. During the experiments, the electrolyte in the cell was stirred using a magnetic stirrer. A Solartron SI 1286 Electrochemical Interface with 1255B frequency analyser system controlled by CorrWare and Zplot software (Scribner Associates, USA) was used to deliver electrical power and measure the electrical response of the system. The electroanalytical techniques employed to investigate the performance of these electrodes were cyclic voltammetry, electrochemical impedance spectroscopy (EIS) and Tafel extrapolation. Additional characterisation of the electrode surface was provided by a Cambridge Instruments Stereoscan 90 scanning electron microscope (SEM).

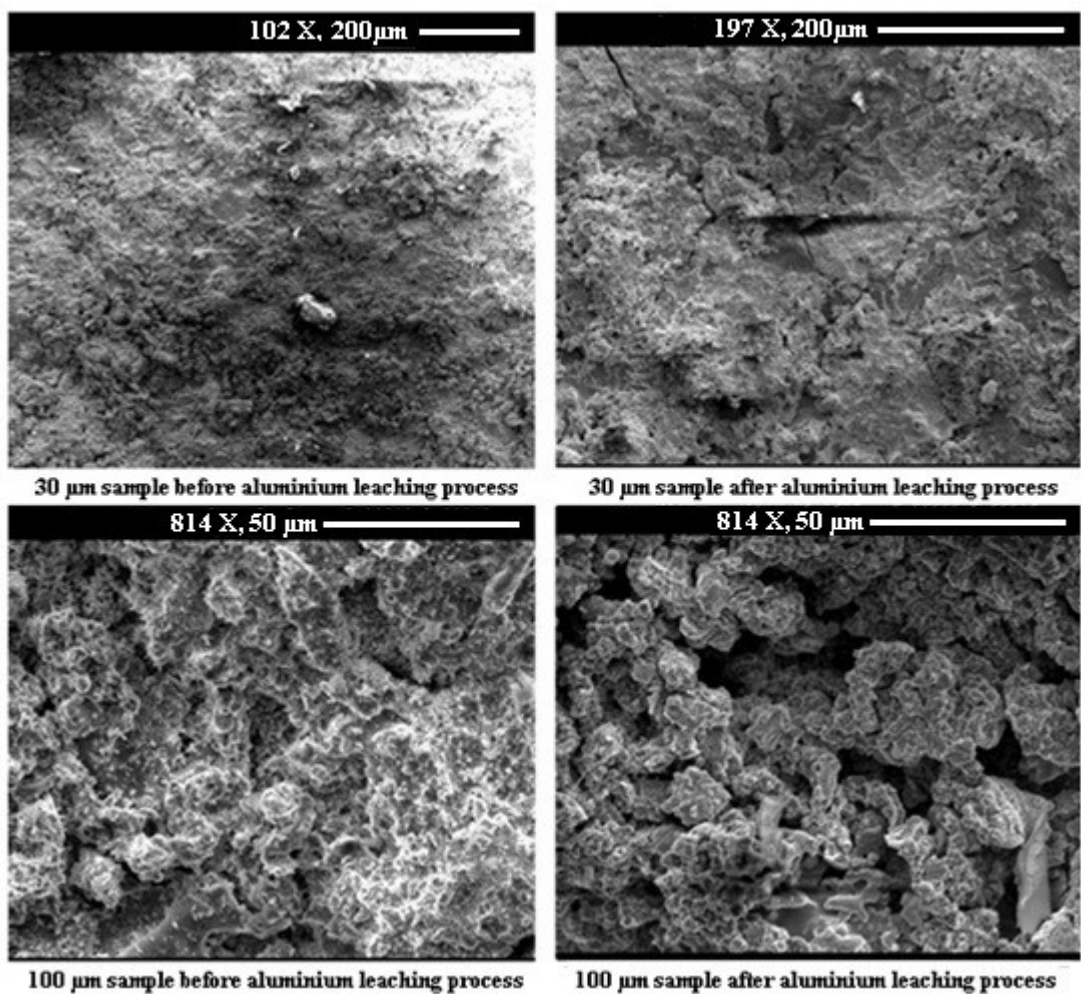
### **6.2.2. Working electrode sample preparation**

The samples obtained from Force Technology consisted of 100 mm  $\times$  100 mm  $\times$  0.5 mm plates covered on both sides with Raney nickel catalyst (50/50 nickel/aluminium) of different thicknesses: 30  $\mu\text{m}$ ; 100  $\mu\text{m}$ ; and 300  $\mu\text{m}$  on a nickel base plate. From the plates, samples of 1 cm  $\times$  1 cm dimension were cut and used as electrodes in the experiments. Subsequently, the samples were soldered on one side to a conducting wire, degreased in an ultrasonic bath and bonded with epoxy resin (Araldite 2022) to isolate and protect against the KOH solution. The epoxy resin used was chosen for its excellent chemical resistance and relatively short bonding time.

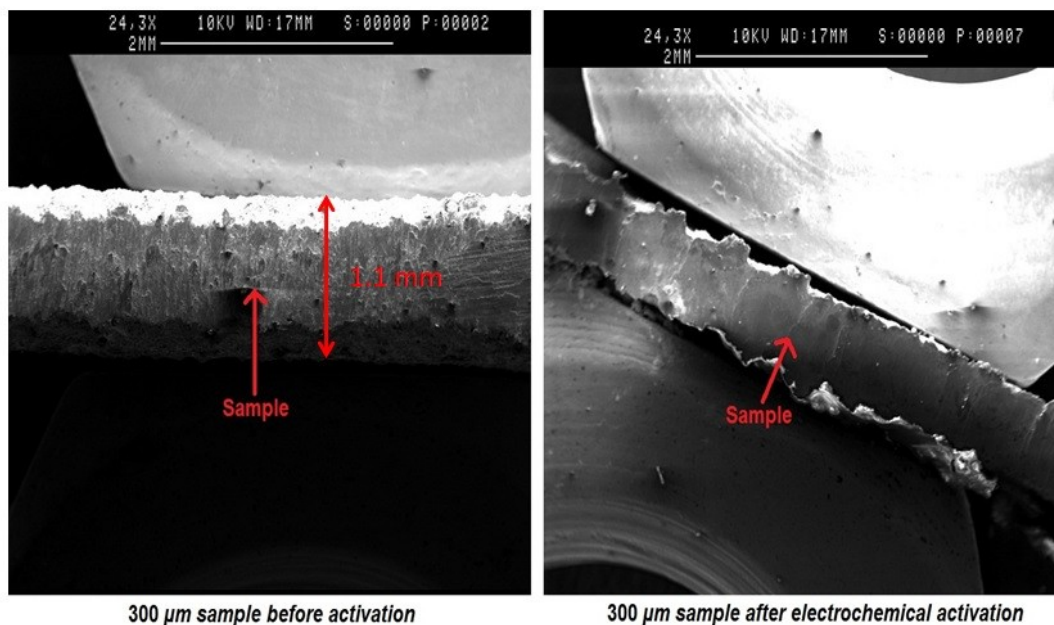
The prepared samples were then chemically activated using a solution containing 30% KOH and 10 wt% sodium/potassium tartrate at 80 °C for 24 h. The aim of this

process was to leach out most of the aluminium from the inter-metallic phases and also make the electrode surface porous [26]. This process of leaching out of the aluminium can be clearly seen on the SEM images (*Figure 6-1*) where the porous structure of the electrodes after activation can be compared to the starting material. The final step in the procedure was that of electrochemical activation. The conditions employed were developed by Force Technology [26] and consisted of: subjecting the sample for 2 h at  $10 \text{ mA cm}^{-2}$ , in the oxygen evolution reaction (OER) region and then for 14 h at  $-200 \text{ mA cm}^{-2}$  in the HER. The aim of the described activation procedures was to prepare each of the samples to be used inside the alkaline electrolyser. Following this, the samples were considered to have been fully activated. Additional SEM images of the samples present cross section of the sample before and after electrochemical activation (*Figure 6-2*). It confirms the fact that surface structure of activated sample is visibly more porous in comparison with the non-activated one and shows that the Raney nickel outer layer was leached out from the electrode surface during activation process.





*Figure 6-1. SEM micrographs of the 30 µm and 100 µm Raney nickel samples before and after chemical activation*



*Figure 6-2. SEM micrographs of the 300  $\mu\text{m}$  Raney nickel samples cross section before and after chemical activation*

### **6.2.3. Experimental procedures employed**

The experimental procedure followed was partly adapted from the work of Ganesh and Lakshminarayanan [16]. Before proceeding with any measurements the electrode was operated at  $200 \text{ mA cm}^{-2}$  (HER) for 10 min to reduce surface oxides and to cathodically clean the surface by the evolution of hydrogen gas. This was followed by keeping the electrode at a potential of  $-0.85 \text{ V}$  for 60 s in order to oxidise any surface hydrides formed during the cathodic polarisation activation step. The potential was then scanned from  $-1.1 \text{ V}$  to  $0 \text{ V}$  and then back to  $-1.1 \text{ V}$  with a scan rate of  $50 \text{ mV/s}$  to obtain the nickel oxidation and reduction characteristics. From the analysis of these results, the electroactive surface area of the sample could be determined as during the forward scan in the potential region beyond  $-0.95 \text{ V}$ , a peak corresponding to  $\alpha\text{-Ni(OH)}_2$  formation occurred and it is this charge ( $514 \mu\text{C cm}^{-2}$ ) associated with the formation of a monolayer of  $\alpha\text{-Ni(OH)}_2$  which allows the real electrochemical surface area of the sample to be evaluated [16, 27, 28].

Subsequently five potentiodynamic scans were performed from  $-0.85$  V to the potential where a current density of  $-300$  mA cm<sup>-2</sup> was obtained (typically at around  $-1.05$  V) and then back to the potential  $-0.9$  V, with a scan rate of  $0.5$  mV/s. During the potentiodynamic scans to these high limits, it was observed that the forward scan exhibited slightly lower overpotential values compared to the reverse scan and this can partly be attributed to the reduction of surface oxides created during prior electrode treatment. During all the potentiodynamic scans, IR compensation based on the current-interrupt method was used. Following the potentiodynamic scans, EIS measurements were undertaken. EIS consisted of 5 consecutive scans over the frequency range from  $100$  kHz to  $0.1$  Hz performed one after another at the potentials of  $-0.95$  V,  $-1.00$  V,  $-1.05$  V,  $-1.10$  V and  $-1.15$  V. The ac sinusoidal voltage applied had an amplitude of  $10$  mV. This overall procedure was repeated at each of the temperatures in the range  $30 - 80$  °C, in steps of  $10$  °C.

### **6.3. Results and discussion**

Following electrochemical activation, it was observed that over a certain period of time, the electrode performance dropped significantly during the potentiodynamic scans. This effect was probably due to the instability and loss of the catalyst layer as coincidentally with this performance drop, a decrease in the electroactive area estimated using the cyclic voltammetry method was also observed. After this initial performance drop however, the electrode performance stabilised and it was from this point onwards that the data reported in this section took place. Although small differences between subsequent scans were found, as long as the variation in potential at the current density of  $-300$  mA cm<sup>-2</sup> did not exceed  $5$  mV, the electrodes were considered satisfactory for electrochemical characterisation. It is very likely that these small offsets in the potential arose from non-uniform oxide reduction or hydride creation on the surface that build a diffusion barrier for hydrogen ions, thus reducing performance and causing catalyst degradation [29, 32]. A comparison between the data provided by Force Technology [26] and that from the present experiments for the potentials required for the  $-300$  mA cm<sup>-2</sup> current density is

shown in *Table 6-1*. As can be seen, although there are some very good agreement in the values obtained, noticeable differences were found for the 30  $\mu\text{m}$  sample, where the experimental results were even better than the Force Technology data set. There was also a substantial lowering in all the potentials recorded for the 100  $\mu\text{m}$  and 300  $\mu\text{m}$  samples compared to the 30  $\mu\text{m}$  sample indicating that the electrochemical activity of these samples was far superior to the 30  $\mu\text{m}$  sample. It could simply be that for this sample, the action of the Al catalyst promoter was not as effective as for the thicker samples due to a more severe loss of aluminium than occurs in the thin sample during the chemical and electrochemical activation steps.

The efficiencies in *Table 6-1* were calculated using *Eq. 3-15*. For this purpose electrode potential was scanned from OCP to the value where HER occurred at the current density of 300  $\text{mA}/\text{cm}^2$ . Then the scanning direction was reversed and potential was gradually increased to the current density value of 300  $\text{mA}/\text{cm}^2$  for OER. The potentials which were achieved both for hydrogen and oxygen evolution reactions at 300  $\text{mA}/\text{cm}^2$  were subtracted from each other, which allowed estimation of the cell voltage (*Table 6-1*). During all the efficiency measurements 3 electrodes system configuration was applied with Hg/HgO reference electrode, IR compensation was included (which eliminated ohmic losses) and scan rate was set for the constant value of 0.05  $\text{mV}/\text{s}$ .

Hydrogen evolution potential (at 300 mA cm <sup>-2</sup> ) /V		
Raney nickel thickness	Force Technology data	Experimental data
30 μm	-1.045	-0.987
100 μm	-0.937	-0.934
300 μm	-0.931	-0.932
Oxygen evolution potential (at 300 mA cm <sup>-2</sup> ) /V		
	Force Technology data	Experimental data
30 μm	0.638	0.640
100 μm	0.610	0.608
300 μm	0.615	0.610
Cell Voltage (at 300 mA cm <sup>-2</sup> ) /V		
	Force Technology data	Experimental data
30 μm	1.683	1.624
100 μm	1.547	1.542
300 μm	1.546	1.542
Cell efficiency (based on Higher Heating Value)		
	Force Technology data	Experimental data
30 μm	88%	91%
100 μm	96%	96%
300 μm	96%	96%

Table 6-1. Force Technology APS electrodes performance [17] compared to current results

### 6.3.1. Cyclic voltammetry

The cyclic voltammograms of the three Raney nickel samples carried out in 30% KOH at 70 °C are shown in *Figure 6-3*. The temperature of 70 °C was selected for the measurements as it is the typical electrolyser operating temperature. The positive scan from -1.1 V for the 30 μm sample reveals a peak at -0.65 V which corresponds to the formation of a α-Ni(OH)<sub>2</sub> passive layer. The broad shoulder for 30 μm sample following the main peak could indicate a broad distribution of sites on the Raney

nickel surface which undergo passivation at different potentials. The current does eventually decrease to the baseline at  $-0.35$  V on the forward scan as the entire available surface becomes passivated. An alternative explanation advanced for this current decay has been attributed to the slow oxidation of incorporated hydrogen within the porous nickel matrix [33] but this is more likely to occur following prolonged cathodic polarisation which was not the case in these cyclic voltammetry measurements. On the reverse sweep, no discernible cathodic current was observed from this passivated surface up to the HER region at  $-1.05$  V. A cathodic current due to the reduction of the  $\alpha$ -Ni(OH)<sub>2</sub> passive layer was observed in this region although it is not visible due to the scaling of the plot. The CV's for the  $100\ \mu\text{m}$  Raney nickel sample and indeed, for the  $300\ \mu\text{m}$  sample were markedly different. Here, two small anodic peaks were found at  $-0.85$  V which can be attributed to the oxidation of adsorbed hydrogen. This was then followed by a large and broad anodic shoulder associated with passivation of the Raney nickel surface. The current did not quite fall back to zero at the end of the cathodic sweep, but on the reverse sweep, the current collapsed as expected for a passive film once the electric field is removed. For this sample, the cathodic current appeared at  $-0.7$  V and this could be attributed to the start of the  $\alpha$ -Ni(OH)<sub>2</sub> reduction and the HER.

In the *Figure 6-3* it can be also seen a cyclic voltammogram which corresponds to the smooth nickel sample. This sample before usage was pre-treated using polishing paper to make the surface as flat as possible with aim to be able to compare porous Raney nickel samples with flat nickel structure. In that case scanning began at the potential of  $-1.3$  V due to the fact that sample had much smaller real surface area, so also HER occurred at lower potentials. As it might be seen cathodic peak corresponding to the reduction of  $\alpha$ -Ni(OH)<sub>2</sub> passive layer demonstrated relatively lower current densities (left scale on the *Figure 6-3*), which confirmed its relatively low surface area. In that case scanning was reversed at the potential of  $-0.2$  V and scanned back to the value of  $-1.2$  V.

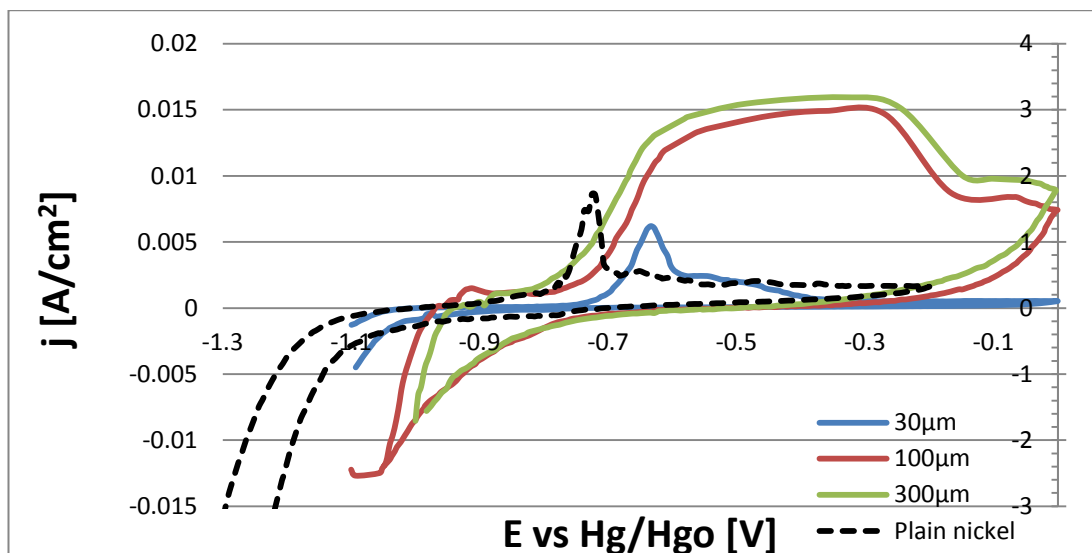


Figure 6-3. Cyclic voltammograms of Raney nickel samples at the temperature of  $70^{\circ}\text{C}$  (right vertical scale) and smooth nickel (left vertical scale). Scan rate =  $50\text{ mV/s}$ .

From the CV data, the electrochemical active area for each sample was evaluated, using as a reference the surface charge under the anodic peak for a smooth nickel electrode [16, 27, 28]. The areas obtained are given in *Table 6-2*. The highest electroactive area, of almost  $2700\text{ cm}^2$  was obtained for the  $300\text{ }\mu\text{m}$  sample closely followed by that of the  $100\text{ }\mu\text{m}$  sample at  $2400\text{ cm}^2$ . The lowest active area ( $480\text{ cm}^2$ ) was for  $30\text{ }\mu\text{m}$  catalyst layer. The data in *Table 6-2* show a large increase in the electroactive area as the catalyst layer thickness is increased from  $30\text{ }\mu\text{m}$  to  $100\text{ }\mu\text{m}$ . This suggests a substantial increase in the porosity of the sample following the chemical and electrochemical activation steps. A further 3-fold increase in the catalyst layer thickness from  $100\text{ }\mu\text{m}$  to  $300\text{ }\mu\text{m}$  however did not yield a corresponding proportional increase in the measured surface area. This could indicate that the period and/or methodology of activation was inadequate for the thickest catalyst sample used resulting in a large proportion of the catalyst layer remaining relatively unaffected by the treatment. The importance of having as high a surface area as possible has been highlighted by several authors [34-36] as the HER efficiency is directly proportional to this. It is worth mentioning that the obtained value for smooth nickel here was about 15 times bigger than theoretical value of

514  $\mu\text{C cm}^{-2}$ . This deviation comes from the fact that in practice even polished, smooth samples surface structures are not ideally flat and normally have a roughness factor value greater than 1 [26]. Additionally measurements were taken at an elevated temperature of 70 °C, markedly higher than standard conditions which the theoretical value refers to.

Sample	Charge /C cm <sup>-2</sup>	Electroactive area/cm <sup>2</sup>
<b>Plain nickel</b>	0.00765	1
<b>Raney nickel - 30 <math>\mu\text{m}</math></b>	3.67	480
<b>Raney nickel – 100 <math>\mu\text{m}</math></b>	18.6	2436
<b>Raney nickel – 300 <math>\mu\text{m}</math></b>	20.64	2696

*Table 6-2. Electroactive area estimation from CV measurements*

Indeed, the impact of temperature on the size of the anodic feature, and hence the effective surface area of the sample obtained from the cyclic voltammograms, is shown in *Figure 6-4* for the 100  $\mu\text{m}$  sample. A similar trend was also found for the 30  $\mu\text{m}$  and 300  $\mu\text{m}$  samples. The figure shows an increase in the current on the rising portion of the broad anodic feature at -0.78 V leading to a higher maximum current. All the curves however converge to a similar value at the end of the anodic scan since as expected by this point, all the electroactive area had become passivated. However, the fact that different apparent peak areas are obtained at the different temperatures is worthy of further discussion. There are several factors which could influence this increase. The first is the increased rate in the electrochemical kinetics with temperature and this is readily seen in the higher currents from the rising portion of the curve which is governed by the Tafel relationship. The kinetics of the chemical reaction leading to the formation of a passivation layer will also be influenced by the temperature through both chemical reaction rates and diffusion coefficients [37]. As is also well known, the solubility of gases present in the solution will decrease with increasing temperature and the gas bubbles might well then be more easily removed from the catalyst surface following their formation.



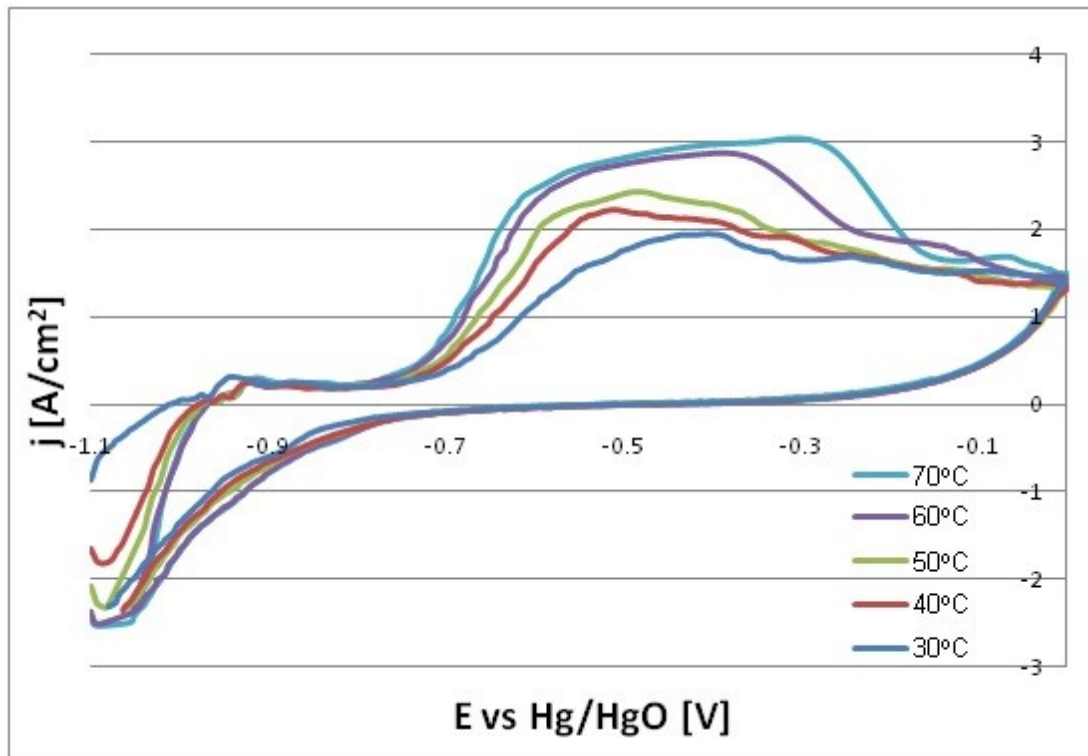


Figure 6-4. Cyclic voltammograms of the Raney nickel 100  $\mu\text{m}$  sample as a function of temperature. Scan rate = 50 mV/s.

### 6.3.2. Potentiodynamic analysis and Tafel extrapolation

Full Tafel analyses of the current–voltage curves from the three Raney nickel samples at different temperatures were carried out. At each of the temperatures examined, five scans were performed and the results of the data median (from five scans) were analysed and used to evaluate the exchange current density ( $j_0$ ), the equilibrium potential  $E_e$ , the cathodic Tafel slope ( $\beta_c$ ) and the potential for a current density of  $300 \text{ mA cm}^{-2}$ . These data are presented in *Table 6-3*.

		Raney nickel catalyst thickness		
		30 $\mu\text{m}$	100 $\mu\text{m}$	300 $\mu\text{m}$
<b>T = 30°C</b>	$E_e/V$	-0.951	-0.944	-0.949
	$E$ (at 300 mA $\text{cm}^{-2}$ )/V	-1.157	-1.028	-1.040
	$j_0$ [ $\text{A}/\text{cm}^2$ ]	0.00031	0.0123	0.0176
	$\beta_c$ [mV/dec]	63.94	67.5	85.0
<b>T = 40°C</b>	$E_e/V$	-0.963	-0.940	-0.948
	$E$ (at 300 mA $\text{cm}^{-2}$ )/V	-1.143	-1.017	-1.031
	$j_0$ [ $\text{A}/\text{cm}^2$ ]	0.00075	0.0131	0.0192
	$\beta_c$ [mV/dec]	65.9	62.4	80.0
<b>T = 50°C</b>	$E_e/V$	-0.947	-0.936	-0.947
	$E$ (at 300 mA $\text{cm}^{-2}$ )/V	-1.105	-1.008	-1.028
	$j_0$ [ $\text{A}/\text{cm}^2$ ]	0.0014	0.0131	0.0201
	$\beta_c$ [mV/dec]	69.0	58.5	79.4
<b>T = 60°C</b>	$E_e/V$	-0.947	-0.936	-0.945
	$E$ (at 300 mA $\text{cm}^{-2}$ )/V	-1.094	-1.0042	-1.028
	$j_0$ [ $\text{A}/\text{cm}^2$ ]	0.0033	0.0149	0.0205
	$\beta_c$ [mV/dec]	73.7	56.5	80.0
<b>T = 70°C</b>	$E_e/V$	-0.953	-0.935	-0.962
	$E$ (at 300 mA $\text{cm}^{-2}$ )/V	-1.077	-1.003	-1.016
	$j_0$ [ $\text{A}/\text{cm}^2$ ]	0.0058	0.0153	0.0232
	$\beta_c$ [mV/dec]	73.5	54.5	55.4
<b>T = 80°C</b>	$E_e/V$	-0.943	-0.931	-0.953
	$E$ (at 300 mA $\text{cm}^{-2}$ )/V	-1.066	-0.994	-1.009
	$j_0$ [ $\text{A}/\text{cm}^2$ ]	0.0079	0.0172	0.0256
	$\beta_c$ [mV/dec]	70.0	56.6	58.6

Table 6-3. Tafel analysis on the catalyst samples as a function of temperature

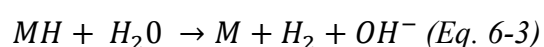
The relationship between these parameters is given by the Tafel's equation:

$$\log|j| = \log j_0 + \left| \frac{\eta}{\beta_c} \right| \quad (\text{Eq. 6-1})$$

where  $\eta$  is overpotential over  $E_e$ , and  $j$  is the current density. The exchange current density and the cathodic Tafel slope are the parameters that are related to the electrocatalytic activity of the material surface, where the higher values of  $j_0$  and lower value of  $\beta_c$  correspond to higher electrocatalytic activity. The equilibrium potential obtained from Tafel analysis indicates where the HER starts to occur [34-36]. The magnitudes of the exchange current density and Tafel slope reported in

*Table 6-3* were in good agreement with literature values pertaining to electrode performance towards the HER reaction [2, 4, 10].

From the Tafel slope values in *Table 6-3*, also reaction determining step was evaluated. The  $\beta_c$  parameters for all the Raney nickel samples considering different temperature values were equal to 54.5 – 85.0 mV/dec. According to the theoretical analysis performed by Pletcher *et al.* [34] for hydrogen evolution reaction, this would indicate the reaction mechanism could be described by the following equations (*Eq. 6-2, Eq. 6-3*) and the rate determining step could be described by the *Eq. 6-3*.



The potentiodynamic data of *Figure 6-5* for the Raney nickel 30  $\mu\text{m}$  sample show the clear impact of temperature on the HER at this surface. The figure reveals a significant increase in the kinetics of the reaction at temperatures above 40 °C. A change in temperature from 30 °C to 80 °C caused the required voltage for the HER at the current density of 300 mA cm<sup>-2</sup> current density to decrease by 91 mV. At the typical electrolyser operating temperature of 70 °C; the potential for the HER was thus only -1.077 V. There is no significant variation in the equilibrium potential for the HER with temperature (-950 mV  $\pm$  6 mV) but as noted above, a substantial shift in the potential required for the 300 mA cm<sup>-2</sup> current density was found. There also appears to be a tendency for the Tafel slope to increase with temperature but again here, the difference over the 30 °C–80 °C range is rather small (*c.a.* 10 mV/decade). Nevertheless, this might be sufficient to suggest a change in the rate determining step for the hydrogen evolution reaction between the lowest and highest temperature values and this could be linked with the decrease in H-atom surface coverage and solubility of H<sub>2</sub> with increasing temperature.

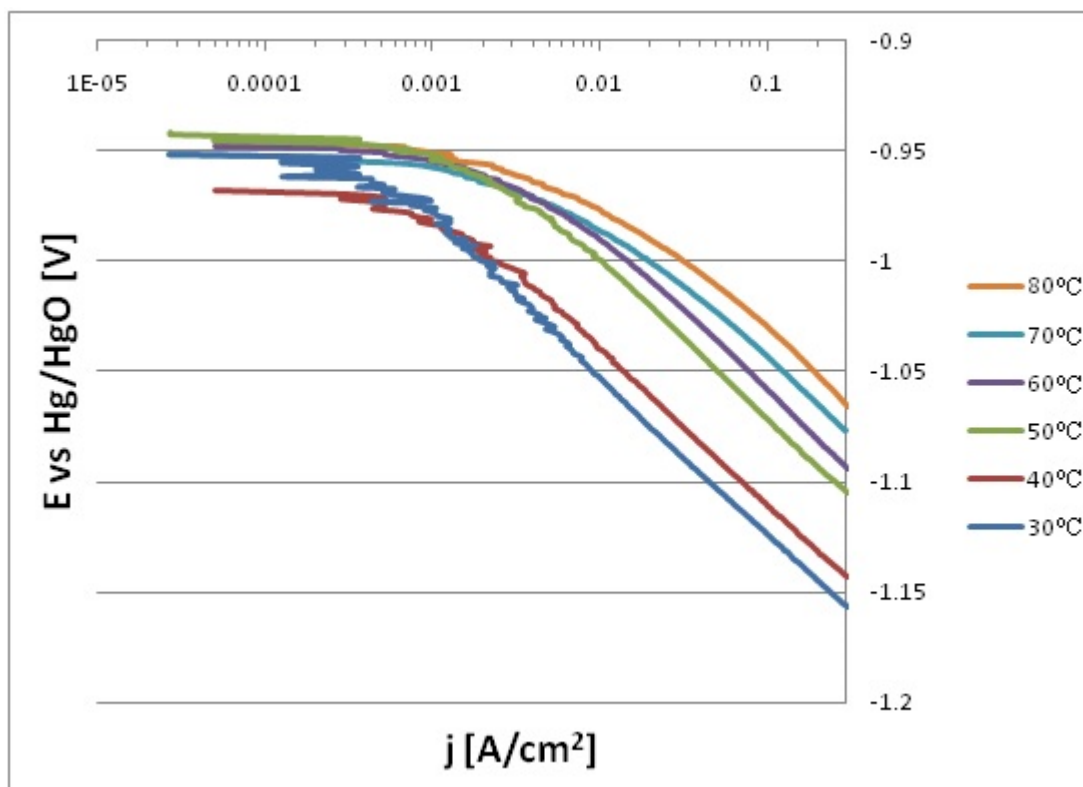


Figure 6-5. Potentiodynamic scans of Raney nickel 30  $\mu\text{m}$  sample as a function of temperature, Scan rate 0.05 mV/s

In contrast, the potentiodynamic data from the Raney nickel 100  $\mu\text{m}$  sample, shown in Figure 6-6, shows only a small variation in the potential for the stipulated 300  $\text{mA cm}^{-2}$  current density over the temperature range examined. The results from the analysis of this data are also presented in Table 6-3. Again, there appears to be a gradual fall in the reversible potential with increasing temperature, from  $-0.944\text{ V}$  at  $30\text{ }^\circ\text{C}$  to  $-0.931\text{ V}$  at  $80\text{ }^\circ\text{C}$ , which is consistent with the temperature dependence of the Nernst equation. As noted above, the change in the potential for  $300\text{ mA cm}^{-2}$  is rather modest, from  $-1.028\text{ V}$  at  $30\text{ }^\circ\text{C}$  to  $-0.994\text{ V}$  at  $80\text{ }^\circ\text{C}$ . Thus temperature has a lesser impact on the electrochemical activity of the 100  $\mu\text{m}$  electrode than on the 30  $\mu\text{m}$  one. The Tafel slope does not show any specific trend with temperature, exhibiting a value close to 60 mV/decade. The data for the 300  $\mu\text{m}$  sample in Table 6-3 shows a reversible potential of *c.a.*  $-0.95\text{ V}$  and a change in the potential with temperature at the current density of  $300\text{ mA cm}^{-2}$  very similar to that of the 100  $\mu\text{m}$  sample, *viz.*, only 31 mV in going from  $30\text{ }^\circ\text{C}$  to  $80\text{ }^\circ\text{C}$ . However, the Tafel slope

obtained for this sample was higher at *c.a.* 80 mV/decade but again did not exhibit much variation with temperature.

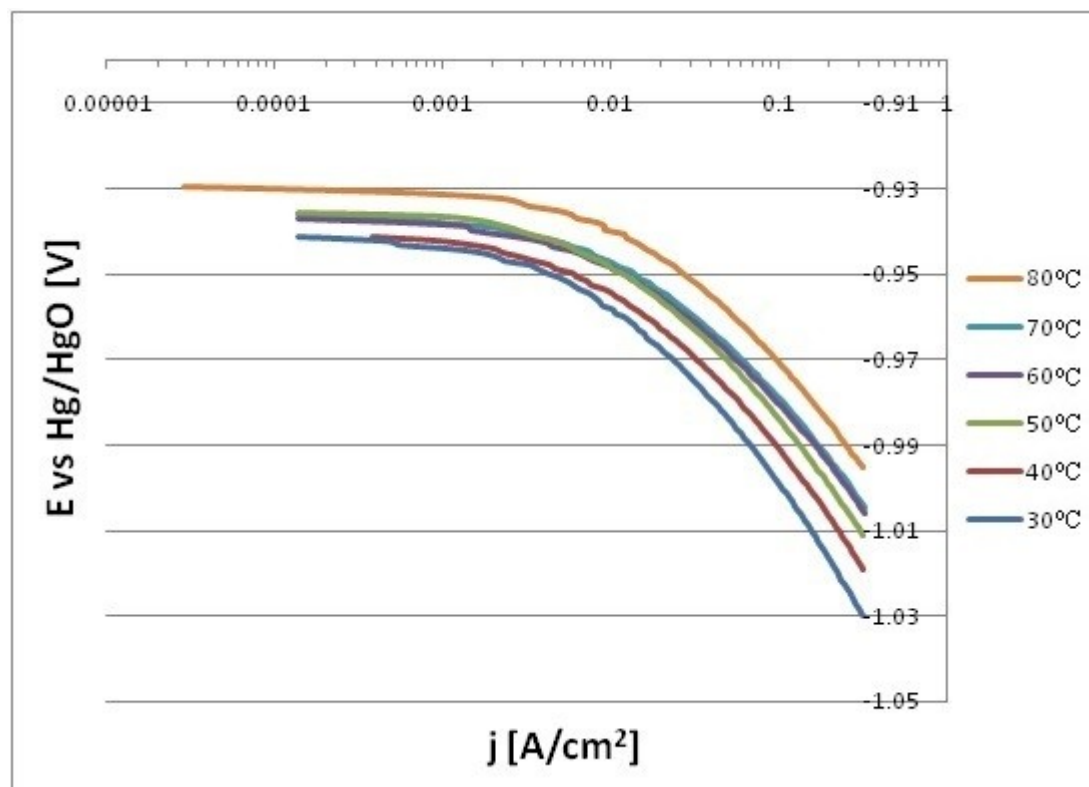


Figure 6-6. Potentiodynamic scans of Raney nickel 100  $\mu\text{m}$  sample as a function of temperature, Scan rate 0.05 mV/s

### 6.3.3. Electrochemical impedance spectroscopy

The EIS measurements were performed at each temperature just after the potentiodynamic scans at potentials more negative than the reversible potential for HER at the electrodes. The impedance data was analysed using the Randles equivalent circuit model shown in Figure 6-7 as this has been widely employed to model EIS data obtained from Raney nickel electrodes [16, 38, 39].

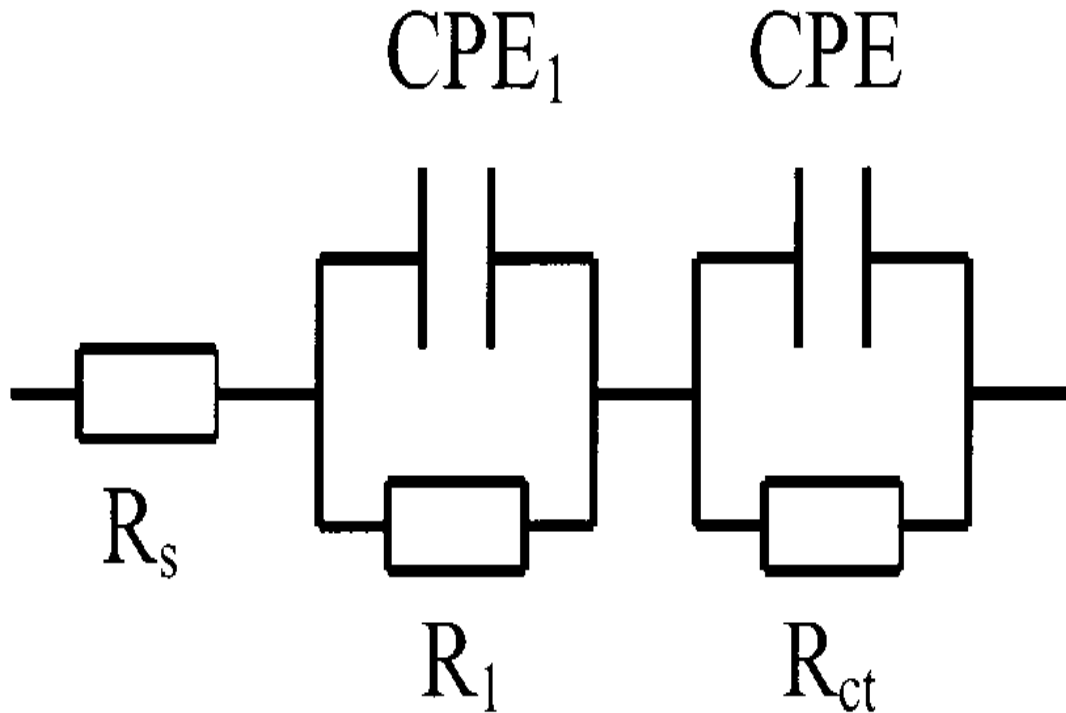


Figure 6-7. Randles equivalent circuit model for Raney nickel [29]

The literature indicates that typical EIS data from Raney nickel electrodes consists of two semicircles in the Nyquist plot format, with the higher frequency one (constant phase element  $CPE_1$  and resistance  $R_1$ ) associated with the electrode's porous structure whereas the lower frequency one depends on the double layer capacitance and charge transfer resistance [16].  $R_s$  parameter is the electrolyte resistance. In this analysis therefore, the focus has been exclusively on the lower frequency feature in order to obtain the charge transfer resistance,  $R_{ct}$  and the double layer capacitance,  $C_{dl}$  from the magnitude (CPE-T) and phase (CPE-P) of the constant phase elements (CPE), according to Eq. 6-4, which originally was developed by Brug *et al.* [40].

$$C_{dl} = \frac{((CPE-T * R_{ct})^{\frac{1}{CPE-P}})}{R_{ct}} \text{ (Eq. 6-4)}$$

The 3-electrode configuration used in these measurements also means that the EIS data obtained were derived exclusively from the Raney nickel samples (the working electrode) examined and not the impedance response from the whole cell. Thus, the

$R_s$  term corresponds to the uncompensated solution resistance between the working and reference electrodes.  $R_{ct}$  is the parameter directly connected to HER electrode kinetics, with a smaller value of  $R_{ct}$  giving a larger  $j_0$  and so, faster electron transfer rate. The double layer capacitance obtained from these measurements is directly proportional to the electrochemical surface area as it indicates the parts of the porous Raney nickel structure accessible to the electrolyte solution. Its value therefore can be influenced by gas bubbles that appear on the electrode surface and block this access. For fitting the data Zview software was used.

The EIS data for the 30  $\mu\text{m}$  sample at different potentials and at temperatures of 30°C, 50°C and 70°C are presented in *Figure 6-8 (A)–(C)* respectively. The fitted values obtained for the EIS data for the 30  $\mu\text{m}$  Raney nickel sample are presented in *Table 6-4*. The  $R_{ct}$  values consistently decreased with increasing temperature and polarisation potential. This is to be expected as the rate of the electrochemical reaction would be increasing under both situations. The trend in the  $C_{dl}$  values though is more difficult to interpret. Its magnitude at the lowest overpotential remained effectively constant below a temperature of 50 °C but then increased to nearly double that value at 80 °C. Furthermore, at all temperatures,  $C_{dl}$  decreased with increasing overpotential. This fall in the double layer capacitance of the Raney nickel electrode at high current densities has also been observed by Rausch and Wendt [41] and it was attributed to the hydrogen bubbles produced by the reaction blocking access of the electrolyte to the electrode surface. In this situation, the available electrochemical surface area would decrease. The impact of temperature could simply be due to any hydrogen bubbles formed at the lower current densities simply being removed from the electrode surface as the solubility of the gas decreases with increasing temperature.

		Applied potential				
		-0.95 V	-1.00 V	-1.05 V	-1.10 V	-1.15 V
<b>T = 30 °C</b>	$R_{ct} / \Omega \text{ cm}^2$	31.355	9.075	1.922	0.700	0.320
	$C_{dl} / \text{F cm}^{-2}$	0.058	0.040	0.023	0.016	0.009
<b>T = 40 °C</b>	$R_{ct} / \Omega \text{ cm}^2$	19.186	4.410	1.282	0.557	0.333
	$C_{dl} / \text{F cm}^{-2}$	0.057	0.039	0.023	0.015	0.011
<b>T = 50 °C</b>	$R_{ct} / \Omega \text{ cm}^2$	7.293	1.374	0.676	0.373	0.291
	$C_{dl} / \text{F cm}^{-2}$	0.044	0.027	0.018	0.012	0.010
<b>T = 60 °C</b>	$R_{ct} / \Omega \text{ cm}^2$	4.488	0.895	0.513	0.342	0.252
	$C_{dl} / \text{F cm}^{-2}$	0.045	0.025	0.018	0.013	0.009
<b>T = 70 °C</b>	$R_{ct} / \Omega \text{ cm}^2$	5.935	0.971	0.467	0.321	0.244
	$C_{dl} / \text{F cm}^{-2}$	0.068	0.040	0.025	0.017	0.013
<b>T = 80 °C</b>	$R_{ct} / \Omega \text{ cm}^2$	3.560	0.724	0.357	0.224	0.184
	$C_{dl} / \text{F cm}^{-2}$	0.091	0.053	0.033	0.023	0.015

*Table 6-4. Fitted parameters obtained for EIS data for the 30  $\mu\text{m}$  sample as a function of temperature and applied potential*



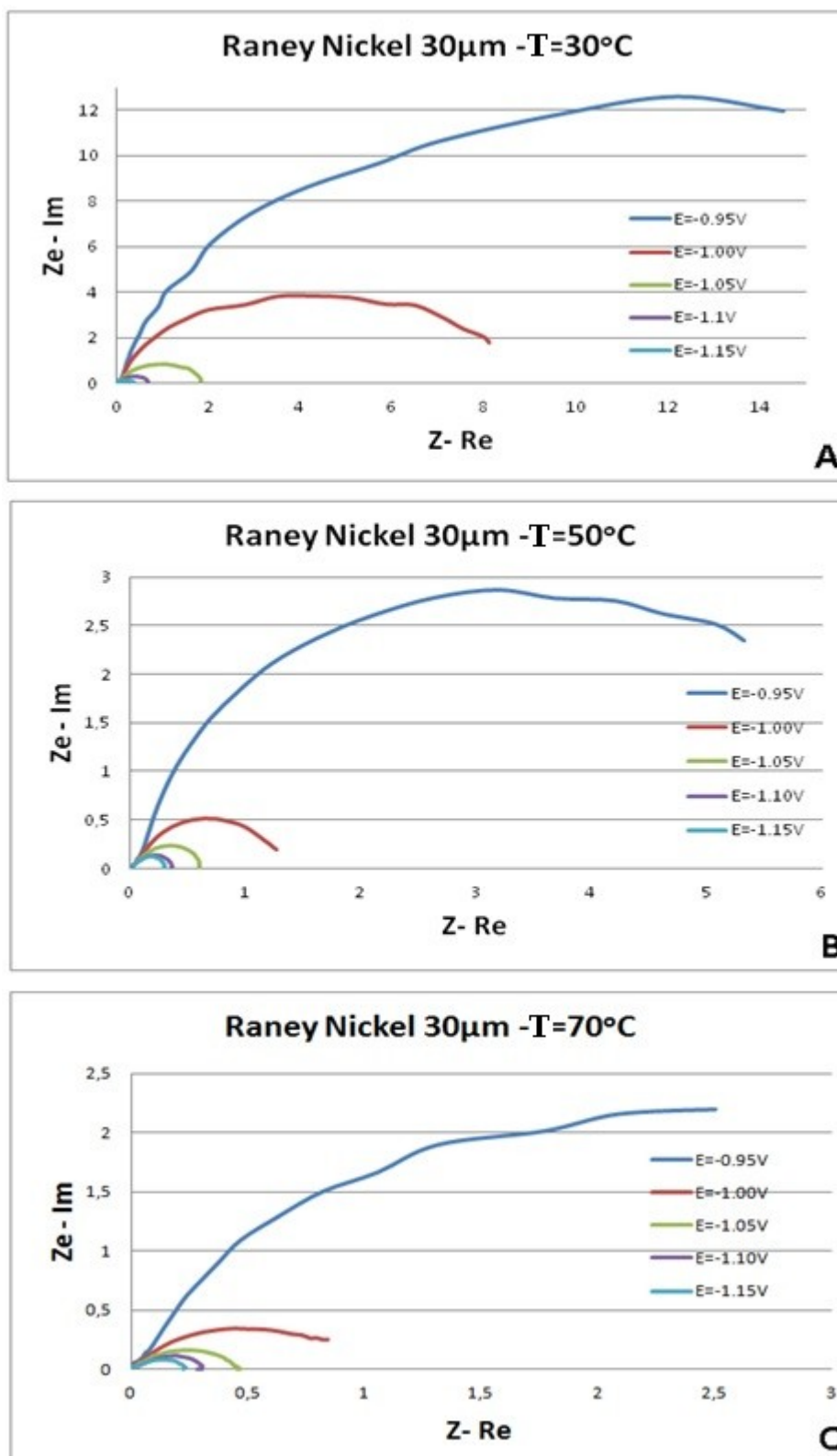


Figure 6-8. EIS data at different temperatures (A) 30°C; (B) 50°C; (C) 70°C for Raney nickel 30 µm sample as a function of potential

The EIS spectra for the Raney nickel 100  $\mu\text{m}$  sample as a function of potential at temperatures of 30  $^{\circ}\text{C}$ , 50  $^{\circ}\text{C}$  and 70  $^{\circ}\text{C}$  are shown in *Figure 6-9 (A)–(C)* respectively. The data for this sample in *Table 6-5* showed a similar trend as to the 30  $\mu\text{m}$  sample with respect to temperature and applied potential except that here, the magnitude of the effective double layer capacitance values (and so, available electrochemical surface area) was much larger, by a factor of  $\sim 20$ . The measured charge transfer resistance was also lower for the 100  $\mu\text{m}$  sample. Indeed, its value was the lowest of all the samples tested indicating that this sample type has highest electrocatalytic activity for HER. It is also seen that on comparison to the 30  $\mu\text{m}$ , the data are noisier (especially at the higher negative potentials) probably due to the influence of gas bubbles that are released from the surface in a non-uniform manner [42-44]. The data of *Table 6-5* shows that  $R_{\text{ct}}$  decreased with increasing temperature and polarisation potential and the capacitance values are much higher for the 100  $\mu\text{m}$  compared to the 30  $\mu\text{m}$  one indicating a higher porosity in the 100  $\mu\text{m}$  sample. As already seen for the 30  $\mu\text{m}$  sample the double layer capacitance of the 100  $\mu\text{m}$  electrode also decreased with the overpotential, but increased with temperature.

		Applied potential				
		-0.95 V	-1.00 V	-1.05 V	-1.10 V	-1.15 V
T = 30 $^{\circ}\text{C}$	$R_{\text{ct}} / \Omega \text{ cm}^2$	0.961	0.208	0.144	0.125	0.127
	$C_{\text{dl}} / \text{F cm}^{-2}$	1.258	0.557	0.279	0.261	0.185
T = 40 $^{\circ}\text{C}$	$R_{\text{ct}} / \Omega \text{ cm}^2$	0.568	0.181	0.110	0.089	0.093
	$C_{\text{dl}} / \text{F cm}^{-2}$	1.111	0.483	0.298	0.199	0.144
T = 50 $^{\circ}\text{C}$	$R_{\text{ct}} / \Omega \text{ cm}^2$	0.321	0.117	0.077	0.084	0.070
	$C_{\text{dl}} / \text{F cm}^{-2}$	1.007	0.467	0.306	0.141	0.128
T = 60 $^{\circ}\text{C}$	$R_{\text{ct}} / \Omega \text{ cm}^2$	0.242	0.111	0.064	0.065	0.056
	$C_{\text{dl}} / \text{F cm}^{-2}$	0.992	0.585	0.447	0.275	0.187
T = 70 $^{\circ}\text{C}$	$R_{\text{ct}} / \Omega \text{ cm}^2$	0.182	0.075	0.061	0.049	0.052
	$C_{\text{dl}} / \text{F cm}^{-2}$	0.910	0.365	0.311	0.314	0.145
T = 80 $^{\circ}\text{C}$	$R_{\text{ct}} / \Omega \text{ cm}^2$	0.156	0.064	0.050	0.054	0.033
	$C_{\text{dl}} / \text{F cm}^{-2}$	1.090	0.434	0.282	0.260	0.240

*Table 6-5. Fitted parameters obtained for EIS data for the 100  $\mu\text{m}$  sample as a function of temperature and applied potential*

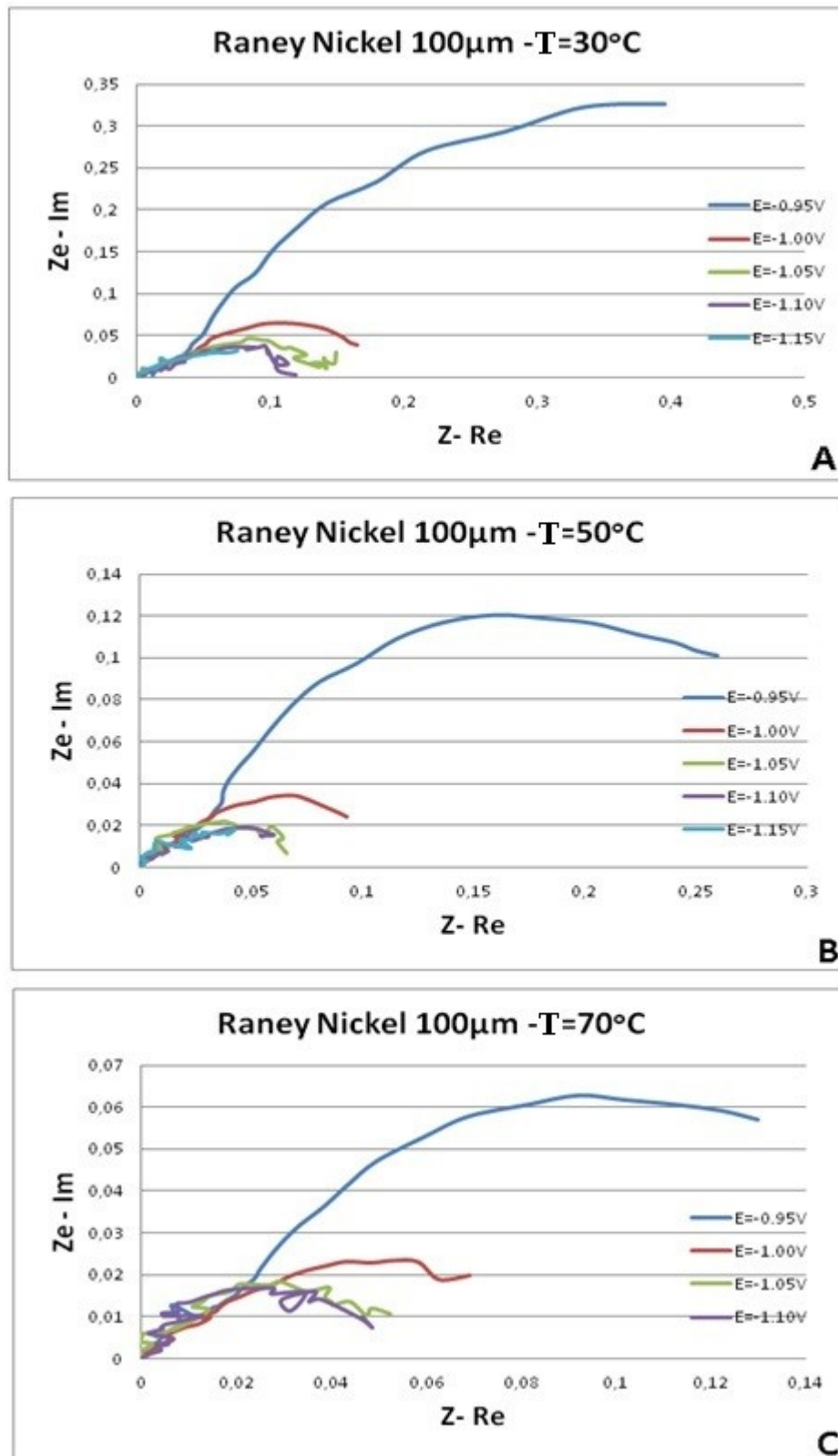


Figure 6-9. EIS data at different temperatures (A) 30°C; (B) 50°C; (C) 70°C for Raney nickel 100 µm sample as a function of potential

The fitted EIS data for the Raney nickel 300  $\mu\text{m}$  sample is presented in *Table 6-6*. This sample generally showed intermediate values of  $R_{ct}$  compared to the other samples, confirming the results obtained from the analysis of the potentiodynamic scans. Apart from the highest temperature studied, the double layer capacitance increased with temperature from 40  $^{\circ}\text{C}$  to 70  $^{\circ}\text{C}$  when measured at the equilibrium potential of  $-0.95\text{ V}$ . A dramatic fall in this value, from  $3.0\text{ F cm}^{-2}$  at 70  $^{\circ}\text{C}$  to  $0.9\text{ F cm}^{-2}$  at 80  $^{\circ}\text{C}$  then occurred indicating again, the influence of gas bubbles formed at this temperature and unable to escape from this highly porous structure. A similar trend was found for this sample, as with the other samples, in the variation in  $C_{dl}$  with increasing overpotential.

		Applied potential				
		$-0.95\text{ V}$	$-1.00\text{ V}$	$-1.05\text{ V}$	$-1.10\text{ V}$	$-1.15\text{ V}$
<b>T = 30 <math>^{\circ}\text{C}</math></b>	$R_{ct}/\Omega\text{ cm}^2$	1.224	0.332	0.197	0.151	0.118
	$C_{dl}/\text{F cm}^{-2}$	2.585	1.688	1.047	0.802	0.521
<b>T = 40 <math>^{\circ}\text{C}</math></b>	$R_{ct}/\Omega\text{ cm}^2$	0.836	0.181	0.123	0.106	0.104
	$C_{dl}/\text{F cm}^{-2}$	2.796	1.457	0.898	0.646	0.642
<b>T = 50 <math>^{\circ}\text{C}</math></b>	$R_{ct}/\Omega\text{ cm}^2$	0.644	0.174	0.109	0.100	0.100
	$C_{dl}/\text{F cm}^{-2}$	3.071	1.648	1.096	1.025	0.523
<b>T = 60 <math>^{\circ}\text{C}</math></b>	$R_{ct}/\Omega\text{ cm}^2$	0.631	0.214	0.131	0.124	0.099
	$C_{dl}/\text{F cm}^{-2}$	3.677	2.302	1.566	1.170	0.790
<b>T = 70 <math>^{\circ}\text{C}</math></b>	$R_{ct}/\Omega\text{ cm}^2$	0.225	0.072	0.047	0.035	0.029
	$C_{dl}/\text{F cm}^{-2}$	2.584	0.882	0.287	0.259	0.200
<b>T = 80 <math>^{\circ}\text{C}</math></b>	$R_{ct}/\Omega\text{ cm}^2$	0.065	0.042	0.023	0.022	0.016
	$C_{dl}/\text{F cm}^{-2}$	0.199	0.237	0.281	0.143	0.221

*Table 6-6. Fitted parameters obtained for EIS data for the 300  $\mu\text{m}$  sample as a function of temperature and applied potential*

It is clear therefore that any comparison between the  $C_{dl}$  values between the samples should be done at relatively low overpotentials and at moderate temperatures, where only small amounts of  $\text{H}_2$  bubbles are being produced. Thus, at  $-0.95\text{ V vs Hg/HgO}$ , it is seen that the 30  $\mu\text{m}$  sample has the lowest electroactive area, followed by the 100  $\mu\text{m}$  sample with the highest area being found for the 300  $\mu\text{m}$  sample. The 30  $\mu\text{m}$  sample also exhibited the lowest electrocatalytic activity towards HER and the 300  $\mu\text{m}$  sample the highest. Considering the higher catalyst amount used in its

production, the enhanced performance is not surprising when compared to the 30  $\mu\text{m}$  sample. However, although from the EIS data, the 100  $\mu\text{m}$  sample displayed lower  $R_{\text{ct}}$  values compared to the 300  $\mu\text{m}$  sample, the cyclic voltammetry and Tafel extrapolation analyses revealed better kinetics and surface area data for the 300  $\mu\text{m}$  sample. The probable reason for this discrepancy is that in case of cyclic voltammetry, the surface structure is investigated in a potential region where HER does not occur and so no hydrogen gas bubbles are produced. Likewise, in case of the Tafel extrapolation experiments, this technique is again based on assumptions that at least in the early part of the current–voltage curve, insignificant  $\text{H}_2$  bubbles are involved. From a mere cost analysis perspective therefore, the 100  $\mu\text{m}$  electrode, using the current activation procedure, is by far the superior electrode for use in an alkaline electrolyser for the HER.

An additional interesting observation which was made during EIS experiments is that the apparent electrolyte resistance increased with an increase in the current density. This observation though does not however carry any physical significance here since the separation between the reference and working electrodes was not measured during the experiments. What can be said though is that the observed trend confirms the theoretical deliberations found in the literature [45-47] regarding the negative influence of bubbles on electrolyte resistance. Higher currents cause more external bubbles to be produced and that increases electrolyte resistance. Furthermore, electrolyte resistance decreases with temperature rise. These observations are presented in *Figure 6-10*. To estimate more precisely the influence of bubbles and temperature on electrolyte resistance, experiments should be carried out using the single cell with a constant distance between electrodes, particularly between reference and working.

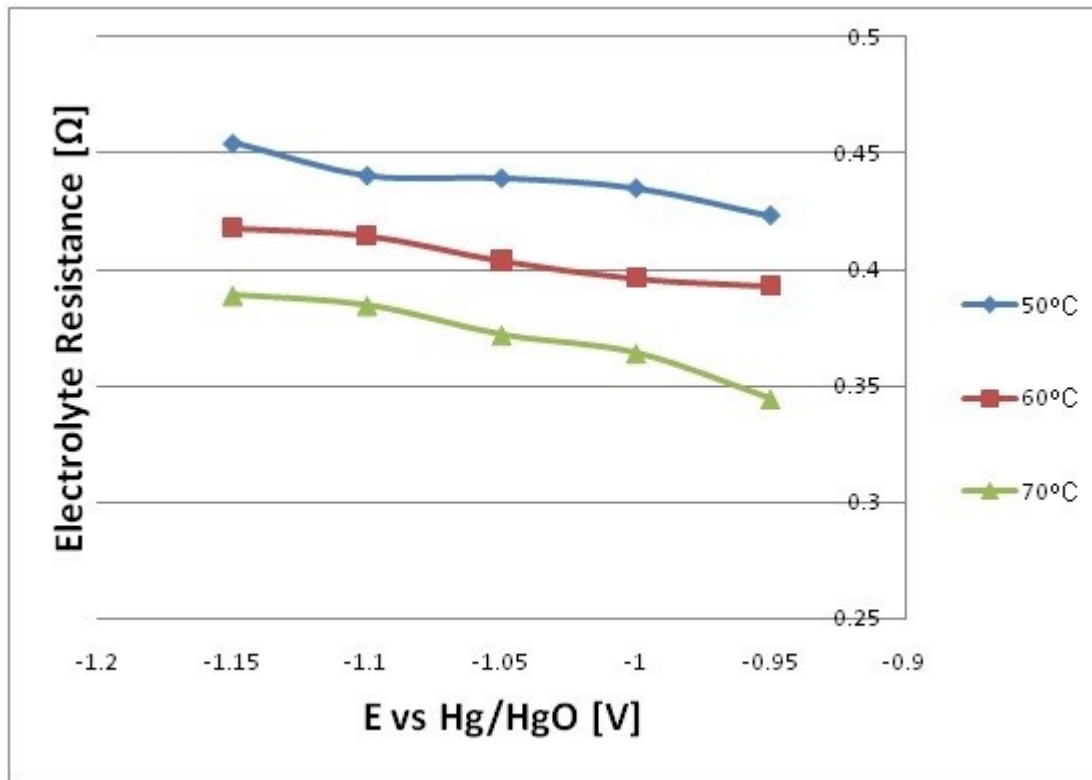


Figure 6-10. Electrolyte resistance as a function of potential and temperature for 100  $\mu\text{m}$  sample

#### 6.4. Conclusions

To our knowledge, this is the first time that the APS technique has been applied to the production of Raney nickel electrodes suitable for water electrolysis. The excellent performance of the APS electrodes towards HER has been confirmed from Tafel analysis and EIS double layer capacitance measurements. Cell efficiency values, based on the Higher Heating Value of hydrogen, in the region of 96% have been obtained for APS Raney nickel layers of 100  $\mu\text{m}$  and 300  $\mu\text{m}$  thicknesses. This has been attributed to the very high electroactive area as well as enhanced kinetics obtained for these samples following the chemical and electrochemical activation procedures.

## References:

1. Z. Zheng, N. Li, C. Wang, D. Li, Y. Zhu, G. Wu. *Ni-CeO<sub>2</sub> composite cathodematerial for hydrogen evolution reaction in alkaline electrolyte*. International Journal of Hydrogen Energy, Vol. 37, 2012, pp. 13921–13932
2. K. Zeng, D. Zhang. *Recent progress in alkaline water electrolysis for hydrogen production and applications*. Progress in Energy and Combustion Science, Vol. 36, 2010, pp. 307–326
3. H. F. Abbas, W.M.A. Wan Daud. *Hydrogen production by methane decomposition: a review*. International Journal of Hydrogen Energy, Vol. 35, 2010, pp. 1160–1190
4. M. S. Yazici. *UNIDO-ICHET support to hydrogen and fuel cell technologies in Turkey*. International Journal of Hydrogen Energy, Vol. 36, 2011, pp. 11239–11245
5. D. Hotza, J.C. Diniz da Costa. *Fuel cells development and hydrogen production from renewable resources in Brazil*. International Journal of Hydrogen Energy, Vol. 33, 2008, pp. 4915–4935
6. M. A. Rosen. *Advances in hydrogen production by thermochemical water decomposition: a review*. Energy, Vol. 35, 2010, pp. 1068–1076
7. <http://www.scotland.gov.uk/Topics/Built-Environment/planning/National-Planning-Policy/themes/renewables>, accessed 14<sup>th</sup> September 2014
8. <http://www.nel-hydrogen.com/home/?pid=159>, accessed 14<sup>th</sup> September 2014

9. D. Pletcher, X. Li, S. Wang. *A comparison of cathodes for zero gap alkaline water electrolyzers for hydrogen production*. International Journal of Hydrogen Energy, Vol. 37, 2012, pp. 7429–7435
10. M. P. Marceta Kaninski, S. M. Miulovic, G. S. Tasic, A. D. Maksic, V. M. Nikolic. *A study on the Co-W activated Ni electrodes for the hydrogen production from alkaline water electrolysis - Energy saving*. International Journal of Hydrogen Energy, Vol. 36, 2011, pp. 5227–5235
11. N. V. Krstajic, V. D. Jovic, L. Gajic-Krstajic, B. M. Jovic, A. L. Antozzi, G.N. Martelli. *Electrodeposition of Ni–Mo alloy coatings and their characterization as cathodes for hydrogen evolution in sodium hydroxide solution*. International Journal of Hydrogen Energy, Vol. 33, 2008, pp. 3676–3687
12. D. Pletcher, X. Li. *Prospects for alkaline zero gap water electrolyzers for hydrogen production*. International Journal of Hydrogen Energy, Vol. 36, 2011, pp. 15089–15104
13. R. Solmaz. *Electrochemical preparation and characterization of C/Ni-NiIr composite electrodes as novel cathode materials for alkaline water electrolysis*. International Journal of Hydrogen Energy, Vol. 38, 2013, pp. 2251–2256
14. G. S. Tasic, S. P. Maslovara, D. L. Zugic, A. D. Maksic, M. P. Marceta Kaninski. *Characterization of the Ni-Mo catalyst formed in situ during hydrogen generation from alkaline water electrolysis*. International Journal of Hydrogen Energy, Vol. 36, 2011, pp. 11588–11595
15. W. M. Martinez, A. M. Fernandez , U. Cano, A. Sandoval. *Synthesis of nickel-based skeletal catalyst for an alkaline electrolyzer*. International Journal of Hydrogen Energy, Vol. 35, 2010, pp. 8457–8462



16. V. Ganesh, V. Lakshminarayanan. *Preparation of high surface area nickel electrodeposit using a liquid crystal template technique*. *Electrochimica Acta*, Vol. 49, 2004, pp. 3561–3572
17. L. Chen, A. Lasia. *Study of the Kinetics of Hydrogen Evolution Reaction on Nickel - Zinc Alloy Electrodes*. *Journal of Electrochemical Society*, Vol. 138, 1991, pp. 3321-3328
18. L. Birry, A. Lasia. *Studies of the hydrogen evolution reaction on Raney nickel– molybdenum electrodes*. *Journal of Applied Electrochemistry*, Vol. 34, 2004, pp. 735–749
19. G. Schiller, V. Borck. *Vacuum plasma sprayed electrodes for advanced alkaline water electrolysis*. *International Journal of Hydrogen Energy*, Vol. 17, 1992, pp. 261–273
20. G. Schiller, R. Henne, P. Mohr, V. Peinecke. *High performance electrodes for an advanced intermittently operated 10-kW alkaline water electrolyzer*. *International Journal of Hydrogen Energy*, Vol. 23, 1998, pp. 761–765
21. G. K. Lohrberg, P. Kohl. *Preparation and use of Raney-Ni activated cathodes for large scale hydrogen production*. *Electrochimica Acta*, Vol. 29, 1984, pp. 1557-1561
22. H. Wendt, H. Hofmann, V. Plzak. *Materials research and development of electrocatalysts for alkaline water electrolysis*. *Materials Chemistry and Physics*, Vol. 22, 1989, pp. 27-49
23. P. Los, A. Rami, A. Lasia. *Hydrogen evolution reaction on Ni-Al electrodes*. *Journal of Applied Electrochemistry*, Vol. 23, 1993, pp. 135-140

24. A. Rami, A. Lasia. *Kinetics of hydrogen evolution on Ni-Al alloy electrodes*. Journal of Applied Electrochemistry, Vol. 22, 1992, pp. 376-382
25. J. Fournier, D. Miousse, J. G. Legoux, Wire-arc sprayed nickel based coating for hydrogen evolution reaction in alkaline solutions. International Journal of Hydrogen Energy, Vol. 24, 1999, pp. 519-528
26. P. T. Nielsen, T. Mathiesen, J. K. Kristensen, L. Hilbert, L. Yde. *Atmospheric plasma spraying of electrodes for conversion of electricity to hydrogen by high temperature alkaline electrolysis of water*. Proceedings of ITSC 2011, Sept. 27-29, Hamburg, Germany
27. I. J. Brown, S. Sotiropoulos. *Electrodeposition of Ni from a high internal phase emulsion (HIPE) template*. Electrochimica Acta, Vol. 46, 2001, pp. 2711–2720
28. I. J. Brown, S. Sotiropoulos. *Preparation and characterization of microporous Ni coatings as hydrogen evolving cathodes*. Journal of Applied Electrochemistry, Vol. 30, 2000, pp. 107-111
29. B. Baranowski. *Electrochemical formation of nickel hydride in alkaline solutions*. Journal of Electroanalytical Chemistry, Vol. 472, 1999, pp. 182–184
30. D. M. Soares, O. Teschke, I. Torriani. *Hydride effect on the kinetics of the hydrogen evolution reaction on nickel cathodes in alkaline media*. Journal of Electrochemical Society, Vol. 139, 1992, pp. 98-105
31. H. E. G. Rommal, P. J. Morgan. *The role of absorbed hydrogen on the voltage-time behaviour of nickel cathodes in hydrogen evolution*. Journal of Electrochemical Society: Electrochemical Science and Technology, 1988, pp. 343-346

32. A. E. Mauer, D. W. Kirk, S. J. Thorpe. *The role of iron in the prevention of nickel electrode deactivation in alkaline electrolysis*. *Electrochimica Acta*, Vol. 52, 2007, pp. 3505–3509
33. D. S. Hall, C. Bock, B. R. MacDougall. *The electrochemistry of metallic nickel: oxides hydroxides, hydrides and alkaline hydrogen evolution*. *Journal of The Electrochemical Society*, Vol. 160, 2013, pp. 235-243
34. D. Pletcher, F.C. Walsh. *Industrial electrochemistry*. 1990 second edition by Blackie Academic & Professional. ISBN: 9780412304101
35. D. Pletcher. *A first course in electrode processes*. 1991 by The Electrochemical Consultancy. ISBN: 0951730703
36. R. Greef, R. Peat, L.M. Peter, D. Pletcher, J. Robinson. *Instrumental methods in electrochemistry*. 1990 by Ellis Horwood Limited. ISBN: 0853128995
37. R. De Levie. *Electrochemical response of porous and rough electrodes*. In *Advances in Electrochemistry and Electrochemical Engineering*; Delahay, P., Tobias, C. T., Eds.; Interscience: New York, 1967; pp. 329-397.
38. C. Hitz, A. Lasia. *Experimental study and modelling of impedance of the HER on porous Ni electrodes*. *Journal of Electroanalytical Chemistry*, Vol. 500, 2001, pp. 213–222
39. M.P. Marceta Kaninski, V.M. Nikolic, G. S. Tasic, Z. Lj. Rakocevic. *Electrocatalytic activation of Ni electrode for hydrogen production by electrodeposition of Co and V species*. *International Journal of Hydrogen Energy*, Vol. 34, 2009, pp. 703-709

40. G. J. Brug, A. L. G. van den Eeden, M. Sluyters-Rehbach, J.H. Sluyters, *Journal of Electroanalytical Chemistry*, Vol. 176, 1984, p. 275
41. S. Rausch, H. Wendt. *Morphology and utilization of smooth hydrogen-evolving raney nickel cathode coatings and porous sintered-nickel cathodes*. *Journal of the Electrochemical Society*, Vol. 143, 1996, pp. 2852-2862.
42. C. Gabrielli, F. Huet, M. Keddam, A. Sahar. *Investigation of water electrolysis by spectral analysis. I. Influence of the current density*. *Journal of Applied Electrochemistry*, Vol. 19, 1989, pp. 683-696
43. C. Gabrielli, F.Huet. *Fluctuation analysis in electrochemical engineering process with two phase flows*. *Journal of Applied Electrochemistry*, Vol. 24, 1994, pp. 593-601
44. N. Richards, H. Gudbrandsen, S. Rolseth and J. Thonstad. *Characterization of the fluctuation in anode current density and "bubble events" in industrial reduction cells*. *Light Metals 2003*, TMS (The Minerals, Metals & Materials Society), 2003
45. N. Nagai, M. Takeuchi, T. Kimura, T. Oka. *Existence of optimum space between electrodes on hydrogen production by water electrolysis*. *International Journal of Hydrogen Energy*, Vol. 28, 2003, pp. 35 – 41
46. N. Nagai, M. Takeuchi, M. Nakao. *Influences of Bubbles between Electrodes onto Efficiency of Alkaline Water Electrolysis*. *Proceedings of PSFVIP-4 June 3-5, 2003, Chamonix, France*.
47. P. Boissonneau, P. Byrne. *An experimental investigation of bubble-induced free convection in a small electrochemical cell*. *Journal of Applied Electrochemistry*, Vol. 30, 2000, pp. 767-775

## **7. Operational tests under variable load conditions of atmospheric plasma spraying Raney nickel electrodes**

### **7.1. Introduction**

Long term, variable load operation is actually one of the major challenges that need to be faced by electrolyzers. Achieving the highest performance over as long period of time as possible was always a key criterion, but today's electrolyzers are additionally aimed to operate with renewable energy sources. This particular application necessitates the need for electrolyser durability under highly variable load environments.

Current literature does not appear to provide sufficient information on degradation issues of commercial alkaline electrolyzers. Indeed, the review performed during this research found only one, publicly available research work dealing directly with this issue. The doctoral dissertation and associated paper of A. Bergen [1, 2] investigated the effects of variable operation on the low-pressure Stuart SRA 6 kW device. During the performed experiments, it was observed that intermittent load had a negative impact on this electrolyser efficiency. This can be seen in *Figure 7-1* which shows how the electrolyser performance dropped during operation when a full shut-down was initiated in each cycle as compared to uninterrupted operation or operation with a minimum holding current of 10 A. Additionally, it can be seen that after turning off the device, there was a marked drop in the voltage over time before it stabilised at a much lower value. The paper concluded that the introduction of control techniques, such as that of a minimum holding current as well as a rest period could minimise the deterioration in the electrolyser performance however, it did not give clear answer what was the cause of performance degradation.

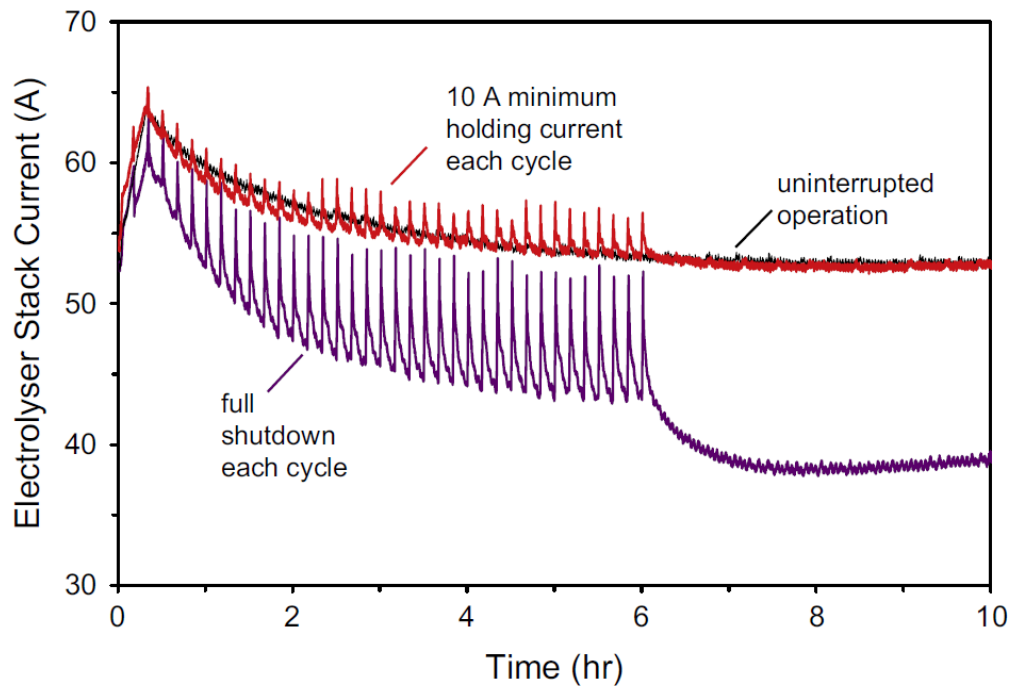
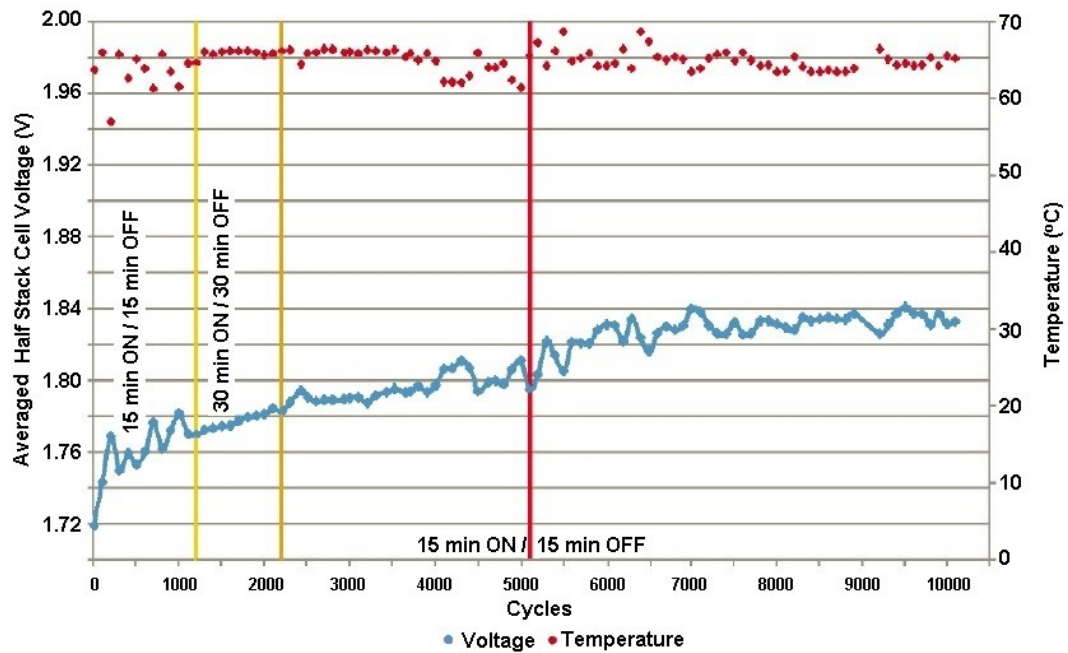


Figure 7-1. Electrolyser response to rapid cycling [1]

The findings of Bergen et al. [1, 2] were partially confirmed by data from Hydrogenics (*Figure 7-2*) [3] where it was shown that although the electrolyser still suffered from degradation effects on intermittent load operation, the impact on performance was reduced. The Hydrogenics electrolyser was operated in constant current mode. In *Figure 7-2*, it can be seen that the cell voltage of the electrolyser increased with the number of on/off cycles performed. The data shows that over 10,000 cycles (over 200 days of operation), performance dropped only by around 7% in comparison with the Stuart SRA where this declined more drastically over a period of 8 hours. It is generally well known that alkaline electrolysers were not able to operate efficiently with variable load until recent years when the new generation of devices were designed to overcome that issue. Hydrogenics might be considered as a successor to the Stuart technology as the two companies merged in 2004 [4]. In this respect therefore, the data from the Stuart SRA 6 kW represents the previous generation of alkaline electrolysers, and so not suitable for intermittent load operation.

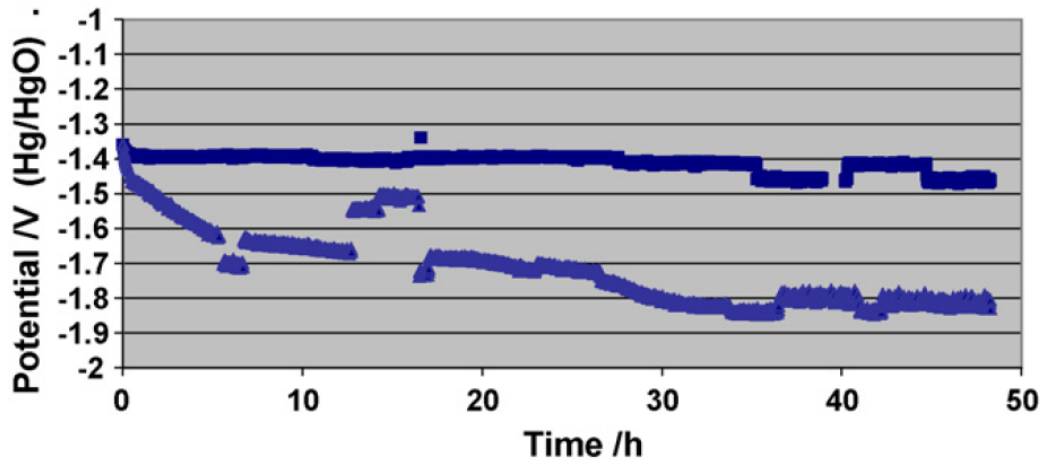


*Figure 7-2. Degradation of Hydrogenics alkaline water electrolyser in a function of intermittent load cycles [3]*

Although available data on commercial alkaline electrolyzers is very limited, the effect of degradation issues on the electrodes has been analysed more broadly. A significant amount of alkaline electrolyzers use nickel or its alloys as electrodes [5], [6]. Hence, an examination of the degradation effects that occur on the various nickel electrodes types could extend our knowledge about the processes that occur inside the commercial electrolyser units.

One of the most common reported concerns about electrode degradation is the deactivation of nickel cathode due to hydrides formation. Hydride creation on the electrode surface during HER is considered to be responsible for building a diffusion barrier for hydrogen atoms reducing performance [7-11]. That normally results in increasing activation and ohmic losses that leads to significant drop in the cathode performance over a time. To prevent this hydride formation, several methods have been proposed, including the application of iron coatings on the electrode surface [10]; addition of compounds of vanadium [12, 13] or molybdenum [14] into the electrolyte and oxidation of the created hydrides by a controlled increase of the

potential to a set level [11]. *Figure 7-3* illustrates the deactivation process of the cathode due to hydrides creation on nickel electrodes and the impact of the addition of an iron coating to the electrode surface in order to prevent its formation.



*Figure 7-3. Cathode polarisation potentials during longer term experiments.  $T = 70^{\circ}\text{C}$ , charging current  $100\text{ mA/cm}^2$ , 100 s averaged currents from three replicate experiments for ( $\blacktriangle$ ) bare Ni and ( $\blacksquare$ ) Ni with Fe coating [10]*

As well as the process of hydride formation, a second reported degradation issue was that connected with intermittent operation of the electrolyser. Some research publications have stated that when electrolyser was left un-polarised for a certain period, its performance decreased when restarted. Divisek *et al.* [15, 16] in their work described this characteristic of Raney nickel electrodes when aluminium or zinc was present within electrode structure. When the electrolyser was left un-polarised, both aluminium and zinc were prone to electrochemical corrosion. They indicated that if the aluminium or zinc content within electrode dropped below a certain level, the electrocatalytic activity of the hydrogen electrode decreased, which led to an increase in the cathodic overpotential (*Figure 7-4*) and consequently, a reduction in the electrolyser performance. The work also mentioned that a lowering of the temperature of operation of the electrolyser unit, could lead to cathode catalyst degradation due to extended hydrides formation at lower temperatures [16].



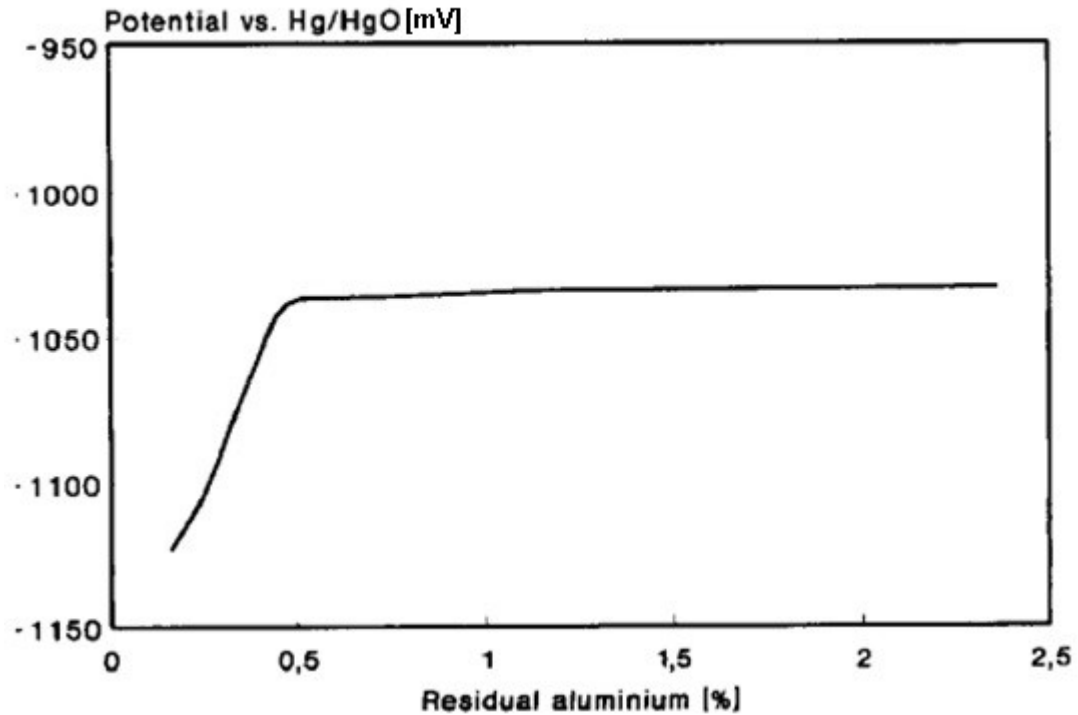


Figure 7-4. Overvoltage of Raney cathode as a function of the residual Al content,  $T=100^{\circ}\text{C}$ ,  $10\text{M KOH}$  [16]

On the other hand Schiller *et al.* [17, 18], demonstrated that it was possible to manufacture Raney nickel electrodes using vacuum plasma spraying (VPS) that were resistant to both hydrides deactivation and intermittent load operation effects. This work is particularly relevant as the VPS method is closely related to that of atmospheric plasma spraying (APS). However, the VPS technique requires more sophisticated equipment for the electrode manufacturing process. They demonstrated that their electrodes in a 10 kW electrolyser suffered minimal degradation following long term (15,000 hours), variable load operation (*Figure 7-5*). During the last 3 cycles of performed tests, the electrolyser was operated without protective current of  $80\text{ mA/cm}^2$ . This in fact means that for certain periods of time it was completely switched off.

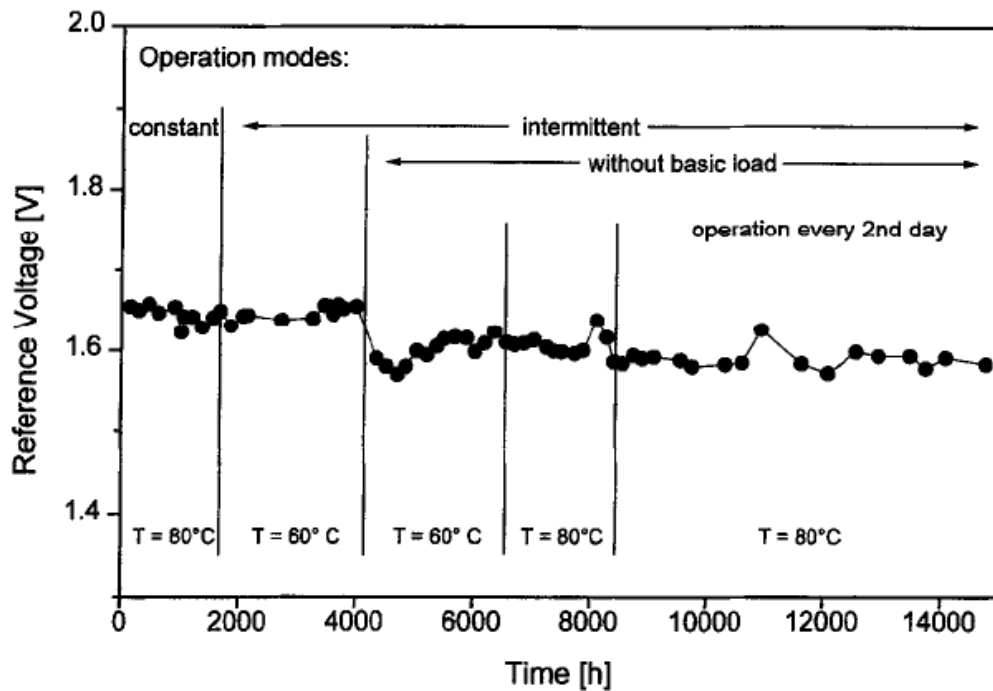
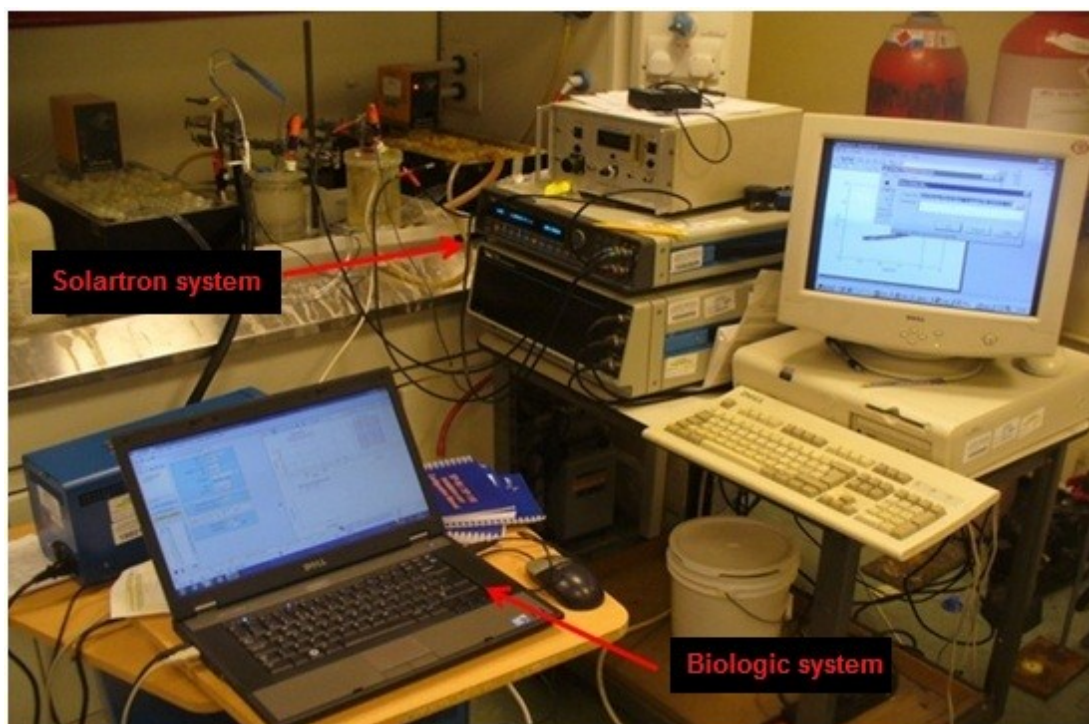


Figure 7-5. Reference voltage of VPS electrodes measured at  $80^{\circ}\text{C}$  and  $300\text{ mA/cm}^2$  as a function of time [18]

Atmospheric plasma spraying (APS) Raney nickel electrodes produced by Force Technology have shown very good initial performance towards the hydrogen evolution reaction (*Chapter 6*). However, their stability against degradation effects on operation over long times period and in variable load environments still had to be established. The understanding of all the phenomena responsible for the degradation of the electrodes surfaces towards HER was critical in order to enable electrode improvements to be carried out and so lead to technological commercialisation of the process. Although the main aim of the experiments performed and reported in this section were focussed on the performance of the APS cathodes, it is worth adding that to complete the work on fully understanding the electrolyser degradation phenomena, the performance of the APS electrodes for the oxygen evolution reaction would also have to be covered, but the latter though is beyond the scope of the present research.

## 7.2. System setup and experimental

The set-up for electrochemical studies consisted of 2 separate systems that were running simultaneously. The application of the duplicate electrochemical control and data acquisition system allowed an increase in the amount of obtained data and in practice doubled up the speed of research work. The configuration of each system was as described in *Chapter 4* including the hardware and chemicals used. As previously stated, the first system was the Solartron 1287/1250 controlled by CorrWARE software and the second system comprised of a Biologic SP-150 electrochemical interface with a 10 A current booster and EC-lab software. The overall layout of the experimental set-up is depicted in *Figure 7-6*, which shows on the right side, the computer connected to Solartron hardware and on the left side, the laptop controlling the Biologic SP-150 interface. In the background, the two electrochemical cells, each in three-electrode configuration, the water bath with temperature controllers and the magnetic stirrers can be seen. All the experiments were carried out using the 100  $\mu\text{m}$  APS sample in the alkaline electrolyte at a temperature of 70°C, unless otherwise stated.



*Figure 7-6.* Biologic (left) and Solartron (right) electrochemical interfaces working two separate experiments in the fume cupboard

### **7.3. Results and discussion**

The experiments carried out with the 100  $\mu\text{m}$  APS electrode examined two main operation themes: (i) long term, stable load operation and (ii) intermittent/variable load operation. The 100  $\mu\text{m}$  samples were chosen in preference to the 30 and 300  $\mu\text{m}$  electrodes because it had been shown to exhibit the best efficiency during initial tests for a moderate amount of catalyst used for its production.

### 7.3.1. Stable load operation and impact of hydride formation

During the operation of the activated electrode under constant load, it was observed that over a period of a few hours, there was a gradual decrease in the electrode performance. *Figure 7-7* shows the decrease in the cathode potential for the HER of the 100  $\mu\text{m}$  sample, operating at a constant current density of  $-300 \text{ mA/cm}^2$  over a period of 24 hours. After this initial period, the electrode response was examined using cyclic voltammetry, Tafel extrapolation and EIS techniques before being switched on again for another 24 hours constant operation cycle. During this 2<sup>nd</sup> cycle, the electrode performance partially recovered in that the cathodic potential for HER was now much lower than at the end of the 1<sup>st</sup> cycle. However, there was then a very rapid fall in electrode performance (compared to that in the 1<sup>st</sup> cycle) and after 6 hours of operation, the cathodic potential reached a value of  $-1.5 \text{ V}$ . Indeed, similar results were obtained when operating the 30  $\mu\text{m}$  and 300  $\mu\text{m}$  electrode samples under different current densities.

The observed deactivation effect here could be ascribed to hydrogen absorption into the metal lattice and leading to the formation of a  $\beta$ -nickel hydride phase [9, 13], [14], which changes H/Ni atomic ratio from  $\leq 0.1$ , to  $\geq 0.6$  [13, 19]. The formation of the hydride phase is considered to change the  $d$ -character of the nickel to  $sp$ -character by filling the  $d$ -band. The  $sp$ -character of the hydride is similar to silver or copper which are less active towards HER than fresh nickel [13]. In *Figure 7-7*, two characteristic regions can also be distinguished. The first one is more steep (before 15 hours/54000 s of the first cycle) and can be attributed to absorption of hydrogen whereas the second one is more gradual (after 15 hours/54000 s of the first cycle) and corresponds to  $\beta$ -hydride formation [13]. Regeneration of the electrode performance between cycles could occur due to the oxidation of hydrides that took place when potential was shifted to potential values more positive than  $-0.9 \text{ V}$  (which happened during the CV analysis between the cycles).

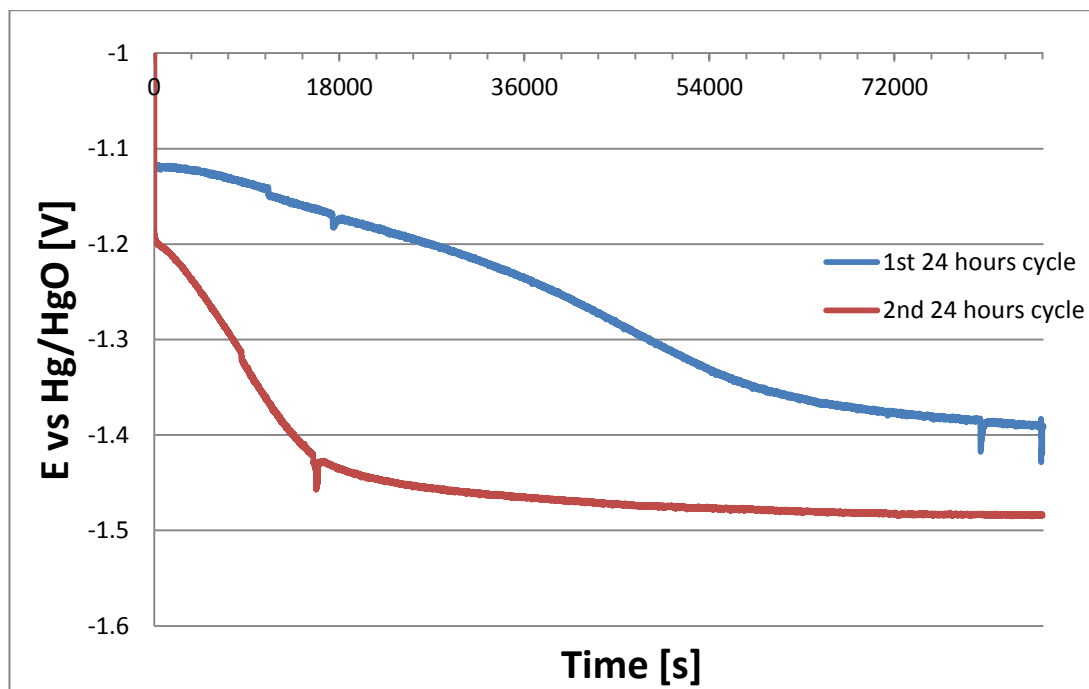


Figure 7-7. Deactivation of Raney nickel 100  $\mu\text{m}$  sample under constant load operation under constant current density of  $300 \text{ mA/cm}^2$

It is also worth noting that a similar behaviour was observed during testing of the different samples from all the available catalysts thicknesses (30, 100 and 300  $\mu\text{m}$ ), which confirms the reproducibility of the presented results. A general trend found was that deactivation took longer when samples with higher surface area were used. This phenomenon can be explained by the fact that it is the geometrical area that is measured and used for the current density. Thus, because of the porous nature of the activated Raney nickel surfaces, the larger sample areas would in fact be subjected to a lower local current densities and so, the surface concentration of adsorbed H-atoms, a precursor to hydride formation, would be lower. Correspondingly, the process time for hydride deactivation also increased when smaller current values were used. Due to this issue of cathode deactivation, several methods to counteract this effect were tested. Firstly, the oxidation process in which the potential was moved to more positive values (*Paragraph 7.3.2*) and secondly, a process of *in-situ* activation by the addition of compounds of molybdenum and vanadium to the electrolyte along with hybrid method of combining the electrolyte activation with

hydrides oxidation were tested (*Paragraph 7.3.3*). Additionally inside *Paragraph 7.3.4* the results of experiments with variable load operation can be found.

### **7.3.2. Oxidation of hydrides on the electrodes**

The results from the initial tests had shown that the APS electrodes were highly prone to deactivation by hydrides formation. One method of minimising this negative impact was that of electrode oxidation. The fundamentals of the oxidation is based on the phenomenon that when the electrode potential is moved from around  $-0.9$  V towards more positive values, the hydrogen incorporated in the nickel oxidises and dissolves into electrolyte solution [11]. Such an operation requires the introduction of special control strategies into the electrolyser operation so as to oxidise the hydrides over certain period of time and so restore performance. On the other hand, it has been reported that repeated oxidation and reduction introduced strain on the catalyst material, which could lead to its mechanical failure [11].

Initially, the oxidation method was tested in a multiple cycle operation where each sample was operated under galvanostatic conditions at the current density of  $-0.3$  A/cm<sup>2</sup> for 30 minutes and subsequently, the operation conditions were switched to potentiostatic mode to  $-0.85$  V for a 60 s period in order to oxidise the hydrides. This was repeated 33 times. As can be seen from *Figure 7-8 (A)*, this did not provide the satisfactory effect, as the electrode performance decreased with every subsequent cycle. However, although it did lead to an initial increase in the performance of the electrode towards HER as the potential was always better than final value achieved in the previous cycle, the oxidation at  $-0.85$  V potential was inadequate to completely restore the electrode performance. *Figure 7-8 (B)*, shows the oxidation current response obtained for the potential step to  $-0.85$  V for some representative cycles. The initial high current spike can be attributed to the double-layer capacitance discharge, induced by the step voltage change. The current density then stabilised at around  $10$  mA cm<sup>-2</sup> after  $\sim 15$  s, which was attributed mainly to hydrides removal effect although the oxidation of adsorbed hydrogen cannot be ruled out. As can be seen, this current density did not vary significantly between the cycles.

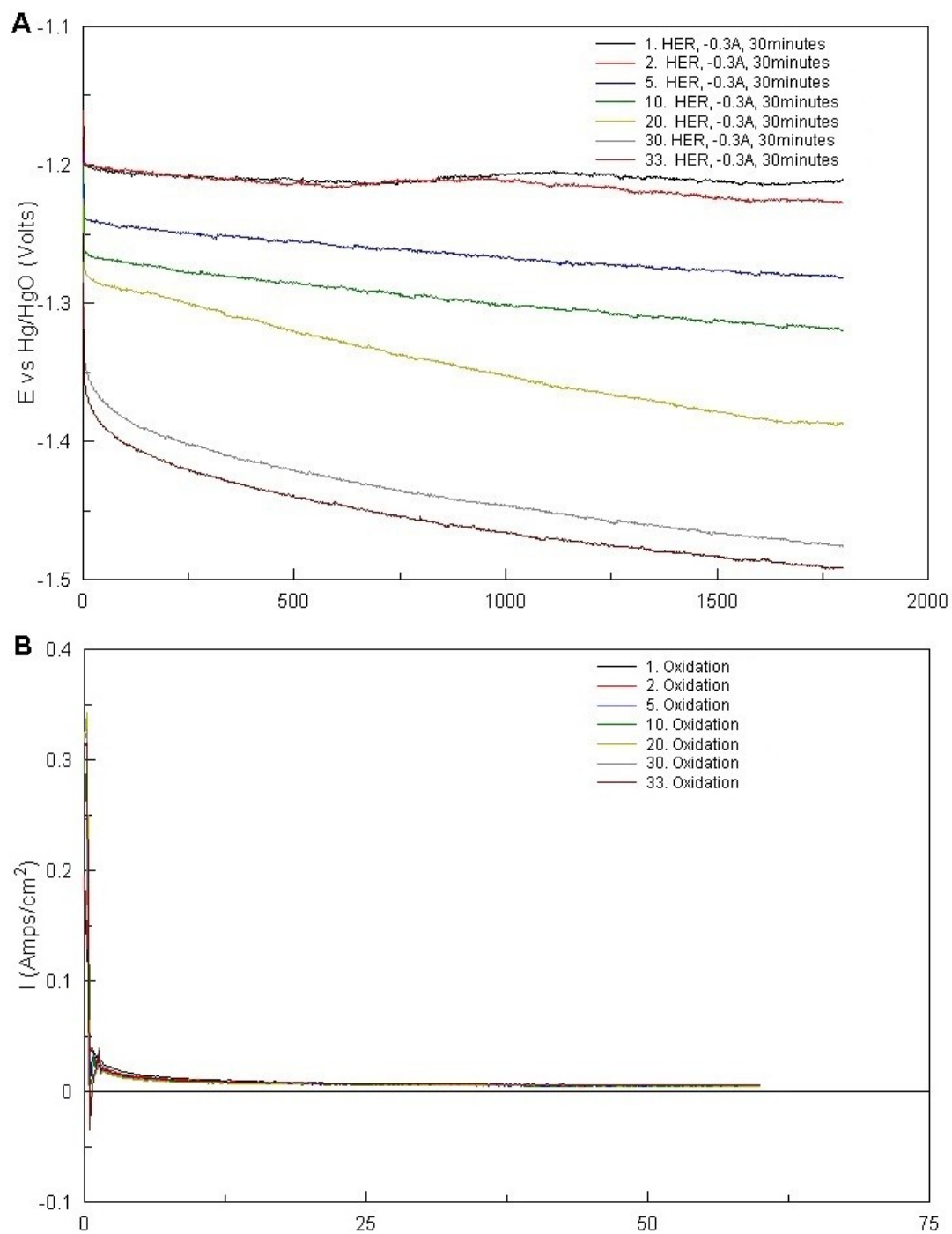


Figure 7-8. A - Operation of 100  $\mu\text{m}$  electrode sample under current density of  $-0.3 \text{ A/cm}^2$ , within subsequent cycles separated with oxidation process, B - Oxidation currents for every cycle under  $-0.85 \text{ V}$  potential



Due to insufficient hydrides removal during this first series of experiments, it was decided to increase oxidation potential up to  $-0.2$  V and at the same time oxidation time was reduced to 5 s. This potential was positive enough to force all the hydrides to react but the reduced time would prevent the formation of surface oxides on the Raney nickel electrode. The results presented in *Figure 7-9(A)* show that such a strategy initially did restore the system performance, at least for the first two oxidation cycles, giving electrode potentials very similar to the initial values from previous tests (*Figure 7-8(A)*). However, as noted, this was only for the first two cycles as for subsequent cycles, although the hydrides layer was completely removed (*Figure 7-9(B)*), there was a gradual decrease in the performance. This was possibly caused by catalyst surface damage due to the high oxidation current. Normally the APS electrodes are designed for current densities of  $0.3$  A/cm<sup>2</sup> but during the oxidation at  $-0.2$  V, the maximum current exceeding  $2.5$  A/cm<sup>2</sup>. Such a large current density was induced by the discharge of double layer capacitance.

This test also showed that during variable load operation, step voltage changes should be avoided as it can induce very high currents densities from the discharge of double layer capacitance. Although this is a non-Faradaic process, it could give rise to local heating effects which could damage or lead to changes to the catalyst structure and/or morphology. Such an effect can be especially notorious when using porous, large surface electrode surfaces that are characterised by high values of capacitance. Also, usually high surface area electrodes are using catalyst coatings, which by definition is less stable than solid material such as nickel or stainless steel plates.

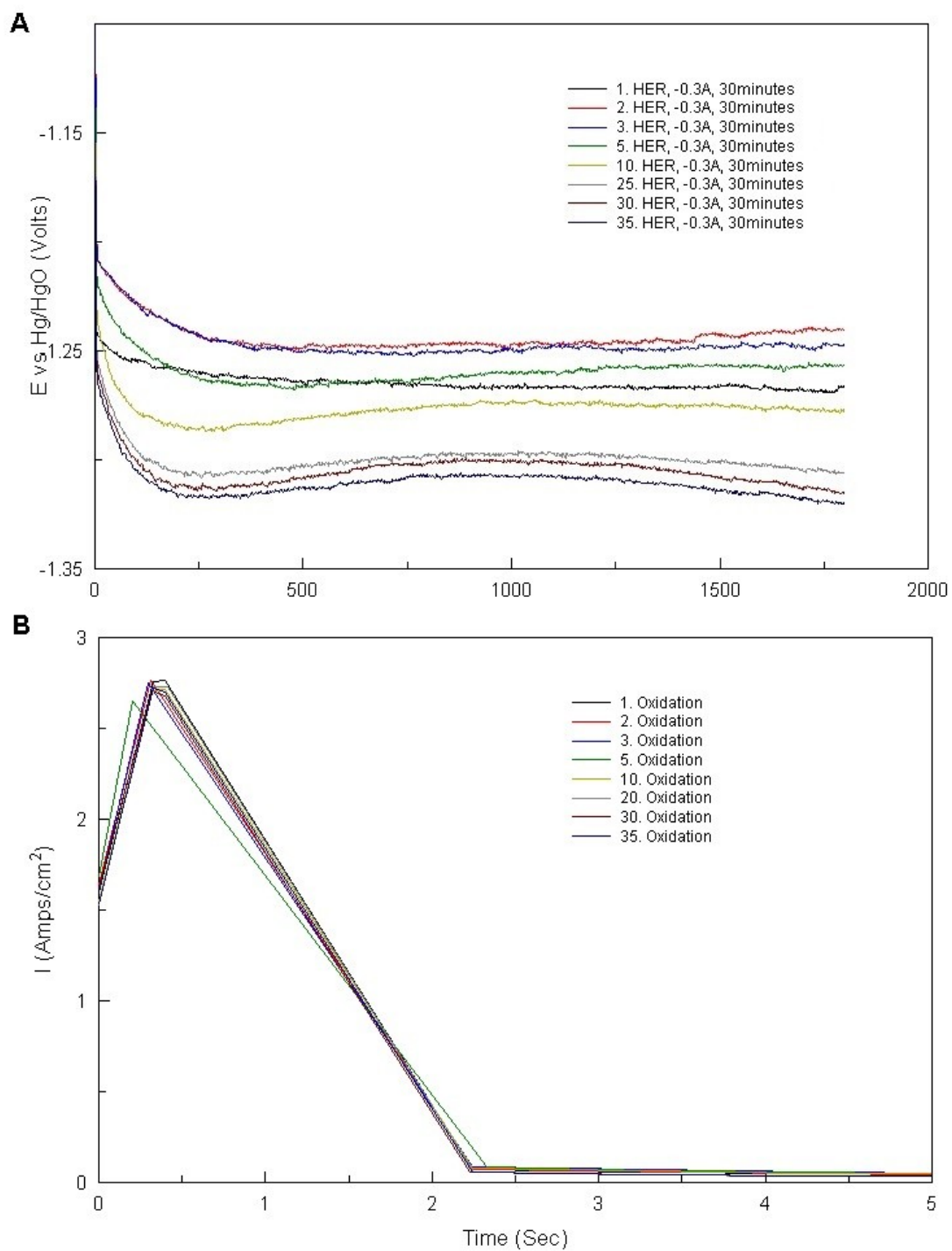


Figure 7-9. A - Operation of 100  $\mu\text{m}$  electrode sample under current density of  $-0.3 \text{ A/cm}^2$ , within subsequent cycles separated with oxidation process, B - Oxidation currents for every cycle at  $-0.2 \text{ V}$  potential

Further experiments were carried out in which various oxidation regimes were tested and these included: short/long duration; high/low currents and different intervals between the cycles. Two main issues were identified after performing such tests. The first was that of insufficient hydrides removal and the second was degradation of the catalysts, if the oxidation process was not carefully controlled. Despite running numerous tests on different samples, none of the procedures tried showed satisfactory results with regards to completely removing hydrides without damaging catalysts surface.

The catalyst degradation due to oxidation was confirmed by cyclic voltammetry and electrochemical impedance spectroscopy analyses. In the case of CV analysis, one of the samples was operated for 20 hours under a current density of  $-200 \text{ mA/cm}^2$  and after each hour, the sample was oxidised for 1 minute at the potential of  $-0.85 \text{ V}$  and then tested by the cyclic voltammetry method. As can be seen from *Figure 7-10(A)* the performance using this procedure initially increased (*i.e.* less negative potential) after first two cycles but this gradually decreased on subsequent cycles. The initial rise in the performance could be attributed to hydrides removal whereas the ensuing fall in the performance could be directly associated to damage to the catalyst structure. *Figure 7-10(B)* shows that with every subsequent cycle, the oxidation peak at  $\sim -0.6 \text{ V}$  in the cyclic voltammogram, associated with  $\text{Ni(OH)}_2$  formation, was smaller. As the charge under the peak is proportional to the available electrochemical surface area, it thus shows that within every subsequent cycle, the active area was decreasing. This provides evidence that the oxidation which occurs during the cyclic voltammetry method can be invasive for sample structure and its use should be minimised to prevent possible sample damage when working with the APS Raney nickel electrodes.

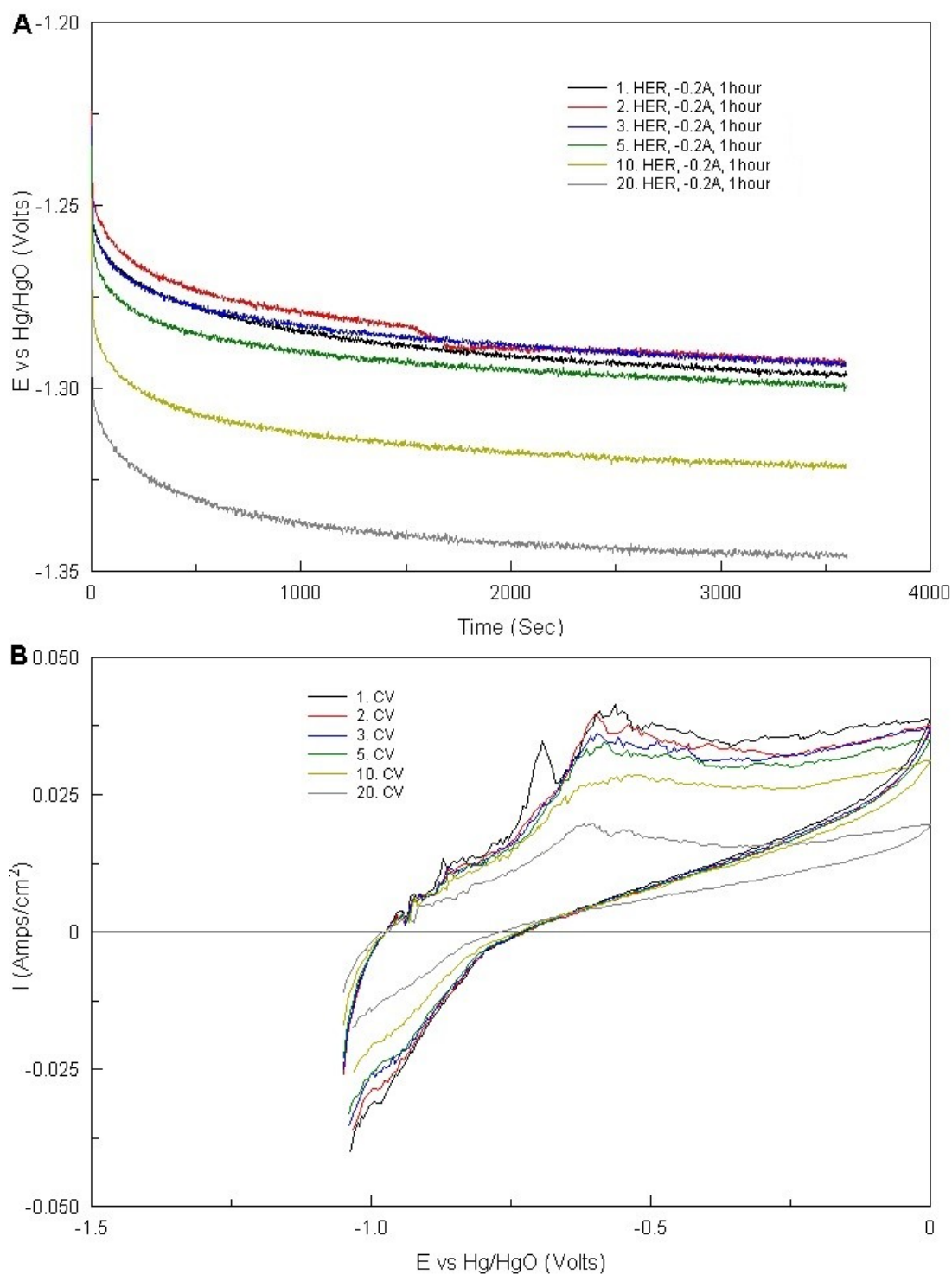


Figure 7-10. A - Operation of 100  $\mu\text{m}$  electrode sample under current density of  $-0.2 \text{ A/cm}^2$ , within subsequent cycles separated CV measurements, B – cyclic voltammograms for each cycle -  $50 \text{ mV/s}$  scan rate

Additional evidence confirming this hypothesis was obtained from EIS measurements. During the first 24 hours, the sample was operated under current density of  $-0.2 \text{ A/cm}^2$  and every hour, the electrolysis reaction was interrupted by the oxidation event carried out using a  $0.3 \text{ A/cm}^2$  current density for one minute duration. Over the next 24 hour period, the hydrides were oxidised every 1 hour using a constant current density of  $0.2 \text{ A/cm}^2$ , until the voltage reached the value of  $-0.2 \text{ V}$ . EIS analysis were performed at the start of the series of experiments and after 24 and 48 hours. Each time, they were preceded by CV and  $j(V)$  curve analysis. *Figure 7-11* shows the  $j(V)$  curves obtained at these times and the double layer capacitance and charge transfer resistance data obtained from the EIS measurements and analyses are presented in *Table 7-1*. Not surprisingly, the  $j(V)$  curves showed a significant drop in the performance after every sequence. Confirmatory data for this was also observed in the change of the EIS parameters shown in *Table 7-1*. Following the first sequence, it can be seen that there is a significant reduction in the double layer capacitance value and an increase of charge transfer resistance. After the second 24 hours cycle, the charge transfer resistance increased further but not the  $C_{dl}$  values, which at the different overpotentials, remained more or less the same. This might suggest that during first 24 hours, the catalyst structure was significantly degraded and the electrochemically active area decreased, which also caused values of  $R_{ct}$  to increase. During second 24 hours, the active area of the electrode did not change significantly but the further loss of the aluminium promoter that occurred decreased the general electrocatalytic activity. Such an effect has been described by Divisek *et al.* [15, 16], and it might also be the reason for the increase in  $C_{dl}$  at the potentials of  $-1.00$  at  $-1.05 \text{ V}$  after the second 24 hours operation sequence. Thus, the loss of electrocatalytic activity would have resulted in a decrease in the reaction rate and concomitantly, the amount of bubbles produced at that overpotential. That could have effectively resulted in a smaller amount of blocked pores and so, an increase in the value of double layer capacitance [20].

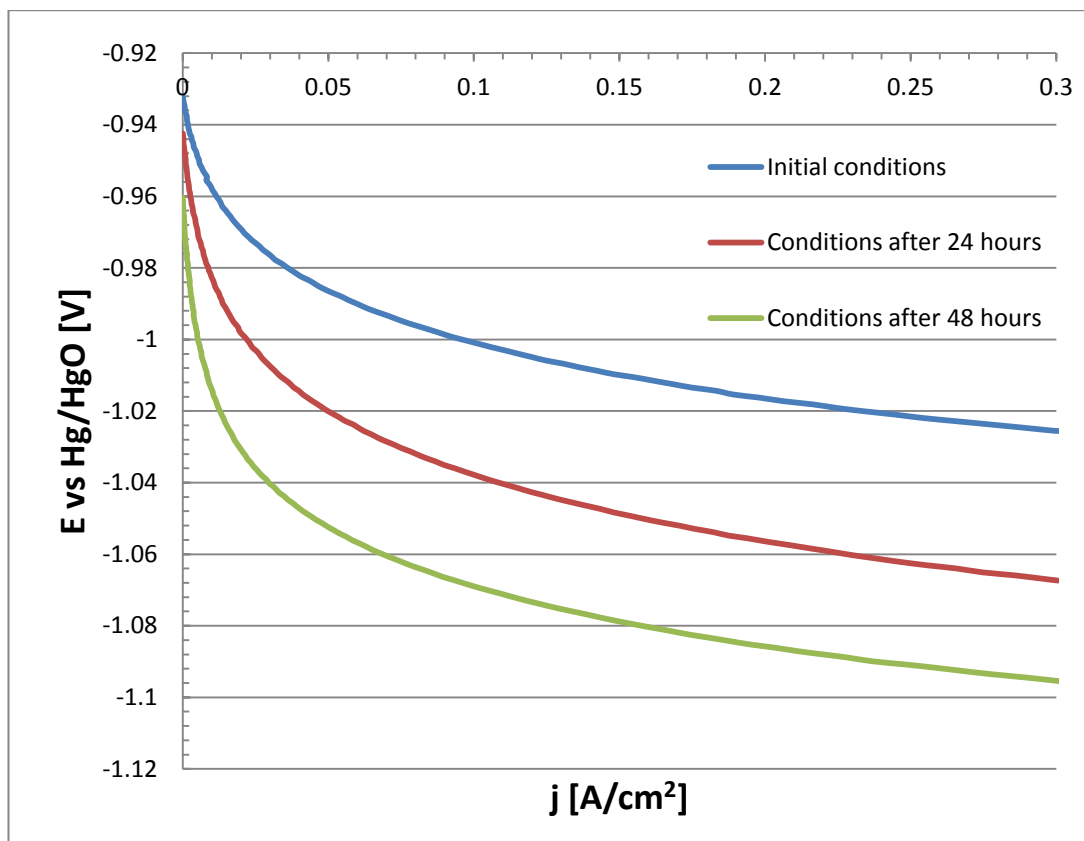


Figure 7-11.  $j(V)$  curve of operated sample initially, after 24 and 48 hours

Initial sample conditions		
E [V]	R <sub>ct</sub> [ $\Omega \cdot \text{cm}^2$ ]	C <sub>dl</sub> [F/cm <sup>2</sup> ]
<b>-0.95</b>	0.989	0.160
<b>-1.00</b>	0.206	0.099
<b>-1.05</b>	0.127	0.074
<b>-1.10</b>	0.101	0.065
<b>-1.15</b>	0.097	0.062
Sample conditions after 24 hours operation with 0.3 A oxidation every hour		
E [V]	R <sub>ct</sub> [ $\Omega \cdot \text{cm}^2$ ]	C <sub>dl</sub> [F/cm <sup>2</sup> ]
<b>-0.95</b>	5.312	0.058
<b>-1.00</b>	0.987	0.038
<b>-1.05</b>	0.588	0.016
<b>-1.10</b>	0.363	0.013
<b>-1.15</b>	0.255	0.011
Sample conditions after 48 hours operation with 0.3 A oxidation every hour		
E [V]	R <sub>ct</sub> [ $\Omega \cdot \text{cm}^2$ ]	C <sub>dl</sub> [F/cm <sup>2</sup> ]
<b>-0.95</b>	18.39	0.061
<b>-1.00</b>	10.25	0.058
<b>-1.05</b>	2.95	0.039
<b>-1.10</b>	0.77	0.016
<b>-1.15</b>	0.43	0.011

*Table 7-1. EIS parameters for 100  $\mu\text{m}$  sample just after activation and after 24 hours and 48 hours operation*

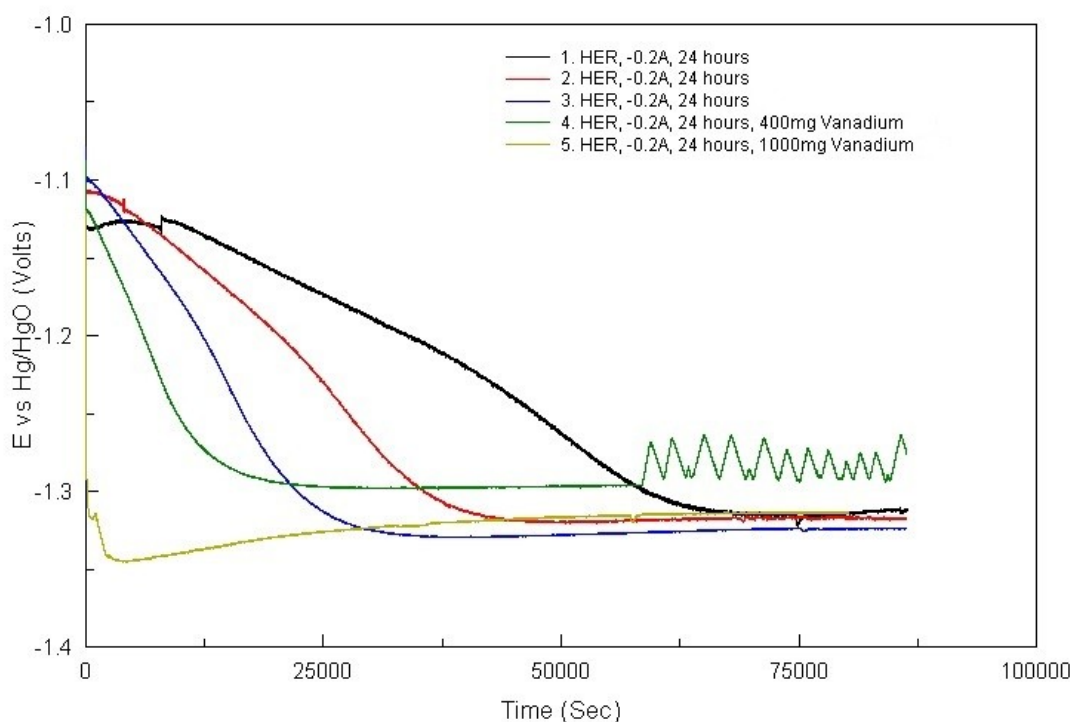
### 7.3.3. In situ activation of the electrolyte

Another method investigated to decrease the influence of hydride formation was that of carrying the activation of the APS electrodes in electrolytes containing compounds of vanadium, molybdenum or iron [10, 12-14, 21-24]. In these experiments, the compounds, vanadium oxide ( $V_2O_5$ ) and/or sodium molybdenum oxide dihydrate ( $Na_2MoO_4 \cdot 2H_2O$ ) were dissolved into the KOH electrolyte during the electrolytic activation process. During cathodic polarisation, this normally results in the deposition of vanadium and molybdenum species onto the electrode surface which could serve to prevent the deactivation effect due to hydride formation [13, 14, 24]. An additional advantage of using compounds of vanadium and molybdenum is that, they are reported to improve electrocatalytic properties in connection with nickel, which would result in better cathode performances for the HER [16, 17, 21, 22].

The initial experiments with vanadium were performed by adding 200 mg/l into the 30% KOH solution, in accordance with the work of Abouatallah *et al* [13]. The vanadium oxide was added to the electrolyte from the very beginning of the experiment, before the electrochemical activation of the electrode. The results obtained (shown in *Figure 7-12*) indicated that the presence of the vanadium, even up to concentrations of 1000 mg/L did not have any major impact on the initial electrode performance, indicating that there was no increase in the electrocatalytic activity. The impact of vanadium on the activation was observed however during long term operation, where a significant reduction in the cathodic potential to *ca.*  $-1.3$  V (from  $-1.5$  V without vanadium *Figure 7-12*) could be seen. After each of the 24 hours cycles, the CV method was applied which resulted in the electrode performance regeneration (due to hydrides oxidation). As can be seen from the figure, the initial deactivation process during the first cycle occurred over a much longer period than in the subsequent cycles. Before the 4<sup>th</sup> cycle, an additional amount of vanadium oxide was added to the electrolyte resulting in an increase in its concentration from 200 mg/L to 400 mg/L. Similarly, before 5<sup>th</sup> cycle, the concentration was increased further to 1000 mg/L. Surprisingly, this last concentration did not serve to reduce the impact due hydrides formation. During the



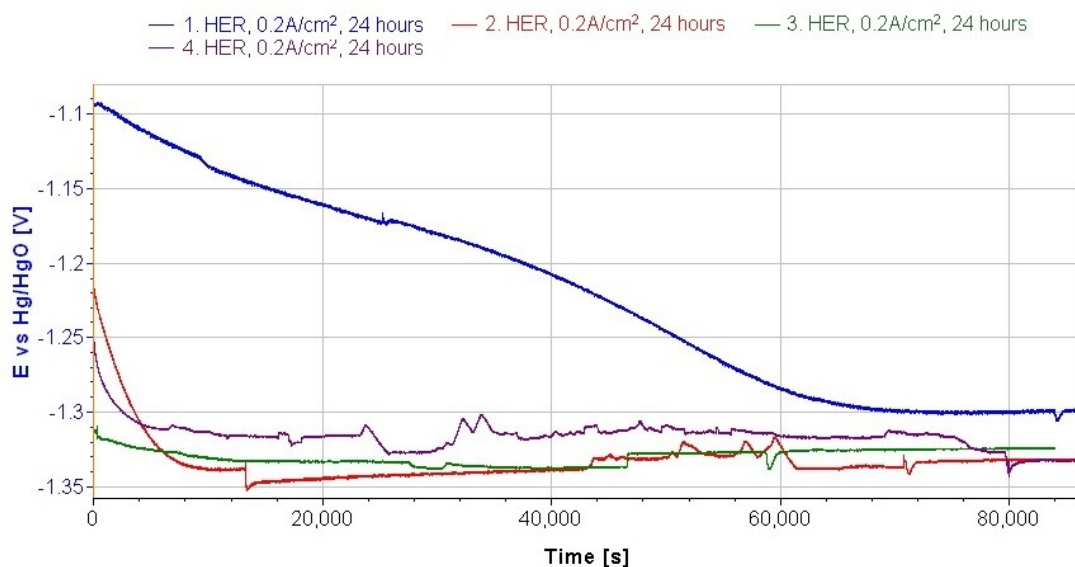
4<sup>th</sup> cycle, some voltage fluctuations were observed and the cause for this is unknown but it is likely to be due to an instrumentation artefact. Similar features were observed several times during the many measurements carried out and it probably could have been caused by the magnetic stirrer, which could have changed the impact due to H<sub>2</sub> bubbles by inducing convection and mechanically moving of the bubbles away from the electrode surface. The small offsets seen in the data between the final plateau values of different cycles comes from the absence of *IR* compensation during the galvanostatic mode of operation. This effect should normally have an impact not exceeding 50 mV. It has to be noted however that *IR* compensation was always applied during current vs potential curve measurements, and its effect is presented later on in this chapter (*Figure 7-14*).



*Figure 7-12. Comparison of the time effect of vanadium influence for Raney nickel cathode performance*

The second compound used in this study and which has been shown to reduce hydrides impact was sodium molybdenum oxide. This was again added at a concentration of 10 mM/L to the KOH electrolyte. Experiments similar to those previously described by Huot *et al.* and Tasic *et al.* [14, 21, 22] were carried out,

where in essence the  $\text{NaMoO}_4$  compound in different concentrations was added to KOH electrolyte to prevent hydrides impacting on the electrodes' performance. It was observed that molybdenum had a very similar effect as to vanadium regarding hydrides inhibition over the first 24 h of operation (*Figure 7-13*). There was a gradual increase in the cathodic potential from the initial value of  $-1.1$  V to the plateau value of  $-1.35$  V by  $\sim 19.5$  h. On subsequent cycles however, the cathodic polarisation occurred much more rapidly and it was completed within  $\sim 2.2$  h, 1.1 h and  $<0.5$  h for cycles 2, 3 and 4 respectively. These effects are much more severe than were observed for the vanadium pentoxide addition and would suggest that the molybdenum compound was not as effective on negating the effect of the hydride formation. Indeed, it can be seen from the data that the recovery of the potential at the start of the next cycle was very poor and non-existent for the 4<sup>th</sup> cycle. An increase of molybdenum concentration to 20 mM/L also failed to have any further impact. It would appear then that the addition of the vanadium and molybdenum to the electrolyte provided only limited initial protection against hydride formation and a subsequent increase in the polarisation for the HER then occurred. Further experimental work involving a combination of vanadium and molybdenum was carried out but no significant reduction in the impact of hydrides was noted in the data.



*Figure 7-13. Comparison of the time effect of molybdenum influence for Raney nickel cathode performance*

Additional tests were performed combining the methods of oxidation and  $V_2O_5$  electrolyte addition to the KOH electrolyte. The initial experiment for the 300  $\mu\text{m}$  sample was carried out in the pure KOH solution at a current density of  $-200 \text{ mA/cm}^2$  but after every 30 min, a 1 min oxidation at a  $200 \text{ mA/cm}^2$  current density was carried out. The data showed the usual performance drop within the 24 hours operation, with the cathode potential decreasing to  $-1.35 \text{ V}$  and this was again attributed to mechanical damage of the sample (*Figure 7-14(A)*). However, as *Figure 7-14(B)* shows, after the addition of  $200 \text{ mg/L}$  of  $V_2O_5$  partial reactivation of the electrode performance towards HER was achieved. The figure indicates that in the presence of the  $V_2O_5$ , the magnitude of voltage change during the 30 min operation drastically reduced and there was even a decrease in the cathode polarisation at the end of that period. This trend can be explained by the fact that the oxidation events were probably still causing some damage to the catalyst structure, but on the other hand, deactivation from further hydrides formation effect was reduced.

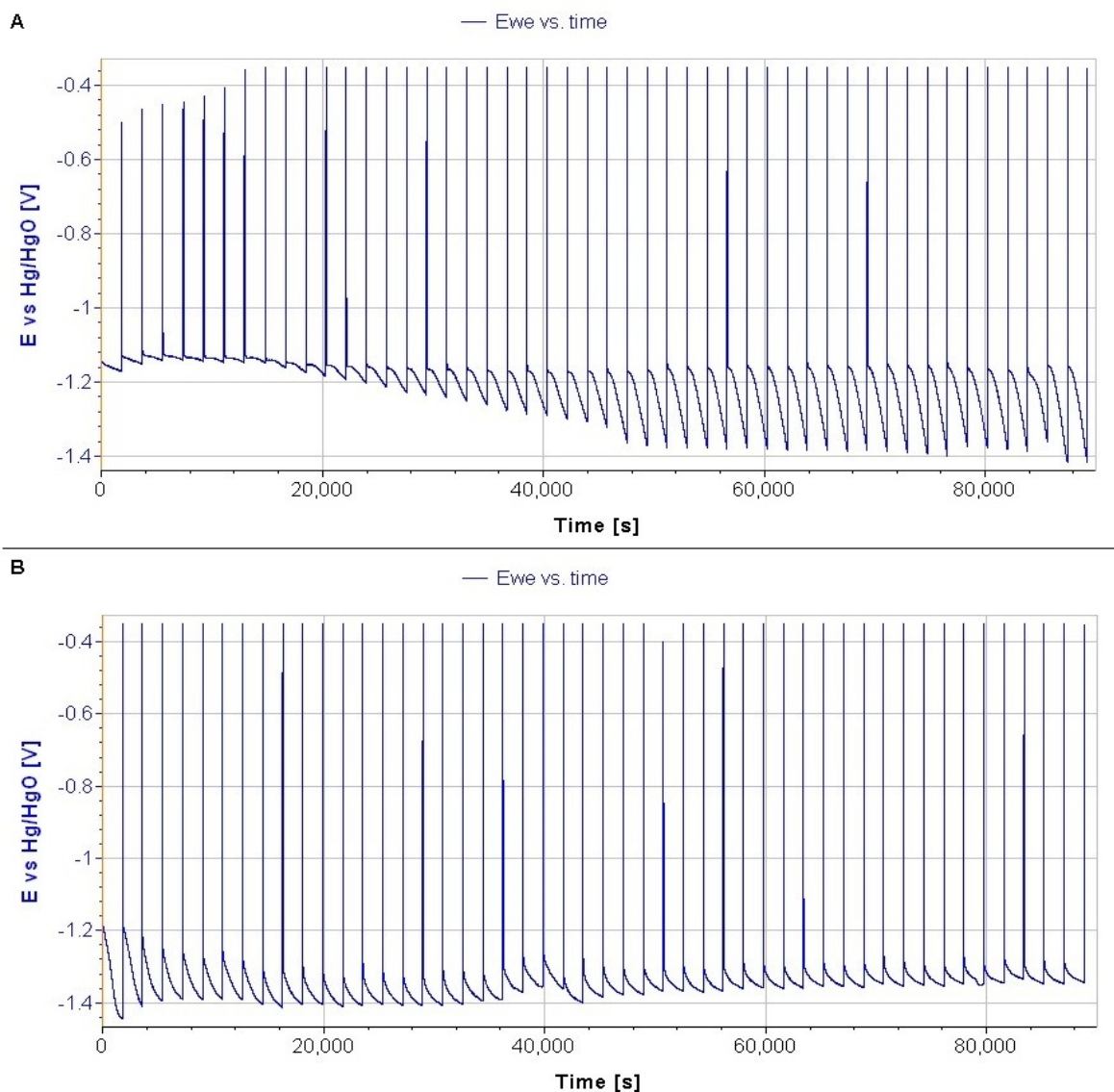


Figure 7-14. A - Deactivation of Raney nickel electrode in stable load with oxidation cycles, B - Reactivation of Raney nickel electrode in stable load with oxidation cycles after adding vanadium to the electrolyte

A comparison of the  $j(V)$  curves for 100  $\mu\text{m}$  samples is presented in Figure 7-15, obtained after reaching the sample hydrides deactivation plateau value. The data were from operation in the pure KOH electrolyte and after addition of the vanadium and/or molybdenum compounds. During these measurements,  $IR$  compensation was applied, which thus eliminated the ohmic losses arising from the electrolyte between the working and reference electrodes. As can be seen, significant differences in performance were observed which confirmed the significant reduction in the

hydrides deactivation effect with the application of the *in-situ* electrolyte addition activation method. Indeed, the *in-situ* activation procedure was able to reduce the hydrogen overpotential by  $\sim 0.2$  V. Additionally it was observed at the higher current density limits, that electrodes activated in molybdenum were slightly superior comparing to those activated with pure vanadium alone. This is in accordance with literature which indicates that molybdenum with nickel showed better electrolytic properties than vanadium with nickel [21]. The best performance here though was achieved using a combination of vanadium and molybdenum. It is worth noting that the potential difference between all samples (apart from that in pure KOH) was small ( $< 15$  mV at  $300 \text{ mA/cm}^2$  current density) and this small difference could have been influenced by other factors such as trace electrolyte contamination, hydrides structure and sample surface mechanical condition.

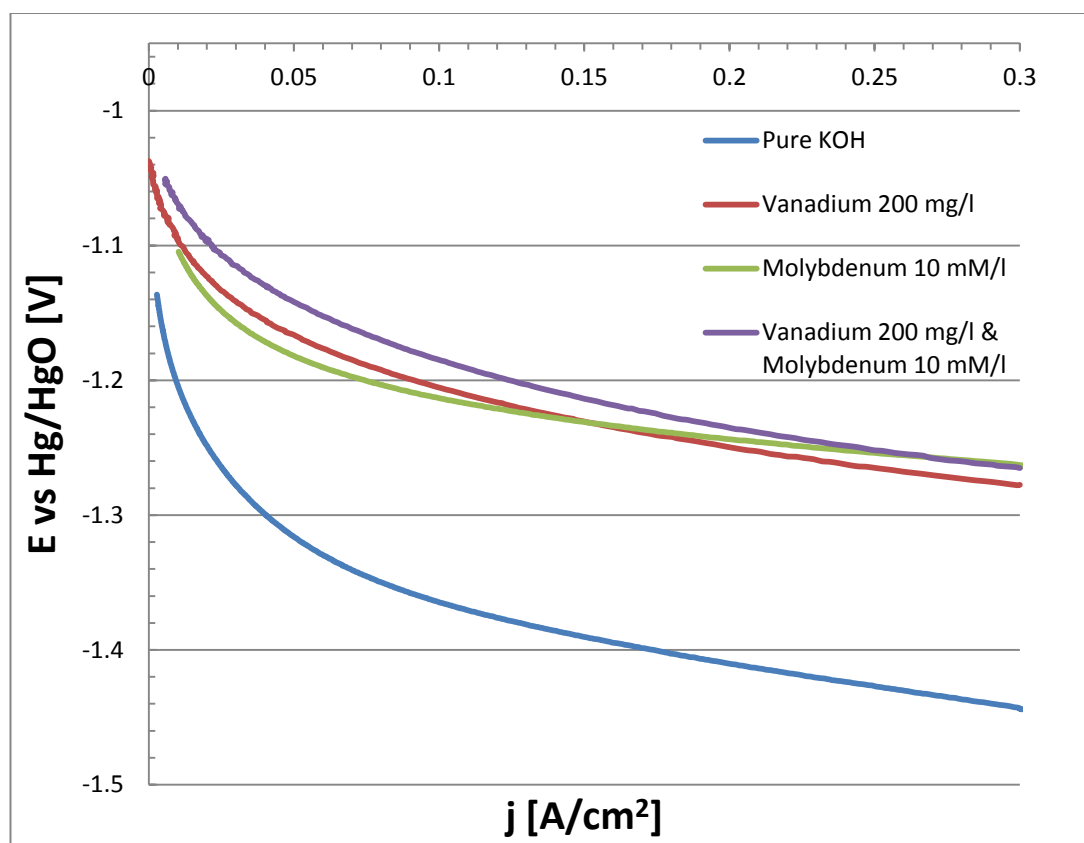


Figure 7-15. Comparison of the performance of Raney nickel electrodes deactivated by hydrides in pure KOH electrolyte and with addition of vanadium and/or molybdenum compounds

#### 7.3.4. Variable load operation

There have been a few recent reports detailing the negative influence of variable load operation on the performance of the electrodes in the alkaline electrolyser [15, 16, 25]. The intermittent load degradation mechanisms in these reports were mainly attributed to hydrides decomposition when the electrode was left in an un-polarised state. Such a process was considered to cause a shift of the cathode rest potential towards positive values where compounds such as: aluminium, zinc and molybdenum within the Raney nickel electrode structure became more prone to corrosion [15, 16, 25]. It was essential therefore that the variable operation tests were also carried out on the APS Raney nickel electrodes in order to compare their performance under these operation conditions.

To investigate the impact of intermittent operation, the APS Raney nickel electrode was operated over 48 hours, employing cycles in which the sample was operated at a current density of  $200 \text{ mA/cm}^2$  for 15 minutes and then subsequently left for 15 minutes at the open circuit voltage. The results from this experiment are shown in *Figure 7-16(A)*. The general trend observed from the data as a whole was that although there was a gradual increase in the polarisation of the electrode with cycling, there was however a decrease in the cathode potential over the first 14 h of operation. If indeed the increased in polarisation arises from hydrides formation, it would appear then that during the initial stages, the 15 min period at open circuit was sufficient to remove most (if not all) of the hydrides formed during cathodic polarisation. Clearly then, following this initial period, hydride removal was not completed as can be seen from the still rising OCP value towards the end of the 15 min period. This then lead to a concomitant decrease in the cathode polarisation voltage during electrolyser operation. Prior to and after these experiment, the  $j(V)$  curve, preceded by the standard oxidation process, were recorded and these are shown in (*Figure 7-16(B)*). As can be seen, the difference between these two curves in the figure is quite small, around 5 mV, even at a current density of  $300 \text{ mA cm}^{-2}$ . This provides supporting evidence that apart from hydrides formation, there was no

other process involved in reducing the electrode performance and it can be concluded that APS electrodes are well suited for intermittent operation.

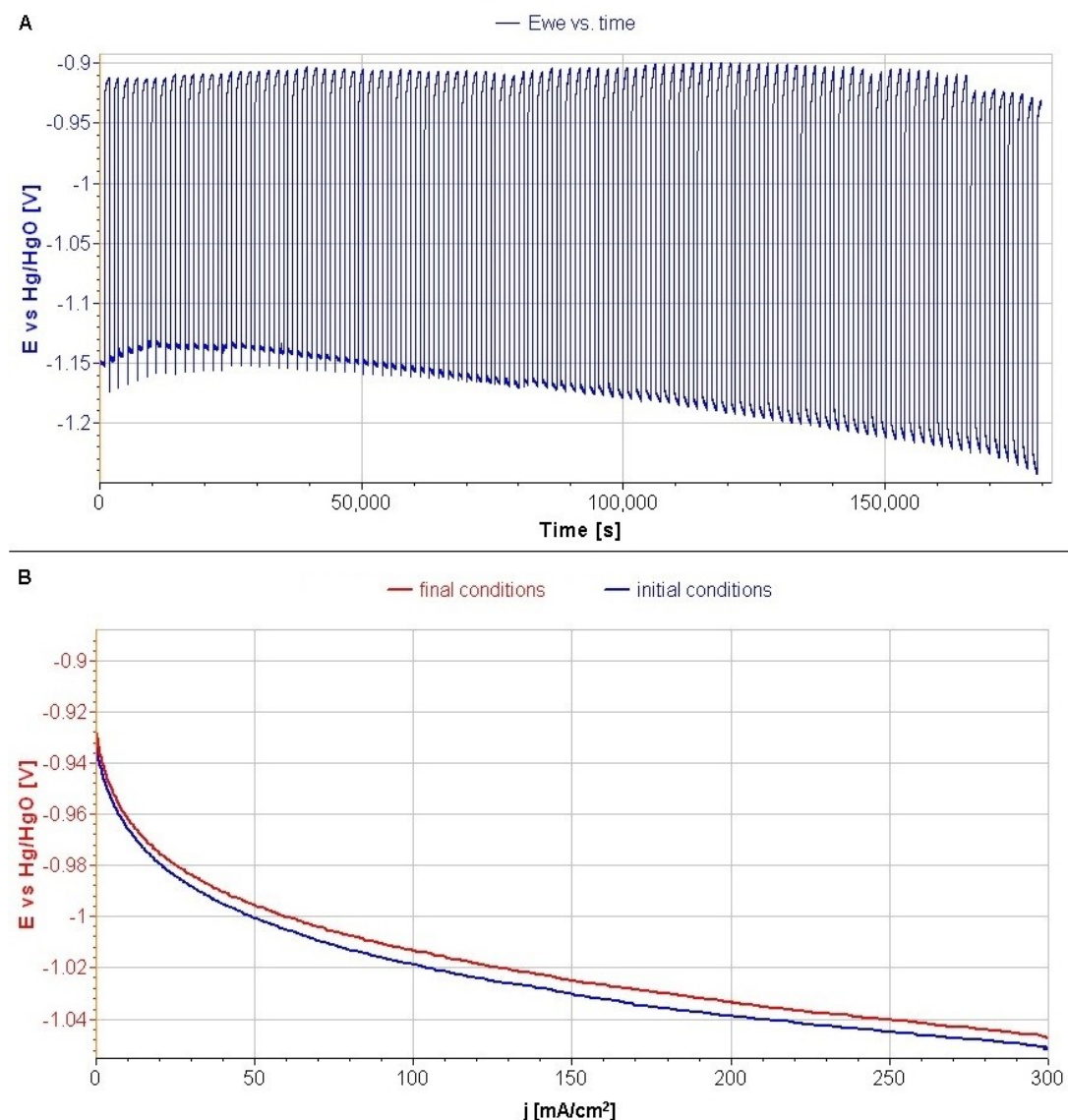


Figure 7-16. A- Intermittent operation time impact, B – Electrodes performances before and after operation

It is worth noting that the shape of the voltage (time) curve is similar to that obtained during cycling (Figure 7-17). As can be seen, during cycling in the beginning of the experiment, the change in the open circuit potential is less significant than what is found later on in the cycling. It might also be observed that the initial OCP was lower and the final voltage value becomes higher the longer the duration of the experiment.

These observations can be again connected to the impact of hydrides that are believed to decrease the cathode open circuit potential [15]. When switching to OCP, hydrides are gradually oxidised and so, the OCP rises with time. On the other hand, the hydrides decomposition process is considered to cause the loss of the residual aluminium promoter and this leads to an increase in the final OCP [15, 25].

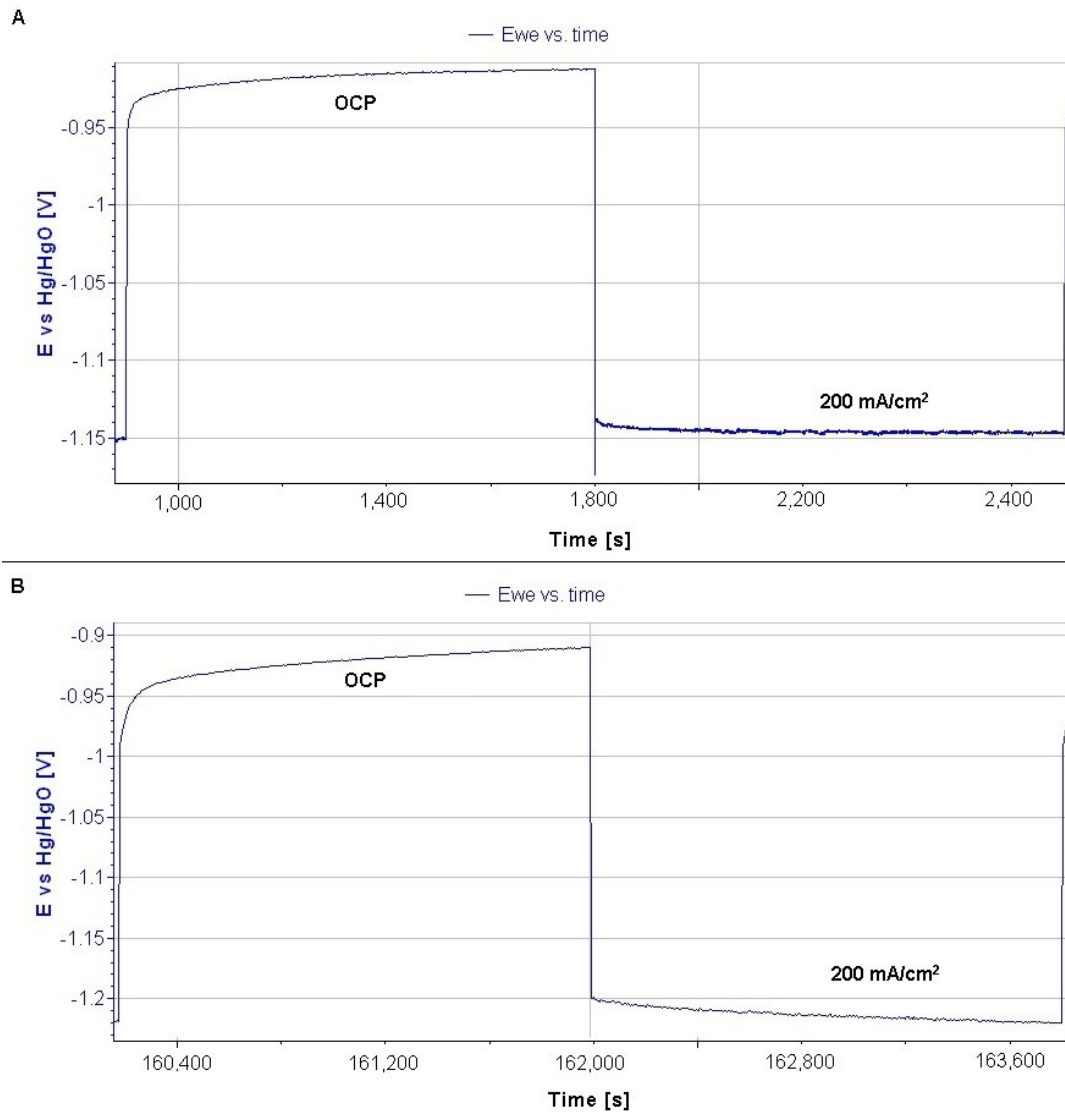


Figure 7-17. Comparison of 5<sup>th</sup> (A) and 90<sup>th</sup> (B) cycles during intermittent load operation



### 7.3.5. Single cell electrolyser tests

The results presented in this paragraph show the data from the testing of the APS electrodes inside a single cell electrolyser unit. As electrodes, the 100  $\mu\text{m}$  APS Raney nickel samples of 1  $\text{cm}^2$  surface area were used. For activation, the same experimental procedure was employed as described previously in *Chapter 6*. The only difference was that the anode electrochemical activation procedure was modified and the anode was not operated for 14 hours in HER, but in OER instead under 200  $\text{mA}/\text{cm}^2$  current density. The purpose here for this change was to avoid hydrides formation that normally occurs during HER and could have led to damage of the catalyst surface structure when it was oxidised. Following electrochemical activation, the performances of the anode and cathode were measured and the data obtained is presented in *Figure 7-18*. The electrode potentials were  $-1.026$  and  $0.576$  V (under 300  $\text{mA}/\text{cm}^2$  current density) for cathode and anode, respectively. These results showed that there was little change in the cathode potential in comparison with the values presented in *Table 6-1* which was in a range previously found. The anode performance was slightly higher (around 50 mV), which could have arisen due to change in activation procedure.

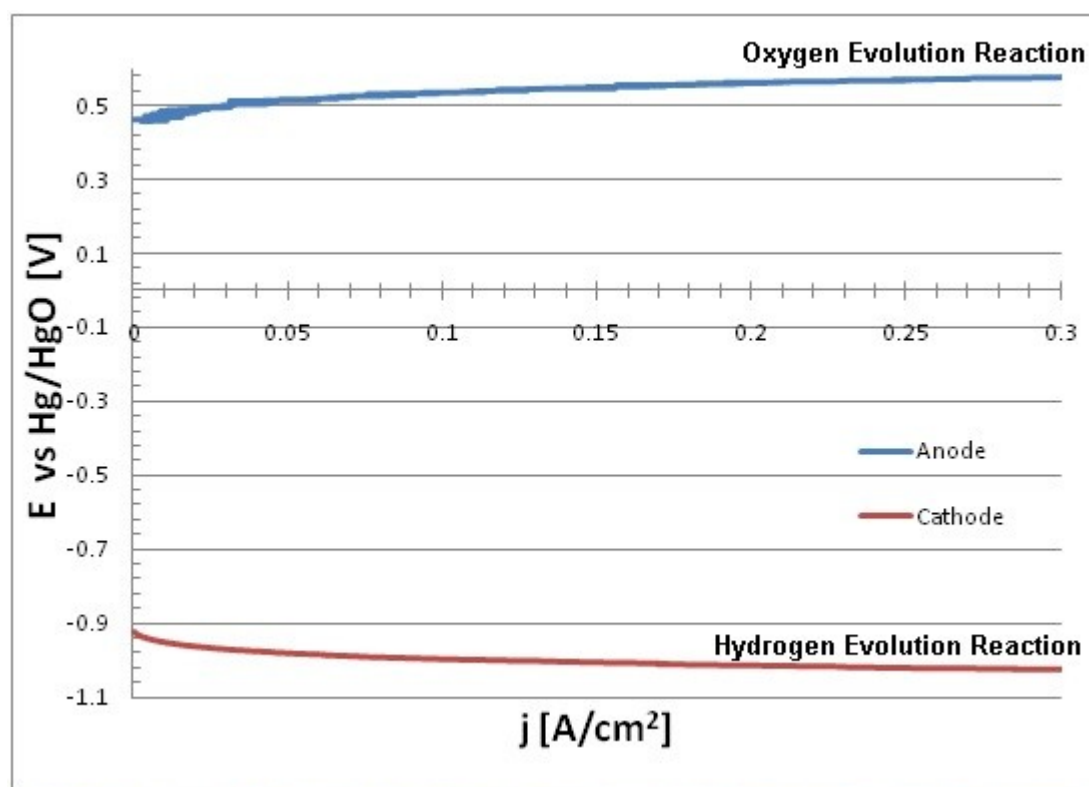


Figure 7-18. Anode and cathode performances measured in 3 electrodes system configuration

The activated electrodes were put inside the single cell electrolyser the performance of the cell was measured (Figure 7-19). As can be seen from the figure, the initial performance of the system was slightly lower than that calculated solely from the difference between cathode and anode voltages. This phenomenon probably could be connected with bubbles formation and their impact on the *IR* compensation method used in the measurements. The *IR* method estimates ohmic drop during by the current interrupt method but at high current densities a lot of gas bubbles are produced, which are dissolving in the electrolyte and causing highly varying resistance values of the electrolyte. The difference between measured and calculated data is smallest at low current densities (~20 mV) and the largest at high current densities (~38 mV) which confirms formed hypothesis about bubbles ohmic drop, which was not compensated by *IR* method. The difference at low current densities might come from the fact that electrodes just after electrochemical activation are still prone to changes in the material structure. For example, hydrides formation normally

occurs on a cathode however, other processes that have not been investigated and lie beyond the scope of this work could still be occurring at the anode.

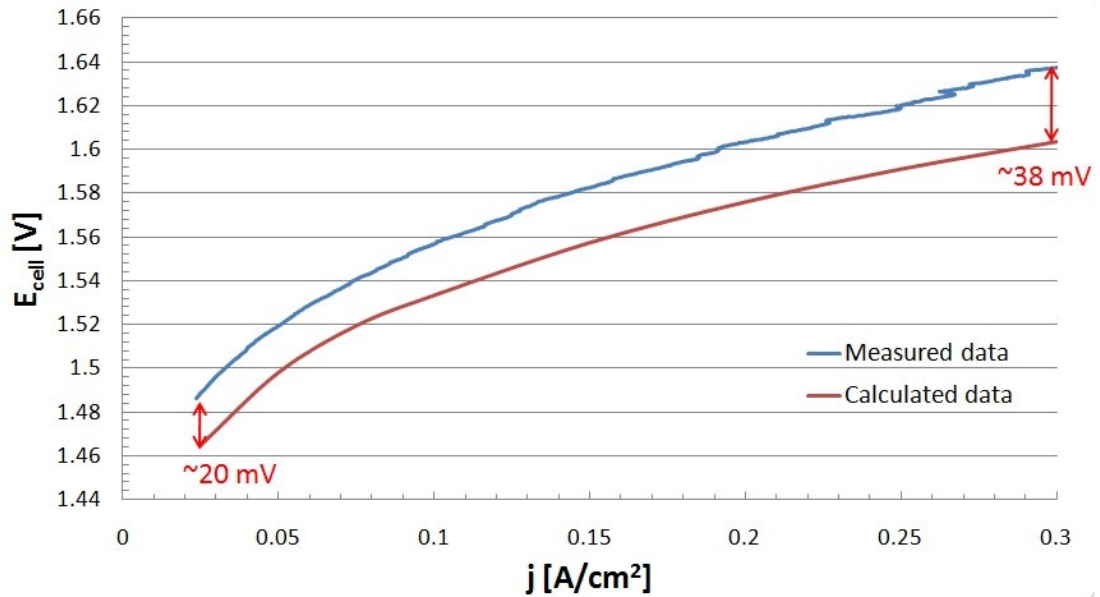
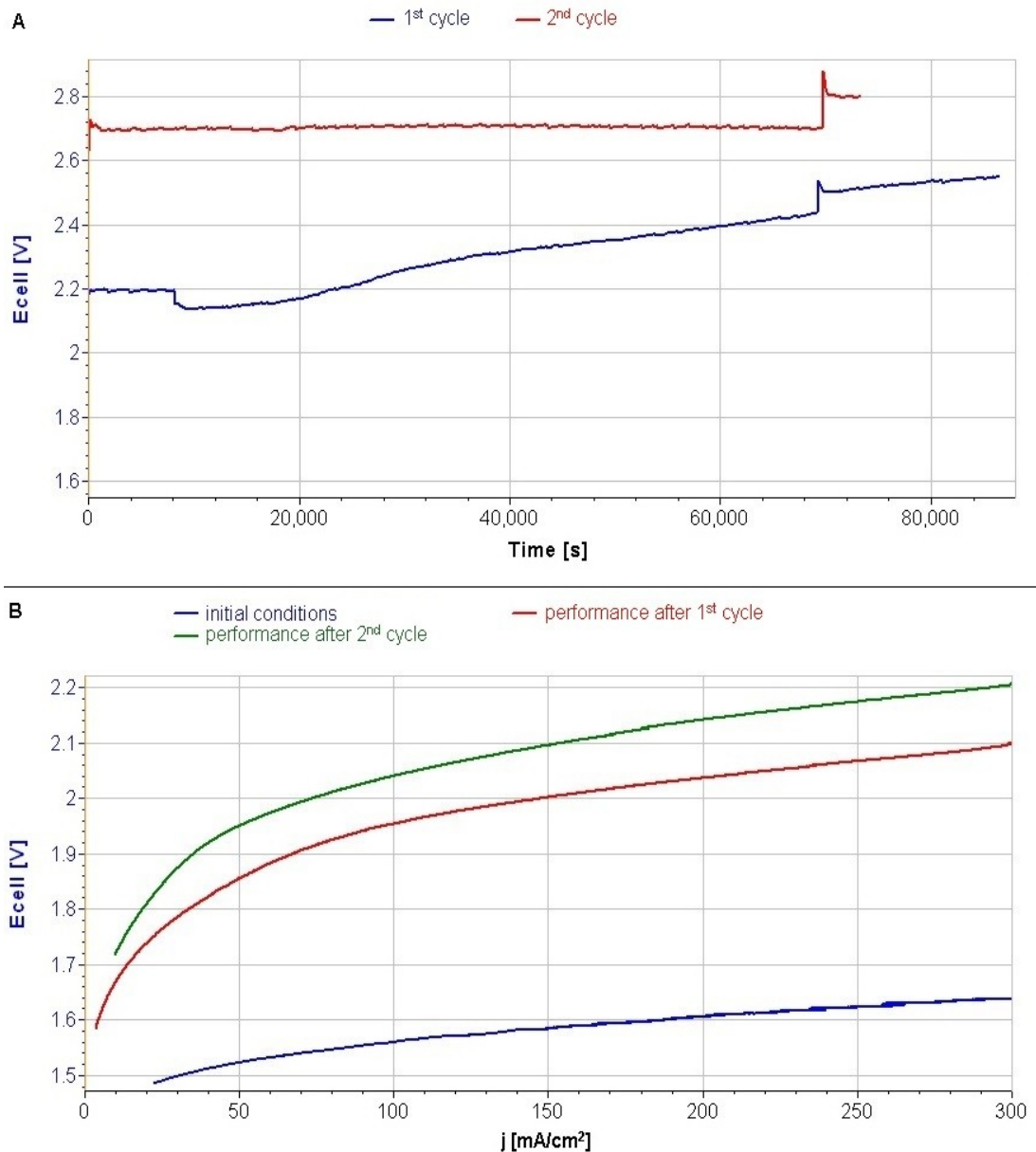


Figure 7-19. Comparison of single cell performances - measured and calculated data – initial conditions

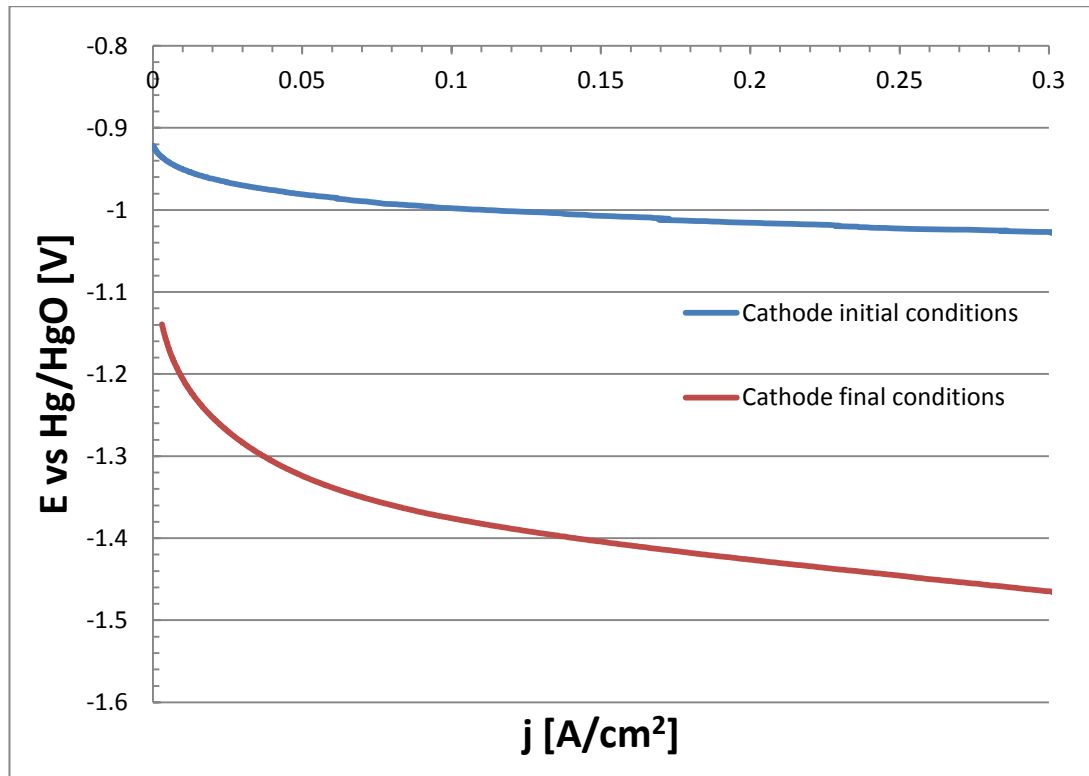
The single cell electrolyser was operated at a constant current density of 200 mA/cm<sup>2</sup> for periods of > 24 hours and 18 hours and the data for these are shown in *Figure 7-20(A)*. During the first 24 hours of operation, the performance of the cell was gradually decreasing. During the 2<sup>nd</sup> cycle however, it seemed to stay pretty much constant. The sudden increase of the voltage towards the end of the second cycle was probably caused by movement of the electrodes, which could have occurred during the replenishment of water into electrolyser. Despite the constant voltage during the 2<sup>nd</sup> cycle, the overall performance of the electrolyser unit still decreased and this can be seen from *Figure 7-20(B)* which compares performances of the electrolyser at the beginning of the experiments and after each of the cycles.



*Figure 7- 20. A - Registered performance change during 1<sup>st</sup> and 2<sup>nd</sup> cycle operation under 200 mA/cm<sup>2</sup> current density, B - Comparison of single cell performances at initial conditions, after 1<sup>st</sup> cycle and after 2<sup>nd</sup> cycle*

In order to see what impact the single cell operation had on the electrolyser performance, the electrodes were dismantled from the electrolyser unit and their characteristics were measured once again using the three electrode system configuration. It can be seen from a *Figure 7-21*, that the cathode performance here

was reduced in a similar fashion as in the experiments conducted previously (*Paragraph 7.3.1*), probably due to hydrides formation effect.



*Figure 7-21. Comparison of cathode initial and final performances*

The cathode though was not the only source for the drop in performance, as the anode performance was also strongly affected, as can be seen from *Figure 7-22*. In this case, the impact was not as large as that of the cathode, but the reasons for the performance losses at this electrode should definitely be investigated further in future work. A final data analysis of the performance was done based on three electrode measurements (*Figure 7-23*) and this was compared to the experimental data obtained from the electrodes before dismounting from the single cell unit. A similar trend was observed, as in case of comparison done during initial tests of the electrolyser (*Figure 7-18*) and the estimated data showed slightly better performance than the experimental one, with the largest difference between the two observed at high current densities, probably due to bubbles impact.

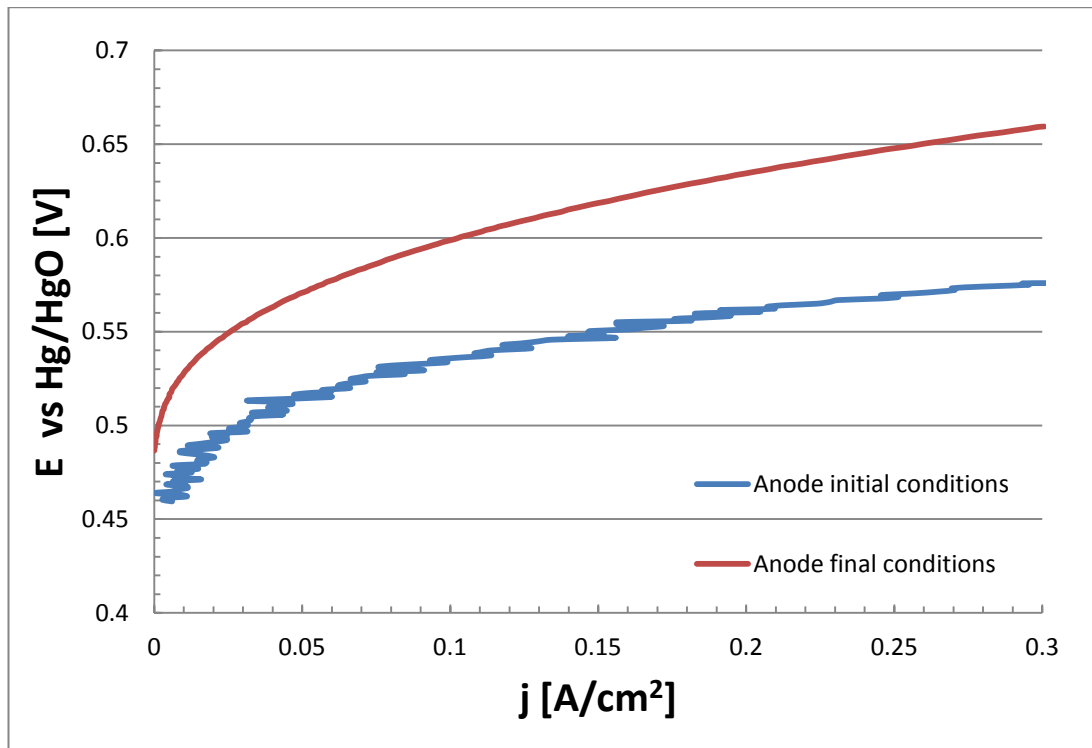


Figure 7-22. Comparison of anode initial and final performances

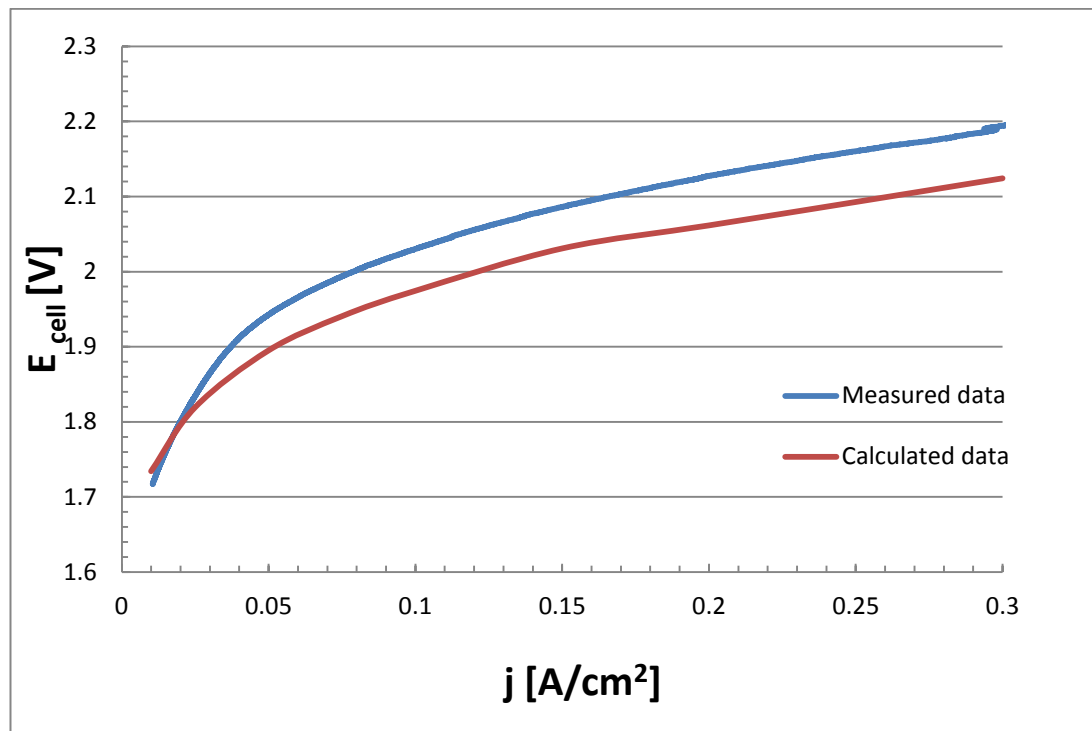


Figure 7-23. Comparison of single cell performances - measured and calculated data – final conditions

## 7.4. Conclusions and summary

The results obtained from this part of the study on the APS Raney nickel electrodes have indicated that the cathodic performance was significantly influenced by the deactivation impact of hydrides formation. Chemical and electrochemical procedures were employed but failed to completely prevent this process from taking place. In the case of *in-situ* electrolyte activation, there was a decrease in the cathodic plateau overpotential, but the overall decrease in the electrode performance was still significant. The different procedures employed involving electrochemical oxidation showed insufficient hydrides removal or caused structural damage to the electrodes surface. There was some success however on using a combination of *in-situ* activation of the electrolyte and the addition of oxides of vanadium and/or molybdenum with electrochemical oxidation techniques as application of those methods decreased the impact of hydrides on the electrodes performance without damaging catalyst structure. The APS Raney nickel electrodes presented good stability for variable load operations with very good initial electrode potential values during the cycling. Before further development of the technology for commercialisation, the deactivation effect needs to be examined further and brought under control. One of the ways of achieving this could be through manufacturing process improvements for example by application of molybdenum coatings. Additional work was done in testing electrodes inside a single cell configuration and these confirmed the findings regarding hydrides impact on cathode performance. Moreover it was found that anode electrode was also partially responsible for overall performance loss in the electrolyser and this should be investigated in future work.

## References:

1. A. Bergen, L. Pitt, A. Rowe, P. Wild, N. Djilali. *Transient electrolyser response in a renewable-regenerative energy system*. International Journal of Hydrogen Energy, Vol. 34, 2009, pp. 64 – 70
2. A. Bergen. *Integration and Dynamics of a Renewable Regenerative Hydrogen Fuel Cell System*. PhD studies dissertation. University of Victoria, Canada, 2008
3. Renewable Hydrogen by Electrolysis: Opportunities and Applications. NSERC Atlantic Canada Wind to Hydrogen Workshop Moncton, 2010, [https://secure.i-toolkit.com/www\\_chfca\\_ca/files/nserc\\_archambault.pdf](https://secure.i-toolkit.com/www_chfca_ca/files/nserc_archambault.pdf), accessed 24<sup>th</sup> October 2013
4. <http://www.prnewswire.com/news-releases/hydrogenics-corporation-succeeds-in-bid-for-stuart-energy-systems-corporation-66227987.html>, accessed 24<sup>th</sup> October 2013
5. K. Zeng, D. Zhang. *Recent progress in alkaline water electrolysis for hydrogen production and applications*. Progress in Energy and Combustion Science, Vol. 36, 2010, pp. 307–326
6. H. Wendt. *Electrochemical Hydrogen Technologies. Electrochemical Production and Combustion of Hydrogen*. Elsevier, 1990
7. B. Baranowski. *Electrochemical formation of nickel hydride in alkaline solutions*. Journal of Electroanalytical Chemistry, Vol. 472, 1999, pp. 182–184



8. D. M. Soares, O. Teschke, I. Torriani. *Hydride effect on the kinetics of the hydrogen evolution reaction on nickel cathodes in alkaline media*. Journal of Electrochemical Society, Vol. 139, 1992, pp. 98-105
9. H. E. G. Rommal, P. J. Morgan. *The role of absorbed hydrogen on the voltage-time behaviour of nickel cathodes in hydrogen evolution*. J of Electrochemical Society: Electrochemical Science and Technology, 1988, pp. 343-346
10. A. E. Mauer, D. W. Kirk, S. J. Thorpe. *The role of iron in the prevention of nickel electrode deactivation in alkaline electrolysis*. Electrochimica Acta, Vol. 52, 2007, pp. 3505–3509
11. D. S. Hall, C. Bock, B. R. MacDougall. *The electrochemistry of metallic nickel: oxides hydroxides, hydrides and alkaline hydrogen evolution*. Journal of The Electrochemical Society, Vol. 160, 2013, pp. 235-243
12. R. M. Abouatallah , D. W. Kirk, J. W. Graydon. *Long-term electrolytic hydrogen permeation in nickel and the effect of vanadium species addition*. Electrochimica Act, Vol. 47, 2002, pp. 2483-2494
13. R. M. Abouatallah, D. W. Kirk , S. J. Thorpe , J. W. Graydon. *Reactivation of nickel cathodes by dissolved vanadium species during hydrogen evolution in alkaline media*. Electrochimica Acta, Vol. 47, 2001, pp. 613–621
14. J.Y. Huot, L. Brossard. *In situ activation by sodium molybdate on various metallic substrates, substrates during alkaline water electrolysis*. International Journal of Hydrogen Energy, Vol. 14, No. 4, 1989, pp. 229-232
15. J. Divisek, B. Mergel, H. Schmitz. *Advanced water electrolysis and catalyst stability under discontinuous operation*. International Journal of Hydrogen Energy, Vol. 15, No. 2, 1990, pp. 105-114

16. J. Divisek, B. Steffen, H. Schmitz. *Theoretical analysis and evaluation of the operating data of a bipolar water electrolyser*. International Journal of Hydrogen Energy, Vol. 19, No. 7, 1994, pp. 579-586
17. G. Schiller, V. Borck. *Vacuum plasma sprayed electrodes for advanced alkaline water electrolysis*. International journal of hydrogen energy, Vol. 17, No. 4, 1992, pp. 261-273
18. G. Schiller, R. Henne, P. Mohr, V. Peineckie. *High performance electrodes for an advanced intermittently operated 10-kW alkaline water electrolyzer*. International journal of hydrogen energy, Vol. 23, No. 9, 1998, pp. 761-765
19. M. L. Wayman, G. C. Weatherly, in: P. Nash (Ed.), *Phase Diagrams of Binary Nickel Alloys*, ASM International, Materials Park, OH, 1991, p. 155
20. S. Rausch, H. Wendt. *Morphology and utilization of smooth hydrogen-evolving raney nickel cathode coatings and porous sintered-nickel cathodes*. Journal of The Electrochemical Society, Vol. 143, 1996, pp. 2852-2862
21. G. S. Tasic, S. P. Maslovara, D. L. Zugic, A. D. Maksic, M. P. Marceta Kaninski. *Characterization of the Ni-Mo catalyst formed in situ during hydrogen generation from alkaline water electrolysis*. International Journal of Hydrogen Energy, Vol. 36, 2011, pp. 11588-11595
22. M. P. Marceta Kaninski, D. P. Saponjic, V. M. Nikolic, D. L. Zugic, G. S. Tasic. *Energy consumption and stability of the Ni-Mo electrodes for the alkaline hydrogen production at industrial conditions*. International Journal of Hydrogen Energy, Vol. 36, 2011, pp. 8864-8868

23. J. Y. Huot, L. Brossard. *Time dependence of the hydrogen discharge at 70°C on nickel cathodes*. International Journal of Hydrogen Energy, Vol. 12, No. 12, 1987, pp. 821-830
  
24. L. Brossard, J. Y. Huot. *In situ activation of cathodes during alkaline water electrolysis by dissolved iron and molybdenum species*. Journal of Applied Electrochemistry, Vol. 21, 1991, pp. 508-515
  
25. W. Hu. *Electrocatalytic properties of new electrocatalysts for hydrogen evolution in alkaline water electrolysis*. International Journal of Hydrogen Energy, Vol. 25, 2000, pp. 111-118

## **8. Design of the prototype of electrochemical measurement device**

As part of the work, a prototype electrochemical control and measuring device was designed and built. Its main functionality was to operate 3 electrochemical cells simultaneously at variable load and to measure the voltage, current and temperature from each cell. Additionally, the device was equipped with a high speed digital camera to capture the images of gas bubbles on the electrode surface and to investigate the impact of bubbles on cell performance.

### **8.1. Hardware design**

The electrochemical power units were based on the OPA-549 high-voltage, high-current operational amplifiers manufactured by Texas Instruments. Each unit had the possibility of delivering continuous currents of up to 8 A (10 A peak current) with an input voltage ranging from -0.5 to 0.5 V [2]. By applying the resistors of 1 and 20 k $\Omega$ , an amplifier gain was set to 21 and that resulted in a maximum output voltage of 10.5 V, which is typically more than enough for single cell testing. The maximum temperature of an amplifier operation was 125°C [2]. Each amplifier was cooled by the heat-sink with thermal resistance of 1 °C/W [1], which allowed delivering a theoretical maximum power of 100 W (assuming normal temperature environmental conditions of 25°C).

The electrochemical device was equipped with voltage, current and temperature sensors. For voltage measuring purposes, National Instruments DAQ NI-6218 was used, with an analog input voltage measuring range of +/- 10 V with 2.7 mV precision [3]. For the purpose of registering the electrical current, LEM current transducers HX-10P/SP2 were used with nominal current of 10 A (30 A measuring range for short time events) and 1% of nominal current accuracy [4]. K-type thermocouples were used to measure the temperature of the cells. The

thermocouples were coated, so as to chemically resist the highly caustic alkaline environment inside the cell. Thermocouple amplifiers (AD595CQ) were used to compensate for the cold junction effect of the thermocouple and also to amplify the voltage. A DC power supply was used to power the sensors and amplifiers.

Acquisition and control was provided by National Instruments NI-6218 data acquisition device (DAQ). Its 2 analog outputs were used to control the amplifiers power output and its analog inputs measured data from the sensors [5]. The DAQ device was connected to the notebook through USB port and controlled by Labview user interface.

The electrochemical measuring system contained three sub-systems. Each of these consisted of an amplifier with voltage, temperature and current sensors. All of the parts were built by soldering electronic components into PCB boards that were subsequently put inside two separated boxes (one for 3 amplifiers *Figure 8-1* and one for 3 sets of sensors *Figure 8-2*). The NI-6218 DAQ device was able to control all three sets of the amplifiers and sensors however, due to having only 2 analog outputs two amplifiers had to be controlled by the same analog output. This obviously caused the limitation where the same type of voltage output had to be produced by two units simultaneously.

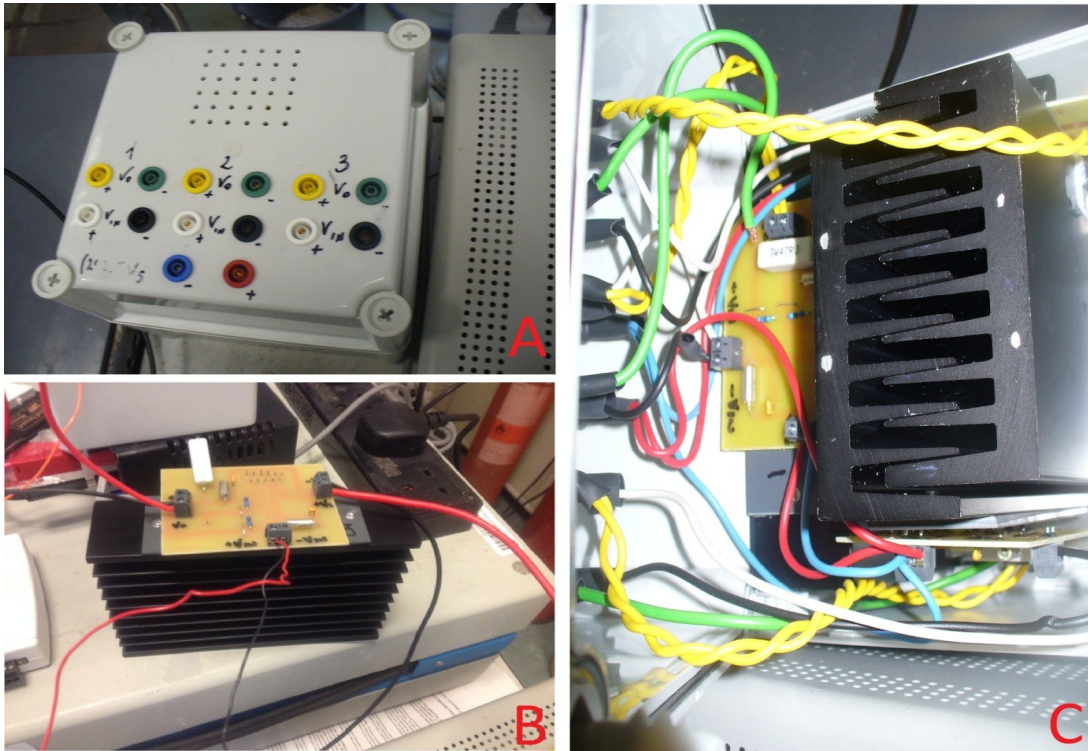


Figure 8-1. Electronic amplifiers box, A – View outside the box, B – view of single amplifier during testing (PCB board + heat sink), C – view inside the box of with the amplifiers

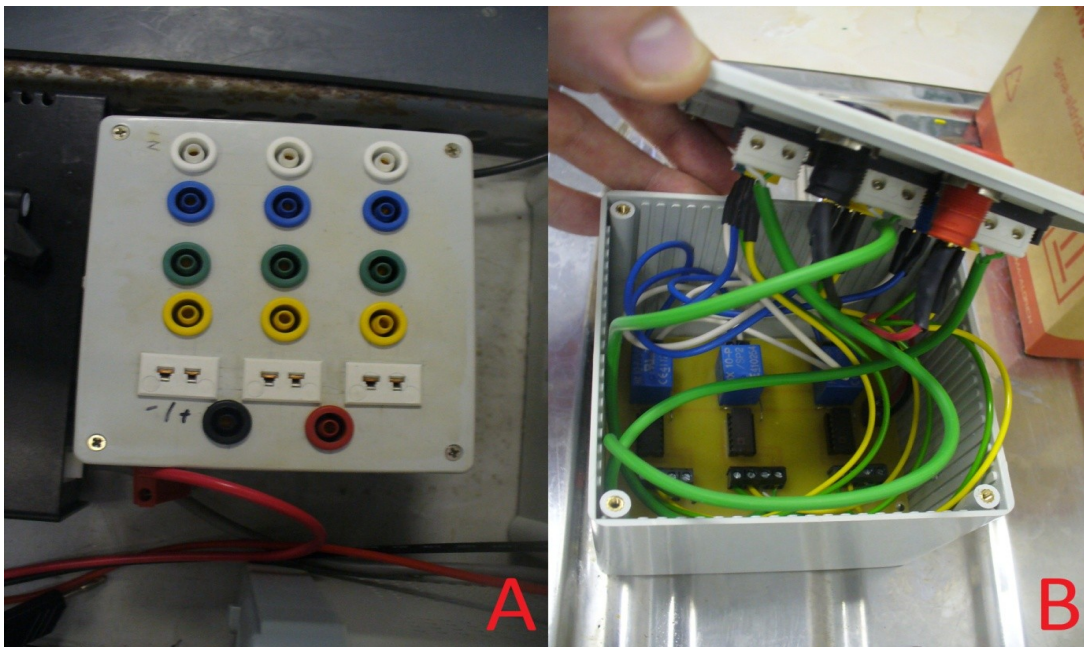
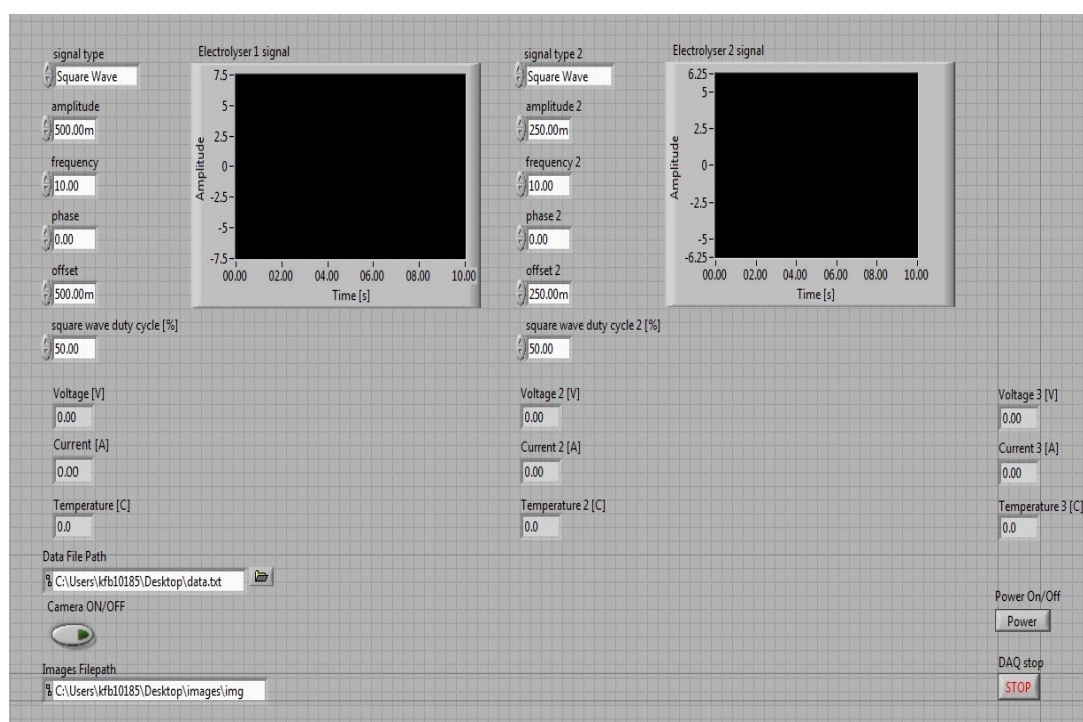


Figure 8-2. Current and temperature sensors box A – view outside the box, B – view inside the box

In *Figure 8-3* it is presented designed Labview user interface for controlling the electrochemical system functionality. The software allowed the generation of square, sine, triangle and saw shape signals. For each type of the signal type, parameters of amplitude, frequency phase, offset could have been set and for the square wave additionally an option of duty cycle regulation was enabled. The collected data from each cell was visualised by interface indicators in real-time and saved in a text file in a computer hard disk. Additionally there existed a possibility of camera application for bubbles effects observation and to save images in graphical format files (for example jpg).



*Figure 8-3. Labview user interface*

Overall system functionality is summarised by a *Figure 8-4*. The system was controlled by a PC computer with Labview user interface, which was connected to DAQ device through USB port. DAQ device was responsible for controlling load of amplifiers for electrolyser units and for collecting the data of voltage, current and temperature from applied sensors. DC power supply was used to power the amplifiers. The system was supplemented by the camera from which images



acquired were saved in a computer disk. During the performed experiments a few different cameras were tested.

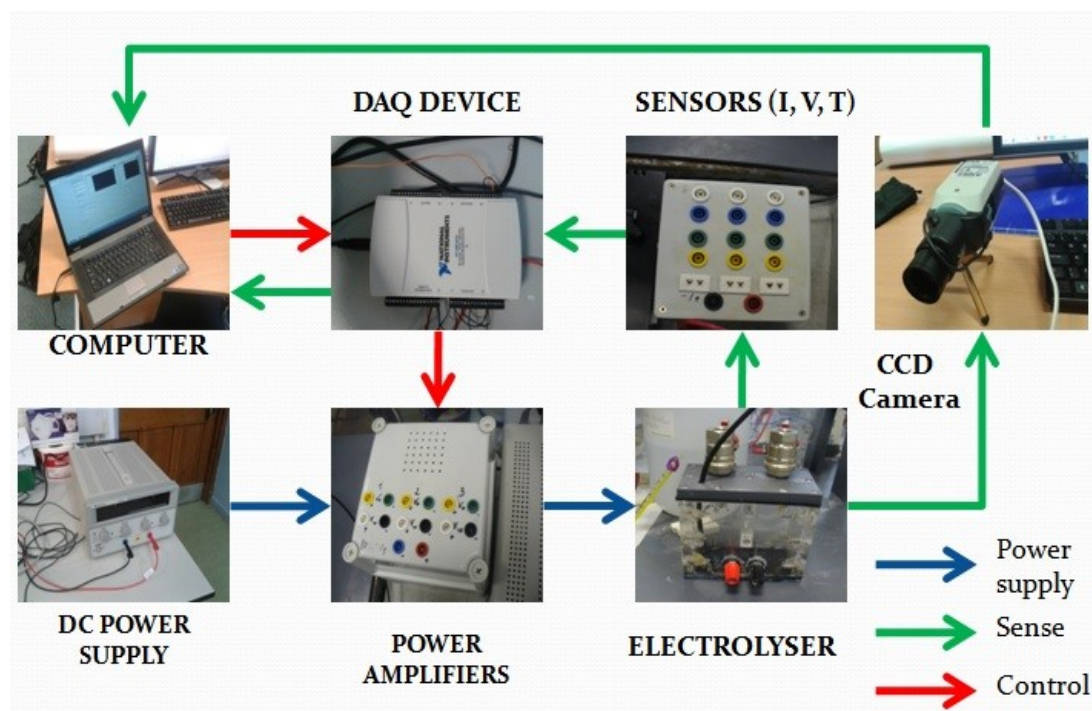


Figure 8-4. Full system overview

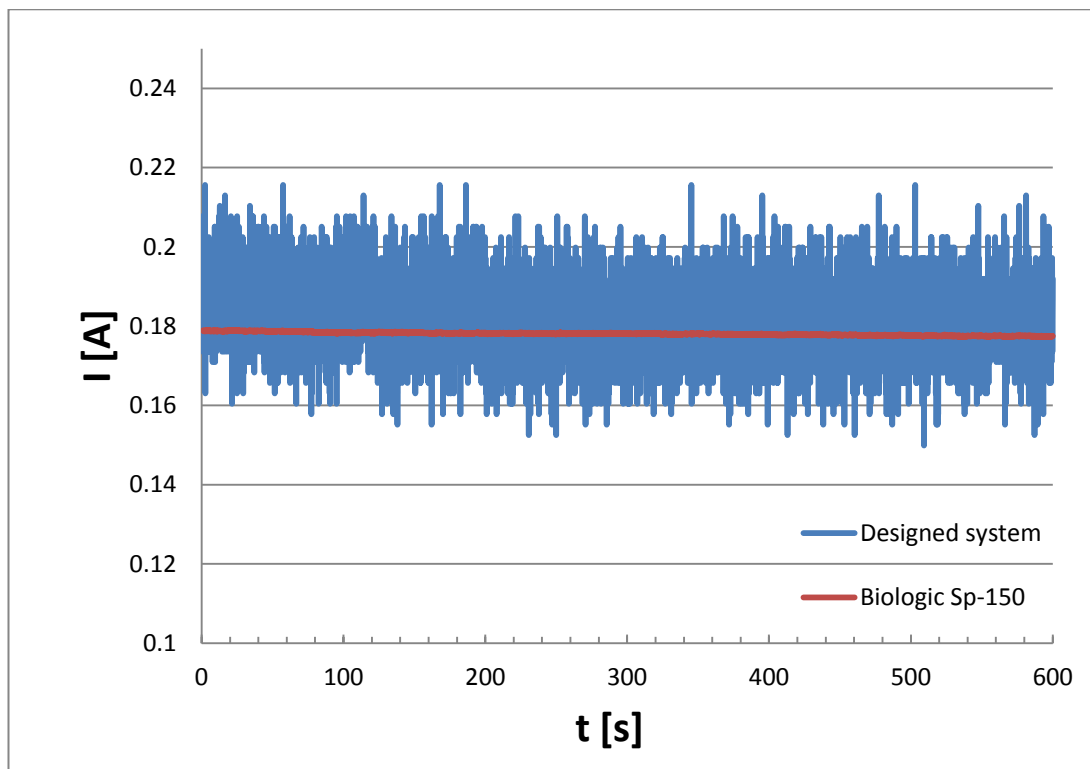
## 8.2. Electrochemical experimental testing

The developed prototype of the electrochemical measuring device was tested during a series of experiments. All the outcomes were compared with the results obtained by Biologic Sp-150 device, to confirm their validity. During experiments a single cell configuration, with two 100  $\mu\text{m}$  APS electrodes with surface area of 1  $\text{cm}^2$  surface each were used. As an electrolyser it was used glass, two compartment device (detailed description can be found in the *Chapter 4* of the thesis), which was operated at a temperature of 25°C. A Celgard 3501 membrane was applied and the distance between the electrodes was set to 15 cm. The low performance of the tested samples (in comparison with the values from *Table 6-1*) was due to: lack of IR compensation,



large distance between the electrodes and the fact that the electrodes were not new samples, but had been tested during previous experiments.

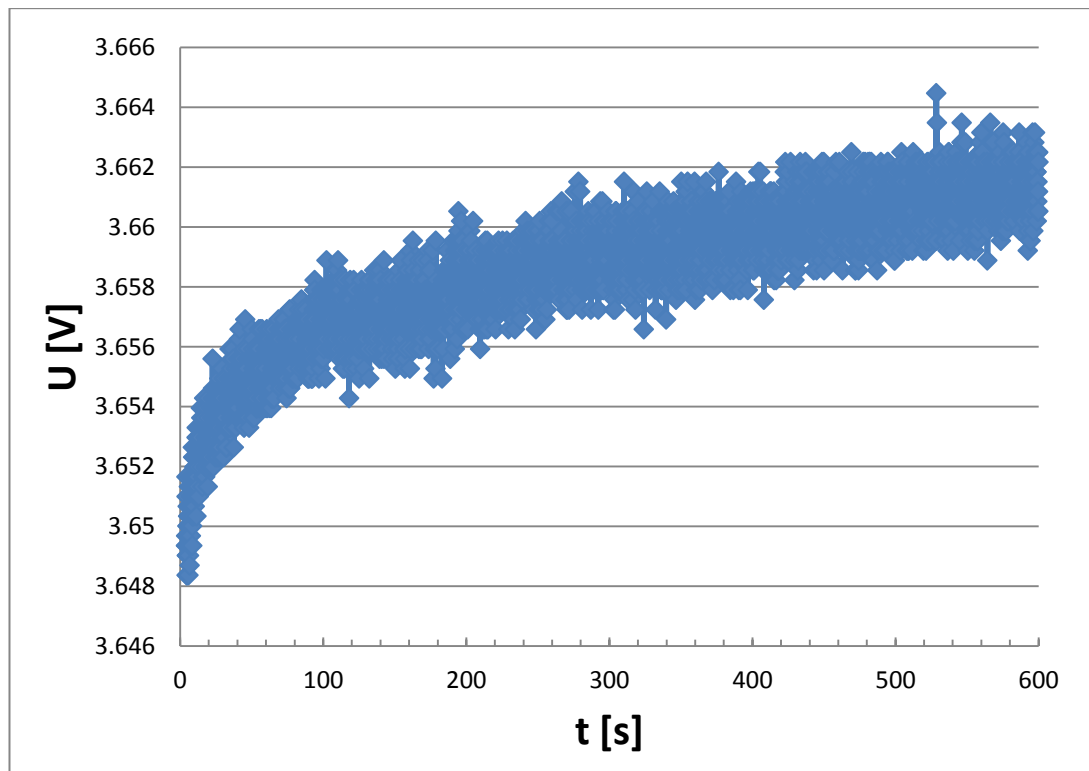
The first experiment tested the potentiostatic mode of operation of the electrochemical device at a potential of 3.65 V for 10 minutes. As can be seen from *Figure 8-5*, the current obtained by the built prototype gave the same value as that obtained by Biologic device, but with considerably more noise. The current fluctuations here did not exceed 0.04 A, which in fact corresponds to the precision value of the sensor:  $\pm 0.1$  A.



*Figure 8-5. Current fluctuations overview under constant load of 3.65 V*

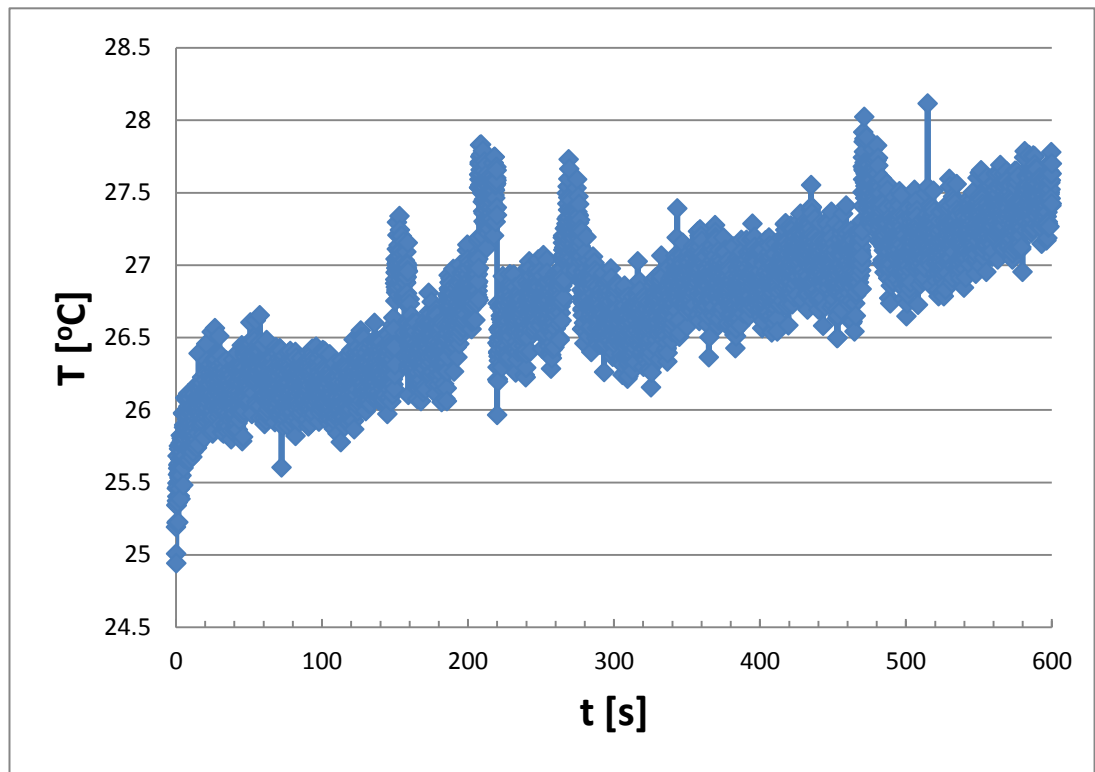
In the *Figure 8-6* it is seen how the initially set voltage value of 3.65 V increased with time. This effect was probably due to thermal drift of the amplifier, which caused output voltage change due to temperature rise. This hypothesis was confirmed by visible asymptotic trend and event time constant of the minutes, which are typical for temperature dynamic events, but also by the fact that voltage value stabilised after a time period when amplifier reached its final operational temperature value. An

OPA549 amplifier manual states that typical output offset voltage is estimated to be around the value of  $420 \mu\text{V}/^\circ\text{C}$  for the gain of 21 [2]. The observed voltage offset did not exceed 15 mV, which corresponds to the temperature rise by  $36^\circ\text{C}$ . Moreover in the *Figure 8-6* it might be seen the voltage fluctuations of around  $\pm 2.5 \text{ mV}$  probably occurred due to limited precision of NI-6218 DAQ analog inputs (the estimated accuracy  $\pm 2.7 \text{ mV}$  [3]).



*Figure 8-6. Voltage time effect overview for theoretically set value of 3.65 V*

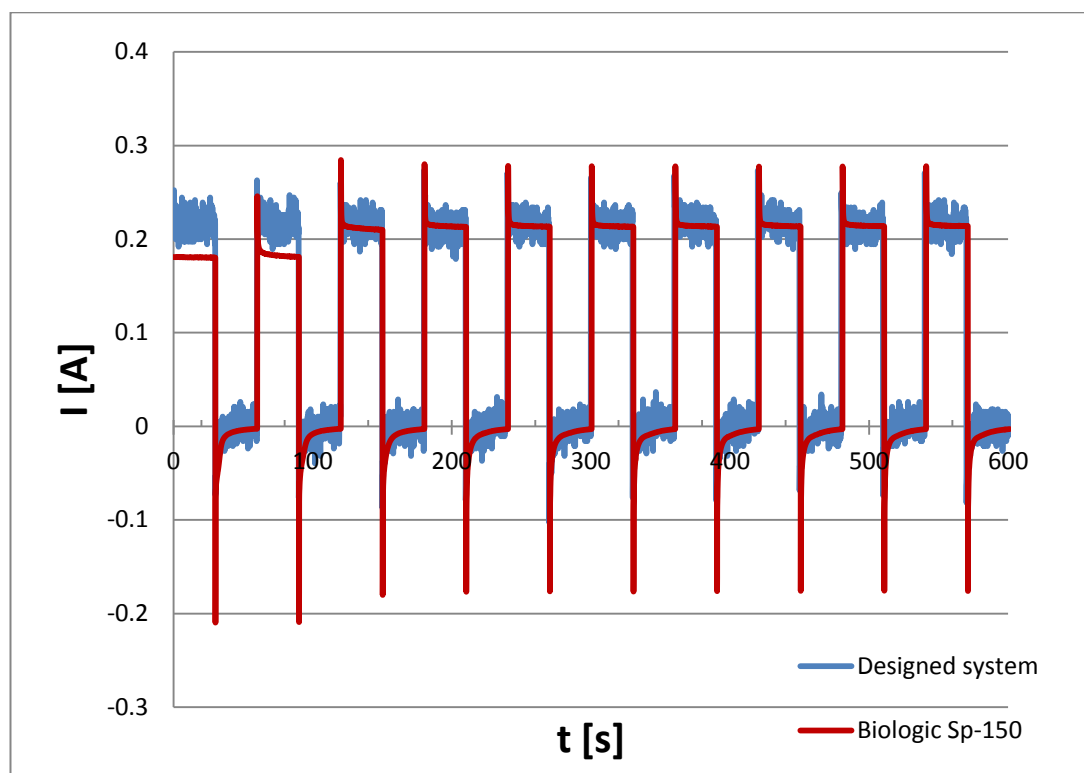
The final observations, done during constant load experiment were in the temperature changes (*Figure 8-7*) that occurred inside the electrolyte. Rise of the temperature during experiment could come from electrical current flow through the electrolyte. As it might be seen temperature fluctuations observed were about  $\pm 0.4^\circ\text{C}$ . For this phenomenon partially was responsible limited voltage input accuracy however, it should be also noted that the used thermocouple sensor itself, could have also caused an error. The sudden temperature changes are considered to be caused by non-uniform temperature distribution inside the electrolyte and sporadic movements of the thermocouple.



*Figure 8-7. Temperature time effect overview under constant load of 3.65 V*

The aim of the next experiment was testing the system during dynamic events. The square wave voltage was applied and switched between the values of 3.65 and 0.7 V every 30 seconds. The total duration of the experiment was set for 10 minutes. As can be seen in a *Figure 8-8* every step-change of the voltage caused induction of a current coming from discharge of the double layer capacitance. It was seen that current registered by built electrochemical device corresponded to the values obtained by the Biologic SP-150 interface. However, its precision was not surprisingly much lower. It can also be seen that initial value of the current registered by the Biologic device was significantly lower during first 2 cycles. This effect was caused by the fact that the surface of the cathode was covered by hydrides in the beginning of the experiments. When the potential was switched towards the value of 0.7 V, the hydrides were oxidised and performance increased. The measurements by

the designed system were done just after experiments with Biologic Sp-150 device, so this effect was not observed then.



*Figure 8-8. Variable load operation comparison (3.65 – 0.7 V, 50% square wave, 1 minute frequency)*

Summarising it can be stated that the electrochemical measuring device, developed within the project demonstrated assumed functionality during performed experiments, but its precision was much lower than in case of commercially available units. *Table 8-1* presents estimated basic parameters specifications. The total price of the described prototype was ~£1,500, where major part of £1,000 was the cost of NI-6218 DAQ. It should be noted that the price of commercially available devices with similar functionality normally exceeds £20,000. The constructed unit obviously needs improvements regarding the precision and probably also reliability which have not been tested over a long period of time. Additionally functionality of common electrochemical techniques such as: Cyclic Voltammetry, Electrochemical Impedance Spectroscopy should be added. On the other hand, the built prototype definitely shows the potential to substantially decrease the costs. The further

development of similar concept might be a good investment for companies where a lot of measuring devices are needed or/and as a commercial market business opportunity.

General parameters	
Number of cells	3
Price	£ 1,500
Power Supply parameters	
Voltage range	0 – 10.5 V
Voltage accuracy	35 $\mu$ V (thermal drift effect not included)
Current range	0 – 10 V
Maximum power	100 W
Voltage sensors	
Range	+/- 10 V
Precision	2.7 mV
Current sensors	
Nominal current	10 A
Range	+/- 30 A
Precision	0.1 A
Temperature sensors	
Range [ $^{\circ}$ C]	From -75 to 250 $^{\circ}$ C
Precision	+/- 1 $^{\circ}$ C

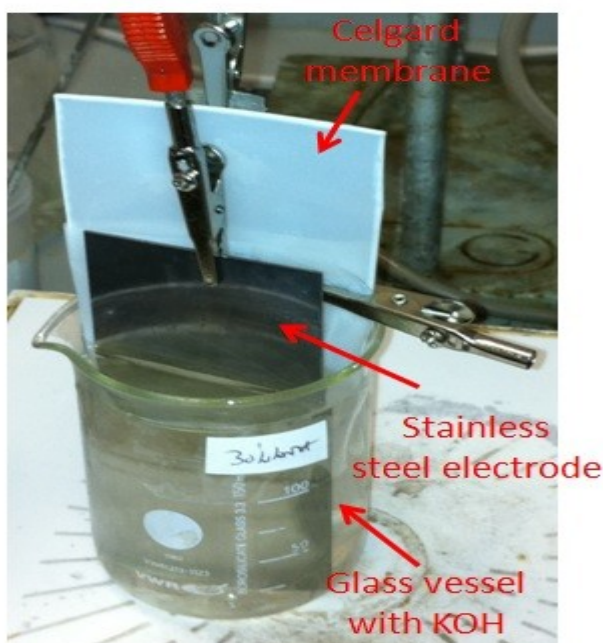
*Table 8-1. Estimated basic parameters of built DAQ device*

### 8.3. Bubbles impact investigation

The experiments describing the bubbles investigations were performed during the early stages of development of the system that has been presented previously in this chapter. The main change was the application of the Texas Instruments OPA-548 operational amplifier (gain 20 set up and maximum current rating of 3 A [6]) and the current sensor HY5P, LEM (5 A maximum current, precision +/-0.05A [7]). All the

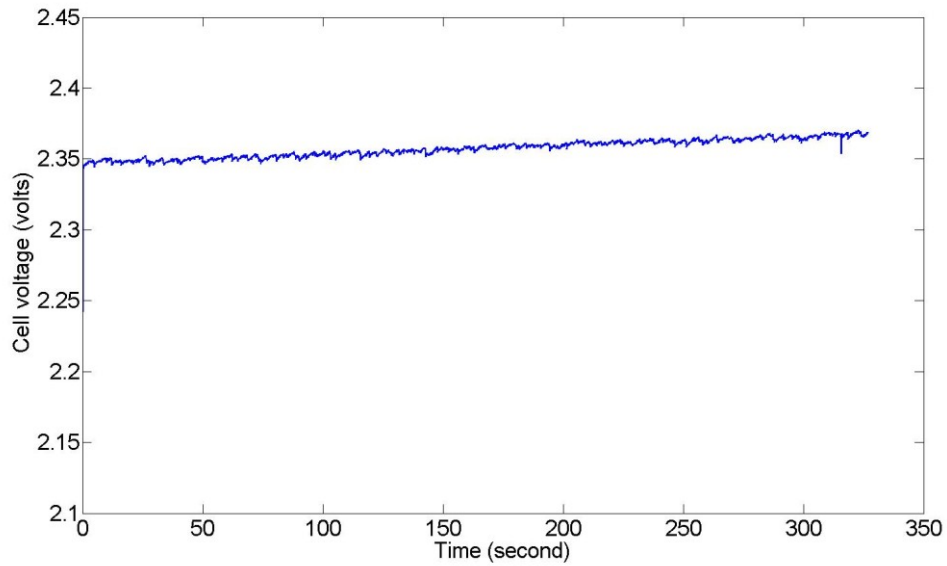
remains of the configuration stayed the same as that of the prototype described in the previous paragraphs.

During the experiment open cell alkaline electrolyser in glass single vessel was used (*Figure 8-9*). The separation gap between two electrodes was set to 2 mm. Stainless steel (grade 316L) mesh was used as a cathode. The active area of the mesh electrode was 3.88 cm<sup>2</sup>. The anode was made of Stainless Steel 316L with active area of 15 cm<sup>2</sup>. A Celgard 5550 membrane was used to separate the oxygen and hydrogen part in the electrolysis cell, and to prevent the gasses from being mixed inside the solution. The images of hydrogen bubbles created on the cathode side during electrolysis process were acquired by Bosch's company Dinion Color Camera with a LTC 3364/50 lens. To transform images from the PAL system of the camera to the digital form a USB Pinnacle's Dazzle DVC90 video card was used. This allowed images digitisation with 25 frames per second rate and resolution of 720 × 576 pixels. The camera was put outside the glass vessel with electrolyser system and its lens was focused into the outer side of the cathode.

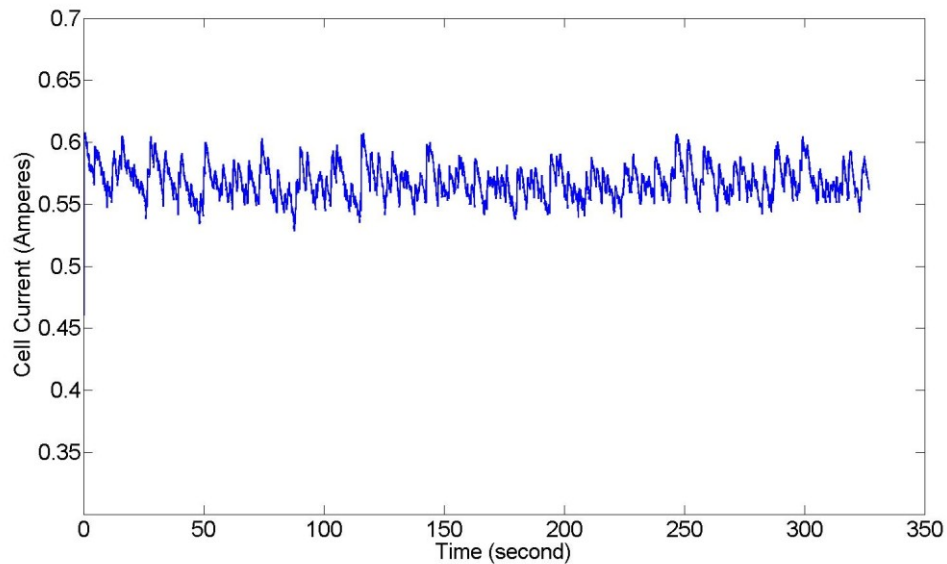


*Figure 8-9. Open cell photo (working electrode was placed on the other side of the membrane)*

For the described configuration a constant voltage of 2.35 V was delivered to the cell for the electrolysis experiment. It can be seen from *Figure 8-10 and Figure 8-11* that the voltage fluctuations during the experiment were minimal while the current fluctuated significantly. The voltage also increased during experiment by  $\sim 20$  mV due to thermal drift effect of the amplifier.

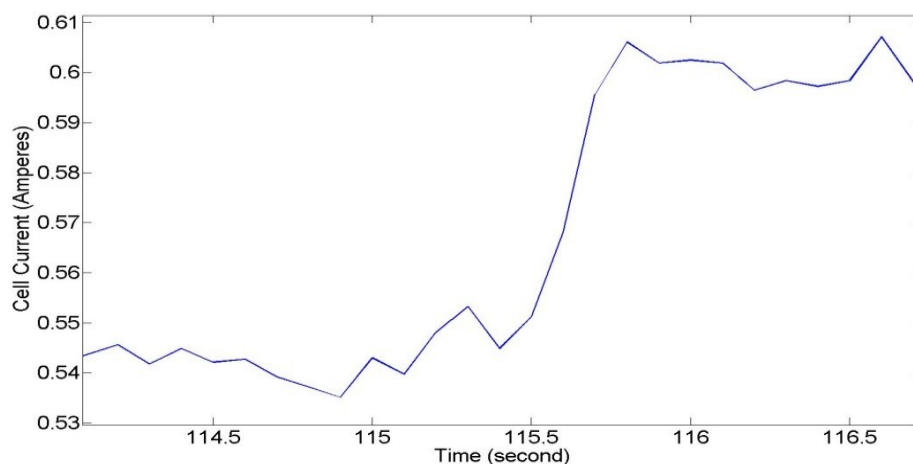


*Figure 8-10. Applied voltage for bubble effect analysis*



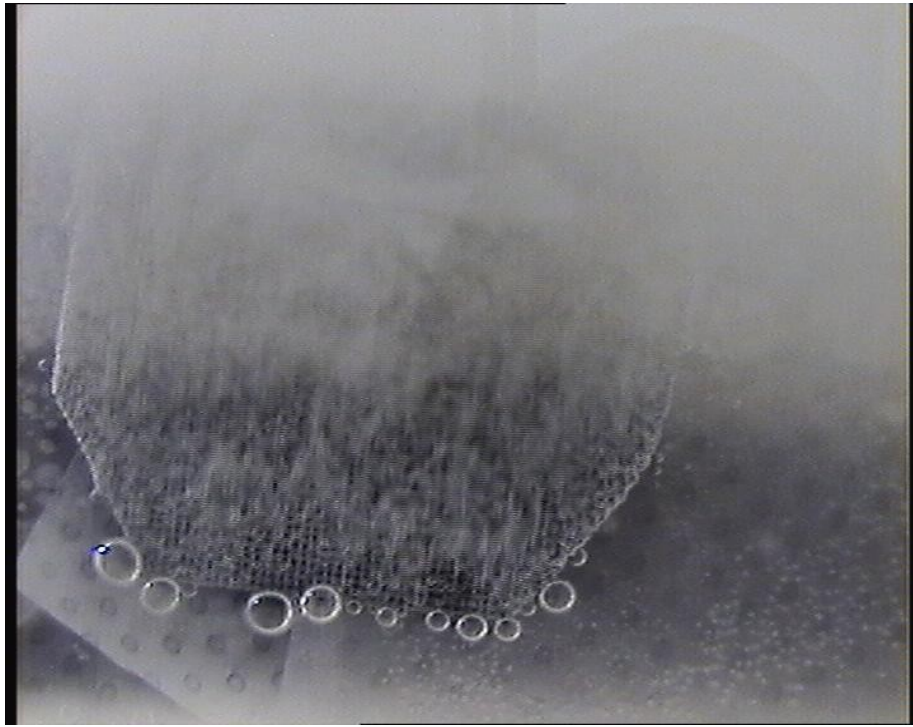
*Figure 8-11. Current with fluctuations caused by bubbles*

During performing the experiment, it was clearly seen that bubbles were accumulating gradually on the electrode surface and once in a while a group of accumulated bubbles was suddenly released from the surface and rose through the electrolyte. Subsequently new bubbles were appearing again on the bubble free electrode surface and released after some time, defining a specific kind of cycle. For analysing the bubbles behaviour, a comparison of the acquired images with the measurements of current was made. This resulted in the observation that all the events when there was a release of bubbles from the electrode, corresponded to the major current fluctuations. Example of this behaviour is illustrated by zoomed figure of current and images of the electrode just before and just after current increase (*Figure 8-12, Figure 8-13, Figure 8-14*) between 115 and 116 second of the measurements.

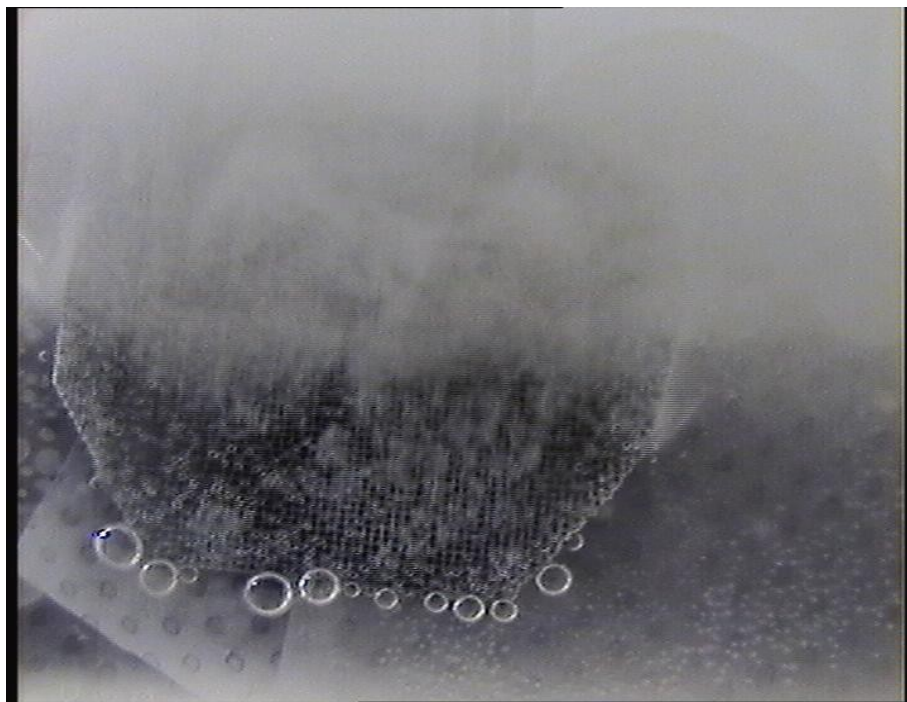


*Figure 8-12. Current fluctuation zoom*





*Figure 8-13. Electrode surface just before bubbles release 115.45 s (mainly all the bottom part is covered with the bubbles)*



*Figure 8-14. Electrode surface just after bubbles release 115.73 s (bottom black region of the electrode shows the area from which the bubbles release occurred)*

The large bubbles visible on the photographs were adhering to the bottom of the electrode. They were very stable and growing throughout the experiment however, any effect of their presence on the system performance was not recognised. Presented images are only examples and similar observations were made in all the moments where sudden increase of current occurred. It is worth noting is that a major release of bubbles never appeared without corresponding increase in current. Also, the test did not allow observations of all the electrode's surface (they were limited only to the bottom part) due to the fact that a lot of bubbles produced during electrolysis process were present in the upper part of electrolyte, covering the electrode and making impossible such an observation using camera.

The results obtained were enough to form an initial hypothesis, viz., that gas bubbles might be the cause of the power fluctuations during the electrolysis process. The physical explanation of this phenomenon might be connected with the fact, that bubbles reduce the active area of the electrode while they are adhered to it [8, 9]. In such a case, the release of the bubbles should cause an instantaneous gain in the active area of the electrode which obviously causes an increase of the current. The described effect was only visible with 2 mm distance between electrodes in system configuration, whereas during the experiments with distance of 1.5 cm between electrodes and the same load, it was not observed. The explanation of this phenomenon might come from the fact that increasing distance between the electrodes causes ohmic losses to rise. Even if bubbles are released in a similar way their impact is not as noticeable on overall system performance as in case of small distance between the electrodes where ohmic losses are minimised. Further experiments clearly need to be done to examine this effect, including bubbles observation with different load, electrode distance, surface area of the electrode and materials.

## **8.4. Conclusions**

This chapter aim was to describe building and testing of a prototype of electrochemical measurement device for the electrodes samples investigation. The experiments performed, confirmed that test results were convergent to the ones obtained by Biologic Sp-150 commercial interface. The built prototype main disadvantage is much lower measurement precision, but on the other hand its price is also much more competitive. Due to that, it is recommended to use such device type for the research projects with limited funding, when large amount of samples need to be analysed. The additional advantage of the product is also application of the digital camera, which enables the functionality of bubbles impact observation. During the performed experimental work the bubbles impact was analysed over few series of experiments and leaded to the identification of the current fluctuations effect.

## References:

1. <http://uk.rs-online.com/web/p/heatsinks/1694252/>, accessed 14<sup>th</sup> September 2014
2. <http://www.ti.com/litv/pdf/sbos093e>, accessed 14<sup>th</sup> September 2014
3. <http://www.ni.com/pdf/manuals/371931f.pdf>, accessed 14<sup>th</sup> November 2013
4. [http://www.lem.com/docs/products/hx%203\\_50-p\\_sp2\\_e%20v07.pdf](http://www.lem.com/docs/products/hx%203_50-p_sp2_e%20v07.pdf), accessed 14<sup>th</sup> September 2013
5. <http://www.ni.com/pdf/manuals/371931f.pdf>, accessed 14<sup>th</sup> September 2014
6. <http://docs-europe.electrocomponents.com/webdocs/0c5d/0900766b80c5dcc2.pdf>, accessed 14<sup>th</sup> September 2014
7. [http://www.lem.com/docs/products/hy\\_sp1\\_e.pdf](http://www.lem.com/docs/products/hy_sp1_e.pdf), accessed 14<sup>th</sup> September 2014
8. K. Zeng, D. Zhang. *Recent progress in alkaline water electrolysis for hydrogen production and applications*. Progress in Energy and Combustion Science, Vol. 36, 2010, pp. 307–326
9. H. Wendt. *Electrochemical Hydrogen Technologies. Electrochemical Production and Combustion of Hydrogen*. Elsevier, 1990

## **9. Feasibility study of wind to hydrogen system for Arctic remote locations – Grimsey island case study**

The aim of this chapter is to provide economical analysis of wind turbine system with hydrogen energy storage application to support diesel electricity generators on the example of Grimsey island.

### **9.1. Introduction**

Electrical power generation for island and remote communities in the Arctic often relies on diesel generators powered by fuel transported over large distances. Nowadays wind energy can be cost competitive with the fossil fuel based electricity generation. The wind energy is broadly considered to be attractive to remote communities and a number of demonstration projects exist around the globe [1]. Hybrid wind-diesel systems can significantly reduce fuel consumption, minimise costs and decrease emissions associated with electricity generation. On the other hand, increasing the energy fraction supplied by wind turbines requires an energy storage mechanism to accumulate any surplus electricity generated during high wind periods and to supply this stored electricity during low wind periods, when there is insufficient wind generation. One of the possibilities which could be suitable for the island of Grimsey in the Arctic is the use of hydrogen storage with an electrolyser/fuel cell system. In such a configuration hydrogen is produced during periods of surplus wind through the electrolyser and subsequently used during times of shortage of wind by the fuel cell to generate electricity to supply the load.

Stored hydrogen could be also used as a fuel for vehicles or boats owned by the island community. This could be the basis of a local hydrogen economy that would make the remote area independent from external supply of fossil fuels. In this chapter a hydrogen system is designed to support electrical diesel generation on Grimsey. Additionally a road map is proposed to make this community 100% energy independent in future.

### 9.1.1. Wind to hydrogen projects review

There are numerous examples of wind-to-hydrogen projects all over the world. Most of them have a demonstration focus, serving as knowledge and technology transfer centres for the local communities [1].

Two most prominent examples are on the island of Unst in Scotland and Utsira island in Norway. The Promoting Unst Renewable Energy (PURE) project on Unst has two 15 kW wind turbines as the main power generation, an electrolyser and a 5 kW fuel cell acting as a backup. It serves both the electrical and thermal load of five business properties. Produced hydrogen is also used to fuel a small vehicle used in the project. The hydrogen energy project on Unst is the first community owned project of this kind in the world [1, 2]. The wind-to-hydrogen project on the Norwegian island of Utsira has a similar architecture with additional flywheels that act as a short-term energy storage [3].

Interest in this type of hybrid system is also high in Canada. The Ramea Island project started as a typical wind-diesel hybrid system with six 65 kW wind turbines. To increase its electrical output it was upgraded with 100 kW turbines and a 90 m<sup>3</sup>/h alkaline electrolyser with 2000 m<sup>3</sup> of hydrogen storage (10 bar). Note that in this installation, four 62.5 kW hydrogen powered internal combustion engine generators are used to produce electricity instead of fuel cells [1].

Prince Edward Island has the strongest wind potential in Canada, and has around 74 MW of installed capacity in wind turbines. For the wind-to-hydrogen project at Prince Edward Island one 60 kW turbine is used together with a 66 Nm<sup>3</sup>/h unipolar electrolyser. The produced hydrogen is used to run a retrofitted diesel generator and a backup fuel cell power unit, as well as fuel for a small hydrogen powered bus that is also included in the demonstration [1].

Spain has a few notable examples of wind-to-hydrogen energy storage systems. The RES2H2 Project located at Gran Canary Island utilises one 500 kW turbine together

with a 5 Nm<sup>3</sup>/h electrolyser. Additionally to hydrogen generation the system also produces drinking water through a reverse-osmosis plant. The IOTHER Project in Aragon region investigates variety of differently sized turbines (80 kW, 225 kW, and 330 kW) as well as PV panels for the purpose of hydrogen energy storage. The goal of this project is to optimise all aspects of hydrogen chain – production, management and efficient use [1].

United States has also carried out a few essential wind-to-hydrogen demonstration projects. The Basin Electric, Wind-to-Hydrogen Energy Pilot Project was used to determine the most optimal mode of operation for the wind turbine/electrolyser system. A dynamic scheduling system used to control the intermittent output of the wind turbine to the electrolyser stack was one of the most prominent deliverables of this research. Another project was a result of the cooperation between National Renewable Energy Laboratory and Xcel Energy and is hosted at NREL's National Wind Technology Center (NWTC) in Colorado. In this demonstration renewable energy from wind turbines and PVs in the form of electrolysed hydrogen is used for transportation as well as long term energy storage [1].

### **9.1.2. Grimsey island description**

Grimsey is a small (5.3 km<sup>2</sup> area) island located 40 km from the north coast of Iceland. Its location makes it the only Icelandic area that is formally part of the Arctic. It has a community of 76 people and a total of 40 buildings. Electrical load is served by three 220 kW diesel generators. This location and a few other remote communities, prevent Iceland from claiming the title of having 100% renewable electricity generation. In 2012 the origins of almost all Icelandic electrical energy were hydro (70.3%) and geothermal (29.7%) power plants. The amount of electricity generated from fossil fuels was below 0.1 % [4].

There have been a lot of studies done so far that have proposed alternative energy solutions for the island. An underwater cable that would connect Grimsey to the national grid was discarded as too costly and technically challenging. It would also disturb the local fishing industry. There have been a few studies of wind power

implementation, both on a large scale (single 660 kW turbine) and also with small scale wind turbines (connected to a water break for heat generation). Another project specified the installation of heat pumps as well as experimental drilling for the possibility of geothermal energy. Lately, research has focused on assessing the feasibility of wood biomass for power generation. The Keilir Institute of Technology was involved in a study of a methanol fuel cells implementation on Grimsey. Data regarding the electric load and other important information about island gathered for the purpose of that research are used in this study. So far, the only advancement in the island energy system was the utilisation of diesel generators' cooling water for space heating in three buildings [5].

The motivation for energy alternatives at Grimsey is that energy generation on the island is heavily subsidised with public funds. It is estimated that in 2011 more than \$400,000 of government subsidies were spent on that purpose. This creates a favourable economic environment for creating a sustainable fossil-fuel-free solution for the island.

## **9.2. Research methodology**

HOMER Legacy v 2.68 software was used to model and propose solutions for Grimsey. HOMER is micropower optimisation software that simulates the operation of a proposed system by making an energy balance calculations for each of the 8,760 hours in a year.

### **9.2.1. Project assumptions and basic model data**

For the purpose of the project only electrical load data was used for modelling different system architectures and existing thermal demand was not included. The peak electric load was 175 kW with an average daily energy consumption of 2.4 MWh. The data was provided by the utility company RARIK and analysed in a bachelor thesis project at Keilir Institute of Technology [6]. *Figure 9-1* presents a comparison of average daily loads for 2010 and 2011. Due to its small population



and lack of commercial and industrial facilities, the island has a residential characteristic with peaks happening in the evening. Hourly averages of electrical load for a whole 2011 were used in the HOMER model discussed.

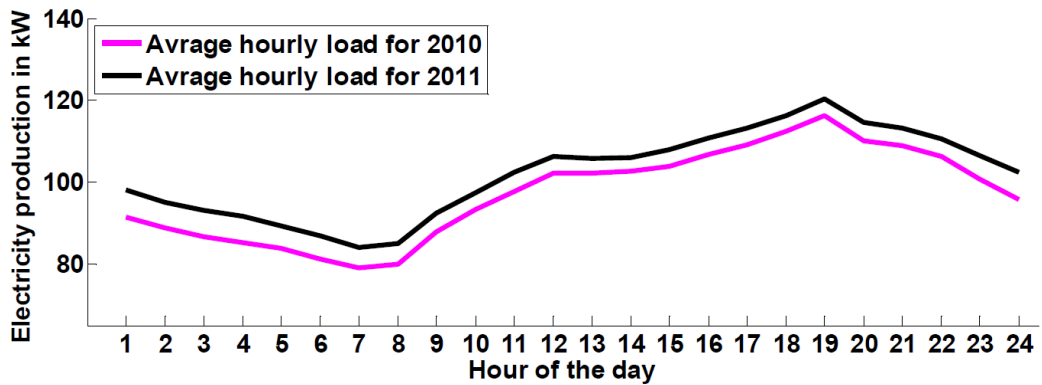


Figure 9-1. Comparison between the average hourly load of 2010 and 2011 [6]

The wind speed data for the island was based on work done in previous studies by the students of the SIT Study Abroad programme [7, 8]. The data used in the model, was collected by the Icelandic Meteorological Office in the year 2008. It represents hourly averages of the wind speed measured at the height of 10 meters above the ground level.

Figure 9-2 presents a yearly distribution of the load profile and monthly average wind speed. There are seasonal peaks visible for both parameters. During the winter months the winds tend to be stronger as is the electricity consumption due to lighting and heating needs.

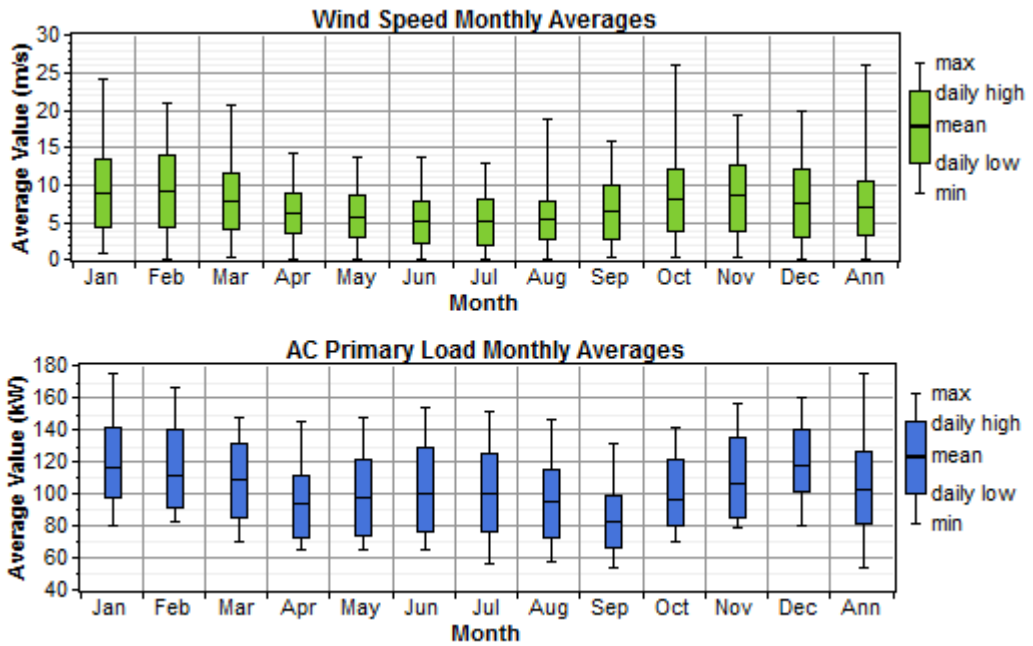


Figure 9-2. Comparison of annual wind and load profile for Grimsey

### 9.2.2. System components and architecture

Figure 9-3 depicts the basic system elements that are being considered in the HOMER model. Three different scenarios were simulated: wind-diesel, wind-diesel-hydrogen and wind-hydrogen systems. For each of mentioned configurations variety of system component combinations and sizes were studied.

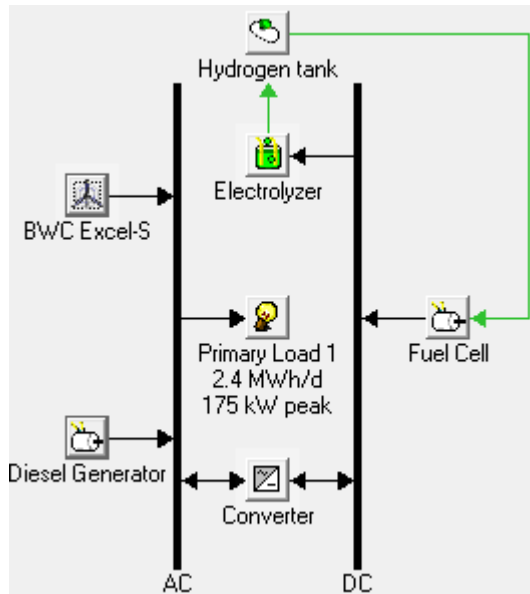


Figure 9-3. System layout in HOMER software

### 9.2.3. Component costs and parameters

US Department of Energy (DOE) and National Renewable Energy Laboratory (NREL) cost reports and conference proceedings were used to estimate the costs of individual components [9-12]. These data were also compared with the numbers received from industrial inquiries. *Table 9-1* presents the costs of all system components together with the most important parameters. It was also assumed that costs can be scaled linearly with the size of the component. As a basis for the hydrogen tank parameters, NREL report [9] mid-term assumptions were used. In case of the electrolyser, the initial cost calculation was based on a price of 430 \$/kW taken from the DOE report [11] for a 2011 alkaline electrolyser system. Additionally to this, the cost of compressor (\$100,000) was added. It was also assumed that electrolyser stack needs replacement every 10 years for 30% of the total electrolyser system cost and 100% of compressor price [9]. Operational costs were assumed to be 5% of initial electrolyser cost yearly [9]. System efficiency was based on the true NEL P-60 electrolyser unit average efficiency and is assumed constant over time and different load conditions. Fuel cell parameters were based on another analysis performed for NREL for stationary proton exchange membrane units, with nominal power over 100 kW assuming that a company produce around fuel cell 100 units

yearly [11]. This system price was also reduced by the cost of the fuel processor subsystem for natural gas reforming, because in the performed study the use of pure hydrogen is assumed. Operation/maintenance costs and lifetime were taken from the same report [11]. Fuel consumption of hydrogen by the PEM fuel cell unit was set to be 0.045 kg/hr/kW, which corresponds to efficiency of around 67% based on higher heating value (HHV) and is assumed constant over the load range, as with the electrolyser. Wind turbine parameters for the Fuhrlander 100 kW units were modelled in the HOMER software. The cost of wind turbine units were taken from Distributed Generation Renewable Energy: Estimate of Costs report by NREL [10], which stated a cost of ~3,600 \$/kW for a wind turbine of size 100 kW-1,000 kW. Maintenance costs were stated there to be 44 \$/kW/year and lifetime of 20 years. A 220 kW diesel generator was modelled, which corresponded to the size of the physical unit installed in Grimsey. The diesel generator efficiency was assumed to be constant over the whole range of load and based on the average fuel consumption of 0.27 l/kWh. Operation and maintenance costs of the diesel generator were neglected. Converter cost estimation was based on an assumption that its costs represent 25-30% of the total costs of electrolyser [9], since both the electrolyser and fuel cell needs a converter to be connected to the grid, this price was doubled. Efficiency of the converter was set to default value for HOMER software.

All the costs used as input to the model were based on current state of the art technology, which probably should be lowered over the next few years, a trend typical for new technologies of this type. The biggest uncertainty is probably for hydrogen fuel/cell technology costs, which is still at the stage of early commercialisation, so finding exact prices was a challenging task.

Component name	Parameter	Value
<b>Hydrogen tank</b>	Size (kg)	85
	Capital (\$)	40,000
	Replacement (\$)	40,000
	O&M (\$/year)	2,000
	Lifetime (years)	20
<b>Electrolyser</b>	Size (kW)	294
	Capital (\$)	326,000
	Replacement (\$)	240,000
	O&M (\$/year)	6,300
	Lifetime (years)	10
	Efficiency (%)	72.4
<b>Wind turbine (Fuhrlander 100 kW)</b>	Capital (\$)	360,000
	Replacement (\$)	360,000
	O&M (\$/year)	3,800
	Lifetime (years)	20
	Hub height (m)	40
<b>Fuel cell</b>	Size (kW)	100
	Capital (\$)	55,000
	Replacement (\$)	55,000
	O&M (\$/year)	2,000
	Lifetime (operating hours)	60,000
	Efficiency (%)	67
<b>Converter</b>	Size (kW)	300
	Capital (\$)	225,000
	Replacement (\$)	225,000
	O&M (\$/year)	0
	Lifetime (years)	20
	Inverter Efficiency (%)	92
	Rectifier Efficiency (%)	85

*Table 9-1. Summary of basic system parameters*

#### **9.2.4. Economical parameters**

Economical values were based on the current situation. Probably the most important economical factor used in analysis was the diesel fuel cost set to be 2.39 \$ for litre, which is an approximate value for Grimsey at the date of this study (September, 2013). This value is higher than a price of diesel on the mainland of Iceland (2.08 \$/l - September, 2013 [13]) and reflects transportation costs for this remote community. The price was estimated based on knowledge that average costs of electricity for Arctic remote locations powered from diesel generators are about 0.65 \$ for kWh according to Windwatcher Systems President, Tom Ellis [14]. Considering the efficiency of a diesel generator of the size used is 0.27 l/kWh, a fuel cost of ~2.39 \$/l was obtained. The fuel price is also likely to increase in the future taking into account world trends of oil price, so it might be considered as rather conservative to be kept on this level for whole project lifetime. Any increase of oil price over this level would surely decrease the payback period calculated for the considered scenarios. The annual interest rate was kept at the HOMER default value of 6%, a realistic estimate for Iceland, for which interest for the period 2008 - 2012 oscillated around this value, according to World Bank [15]. Project lifetime was set to be 20 years which is typical lifetime for wind turbines, the most expensive part of the investment, and stack replacement has already been accounted for. The maximum annual capacity shortage was decreased to 0% and the rest of the parameters were kept at their default values.

### **9.3. Results and discussion**

Three scenarios for the implementation of a wind-hydrogen infrastructure are analysed. They might each be considered independently, but it is suggested to treat them successively as a roadmap, because each of them introduces more sophisticated infrastructure and each further scenario uses all parts of the system from the previous one. According to this approach for Grimsey, it is initially suggested to install a classic wind-diesel system. This should be followed by a wind-hydrogen-diesel system; and finally a by a wind-hydrogen system that can deliver the 100%

renewable energy scenario.

### 9.3.1. Wind-diesel system

As an initial step of introducing renewable energy to the Grimsey society, the deployment of wind turbines was considered. As an example, wind turbines parameters of the Fuhralander 100 kW were used for simulations. It was assumed that 100 kW wind turbines should be suitable for Grimsey as several wind turbines of this type are able to supply the whole island's electricity needs. Such a configuration also provides redundancy in case any turbine would need to be shut-down for maintenance work or due to accidental damage. On the other hand one larger wind turbine would decrease initial cost, however in case of any accidental shut-down the entire community would need to use expensive diesel generator electricity. An additional challenge with practical project implementation is that wind turbines would need to be resistant to the difficult environmental conditions that are expected to occur in the Arctic. It is worth noting that there have already been systems employed which operate in similar conditions, for example in Antarctica [16]. In this case gearbox-less, direct drive, wind turbines mounted on steel towers were able to operate without any major issues.

During the performed simulations there were considered scenarios with up to 6 wind turbines. Simulation outputs showed that the optimal configuration, taking into account net present costs (NPC) of operation for 20 years, requires the installation of 3 wind turbines (*Table 9-2*). It might be seen that cost of energy (COE) is the lowest for this scenario, diesel usage is reduced for over 50% and the renewable energy fraction is supposed to be around 76%. Note that the initial cost of each wind turbine is around \$360,000 or \$1,080,000 for the whole investment. The estimated simple payback period (SPP) is below 4 years with internal rate of return (IRR) equal 26.2%, which is reasonable value, close to Enerpower company estimation which calculates 100 kW turbine typical payback period to be 3.8 years [17]. Further increase in wind turbines amount over 3 units does not result in any decrease in energy costs. This is connected with the unpredictable character of wind and excess electricity amount produced that is not possible to be consumed immediately by the existing load.

Wind Turbines [Amount]	Initial costs [\$]	Opt. costs [\$/yr]	Net Present Costs [\$]	Costs of Energy [\$/kWh]	RE fraction	Diesel cons. [l/yr]	SPP [yrs]	IRR [%]	Excess electricity [kWh/yr]
0	0	578,856	6,639,435	0.648	0	242,199			
1	360,000	446,731	5,483,966	0.535	0.4	185,327	2.72	36.6	238,693 (21.1%)
2	720,000	376,134	5,034,232	0.491	0.61	154,198	3.74	28	571,872 (39.0%)
3	1,080,000	293,555	4,447,056	0.434	0.76	118,057	3.88	26.2	886,556 (49.8%)
4	1,440,000	263,026	4,456,893	0.435	0.82	103,693	4.56	21.5	1,281,646 (58.9%)
5	1,800,000	244,103	4,599,844	0.449	0.87	94,185	5.46	17.9	1,694,661 (65.5%)
6	2,160,000	230,566	4,804,571	0.469	0.89	86,931	6.88	15.2	2,115,980 (70.3%)

Table 9-2. Simulation results for wind-diesel systems

Figure 9-4 presents percentage of excess electricity generated and net present costs of the investment over lifetime as a function of wind turbines amount installed. It might be seen that with every wind turbine amount of excess electricity increases. NPC value of the investment decreases until the value of 3 wind turbines and then it starts to slowly rise with any additional wind turbine. In the scenario with 3 wind turbines almost half of the energy generated consists of an excess load (49.8%) and in case of 6 wind turbines this amount rises to 70%. This non consumable energy



reduces system efficiency. Due to that feasible solution is an application of energy storage mechanism, which enables possibility of energy accumulation over a period of time and to use it more effectively, when there exists a demand.

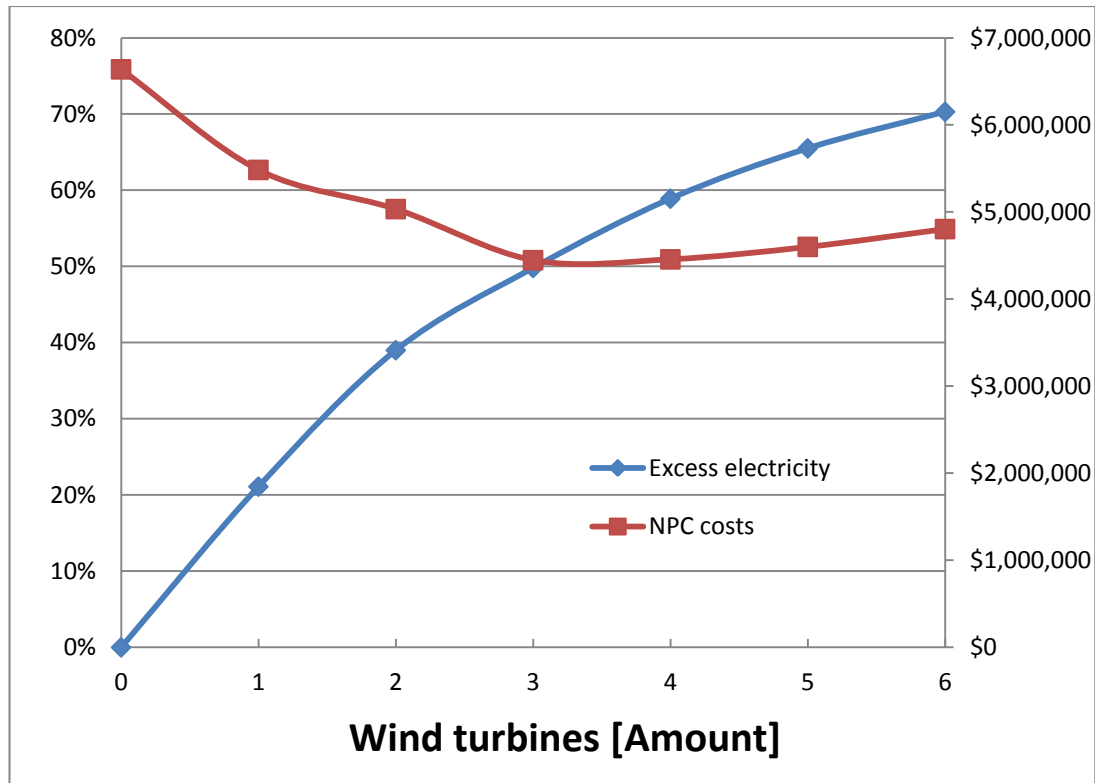


Figure 9-4. Percentage of excess electricity generated and net presents costs of the investment over lifetime in a function of wind turbines amount

### 9.3.2. Wind-diesel-hydrogen system

Analysis of the wind-diesel case showed that over certain amount of wind energy fraction substantial storage is needed. This situation occurs due to the variability and intermittency of power delivered by wind turbines. When wind blows at a time when there is no electrical load, or the wind potential exceeds the needs of the community, the wind turbines' output power has to be limited and wind potential is lost. To overcome this issue, different on site storage systems are proposed in the literature. The most popular ones are: batteries; fly wheels; compressed air energy storage (CAES), super capacitors or hydrogen [18-20]. The definitive advantage of a hydrogen system among other technologies is that it is suitable for long term storage

covering up to weeks/months, whereas the most popular alternative; batteries, are considered to store energy for maximum time of few days [19, 20], as are flywheels and CAES [20]. In the conditions on Grimsey there occur significant electrical load and wind variations over the seasons and such long term storage might be indispensable (*Figure 9-2*). Hydrogen technology also can provide high power outputs without any problems, which is the limiting factor of lead-acid batteries that are currently a popular energy storage choice [20].

Optimal results for the wind-hydrogen-diesel (WHD) system were achieved for parameters showed in a *Table 9-3*. Sensitivity parameters show sizes that were considered during system optimisation. For example in the case of wind turbines, sizes were considered for each wind turbine and the electrolyser size was considered in 50 kW steps. It was assumed that optimal results were obtained for the cheapest option taking into account NPC factor (similarly as in wind-diesel system), so the system is assumed to be not 100% renewable and some energy would be still generated from diesel.

Wind turbines [Amount]	Electrolyser Size [kW]	Fuel Cell Size [kW]	Hydrogen Tank Size [kg]	Converter Size [kW]	
<b>3</b>	150	150	250	200	
<b>1</b>	50	50	50	50	<b>Sensitivity parameters</b>

*Table 9-3. Optimal size of components for wind-hydrogen-diesel electricity generation system with sensitivity of each parameter considered*

Economical parameters of the WHD system in comparison to the pure existing diesel configuration are presented in *Table 9-4*. Comparing to the wind-diesel system it is seen that there is a substantial increase over the initial costs, however the simple

payback period, the internal rate of return and net present costs are reduced due to much lower yearly operational costs. This shows the application of storage technology for a wind-diesel system as very beneficial. An additional advantage is that 92% of the electricity is projected to be obtained from a renewable energy source (wind) inside the proposed system, reducing diesel consumption by about 85%, which would significantly decrease emissions. It might be also observed that in comparison with wind-diesel system after application of hydrogen, excess electricity amount decreased from 886,556 (Table 9-2) to 232,269 kWh/year (Table 9-4).

System type	Initial costs [\$]	Opt. costs [\$/yr]	Net Present Costs [\$]	Costs of Energy [\$ kWh]	Ren. energy fraction	Diesel cons. [l/yr]	SPP [yrs]	IRR [%]	Excess electricity [kWh/yr]
<b>Diesel</b>	0	578,856	6,639,435	0.648	0	242,199			
<b>WHD</b>	1,592,307	124,939	3,025,344	0.295	0.92	35,058	3.68	28.6	232,269 (14%)

Table 9-4. Economical comparison of wind-hydrogen-diesel electricity generation system with diesel

Figure 9-5 shows the NPC for the 20 years operational period of each of the used components. The biggest costs are connected with wind turbines that are equal to \$1,210,000 of which majority is the initial investment. As it might be seen despite the reduction of diesel consumption, down to 8% comparing to the base case diesel scenario, money spent on oil still remains significant at \$960,000. Electrolyser and fuel cell costs are the next largest costs, estimated to be respectively \$271,000 and \$247,000. Slightly lower would be the cost of hydrogen tank (\$185,000) and converter (\$150,000).

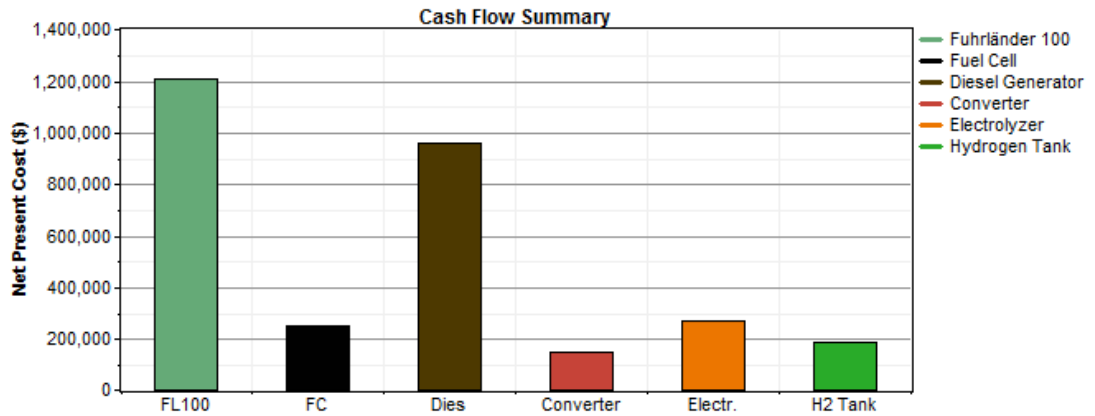


Figure 9-5. Lifetime cash flow summary of WHD system

In this scenario, it is interesting to observe the hydrogen storage level each month in comparison with the monthly excess electricity production and diesel generation (Figure 9-6). The diesel generator would be mainly used during the months of June, July and August, when the lowest wind potential and relatively high electricity demand are observed (Figure 9-2). Significant increase in stored hydrogen is seen due to rise in wind speeds from September until March. The hydrogen storage average level peaks in January, from when it slowly decreases until June, when it reaches its minimum level. Figure 9-6 shows also that during the months of January, February and November hydrogen energy storage was never emptied completely. Performing the detailed results analysis it was also found that the only months which did not require energy storage for a period longer than a week were June, July and August. This shows a definitive need of storage technology for periods of weeks, which justifies the usage of hydrogen storage for Grimsey. Worth noting is that, in potential future analysis there might be also considered a scenario with an application of hybrid energy storage system where both long-term and short-term storage technologies would be applied simultaneously. Regarding the amount of excess electricity there is observed a visible trend, that it is the highest during the windiest months with the lowest electricity demand (Figure 9-2). Additionally during the months of June, July it might be observed, that the excess electricity amount is only caused by limited power of electrolyser unit as hydrogen storage tank is never completely full. During any other months excess energy might be also be induced by limited hydrogen storage tank capacity.

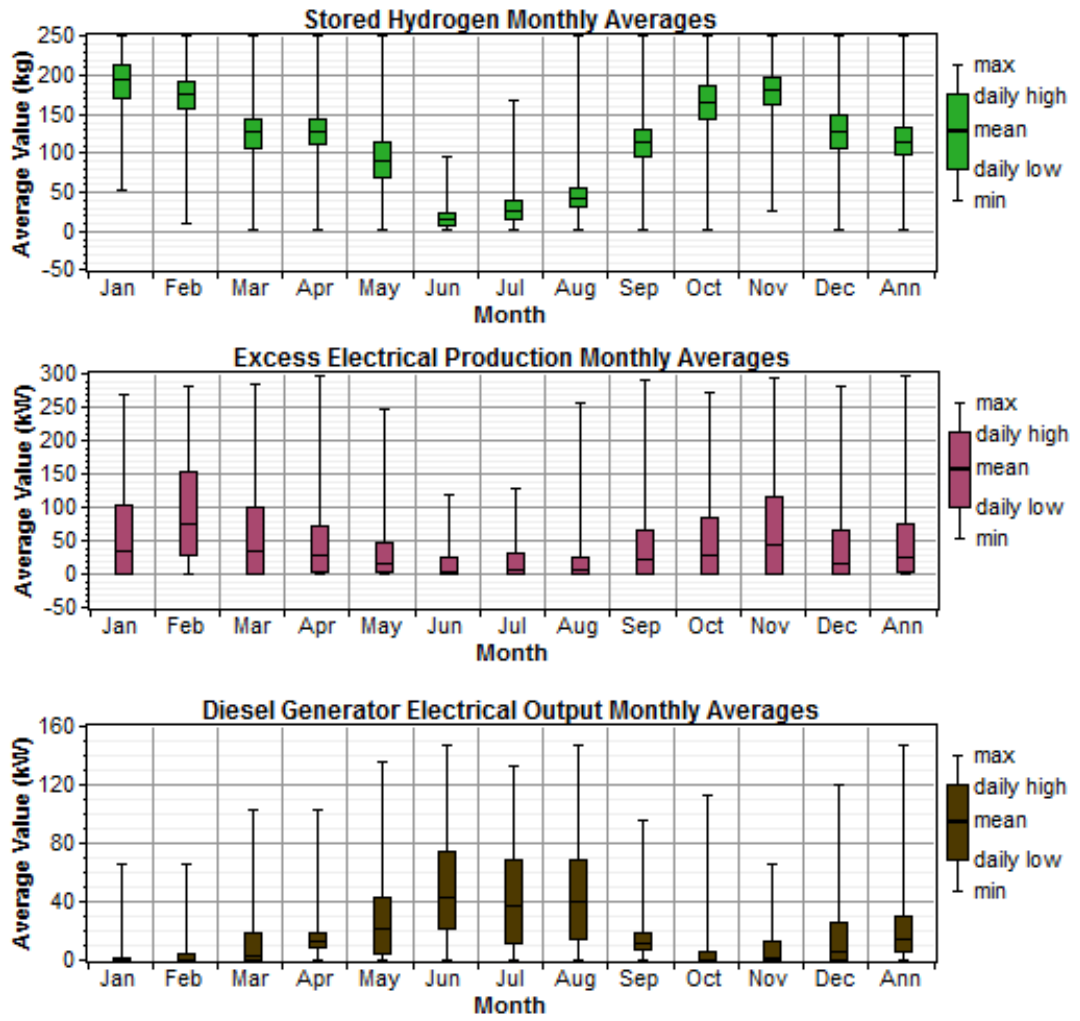


Figure 9-6. Comparison of stored hydrogen, excess electrical production and diesel generation monthly – WHD system

### 9.3.3. Wind-hydrogen system

Wind to hydrogen (WH) system is the scenario where Grimsey is assumed to be 100% energy independent and the diesel generator is not needed anymore. Optimal results of this simulation are presented in a *Table 9-5*. As it might be seen, such a configuration requires a significant increase in the number of wind turbines, storage capacity, electrolyser and converter powers, which drastically increases the initial costs compared to the system supported by diesel. Despite a reduction of operational costs, such a configuration for today is less cost-effective than the WHD system taking into account NPC value (*Table 9-6*). It is interesting to note that NPC and cost of electricity for this configuration is the same as in case of optimal WD system however, very high initial costs prevent our recommendation of this system for implementation at the current state of the art. Practical transition from a 92% (WHD system) to 100% renewable system (WH system) would require doubling the initial cost investment, increasing the average cost electricity and simple payback period factors. Clearly diesel fuel provides a very cheap long term means of energy storage.

Wind turbines [Amount]	Electrolyser Size [kW]	Fuel Cell Size [kW]	Hydrogen Tank Size [kg]	Converter Size [kW]	
7	300	150	850	300	
1	50	50	50	50	<b>Sensitivity parameters</b>

*Table 9-5. Optimal size of components for wind-hydrogen electricity generation system with sensitivity of each parameter considered*

System type	Initial costs [\$]	Opt. costs [\$/yr]	Net Present Costs [\$]	Costs of Energy [\$ / kWh]	Ren. energy fraction	Diesel cons. [l/yr]	SP [yr]	IRR [%]	Excess electricity [kWh/yr]
<b>Diesel</b>	0	578,856	6,639,435	0.648	0	242,199			
<b>WH</b>	3,555,986	77,694	4,447,135	0.434	1.00	0	6.99	12.9	1,773,661 (52.9%)

*Table 9-6. Economical comparison of wind-hydrogen electricity generation system with diesel*

The main reason for such a drastic increase of cost are low wind conditions during the months of June, July and August (*Figure 9-6*). In this period excess electricity is the lowest and a large amount of electricity is generated from hydrogen, which was previously accumulated for the winter months. It is interesting to note that during winter there exist a lot of periods when the hydrogen storage is full and a surplus of electricity still occurs. For this reason options to use hydrogen for other onsite purposes, for example house heating, fuelling vehicles and/or boats, should definitely be considered. Such an onsite demand for produced hydrogen could improve the economics of the 100% renewable energy scenario. Worth noting that in case of using hydrogen to external needs, there might also occur an issue with the water supply. In the described system for considered maximum hydrogen storage of 850 kg, there would be needed 7650 kg of very pure, distilled water. This amount for example could be transported to the island once and then, it might be kept in a closed loop cycle. Namely water produced as a side product in a fuel cell reaction would be captured and re-used for hydrogen production in electrolyser. On the other hand if hydrogen applications would be extended to fuelling of vehicles or ships, implementation of such water capturing system would require more sophisticated design.

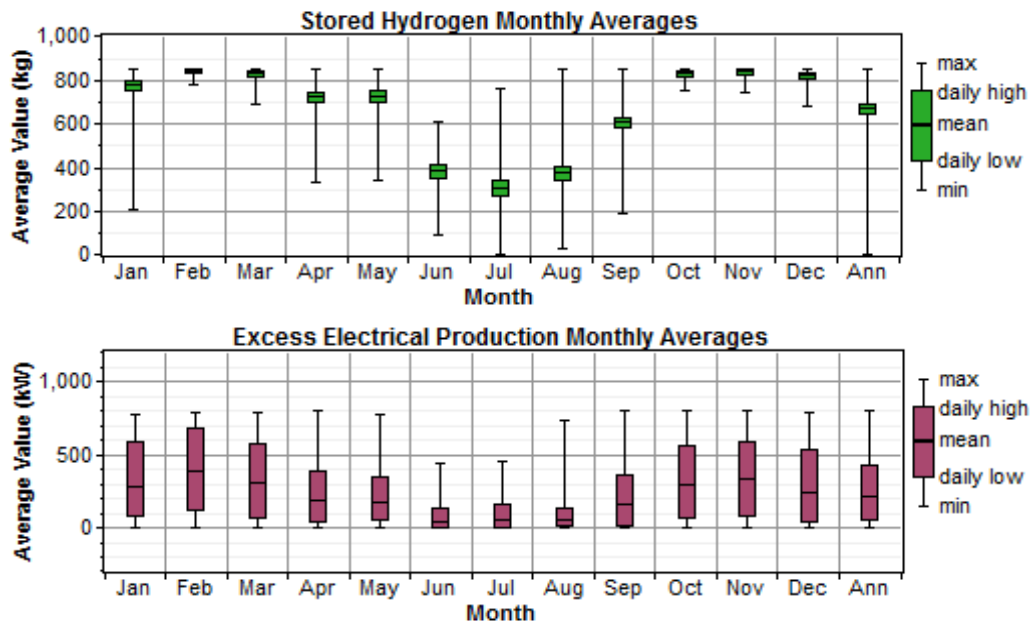


Figure 9-7. Comparison of stored hydrogen, excess electrical production - WH system

#### 9.4. Conclusions

Three scenarios of wind-diesel, wind-diesel-hydrogen and wind-hydrogen systems have been proposed for implementation to support the Grimsey electrical grid. Practically all the proposed systems reduced the running costs during the lifetime of 20 years however each of them required a substantial amount of initial investment. For current practical implementation, the author recommends the wind-hydrogen-diesel system as it has the lowest costs of operation from all mentioned configurations and is characterised by moderate costs of investment.

Wind hydrogen infrastructure for the island, can be introduced slowly step by step by firstly deploying wind turbines and then adding hydrogen storage. Third step of this road-map would be switching for 100% renewable electricity generation, which is not advised for now. In the future when it is probable that renewable energy technology investment prices will decrease and oil prices will rise, wind to hydrogen system might become more cost-effective. It is worth noticing that when a 100% renewable energy system is examined, optimal storage is not able to consume a



major part of excess energy and some alternatives for using this excess electricity should be considered, for example application of hydrogen for vehicles and boats across the community.

Summarising, the described scenarios only take into account the electrical load for Grimsey which is dominated by space and water heating. Hydrogen can also be used for heating using specially designed hydrogen boilers or through electrical energy delivered from a fuel cell device. If electricity is to be used for heating it would make sense also to explore the use of heat pumps. The proposed systems show very good results in supporting the island's electrical load however, before any practical implementation is made, heating needs should be carefully considered.

Finally, achieved result of less than four year payback period of the entire system, should start serious discussion about hydrogen applications in the northern part of the globe. The Arctic area characteristic features are: excellent wind potential with seasonal variations [21], high energy prices [14] that seem to be very similar to the modelled case. Due to that it might be worth to consider implementation of wind-hydrogen system also for other arctic remote communities.

## References:

1. K. Harrison, R. Remick, G. Martin. *Hydrogen Production: Fundamentals and Cas Study Summaries*. World Hydrogen Energy Conference, Essen, Germany, 2010
2. [http://www.ingenia.org.uk/ingenia/issues/issue37/Issue37\\_InBrief.pdf](http://www.ingenia.org.uk/ingenia/issues/issue37/Issue37_InBrief.pdf), accessed 14<sup>th</sup> September 2014
3. [http://www.iphe.net/docs/Meetings/Brazil\\_3-05/Norway\\_Utsira\\_Wind\\_H2.pdf](http://www.iphe.net/docs/Meetings/Brazil_3-05/Norway_Utsira_Wind_H2.pdf), accessed 14<sup>th</sup> September 2014
4. Statistics Iceland. <http://www.statice.is/Statistics>, accessed 14<sup>th</sup> September 2014
5. H. Þ. Ingason, Á. Ragnarsson, Þ. I. Sigfússon. *Sjálfbært Orkukerfi í Grímsey*. Ministry of Industries and Innovation, 2003.
6. K. H. Jakobsson. *Fuel Cell based Combined Heat and Power in Grímsey*. Faculty of Electrical and Computer Engineering, School of Engineering and Natural Sciences, Reykjanesbær, 2012.
7. M. Brancato. *Alternative Energy Systems for Grímsey, Iceland*. SIT Iceland, 2010.
8. V. Rolin. *Wind Energy Potential In the West Fjords of Iceland*. SIT Iceland, 2009
9. G. S. J. Levene. *Wind Energy and Production of Hydrogen and Electricity - Opportunities for Renewable Hydrogen: Preprint*. POWER-GEN Renewable Energy and Fuels Technical Conference, Nevada, 2006.

10. NREL. *Distributed Generation Renewable Energy Estimate of Costs and Useful Life*. 2012, [http://www.nrel.gov/analysis/tech\\_cost\\_dg.html](http://www.nrel.gov/analysis/tech_cost_dg.html), accessed 14<sup>th</sup> September 2014
11. B. D. James, A. B. Spisak, W. G. Colella. *Manufacturing Cost Analysis of Stationary Fuel Cell Systems*. Strategic Analysis report for NREL. September 2013
12. U.S. Department of Energy. *Fuel Cell Technologies Office Multi-Year Research, Development and Demonstration Plan*. July 2013, <http://www1.eere.energy.gov/hydrogenandfuelcells/mypp/pdfs/production.pdf>, accessed 14<sup>th</sup> September 2014
13. <http://www.fuel-prices-europe.info/>, accessed 14<sup>th</sup> September 2014
14. Windwatcher, eWON. *Solving Arctic Power Generation issues, in a Colorado Office*. 9<sup>th</sup> April 2013 [http://www.ewon.biz/en/windwatcher-and-ewon-solving-arctic-power-generation-issues-in-a-colorado-office.html?cmp\\_id=7&news\\_id=2894](http://www.ewon.biz/en/windwatcher-and-ewon-solving-arctic-power-generation-issues-in-a-colorado-office.html?cmp_id=7&news_id=2894), accessed 14<sup>th</sup> September 2014
15. <http://data.worldbank.org/indicator/FR.INR.RINR/countries>, accessed 14<sup>th</sup> September 2013
16. <http://www.antarctica.gov.au/living-and-working/station-life-and-activities/renewable-energy/wind-power>, accessed 14<sup>th</sup> September 2014
17. <http://www.enerpower.ie/page/wind/wind-turbine-payback-period>, accessed 14<sup>th</sup> September 2014
18. M. Hessami, H. Campbell, C. Sanguinetti. *A feasibility study of hybrid wind power systems for remote communities*. Energy Policy, Vol. 39, 2011, pp. 877–886

19. E. Gray, C. J. Webb, J. Andrews, B. Shabani, P. J. Tsai, S. L. I. Chan.  
*Hydrogen storage for off-grid power supply*. International Journal of Hydrogen Energy, Vol. 36, 2011, pp. 654- 663
  
20. International Electrotechnical Commission. *Electrical Energy Storage. White paper*. December 2011
  
21. <http://visibleearth.nasa.gov/view.php?id=56893>, accessed 14<sup>th</sup> September 2014

## 10. Summary

The main aim of the research work was the investigation of Raney nickel electrodes produced by atmospheric plasma spraying (APS) method for use in alkaline electrolyser. To achieve this goal, an electrochemical measurement system was designed, along with the experimental procedures/strategies, based in a large part on detailed literature review of the current state of art of the alkaline water electrolysis technology.

The tests performed on the electrodes confirmed the excellent initial performance (from company literature) towards the hydrogen evolution reaction (HER) and showed that the technology had potential to be developed further. During the work, detailed electrochemical characterisation of the electrodes was performed using the techniques of Tafel extrapolation, cyclic voltammetry and electrochemical impedance spectroscopy. Additionally, the surface of the electrodes was examined by scanning electron microscopy. The conclusions from the characterisation work were, that the overall performance of the tested samples were attributed to the very high electrochemical active area and to the enhanced kinetics obtained for hydrogen evolution reaction following the chemical and electrochemical activation procedures.

The second part of the investigation work on these APS electrodes was aimed at establishing the stability during long-term, variable load operation and to identify degradation mechanisms and so develop strategies to minimise their impact. Such work was invaluable before any further technology commercialisation was carried out towards the implementation of the APS electrodes in industrial alkaline electrolyser units. The results obtained showed that hydrides formation was a main source of deactivation for the cathodes and could reduce their performance drastically after less than 48 hours of continuous operation. To prevent this effect, techniques of hydrides oxidation and the use of additives to the electrolyte were tested, but neither could eliminate it completely. The overall work conclusion was that suppressing the hydrides impact was possible, but only through by improving electrode manufacturing process for example by application of special coatings. The performed research also resulted in some additional outcomes. One of them was the

development of an electrochemical measurement device from concept to initial prototype, which was built using cheap electronic components. The device showed the same functionality as commercial instruments. It was thus able to deliver any type of variable load voltage to multiple electrode samples, register current, voltage, temperature parameters and its price was over ten times lower in comparison with actually available units on the market. The system had a unique functionality allowing bubbles impact observation through a USB camera. This in fact created a motivation for further concept development. For example, this or similar systems could be implemented if a large number of tests of the electrodes needed to be carried out and limited funds were available.

Finally, as a final part of the research project, the hydrogen technology commercialisation possibility was investigated. An economical case study for Grimsey island was performed and this indicated that the application of hydrogen storage could effectively increase hybrid wind energy-diesel systems efficiencies.

### **10.1. Future work**

The main future work should focus on further tests and improvements of Raney nickel APS electrodes. During the work performed, the initial version of those electrodes was tested as cathodes and it was found that the deactivation towards HER due to hydrides formations occurred. To prevent this deactivation process, the new version of the APS electrodes with molybdenum coatings is suggested to be produced. Addition of molybdenum should also improve the efficiency of hydrogen evolution reaction. The experimental work performed showed that as yet unidentified deactivation processes for anode electrodes also occurred and these should be also investigated in detail. Moreover there exists an opportunity of improving efficiencies of oxygen evolution reaction by mixing Raney nickel with active oxides compounds such as  $\text{Co}_3\text{O}_4$  and/or LSCF (lathanum strontium cobalt iron oxide). Additional benefits are expected from optimising the electrode production process by minimising the amount of catalyst usage with application of alternative cheaper materials. This could be done for example by finding an optimal catalyst layer and

catalyst layered plate thicknesses and/or substitute nickel plates with cheaper alternatives, such as stainless steel. Such new versions of the electrodes would need to be subsequently tested during long-term variable load operation, which might be done using the developed during this project experimental techniques and system.

Additional experiments might be done with the designed prototype of the electrochemical measurement device, so that functionality could be extended by adding new software to enable for example current control operations, cyclic voltammetry, Tafel extrapolation options, which normally can be found in commercially available units. The prototype also needs to be tested during long-term operational conditions since the performed analyses were only short-term operations listing several days only.

Finally, further work might be performed regarding the economical study of hydrogen storage system on Grimsey. This study could be extended to include heat demand and investigate other renewable generation technologies such as heat pumps, that might improve the achieved results. The study could be an initial point of solving Grimsey energy prices problem, for example, by initiating practical wind-hydrogen system implementation.

## **APPENDIX: List of Publications**

### **Journal publications:**

D. Chade, L. Berlouis, D. Infield, A. Cruden, P. Nielsen, T. Mathiesen. *Evaluation of Raney nickel electrodes prepared by atmospheric plasma spraying for alkaline water electrolyzers*. International Journal of Hydrogen Energy 38 (2013), pp. 14380 – 14390

### **Conference publications:**

D. Chade, L. Berlouis, D. Infield, A. Cruden, P. Nielsen, T. Mathiesen. *Evaluation of Raney nickel electrodes prepared by atmospheric plasma spraying for alkaline water electrolyzers*. World Renewable Energy Congress 2013, Perth, Australia

D. Chade, T. Miklis, D. Dvorak. *Feasibility study of wind to hydrogen system for Arctic remote locations – Grimsey island case study*. Arctic Energy Summit 2013, Akureyri, Iceland

M. Kiaee, D. Chade, A. Cruden, D. Infield. *The performance of alkaline electrolyzers during operation with intermittency of wind power*. 4<sup>th</sup> World Hydrogen Technologies Convention 2011, Glasgow, United Kingdom

### **Posters:**

A. Cruden, D. Infield, M. Kiaee, T. Douglas, D. Chade. *Alkaline electrolyzers and their role in the performance improvement of electrical grid*. SuperGen Hydrogen-delivery industry day, Birmingham, September 2011.